



**US Army Corps
of Engineers®**
Engineer Research and
Development Center

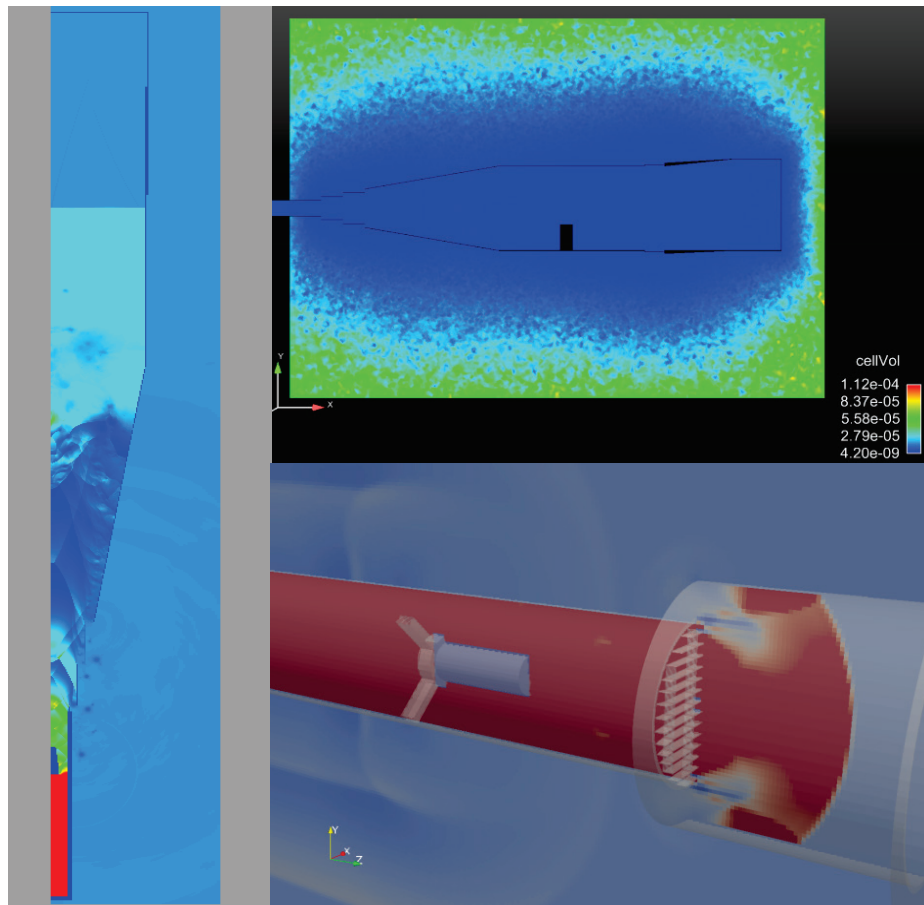
ERDC
INNOVATIVE SOLUTIONS
for a safer, better world

Modeling the Blast Load Simulator Airblast Environment Using First Principles Codes

Report 1, Blast Load Simulator Environment

Gregory C. Bessette, James L. O'Daniel, Stephen A. Akers,
Alyson A. Armstrong, Gustavo Emmanuelli, Clayton Mord,
and Richard A. Weed

November 2016



The U.S. Army Engineer Research and Development Center (ERDC) solves the nation's toughest engineering and environmental challenges. ERDC develops innovative solutions in civil and military engineering, geospatial sciences, water resources, and environmental sciences for the Army, the Department of Defense, civilian agencies, and our nation's public good. Find out more at www.erdc.usace.army.mil.

To search for other technical reports published by ERDC, visit the ERDC online library at <http://acwc.sdp.sirsi.net/client/default>.

Modeling the Blast Load Simulator Airblast Environment using First Principles Codes

Report 1, Blast Load Simulator Environment

Gregory C. Bessette, James L. O'Daniel, Stephen A. Akers,
Alyson A. Armstrong, and Gustavo Emmanuelli

*Geotechnical and Structures Laboratory
U.S. Army Engineer Research and Development Center
3909 Halls Ferry Rd
Vicksburg, MS 39180-6199*

Clayton Mord and Richard A. Weed

*Center for Advanced Vehicular Systems (CAVS)
Mississippi State University
Mississippi State, MS 39762*

Report 1 of a series

Approved for public release; distribution is unlimited.

Prepared for Defense Threat Reduction Agency, Nuclear Technologies Directorate
Ft. Belvoir, VA 22060-6201

Under Project 444856, "Nuclear Airblast and Thermal Environments Testing and Modeling"

Abstract

The Blast Load Simulator (BLS) at the U.S. Army Engineer Research and Development Center (ERDC) has been utilized for applying simulated blast loads on structures for more than a decade; however, the experimental efforts to date have not included a computational modeling component. The Defense Threat Reduction Agency tasked ERDC to conduct an integrated experimental/computational program to evaluate several first principles codes (FPCs) for modeling airblast environments typical of those encountered in the BLS. The FPCs considered were CTH, DYSMAS, Loci/BLAST, RAGE, and SHAMRC. These codes afforded a range of numerical solvers and equation of state options for the modeling effort. The FPCs were evaluated against data generated in the BLS. Three experimental configurations were considered for the validation. These included two empty configurations, with comparisons drawn against reflected pressures measured at the downstream end wall. The third included a box-like structure in the flow field. The structure was instrumented on the exposed surfaces to provide a more challenging scenario for the model comparisons. The purpose of the integrated program was to assess computational accuracy and cost of the aforementioned FPCs and identify any shortcomings in the physics modeling and areas for future improvement. Findings from the integrated program are discussed in this report.

DISCLAIMER: The contents of this report are not to be used for advertising, publication, or promotional purposes. Citation of trade names does not constitute an official endorsement or approval of the use of such commercial products. All product names and trademarks cited are the property of their respective owners. The findings of this report are not to be construed as an official Department of the Army position unless so designated by other authorized documents.

DESTROY THIS REPORT WHEN NO LONGER NEEDED. DO NOT RETURN IT TO THE ORIGINATOR.

Contents

Abstract.....	ii
Figures and Tables.....	iv
Preface	vi
Unit Conversion Factors.....	vii
1 Introduction	1
1.1 Objective.....	1
1.2 Purpose and scope.....	1
2 BLS Overview and Test Configurations	3
2.1 General description	3
2.2 GSA configuration, calibration Tests 30a and 30b	7
2.3 Calibration tests with 8-ft×8-ft C2SQ configuration	8
2.4 BLS 8-ft×8-ft C2SQ configuration with box.....	12
3 Modeling Approach and Comparisons	16
3.1 Overview.....	16
3.2 GSA configuration, calibration Tests 30a and 30b	19
3.3 Calibration tests with 8-ft×8-ft C2SQ configuration	24
3.4 BLS 8-ft×8-ft C2SQ configuration with box.....	29
3.5 Qualitative assessment of accuracy.....	36
3.6 Computational cost	38
4 Summary and Recommendations.....	43
References.....	45
Appendix A: CTH Modeling	48
Appendix B: DYSMAS Modeling.....	80
Appendix C: LOCI-Blast Modeling.....	111
Appendix D: RAGE Modeling	137
Appendix E: SHAMRC Modeling.....	167
Report Documentation Page	

Figures and Tables

Figures

Figure 1. BLS residing within tunnel structure.....	3
Figure 2. Basic GSA configuration.	3
Figure 3. Driver section.	4
Figure 4. Striker assembly, striker, and flange.....	4
Figure 5. Grill placement in the BLS.....	5
Figure 6. Photograph of grill.	5
Figure 7. Instrumentation layout on target wall for GSA configuration.	8
Figure 8. BLS 8-ft×8-ft C2SQ configuration.	9
Figure 9. Circle-to-square transition section C2SQ.	9
Figure 10. Square section SQ1.....	10
Figure 11. Square transition for target vessel face.....	10
Figure 12. View towards target vessel.	11
Figure 13. Typical mounting system for the side-on pressure gauge.	11
Figure 14. Instrumentation layout on target wall.	12
Figure 15. BLS 8 ft×8 ft C2SQ configuration with box.	13
Figure 16. View of box in BLS, looking toward the target vessel.	13
Figure 17. Box location and overall dimensions.	13
Figure 18. Box instrumentation, front and back sides.	14
Figure 19. Box instrumentation, top.	14
Figure 20. Box instrumentation, left and right sides.	14
Figure 21. Active gauges on target wall.	15
Figure 22. FPC comparisons with measured data, GSA configuration.	21
Figure 23. Early time comparison for gauge PE without time-shifting.	22
Figure 24. Individual FPC comparisons for gauge PE.....	22
Figure 25. Gauge comparisons for Test 30a.	24
Figure 26. FPC comparisons with measured data, 8-ft×8-ft C2SQ configuration.....	25
Figure 27. Individual FPC comparisons for gauge P1.	27
Figure 28. Individual FPC comparisons for side-on gauge PR.....	28
Figure 29. FPC comparisons for front face gauge PBF1.	31
Figure 30. FPC comparisons for top face gauge PBT2.....	32
Figure 31. FPC comparisons for right face gauge PBR1.	33
Figure 32. FPC comparisons for back face gauge PBB1.	34
Figure 33. FPC comparisons for target wall gauge P9.	35

Tables

Table 1. Brief description of FPCs used in BLS modeling.	18
Table 2. Summary of FPC problem setup for GSA configuration.	19
Table 3. Time-shifts applied to GSA configuration calculations.	21
Table 4. Summary of FPC problem setup for 8-ft×8-ft C2SQ configuration.	25
Table 5. Time-shifts applied to 8-ft×8-ft C2SQ configuration calculations.	26
Table 6. Summary of FPC problem setup for 8-ft×8-ft C2SQ with box configuration.	30
Table 7. Time-shifts applied to 8-ft×8-ft C2SQ with box configuration calculations.	30
Table 8. Qualitative rankings for code accuracy by tiers.	37
Table 9. FPC computational cost comparison, GSA configuration.....	39
Table 10. FPC computational cost comparison, 8-ft×8-ft C2SQ configuration.	39
Table 11. FPC computational cost comparison, 8-ft×8-ft C2SQ configuration with box.	40
Table 12. FPC costs scaled to 100 msec and fully 3-D calculation.	41

Preface

This study was conducted for the Defense Threat Reduction Agency (DTRA) under Project 444856, “Nuclear Airblast and Thermal Environment Test and Modeling.” The DTRA technical monitor was Culbert B. Laney.

The work was performed by the Structural Mechanics Branch (SMB) of Geosciences and Structures Division (GSD), U.S. Army Engineer Research and Development Center, Geotechnical and Structures Laboratory (ERDC-GSL). The ERDC manager for this program was Dr. James L. O’Daniel. The calculations discussed in this report were carried out on high performance computing systems available at the Department of Defense (DoD) Supercomputing Centers as well as at Mississippi State University.

At the time of publication, Bradford A. Steed was Chief, SMB; James L. Davis was Acting Chief, GSD; and Pamela Kinnebrew was the Technical Director for Force Protection. The Deputy Director of ERDC-GSL was Dr. William P. Grogan and the Director was Bartley P. Durst.

COL Bryan S. Green was the Commander of ERDC, and Dr. Jeffery P. Holland was the Director.

Unit Conversion Factors

Multiply	By	To Obtain
atmosphere (standard)	101.325	kilopascals
bars	100	kilopascals
feet	0.3048	meters
foot-pounds force	1.355818	joules
inches	0.0254	meters
inch-pounds (force)	0.1129848	newton meters
pounds (force)	4.448222	newtons
pounds (force) per foot	14.59390	newtons per meter
pounds (force) per inch	175.1268	newtons per meter
pounds (force) per square foot	47.88026	pascals
pounds (force) per square inch	6.894757	kilopascals
pounds (mass)	0.45359237	kilograms
pounds (mass) per cubic foot	16.01846	kilograms per cubic meter
pounds (mass) per cubic inch	2.757990 E+04	kilograms per cubic meter
pounds (mass) per square foot	4.882428	kilograms per square meter
pounds (mass) per square yard	0.542492	kilograms per square meter
square feet	0.09290304	square meters
square inches	6.4516 E-04	square meters

1 Introduction

1.1 Objective

The Blast Load Simulator (BLS) at the U.S. Army Engineer Research and Development Center (ERDC) in Vicksburg, MS has been utilized for applying simulated blast loads on structures for more than a decade; however, the experimental efforts to date have not included a computational modeling component. The Defense Threat Reduction Agency (DTRA) J9NTE tasked ERDC to conduct an integrated experimental and computational program to evaluate several first principles codes (FPCs) for modeling airblast environments typical of those encountered in the BLS. This integrated program will assess both computational accuracy and cost, as well as identify any shortcomings in the physics modeling and areas for future improvement.

1.2 Purpose and scope

DTRA has tasked ERDC to conduct an integrated experimental and computational program to evaluate a number of FPCs commonly used within the Department of Defense (DoD) community for modeling airblast. The codes include the CTH code developed by Sandia National Laboratories (McGlaun et al. 1990; Crawford et al. 2013b); Dynamic System Mechanics Advanced Simulation (DYSMAS) developed by the U.S. Navy, Naval Surface Warfare Center, Indian Head (Harris et al. 2014); Radiation Adaptive Grid Eulerian (RAGE) developed by Leidos, formerly Science Applications International Corporation (SAIC) (Gittings et al. 2008); and the Second-Order Hydrodynamic Automatic Mesh Refinement Code (SHAMRC) developed by Applied Research Associates (Crepeau et al. 2012). An additional code, Loci/BLAST (Luke 1999; Thompson et al. 2012b), was also considered in the evaluation. The Loci/BLAST code is under development at the Mississippi State University (MSU), Center for Advanced Vehicular Systems. The DoD codes utilize Eulerian solvers of various types, all relying on a structured mesh. The Loci/BLAST code utilizes an unstructured mesh, providing a well-rounded evaluation of capabilities for modeling airblast. There are other codes capable of modeling airblast; however, the ones chosen are thought to have a fairly broad user base with ongoing support on a number of DoD High Performance Computing (HPC) platforms.

The FPCs were evaluated against data generated in the BLS. Specifically, three experimental configurations were considered for the current model validation effort. These included two empty configurations of the BLS, with comparisons drawn against reflected pressures measured at the downstream end wall. The third case included a box-like structure placed in the flow field. The structure was instrumented on the exposed surfaces to provide a more challenging scenario for the model comparisons.

The FPCs evaluated here are in common use within the DoD. They utilize varied numerical approaches for solving the conservation equations. Thus, the model assessment extends beyond just matching experimental data to include the viability of a numerical solver to model this class of airblast problem. The longer term goal is to simulate complex three-dimensional (3-D) environments, which include a number of obstacles in the flow field. It is important to understand the capabilities (both strengths and weaknesses) of each FPC in a simplified setting before tackling more complicated problems. Although several of the BLS configurations could be approximated as axisymmetric, the emphasis for the FPC comparisons was on 3-D modeling as this provides a better indication of a code's performance for handling realistic applications.

This report focuses on the computational effort. A summary of the BLS experimental program is provided herein to provide background for the modeling effort. The summary should provide adequate detail of the three BLS test configurations considered and insight into repeatability of the data. Further details on the BLS and the overall experimental program can be found in Dallriva et al. (2016). The main body of this report deals with the model comparisons and assessment of FPC capability. One should recognize that each code (and solver) is unique. The analysts conducting the calculations were given the flexibility to model the BLS tests in their own way. Further, they were encouraged to explore equation of state (EOS) options, conduct mesh resolution studies, and investigate varied approaches for modeling the BLS driver section. An appendix is devoted to each FPC considered to allow for a detailed discussion of the model setup, the reasoning behind choices made in the setup, and lessons learned during the course of the modeling. The main body of this report focuses on the bigger picture, looking for overall trends and areas for improvement needed in the physics modeling.

2 BLS Overview and Test Configurations

2.1 General description

The BLS, located at ERDC, is housed in a tunnel structure for noise suppression and containment as depicted in Figure 1. The BLS is composed of a series of modular sections that allow flexibility in prescribing the downstream airblast environment. The basic configuration considered for this work is depicted in Figure 2. This particular setup is referred to as the Government Services Administration (GSA) configuration. It is composed of (1) a constant diameter driver section with a striker mechanism and diaphragm, (2) a continuously vented cone (CVC) section and conical expansion section, denoted as GSA C1, (3) a second non-vented conical expansion section, denoted as GSA C2, (4) two constant diameter transition (TR) sections, denoted as GSA TR1 and TR2, (5) a constant diameter, telescoping section, denoted as the GSA-Cascade, and (6) the target vessel. All of the sections depicted in Figure 2 are circular. It should be reiterated that the BLS is modular, and the basic configuration shown here is only one of many possibilities. A general overview of the BLS is provided here. Details on the specific configurations tested will be discussed in subsequent sections.

Figure 1. BLS residing within tunnel structure.

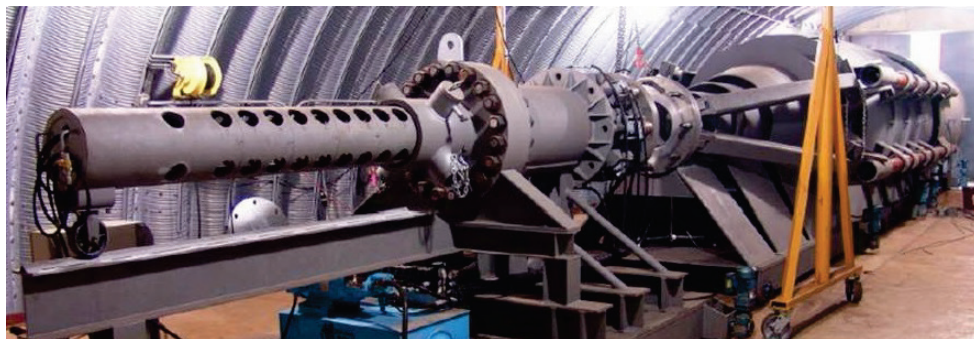
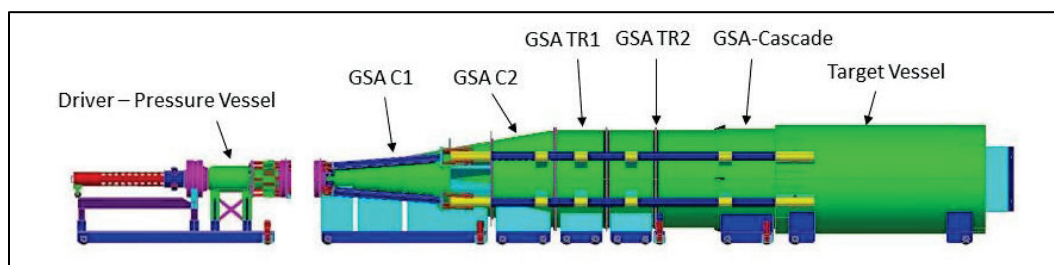
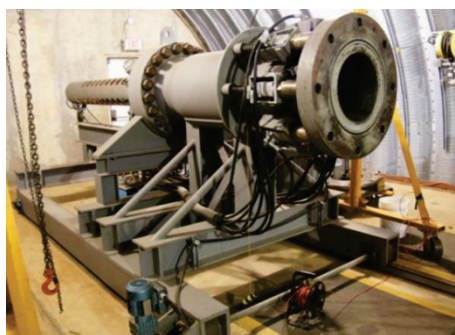


Figure 2. Basic GSA configuration.

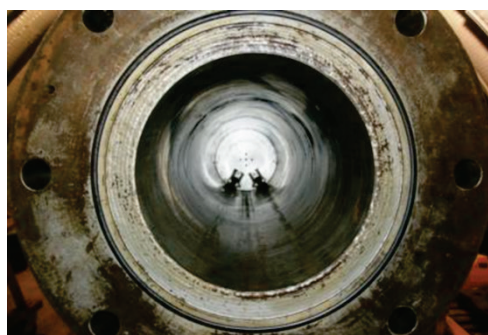


The driver section is depicted in Figure 3. The driver diameter is fixed, having an inside diameter of 16 in. The length can be varied from 18 to 66 in. in 6-in. increments. This allows flexibility in controlling the loading pulse duration. During operations, a diaphragm is placed on the downstream end to enclose the pressure vessel. The driver is then pressurized to the desired test (burst) condition. A striker mechanism is placed outside of the diaphragm and subsequently used to rupture it. Following rupture, the pressurized gas vents into the downstream BLS sections. The striker assembly (without the diaphragm) is depicted in Figure 4. The actual striker mechanism resides outside of the pressure vessel. The flange section of the assembly is bolted to the driver with the diaphragm on the inside to seal the pressure vessel during test operations. The BLS can accommodate mixed gases (e.g., helium and air); however, for the tests reported herein, the mixture was limited to 100 percent air to reduce uncertainty in the EOS modeling by the FPCs.

Figure 3. Driver section.



(a) Driver.

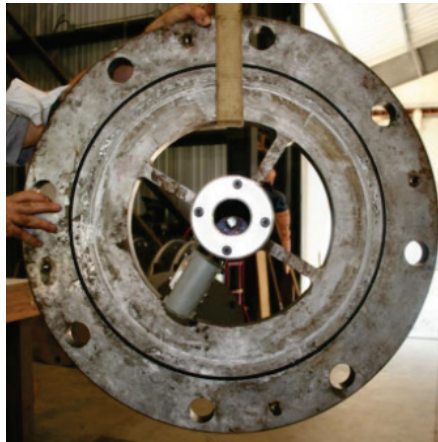


(b) Interior view.

Figure 4. Striker assembly, striker, and flange.



(a) Exterior view.



(b) Interior view.

The rupture of the diaphragm results in the generation of fragments that travel downstream. These fragments can adversely impact test structures placed within the BLS as well as damage other interior components and instrumentation. A grill is typically included in the test setup to trap fragments and mitigate any damage to downstream components. The location of the grill in the BLS is shown in Figure 5. A photograph of the grill is provided in Figure 6. The outside diameter of the grill is 17-5/8 in. The horizontal and vertical bars in the grill are 1/8-in. thick with a depth of 1 in. The spacing between the horizontal and vertical bars is 1 and 4 in., respectively.

Figure 5. Grill placement in the BLS.

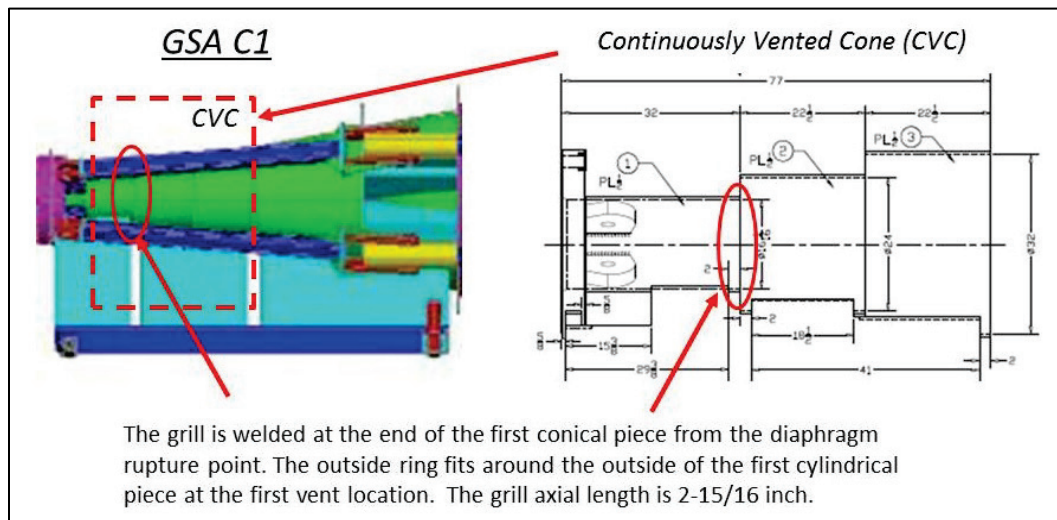


Figure 6. Photograph of grill.



The CVC cross section depicted in Figure 5 is composed of three cylindrical sections, referred to as CVC-1, -2, and -3. CVC-1 has a length and inner diameter of $31\frac{7}{8}$ and $16\frac{1}{16}$ in., respectively. CVC-2 has a length and inner diameter of $22\frac{1}{2}$ and 24 in., respectively. CVC-3 has a length and inner diameter of $22\frac{1}{2}$ and 32 in., respectively. The shell thickness for each section is $\frac{1}{2}$ in. The first and second sections overlap by $2\frac{15}{16}$ in. when the grill is attached to CVC-1. There are cylindrical vents at each overlap of the CVC sections. This is the primary means for the gas blow-down in the BLS.

The CVC connects to an expanding conical section having a 20-deg cone angle. The length of the expansion section is $79\frac{13}{32}$ in. The inside diameter of this cone at the upstream and downstream sides is 40 and 68 in., respectively. The CVC and attached cone comprise the GSA C1 section. The shell thickness is $\frac{1}{2}$ in.

The GSA C2 is the next downstream section. It also has a 20-deg cone angle. The length of this section is $58\frac{1}{8}$ in. The inside diameter of the C2 cone at the upstream and downstream sides is 68 and $88\frac{1}{2}$ in., respectively. The shell thickness is $\frac{1}{2}$ in.

A series of constant diameter sections reside downstream of GSA C2. These are the two transition sections (TR1 and TR2) and the Cascade. The length and inner diameter of each of the transition sections is 46 and $88\frac{1}{2}$ in., respectively. The shell thickness for the transition sections is $\frac{1}{2}$ -in. The Cascade is a telescoping section that allows for a variable length. The upstream Cascade section has a length and inner diameter of 58 and $88\frac{1}{2}$ in., respectively. The downstream Cascade section has a length and inner diameter of 52 and 91 in., respectively. The shell thickness for each is $\frac{1}{2}$ in. There is a slight radial gap between the Cascade sections to facilitate the telescopic movement.

The target vessel at the far end of the BLS serves as a reaction mass. It has a flat wall on one end (the left side of the vessel in Figure 2) that has reflected pressure gauges embedded within it. This is commonly referred to as either the calibration plate or target wall, depending on the nature of the test. This report will make use of the latter term, as it is more general. Reflected pressure data on the target wall were captured in all of the tests outlined in this report. The BLS is modular, allowing for additional sections to be included in the configuration. There is no restriction that the

added sections be circular. In fact, two of the configurations discussed herein had square cross sections. The only stipulation is that the transition of the blast front between sections be smooth and have a negligible effect on the waveform.

The expansion and transition sections downstream of the CVC are designed to help facilitate the formation of a planar shock front. The amplitude and duration of the pulse are largely defined by the burst pressure and the driver length. An ideal waveform is one that has an initial peak followed by an exponential decay. In practice, the character of the pulse can differ from the ideal. When the computational effort was started, the BLS was undergoing a number of design iterations, with the waveforms differing slightly from the ideal. This is irrelevant for the modeling effort, as the FPCs should be able to capture the form and character of the measured waveform. For the tests reported herein, the burst pressure was 1,298 psig for all cases. This ensured that the initial conditions were consistent for the FPC comparisons.

As mentioned earlier, three different BLS configurations were considered for the FPC comparisons. In all cases, the BLS was operating in a closed configuration, with the only venting occurring in the CVC section. In other words, there were no longitudinal gaps between sections. In practice, there was some venting at the seals between sections; however, this is thought to be minimal, with venting and blow-down controlled mainly by the openings in the CVC.

The BLS configurations considered for the FPC comparisons are outlined in the ensuing discussion. These are referred to by their base configuration name, or simply as the first, second, or third case modeled. It is important to note that the configuration name is a generic term and does not refer to any specific test series. The naming convention used here is strictly for convenience in the reporting of the FPC results.

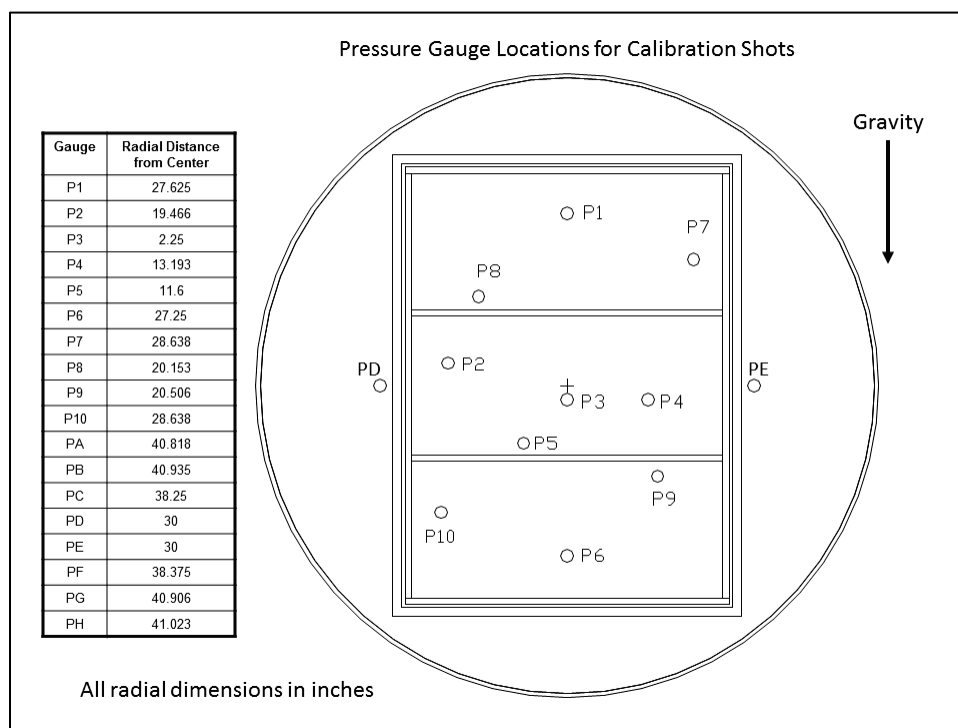
2.2 GSA configuration, calibration Tests 30a and 30b

The first case modeled considered the GSA configuration depicted in Figure 2. This configuration was utilized in the early calibration testing, which varied the driver length, burst pressure, and gas mixture. Tests 30a and 30b were considered for the analysis. The setups for these two tests were identical, providing some indication of test repeatability. For these tests, the driver length was 66 in., and the burst pressure was 1,298 psig.

The driver gas was composed of 100-percent air. The ambient temperature was nominally 77°F. The overall length of the Cascade section was 98-3/16 in., resulting in an overlap of 11-13/16 in. between the upstream and downstream sub-sections. The dimensions of all other BLS sections are as discussed in the general overview.

Gauges were embedded in the target wall to measure the reflected pressure. The instrumentation layout is shown in Figure 7. Only the radial gauge distances were available at the time the analyses were started. This was not an issue since the measured data exhibited little sensitivity to gauge location. Thus, the analysts could specify the gauge location in terms of radial distance from the centerline, as the measured data were largely independent of azimuth.

Figure 7. Instrumentation layout on target wall for GSA configuration.



2.3 Calibration tests with 8-ft×8-ft C2SQ configuration

The second case modeled was an extension of the first (see Figure 8). Two sections were added, a circle-to-square transition (C2SQ) and a square section (SQ1). A square target vessel with an 8-ft by 8-ft target mated with section SQ1. Dimensioned drawings for these additions are provided in Figures 9 through 11. An interior view looking towards the target vessel is provided in Figure 12. Section C2SQ did not mate perfectly with the

Cascade resulting in an overlap at the radial extents. The largest overlap on the left-hand side was 1-1/4 in. (with respect to the view towards the target vessel). Similarly, the largest overlap on the right-hand side was 2-3/8 in.

A side-on pressure gauge PR was placed in the center of GSA TR2. The axial location is depicted in Figure 8. The gauge resided on the centerline of the BLS and was placed 23 ft 8-7/16 in. downstream of the driver. A typical mounting system for the side-on pressure gauge is shown in Figure 13. In addition, the target wall was instrumented to measure the reflected pressure across the surface. The instrumentation layout is shown in Figure 14.

Figure 8. BLS 8-ft×8-ft C2SQ configuration.

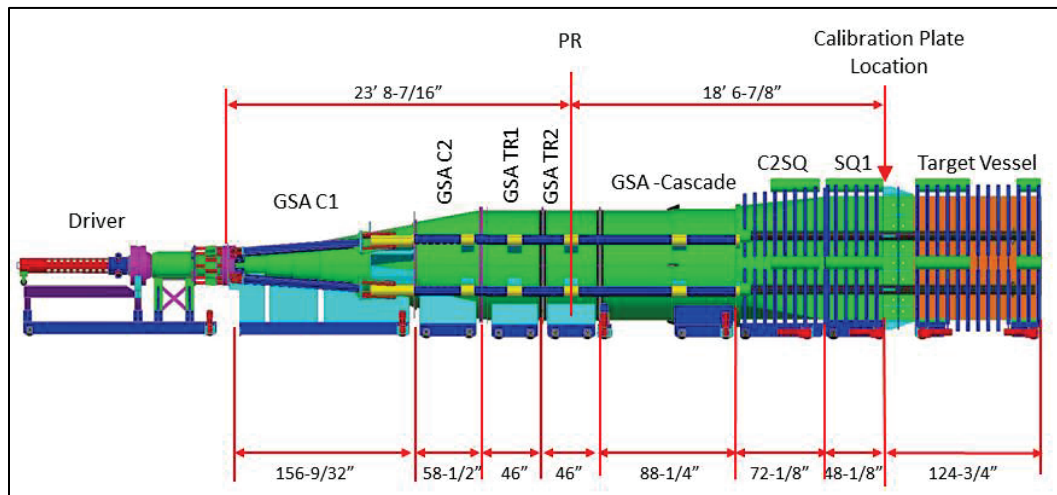


Figure 9. Circle-to-square transition section C2SQ.

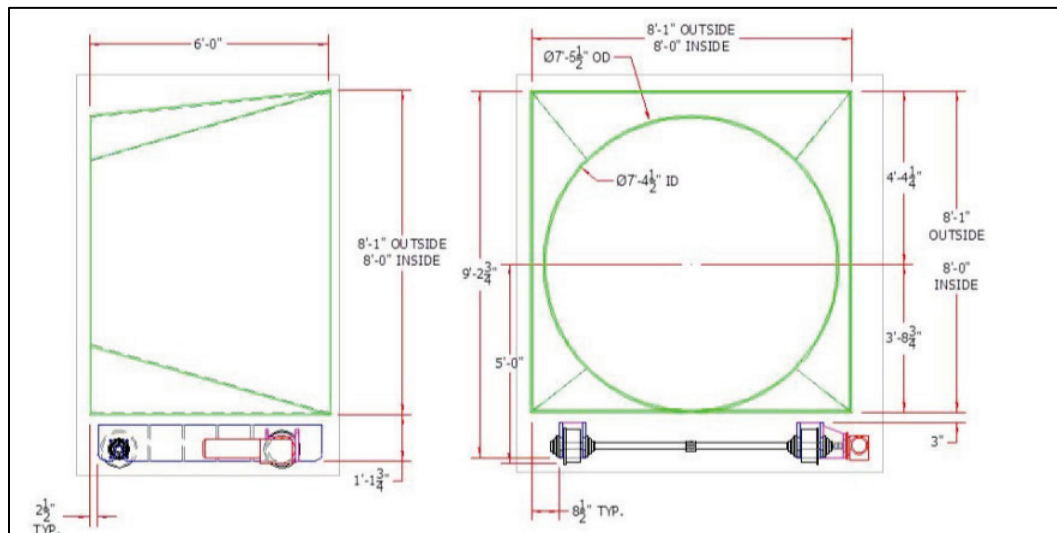


Figure 10. Square section SQ1.

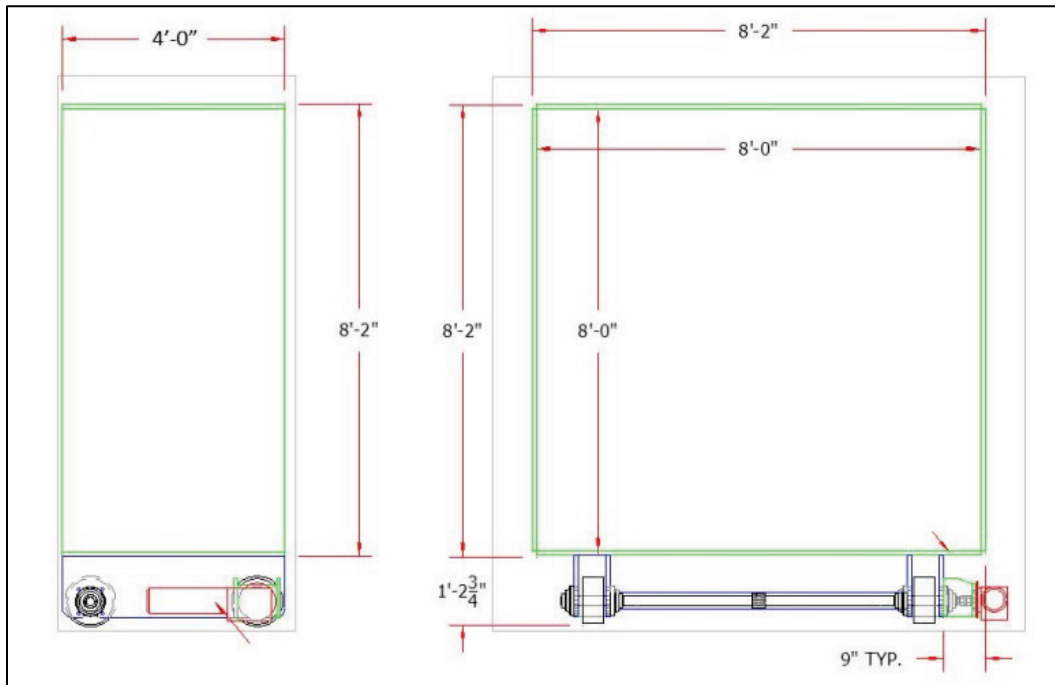


Figure 11. Square transition for target vessel face.

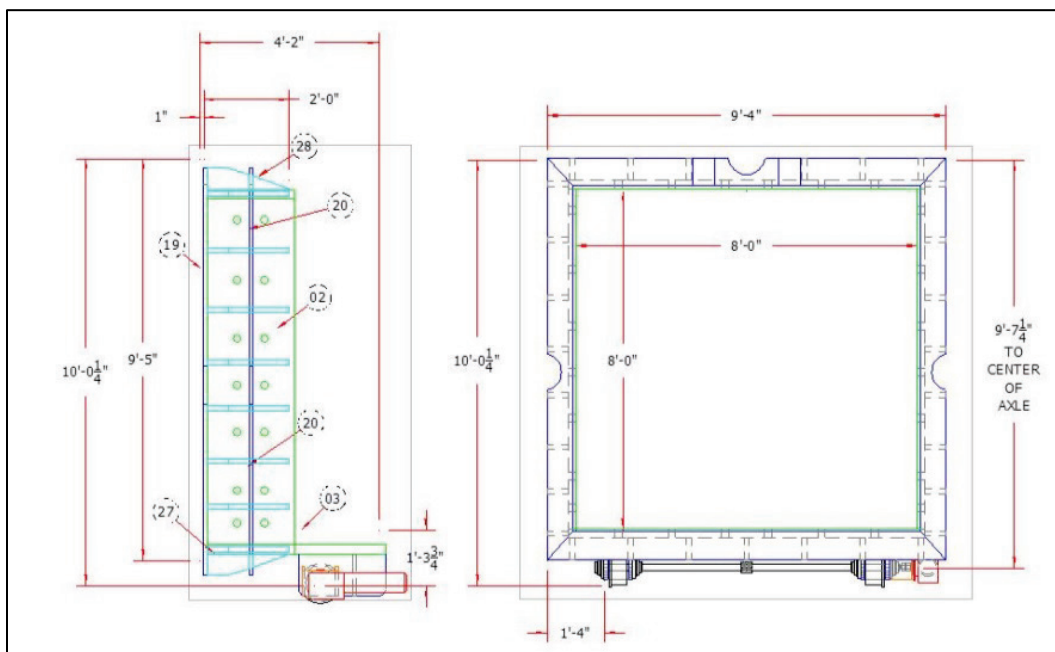


Figure 12. View towards target vessel.

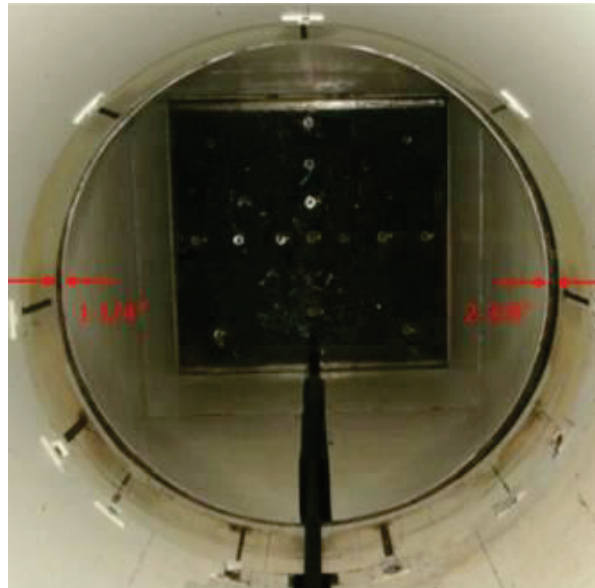


Figure 13. Typical mounting system for the side-on pressure gauge.



(a) Mount to sidewall

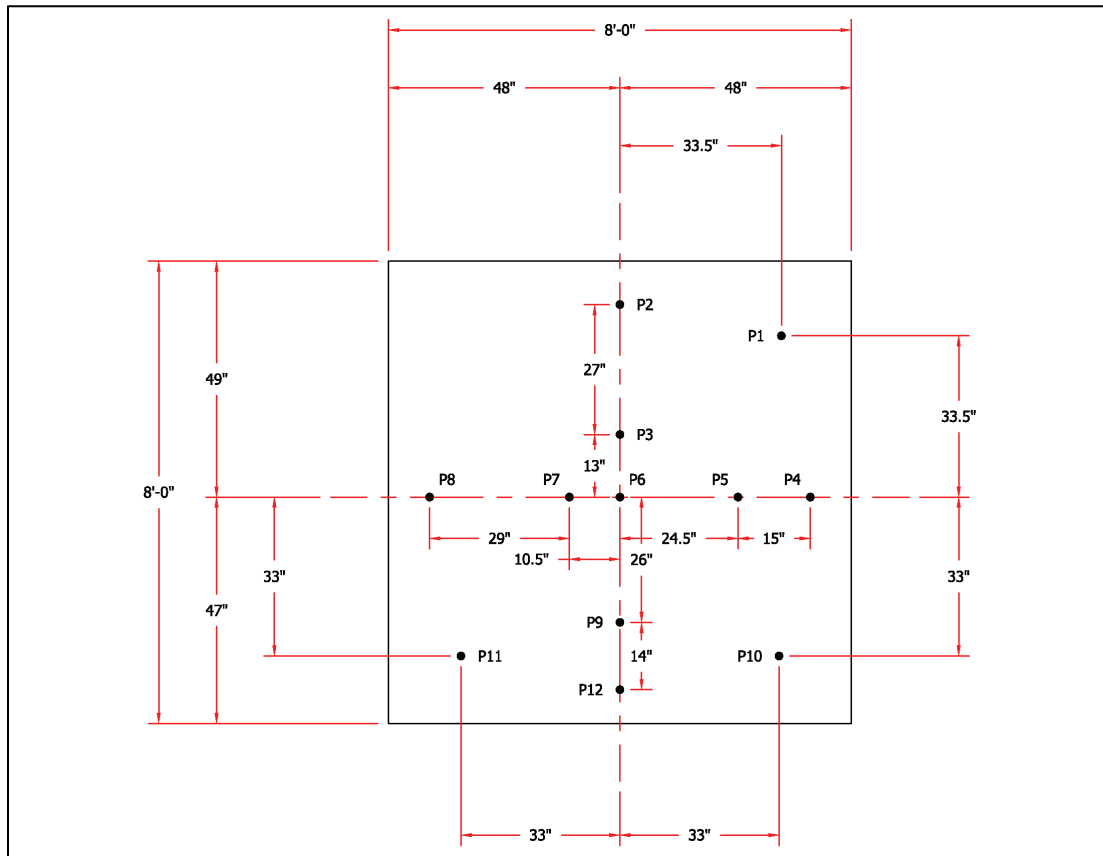


(b) Gauge, side view



(c) Gauge, end-on view

Figure 14. Instrumentation layout on target wall.



2.4 BLS 8-ft×8-ft C2SQ configuration with box

For the third case modeled, the BLS configuration was identical to that of the second with the exception of a box structure placed in section C2SQ (see Figure 15). An interior view is provided in Figure 16, where the viewer is looking towards the target vessel. The box was positioned along the centerline of the BLS (see Figure 17). The length, width, and height of the box were 13, 13, and 18 in., respectively. It sat on a pedestal, so that its base was level with the Cascade floor. The box was instrumented with pressure gauges to characterize the time-varying flow around it. The box was instrumented on all exposed surfaces, as depicted in Figures 18 through 20. In the nomenclature, PBF refers to the front side gauges; PBB refers to the back side; PBT refers to the top; PBL refers to the left side; and PBR refers to the right side. The orientation of the left and right sides are defined looking from the target vessel towards the driver, i.e., opposite of the gunner's point of view. There was reduced instrumentation on the target wall, with only gauges P3 and P9 being active (see Figure 21).

Figure 15. BLS 8 ft×8 ft C2SQ configuration with box.

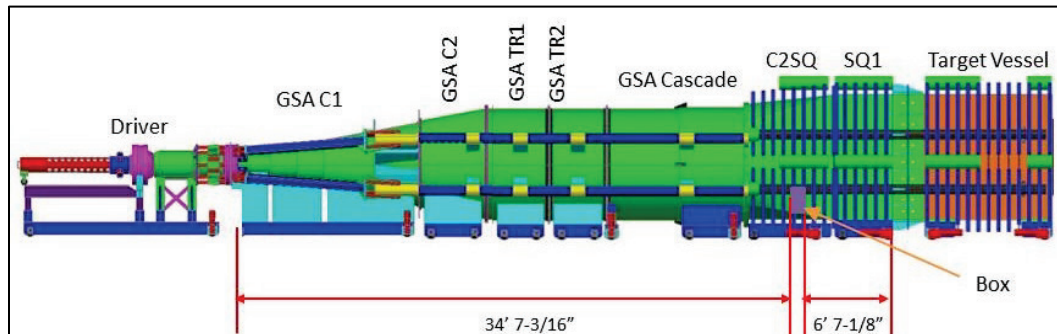


Figure 16. View of box in BLS, looking toward the target vessel.

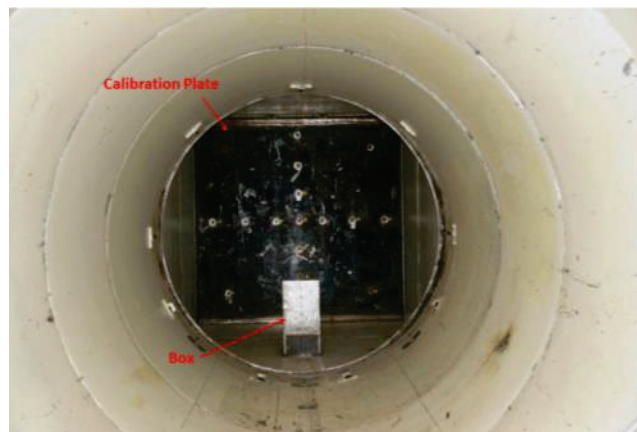


Figure 17. Box location and overall dimensions.

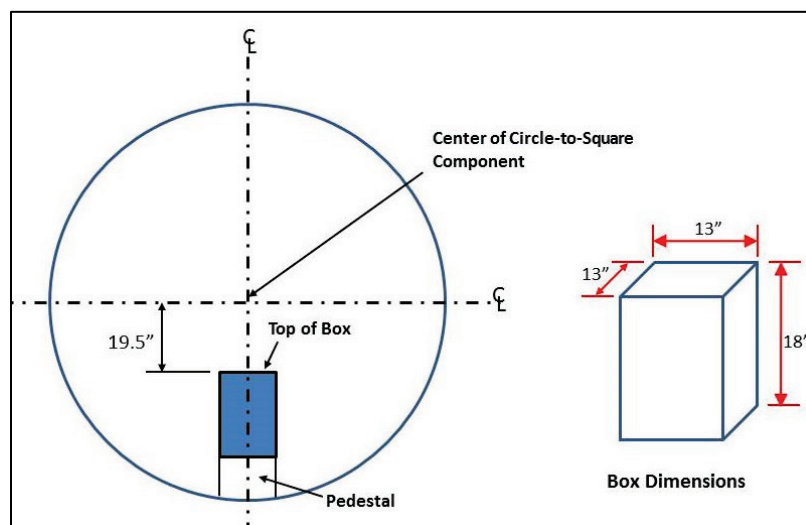


Figure 18. Box instrumentation, front and back sides.

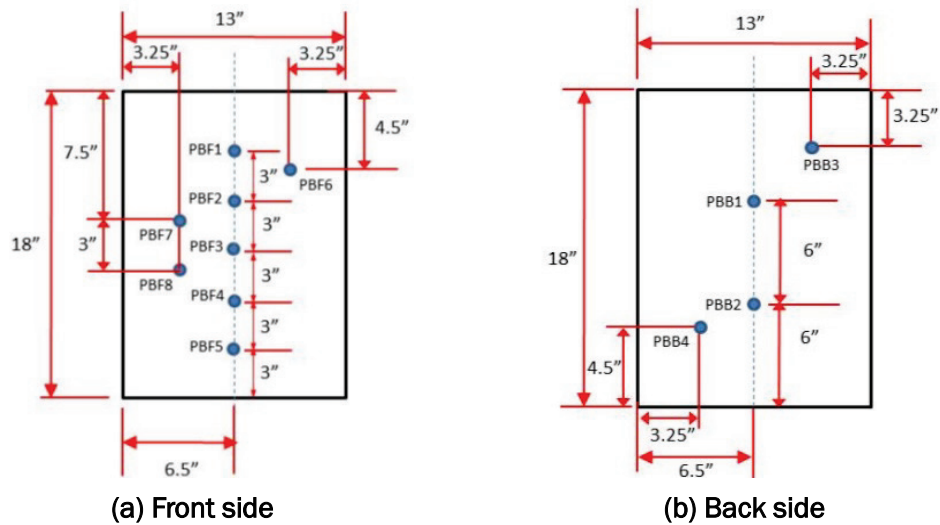


Figure 19. Box instrumentation, top.

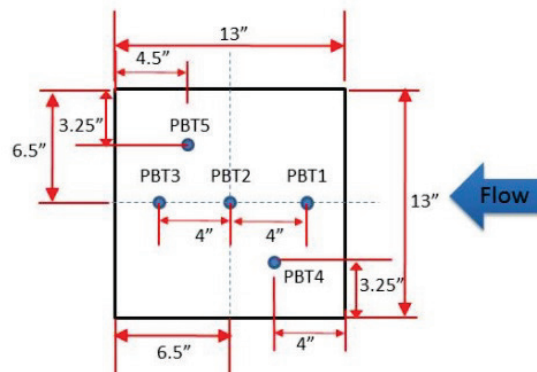


Figure 20. Box instrumentation, left and right sides.

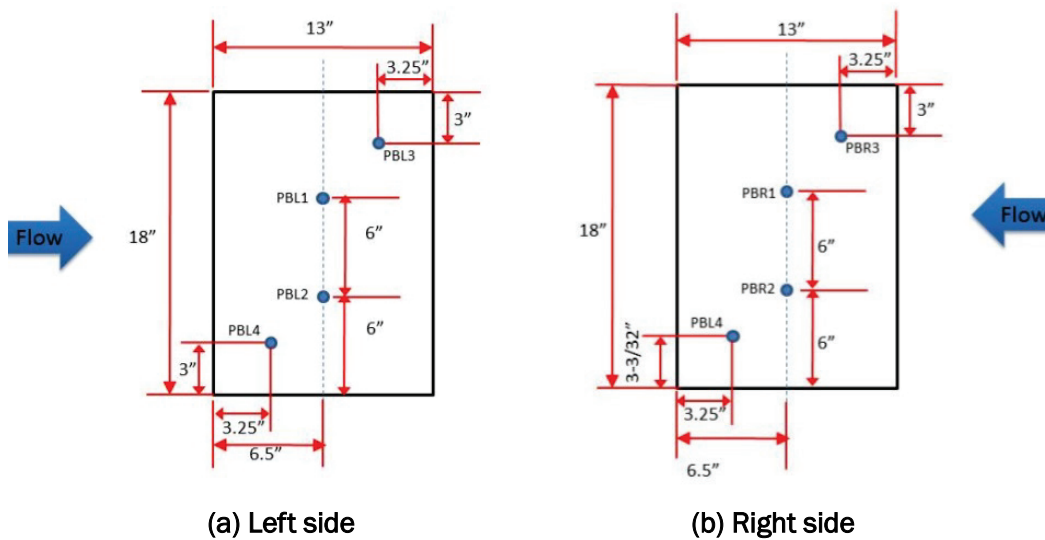
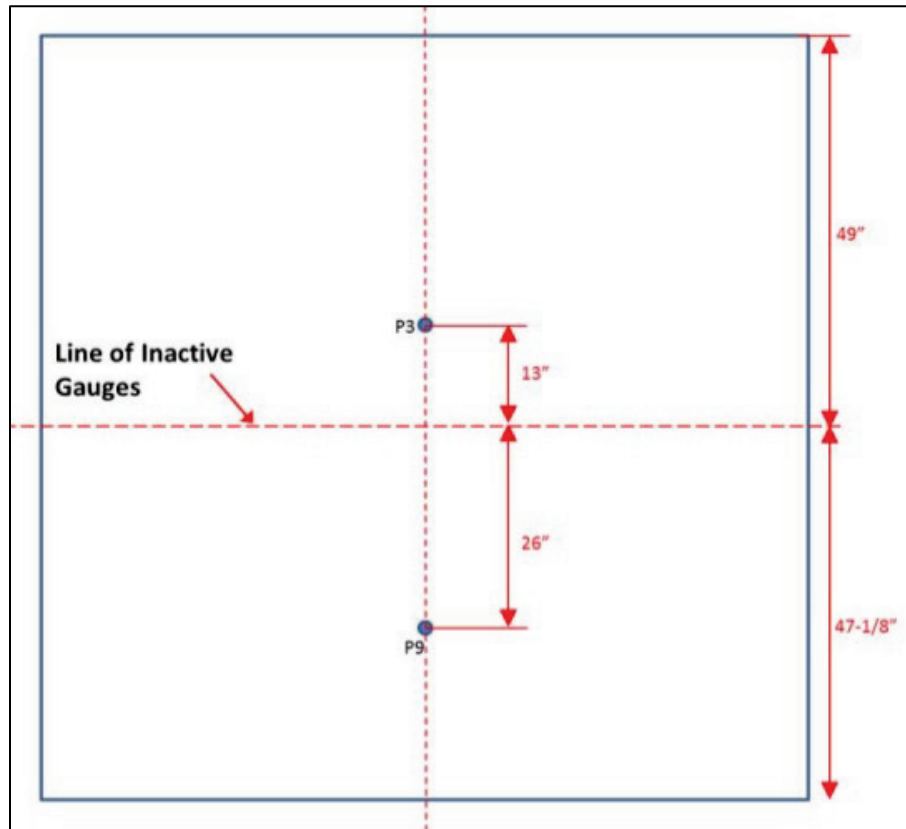


Figure 21. Active gauges on target wall.



3 Modeling Approach and Comparisons

3.1 Overview

The FPCs chosen for the BLS modeling effort were CTH, DYSMAS, Loci/BLAST, RAGE, and SHAMRC. With the exception of Loci/BLAST, the codes listed are in common use within the DoD for modeling airblast applications. The DoD codes utilize Eulerian solvers of various types, all relying on a structured mesh. The Loci/BLAST code differs in that it utilizes an unstructured mesh. There are other codes capable of modeling airblast; however, the ones chosen are thought to have a fairly broad user base with ongoing support on a number of DoD HPC platforms.

The chosen codes represent an array of numerical approaches for modeling airblast applications. Our goal was to first assess the capability of each for modeling the airblast environment encountered within the BLS. This entailed a close look at the strengths and weaknesses of each code for modeling this application, and determining any shortfalls in the underlying physics models that should be addressed. The assessment also considered the computational cost and feasibility of a particular FPC for modeling a BLS event. Although the first two cases can be approximated as axisymmetric, the emphasis was on 3-D modeling as this provides a better indication of a code's performance for handling realistic applications. Thus, 3-D calculations were conducted for all cases discussed in this report; however, planes of symmetry were permitted across the centerline axis of the BLS. The use of symmetry conditions was at the modeler's discretion.

The results from each FPC were compared against the experimental data to assess accuracy and trends. These comparisons were qualitative in nature, as no in-depth uncertainty analysis was conducted. It should be noted that repeat experiments were performed for all of the cases modeled. In general, the experimental data were highly repeatable. Some differences were noted later in time; however, this should not be surprising as the timescale spanned out to the 60- to 100-msec range. The comparisons focused on the time of arrival (TOA), pressure, and impulse. The emphasis was not just on capturing the peaks, but also considered the ability of the codes to capture the time-dependent nature of the waveform. The history was important, as it provided insight into the complex wave interaction that occurred later in time.

All of the calculations discussed in this report were open, i.e., the analysts had access to the experimental data prior to conducting the calculation. The goal of the computational effort was to have an honest and open assessment of each code's capability. Regular teleconferences were conducted to foster communication between the analysts and encourage openness. Without this openness, one cannot get a clear assessment of the strengths and weaknesses of the individual codes, nor a path forward for future model development. Future efforts will move toward blind calculations, where the modeler does not have access to the measured data beforehand.

Table 1 provides a brief description of the FPCs used in the BLS modeling. Further details on the numerical solver and features unique to each code are outlined in the appendices. An appendix is devoted to each FPC considered to allow for a detailed discussion of the model setup, the reasoning behind choices made in the setup, and lessons learned during the course of the modeling. The discussion for each code is in alphabetical order to avoid any perception of favoritism. Similarly, the order of the appendices follows this alphabetical listing. Thus, CTH is discussed in Appendix A, DYSMAS in Appendix B, etc.

The emphasis in this section is on the bigger picture, which involves overall comparisons of FPC performance. Performance entails an assessment of accuracy (i.e., ability to replicate the measured data) as well as computational cost in conducting 3-D analyses. The overarching goal is to assess the strengths and weaknesses of each of the FPCs and identify potential areas for improvement needed in the physics modeling.

Before proceeding with the comparisons, it is worthwhile to first outline the modeling challenges posed by the BLS setup. These challenges arise due to the disparate length and time scales that will be encountered in the modeling. The thin shell of the BLS structure (0.5-in.) drives much of the resolution requirement. In general, one needs several cells across the thickness of this thin structure to adequately capture it in the model. Meeting this resolution requirement can lead to excessively long run times – due to the resulting large number of cells and small time-step - that are intractable for 3-D analyses. It is not just a matter of resolving the shell thickness, but also the need to adequately resolve the shell along the full length of the BLS (about 40 ft). Furthermore, there are additional

Table 1. Brief description of FPCs used in BLS modeling.

FPC	Brief Description
CTH	Structured Eulerian code with two-step solution approach involving a Lagrangian step followed by a remap. Explicit finite volume approximation applied to conservation equations for Lagrangian step on a staggered mesh. Remap based on second-order-accurate van Leer scheme. Code supports wide range of EOS options and sophisticated material strength models.
DYSMAS	Coupled Euler/Lagrange code. Structured Eulerian code Gemini solves the Eulerian problem using a time-split, second order Godunov method based on a Monotonic Upstream Centered Scheme for the Conservations Laws (MUSCL). Lagrangian problem solved using the ParaDyn explicit Lagrangian finite element code. DYSMAS loosely couples the two solution domains.
Loci/BLAST	Unstructured, fully Eulerian, CFD code that uses a Harten-Lax-van Leer-Enfheldt (HLLC) approximate Riemann solver to compute fluxes at cell faces and least-squares reconstruction coupled with a nodal Baldwin-Barth limiter to provide second-order spatial accuracy. Explicit time integration performed using a two-stage second-order Total Variation Diminishing (TVD) Runge-Kutta scheme.
RAGE	Structured, fully Eulerian, CFD code that uses a two-shock or single-intermediate-state approximate Riemann solver with an alternating-direction-explicit technique in the shock capturing. Robust AMR that is continuous in both space and time with adaption triggered by changes in state and/or first-order truncation error.
SHAMRC	Structured Eulerian code that uses a two-step approach involving a Lagrangian step followed by a remap. Conservation equations solved using a modified Lax-Wendroff finite difference approximation on a staggered mesh. Remap based on second-order accurate van Leer scheme with an alternating direction integration scheme.

complicated thin structures such as the catch grill that may require increased resolution if included in the model.

The time scale is also an issue. In general, it takes 20 to 25 msec for the shock front to traverse the full length of the BLS (varies depending on the configuration). The time duration needed to fully capture the loading pulse is on the order of 50 msec. Time-steps are likely on the microsecond timescale. Thus, it will take a considerable number of cycles to conduct the calculation to completion. So one should expect that any BLS calculation will be highly resolved and long running.

3.2 GSA configuration, calibration Tests 30a and 30b

The modeling began with the GSA configuration, which represented the simplest of the three cases. The geometry can easily be approximated as axisymmetric if the flange cross-bars and grill are omitted from the model. The modelers took advantage of this fact by conducting two-dimensional cylindrical (2-DC) analyses early on. This allowed them to investigate modeling options such as mesh resolution, EOS selection, hydrodynamic treatment options, etc. in a 2-DC setting that allowed high turnaround calculations. The early 2-DC modeling served as a foundation for all follow-on 3-D analyses. All discussion of the early 2-DC modeling is provided in the appendices. The reporting in this section focuses solely on the 3-D analysis results.

The approach taken by each modeler differed. This is reflected in the summary provided in Table 2. The table summarizes parameters pertinent for ensuing code-to-code comparisons. These include the symmetry conditions, mesh resolution, EOS selected for the air, approximate total cell count, and inclusion of the grill in the model. Further details on problem setup and assumptions can be found in the appendices. In most cases, the resolution was fixed within the region of interest, i.e., the immediate region encompassing the BLS; however, there are cases where the resolution varied within this domain. Loci/BLAST utilizes an unstructured mesh. The mesh was composed of tetrahedral elements. The nominal resolution within the air space was 2.5 cm, with a finer resolution employed near the vents and grill. The RAGE calculation utilized AMR. The resolution

Table 2. Summary of FPC problem setup for GSA configuration.

FPC	Model Geometry	Mesh Resolution (cm)	EOS for Air	Approximate No. of Cells (millions)	Grill Included?
CTH	Half-symmetry	0.5	SESAME	395	No
DYSMAS	Fully 3-D	1.0	Ideal Gas	136	Yes
Loci/BLAST	Fully 3-D	1.3 – 2.5	Ideal Gas	52	Yes
RAGE	Quarter-symmetry	0.5 (AMR)	Ideal Gas	13 - 279	No
SHAMRC	Half-symmetry	0.5	Doan-Nickel	1024	No

reported is the size of the finest cell in the mesh. The use of AMR also resulted in a continual growth of the problem size. The cell counts reported in the table are for the beginning and end of the calculation.

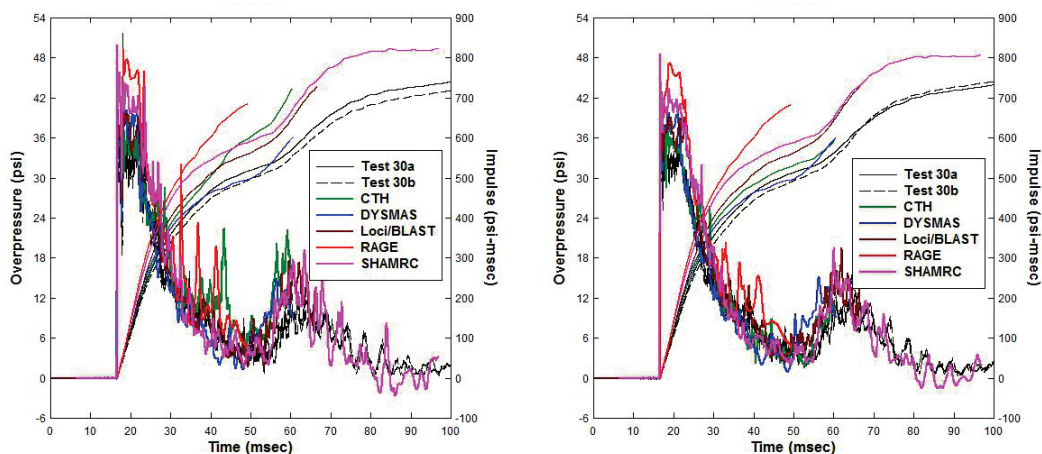
Most modelers only ran a single calculation; however, for SHAMRC, two variations were considered for this first case. The first was a coarser-meshed 1.0-cm resolution calculation that was fully 3-D. The second was a medium-meshed 0.5-cm resolution calculation that employed a single plane of symmetry. The latter was chosen for the subsequent comparisons due to its higher resolution. As outlined in Appendix E, there was little difference in results for the two calculations.

Comparisons of the measured and calculated pressure histories at select gauges located on the target wall are provided in Figure 22. The figure only contains comparisons for three gauges, P3, P4, and PE. The measured (and calculated) results were generally consistent across the target wall, and one need only consider a subset to assess code performance. The radial distance from the BLS centerline for these gauges was 2.25, 13.2, and 30 in., respectively. Thus, the gauges selected span the full range of radial offsets across the target wall. Unless stated otherwise, the calculated results were time-shifted so that their arrival times coincided with the measured arrival. This was done to ease comparisons of the waveforms. In all cases, the calculated TOA lagged the measured arrival time. The time-shifts applied to the target wall gauges for each FPC are outlined in Table 3. An example of the non-shifted results for gauge PE is provided in Figure 23 to illustrate the relative difference in arrival times calculated by each of the FPCs. It can be difficult to interpret results for an individual code from the overlaid data in Figure 22. Comparisons on an individual basis are provided for gauge PE in Figure 24. These comparisons are representative of those noted at the other gauge locations.

In general, one notes excellent overall agreement with the measured data for CTH, DYSMAS, and Loci/BLAST. The general character of the calculated waveform for SHAMRC is excellent, with the exception of the overprediction of the initial peak pressure. The overprediction is on the order of 20 to 25 percent. This initial overprediction leads to a corresponding overprediction in the integrated impulse. RAGE exhibits similar issues, but to a much greater degree with further overprediction of the initial peak pressure (on the order of 35 to 40 percent). It is worth

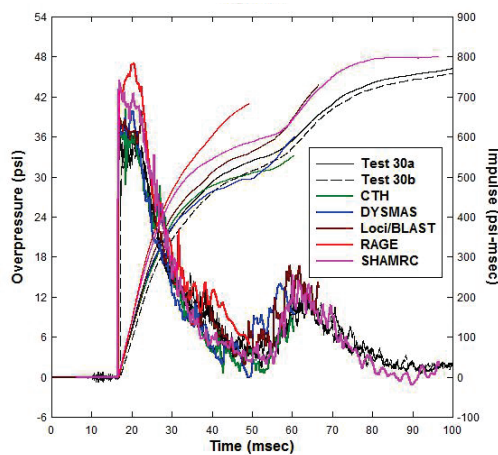
noting that these same overpredictions were noted in the 2-DC RAGE calculations

Figure 22. FPC comparisons with measured data, GSA configuration.



(a) Gauge P3.

(b) Gauge P4.



(c) Gauge PE.

Table 3. Time-shifts applied to GSA configuration calculations.

FPC	Target Wall Gauges (msec)
CTH	-4.59
DYSMAS	-2.16
Loci/BLAST	-3.42
RAGE	-3.15
SHAMRC	-3.72

Figure 23. Early time comparison for gauge PE without time-shifting.

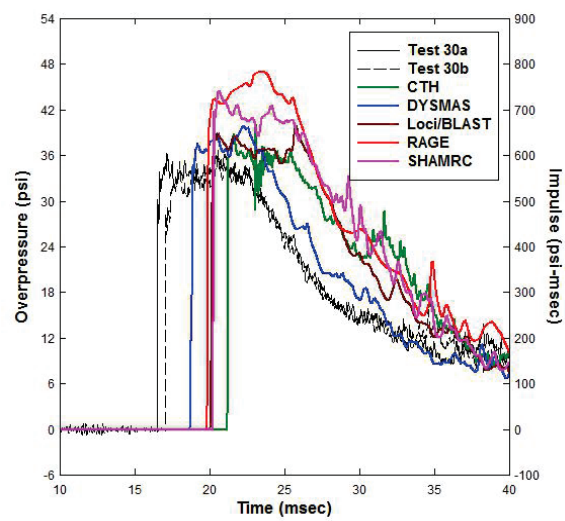


Figure 24. Individual FPC comparisons for gauge PE.

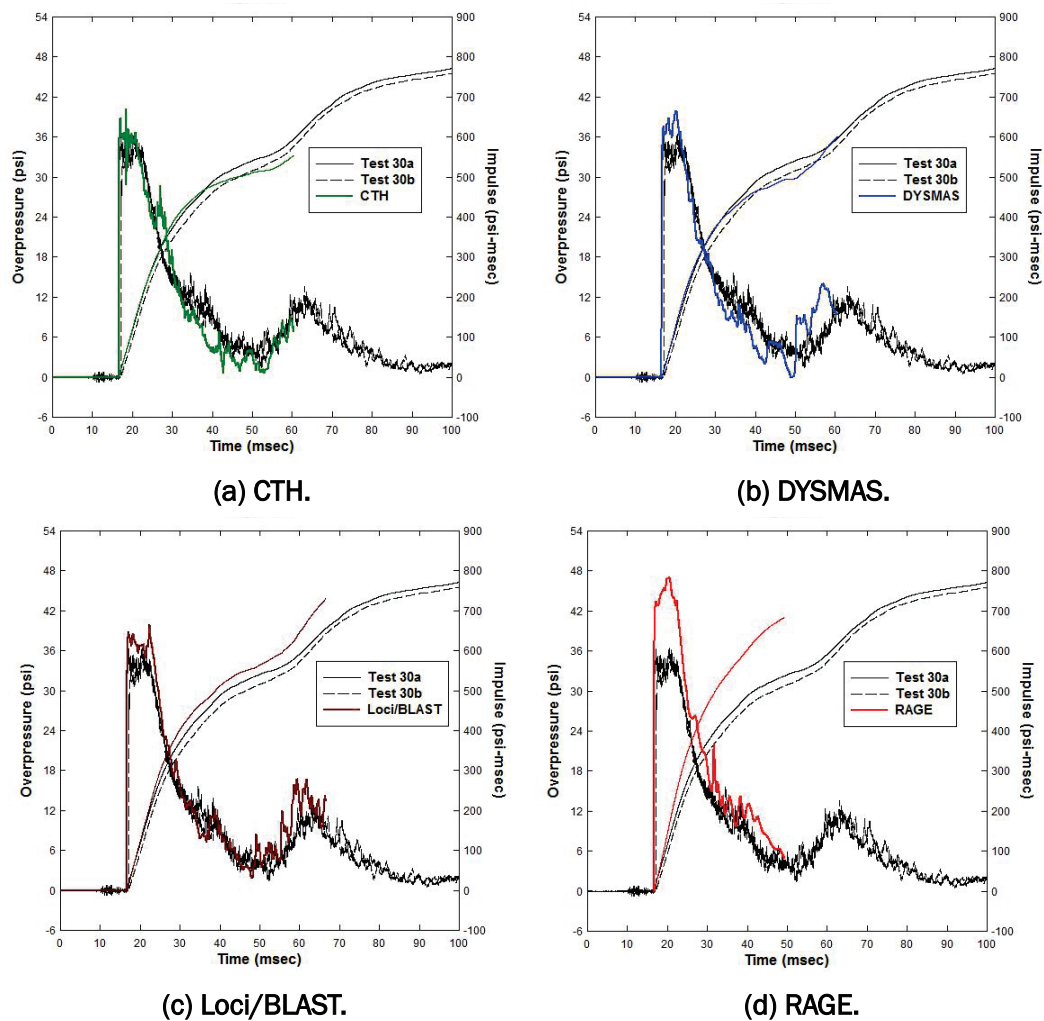
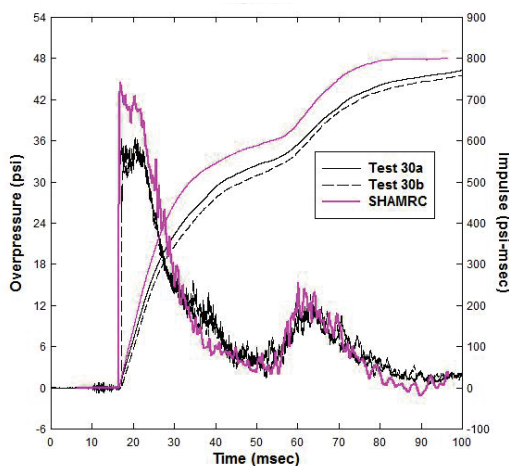


Figure 24. (Continued).



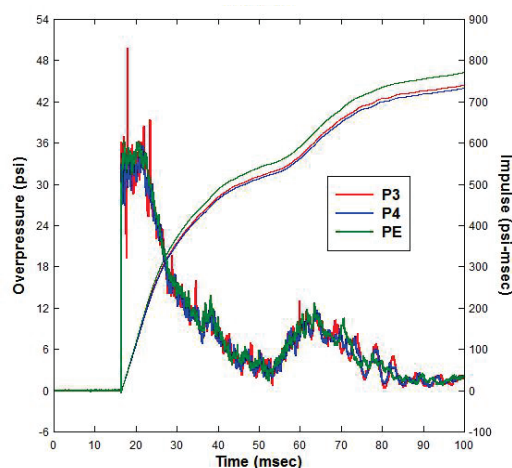
(e) SHAMRC.

(see Appendix D). Both convergence and sensitivity studies were conducted; however, they did not shed insight as to the source of the severe overpredictions noted with RAGE. Due to time constraints, it was decided to move forward with the 3-D RAGE calculations with the expectation that it would overpredict both the initial peak pressure and integrated impulse.

All codes exhibit increased noise in the solution at gauge P3. This gauge is near to the centerline of the BLS (2.25-in. offset). The BLS walls and any symmetry planes in a calculation act as perfect reflectors, and it is conjectured that this idealization induces ringing in the solution due to the axisymmetric nature of the problem setup. The ringing is still evident in the fully 3-D calculations of DYSMAS and Loci/BLAST, but to a slightly lesser extent as compared to those using a plane of symmetry. The ringing behavior is clearly exaggerated in the RAGE calculation, and appears to be pervasive throughout the calculation. The ringing in the solution at the various gauge locations dampens out with increasing radial offset from the centerline.

The ringing behavior noted at gauge P3 is evident in the measured data, but to a far lesser degree. This is illustrated in Figure 25 where the measured data for the three gauges from Test30a are overlaid. In reality, the walls of the BLS are not perfect reflectors either due to surface roughness or perturbations in the shell thickness along the length. These imperfections offset the timing of reflections and effectively cancel out much of the shock superposition that is observed in the calculations.

Figure 25. Gauge comparisons
for Test 30a.



3.3 Calibration tests with 8-ft×8-ft C2SQ configuration

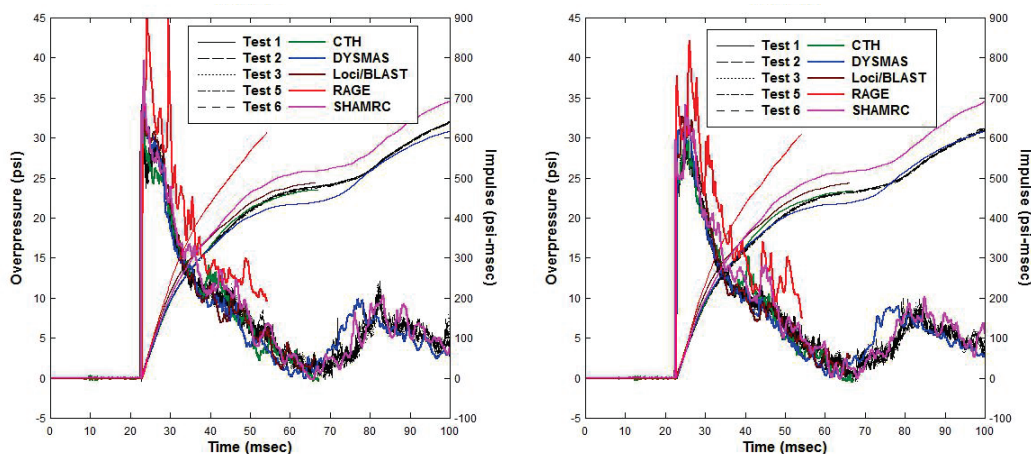
The 8-ft×8-ft C2SQ configuration is an extension of the first case. It involves the addition of the C2SQ and SQ1 sections to the standard GSA configuration. All modeling of this case was conducted in 3-D. Table 4 summarizes the problem setup associated with each FPC. Further details on problem setup and assumptions can be found in the appendices. A comparison of the measured and calculated pressure histories at select gauges is provided in Figure 26. The figure contains comparisons for three gauges on the target wall (P6, P5, and P1) along with the side-on pressure gauge PR. The radial distances of the target wall gauges from the BLS centerline were 10.625, 24.5, and 46.72 in. for gauges P6, P5, and P1, respectively. Thus, the gauges selected provide a good indication of the influence of radial offset on the data. The measured (and calculated) data were fairly consistent across the target wall, indicating that the incoming shock front was relatively planar. All calculated results were time-shifted to match the measured arrival time. The time shifting was done to ease comparisons of the waveform. The time-shifts applied for each FPC calculation are outlined in Table 5. It can be difficult to interpret results for an individual code from the overlaid data in Figure 26. Comparisons on an individual basis are provided for gauge P1 in Figure 27. These comparisons are representative of those noted at the other gauge locations. Similarly, individual comparisons for the side-on pressure gauge PR are provided in Figure 28.

In general, one notes excellent overall agreement with the measured data at the target wall for CTH, DYSMAS, and Loci/BLAST. It is apparent that both the initial peak and rate of decay are captured well in the first pulse.

Table 4. Summary of FPC problem setup for 8-ft×8-ft C2SQ configuration.

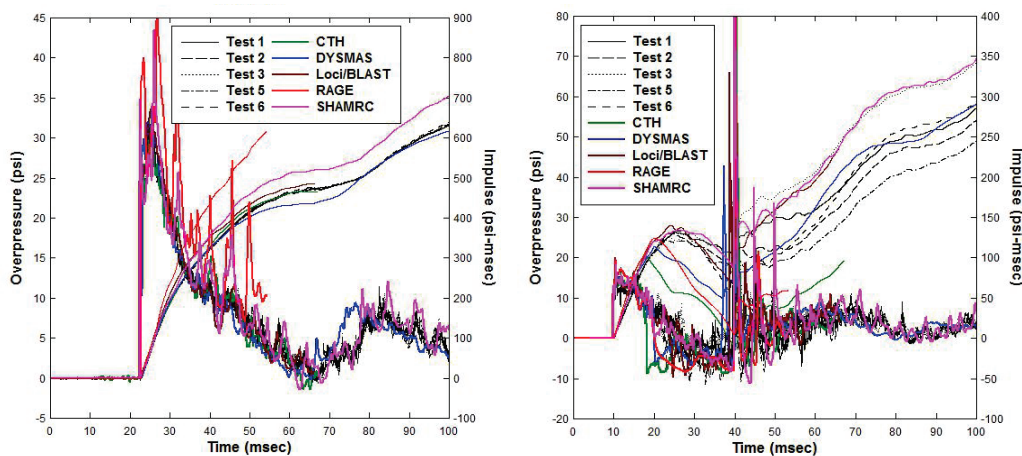
FPC	Model Geometry	Mesh Resolution (cm)	EOS for Air	Approximate No. of Cells (millions)	Grill Included?
CTH	Half-symmetry	0.5	SESAME	473	No
DYSMAS	Fully 3-D	1.0	Ideal Gas	166	Yes
Loci/BLAST	Fully 3-D	1.3 – 2.5	Ideal Gas	53	Yes
RAGE	Half-symmetry	0.5 (AMR)	Ideal Gas	39 - 509	No
SHAMRC	Half-symmetry	0.5	Doan-Nickel	1088	Yes

Figure 26. FPC comparisons with measured data, 8-ft×8-ft C2SQ configuration.



(a) Gauge P1.

(b) Gauge P5.



(c) Gauge P6.

(d) Gauge PR.

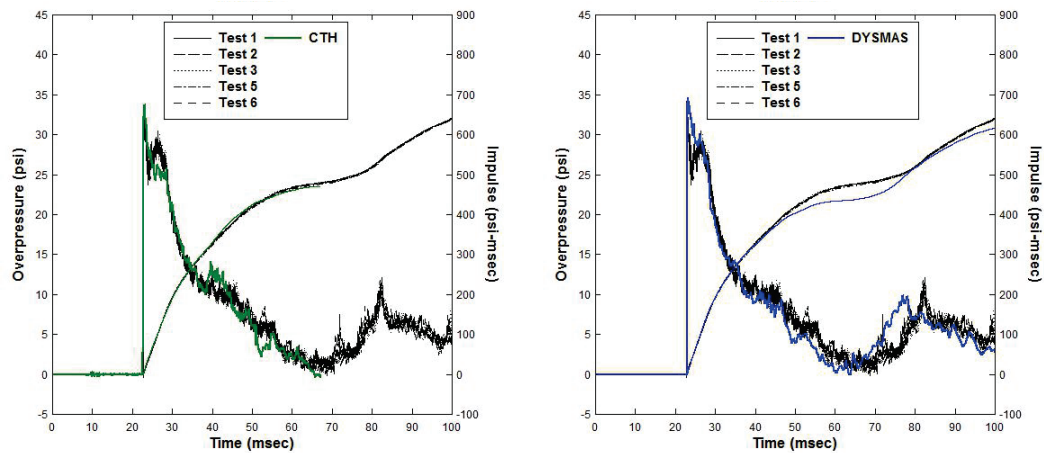
Table 5. Time-shifts applied to 8-ft×8-ft
C2SQ configuration calculations.

FPC	Target Wall Gauges (msec)	Side-on Gauge PR (msec)
CTH	-4.80	-4.80
DYSMAS	-1.15	0
Loci/BLAST	-3.67	-3.96
RAGE	-2.93	-3.79
SHAMRC	-3.92	-4.06

SHAMRC falls into the next tier and is a very close second. The general character of the calculated waveform for SHAMRC is excellent; however, there is an overprediction of the peak pressure. The overprediction is transient in nature but sufficient to induce an earlier rise in the impulse, and hence, an overprediction of the final value. If not for these transients, SHAMRC would have performed equally well. Overall, RAGE results compared poorly. The initial peak was significantly overpredicted, which results in a significant overprediction of the impulse (on the order of 40 percent at the time the calculation was terminated).

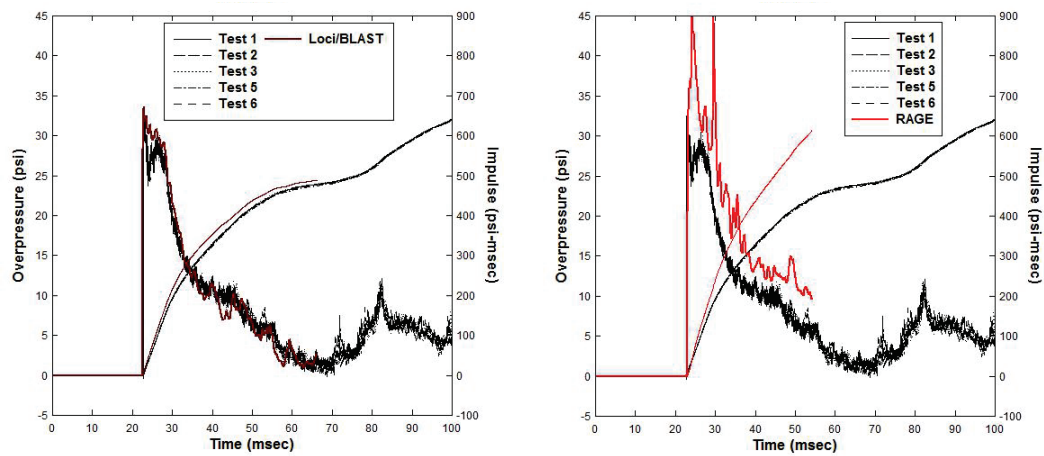
The comparisons for the side-on pressure gauge PR are mixed. All codes capture the form and character of the initial peak associated with the pulse; however, a number of them have drop-offs during the initial decay. This is clearly evident for CTH, DYSMAS, and RAGE. All of the codes capture the later time spike; however, the timings differ. CTH, Loci/BLAST, RAGE, and SHAMRC all capture the timing and amplitude of the first spike reasonably well. Both SHAMRC and RAGE appear to capture the timing of successive spikes exceedingly well, albeit there are differences in amplitude that are most notable for SHAMRC. Beginning at about 20 msec, there is significant variability in the impulse derived from the measured data. This is likely the result of the interface (contact surface) between the driver and drier air impinging on the gauge. This contact surface produces turbulence that affects the degree of repeatability among the tests.

Figure 27. Individual FPC comparisons for gauge P1.



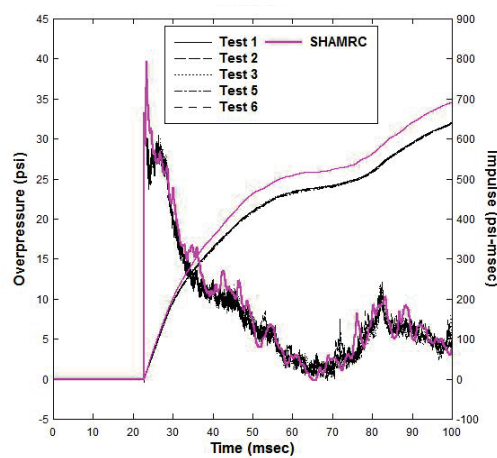
(a) CTH.

(b) DYSMAS.



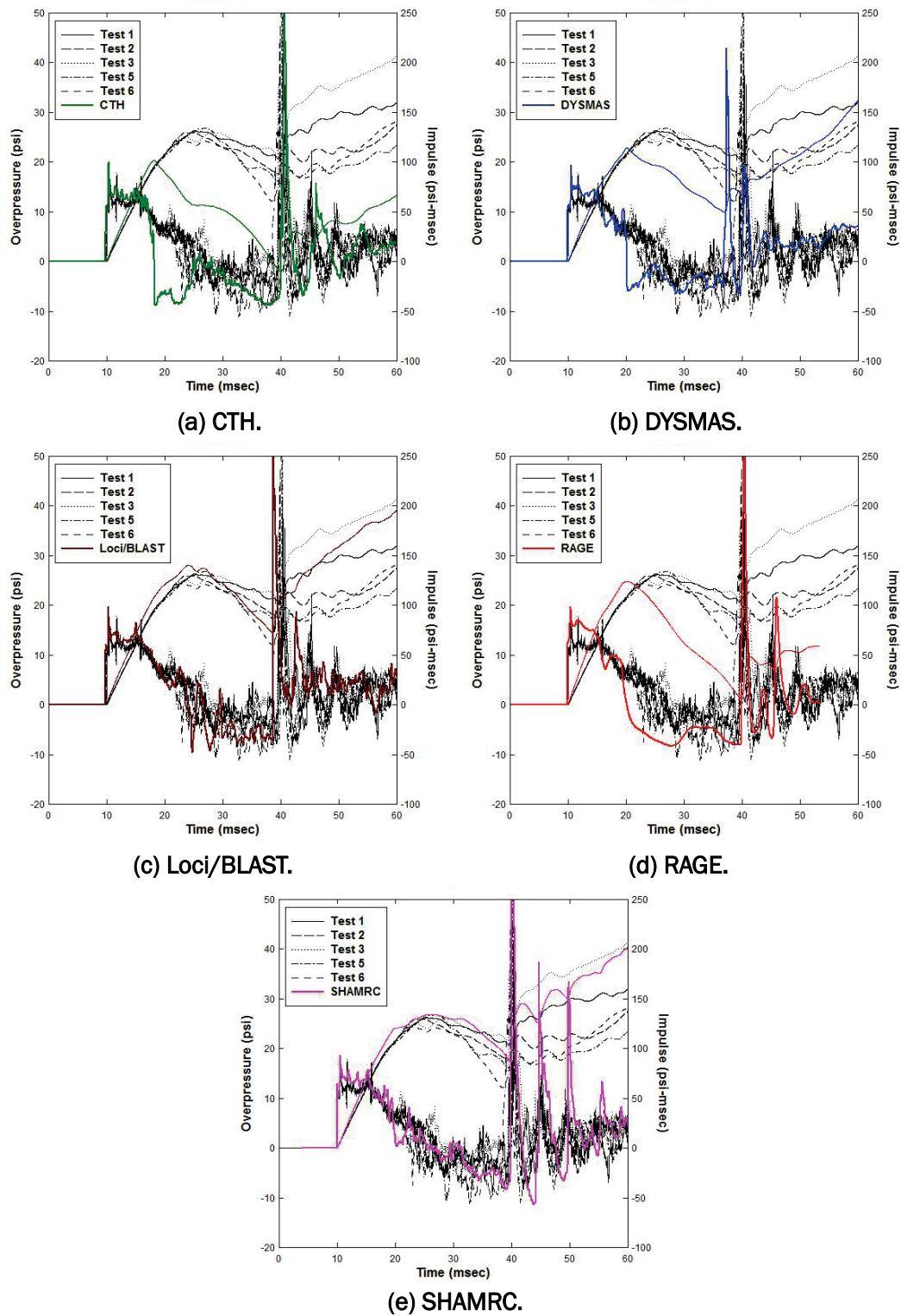
(c) Loci/BLAST.

(d) RAGE.



(e) SHAMRC.

Figure 28. Individual FPC comparisons for side-on gauge PR.



3.4 BLS 8-ft×8-ft C2SQ configuration with box

The 8-ft×8-ft C2SQ with box configuration is an extension of the second case. It involves the addition of an instrumented box in the C2SQ section. All modeling of this case was conducted in 3-D. Table 6 summarizes the problem setup associated with each FPC. Further details on problem setup and assumptions can be found in the appendices. All calculated results were time-shifted to match the measured arrival time. The time-shifts applied for each FPC calculation are outlined in Table 7. A comparison of the measured and calculated pressure histories at select gauges on the box and target wall are provided in Figures 29 through 33. The comparisons are limited to one gauge on each face of the box, as well as a single gauge on the target wall. The comparisons shown are representative of those noted at the other gauge locations on each box face and the target wall.

Comparison of results for this third case is much more subjective given the increased complexity of the BLS configuration. When viewing the data for box gauges (measured and calculated), one notes two distinct peaks. The first is associated with the original incident wave propagating in the downstream direction. The second is associated with the reflected wave that is traveling upstream after reflecting off of the target wall. One should expect the latter to be the more challenging of the two to capture computationally. Overall, one notes excellent correlation between the measured and calculated results for Loci/BLAST and SHAMRC. Here, the complete waveform is replicated exceedingly well, with only a slight overprediction for the initial peak pressure. The next tier is composed of CTH and DYSMAS. Both codes capture the general form and character of the waveform; however, disparities arise in the rate of decay associated with each pulse. This is more of an issue for CTH, where there is a sudden drop-off in the pressure history following arrival of the reflected shock. This results in a noticeable underprediction in the impulse at later times. Overall, RAGE performed poorly. In particular, RAGE tends to overpredict the peak pressure for the reflected shock, with a much slower decay than observed experimentally. The net effect is a substantial overprediction in impulse at later times. With the exception of RAGE, all codes provided reasonable correlation with the measured data for the target wall gauges.

Table 6. Summary of FPC problem setup for 8-ft×8-ft C2SQ with box configuration.

FPC	Model Geometry	Mesh Resolution (cm)	EOS for Air	Approximate No. of Cells (millions)	Grill Included?
CTH	Half-symmetry	0.5	SESAME	473	No
DYSMAS	Fully 3-D	1.0	Ideal Gas	166	Yes
Loci/BLAST	Fully 3-D	1.3 – 2.5	Ideal Gas	69.9	Yes
RAGE	Half-symmetry	0.5 (AMR)	Ideal Gas	39 - 478	No
SHAMRC	Half-symmetry	0.5	Doan-Nickel	1088	Yes

Table 7. Time-shifts applied to 8-ft×8-ft C2SQ with box configuration calculations.

FPC	Box Gauges (msec)	Target Wall Gauge (msec)
CTH	-4.11	-4.11
DYSMAS	-1.43	-0.63
Loci/BLAST	-3.18	-2.78
RAGE	-2.93	-2.49
SHAMRC	-3.50	-3.30

Figure 29. FPC comparisons for front face gauge PBF1.

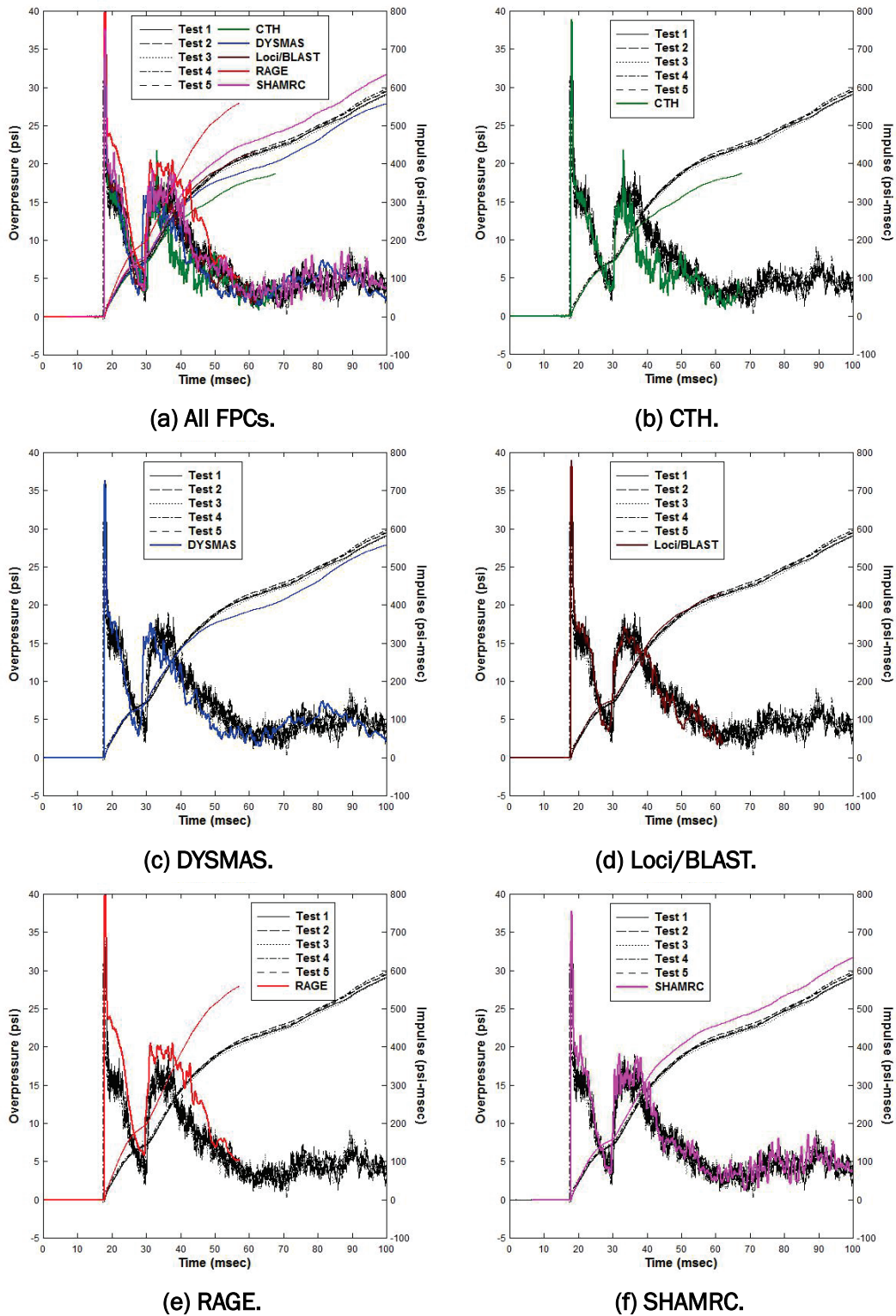


Figure 30. FPC comparisons for top face gauge PBT2.

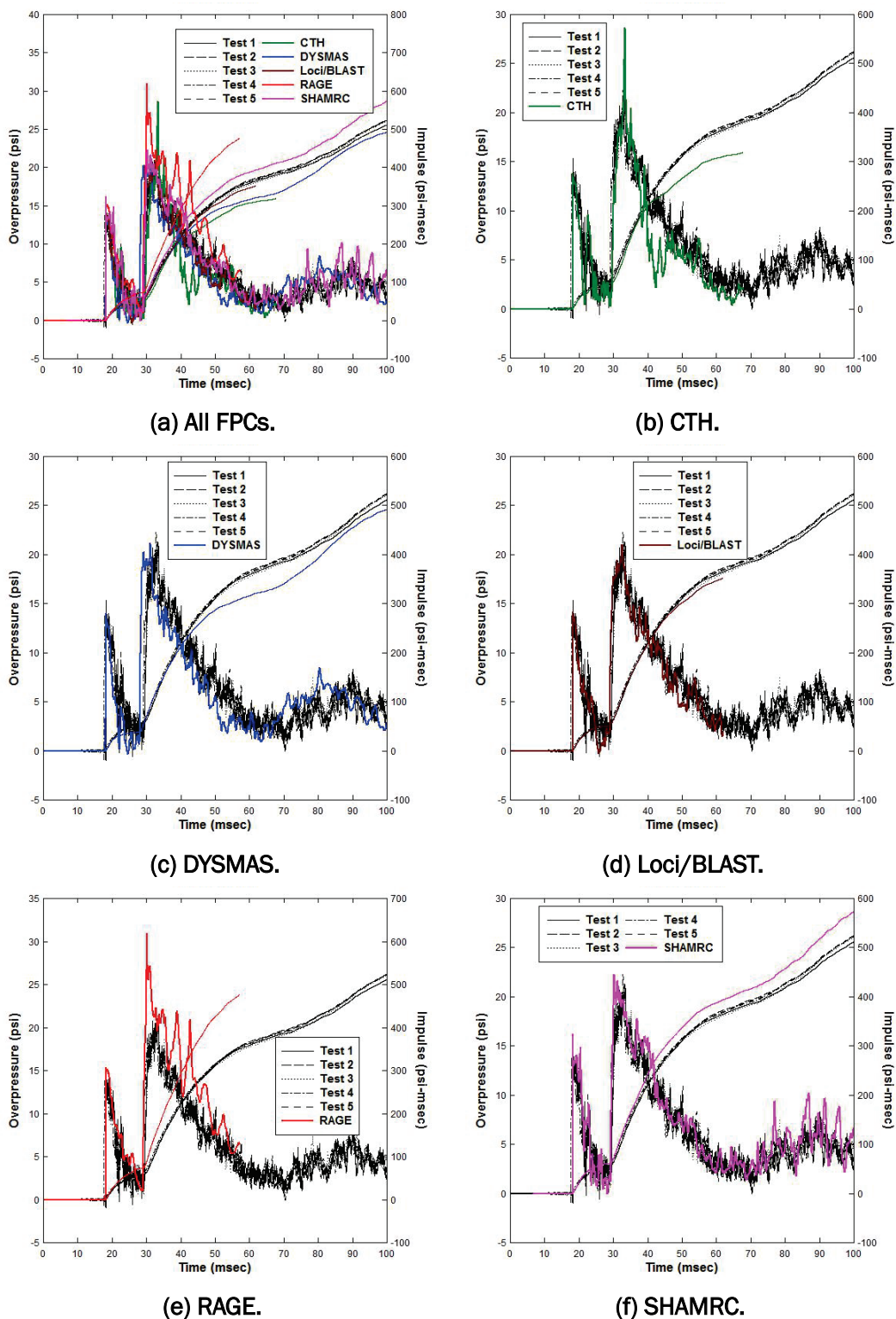


Figure 31. FPC comparisons for right face gauge PBR1.

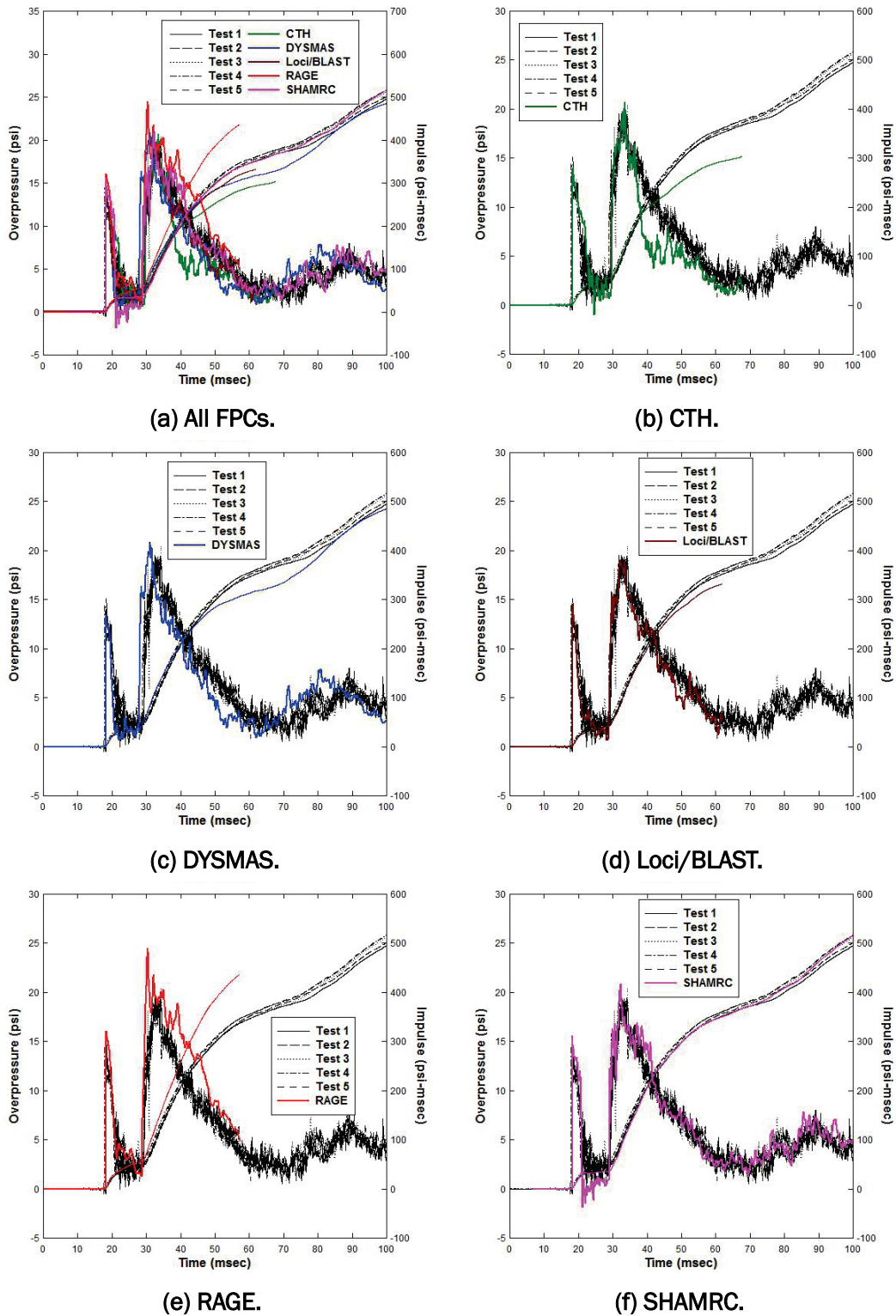


Figure 32. FPC comparisons for back face gauge PBB1.

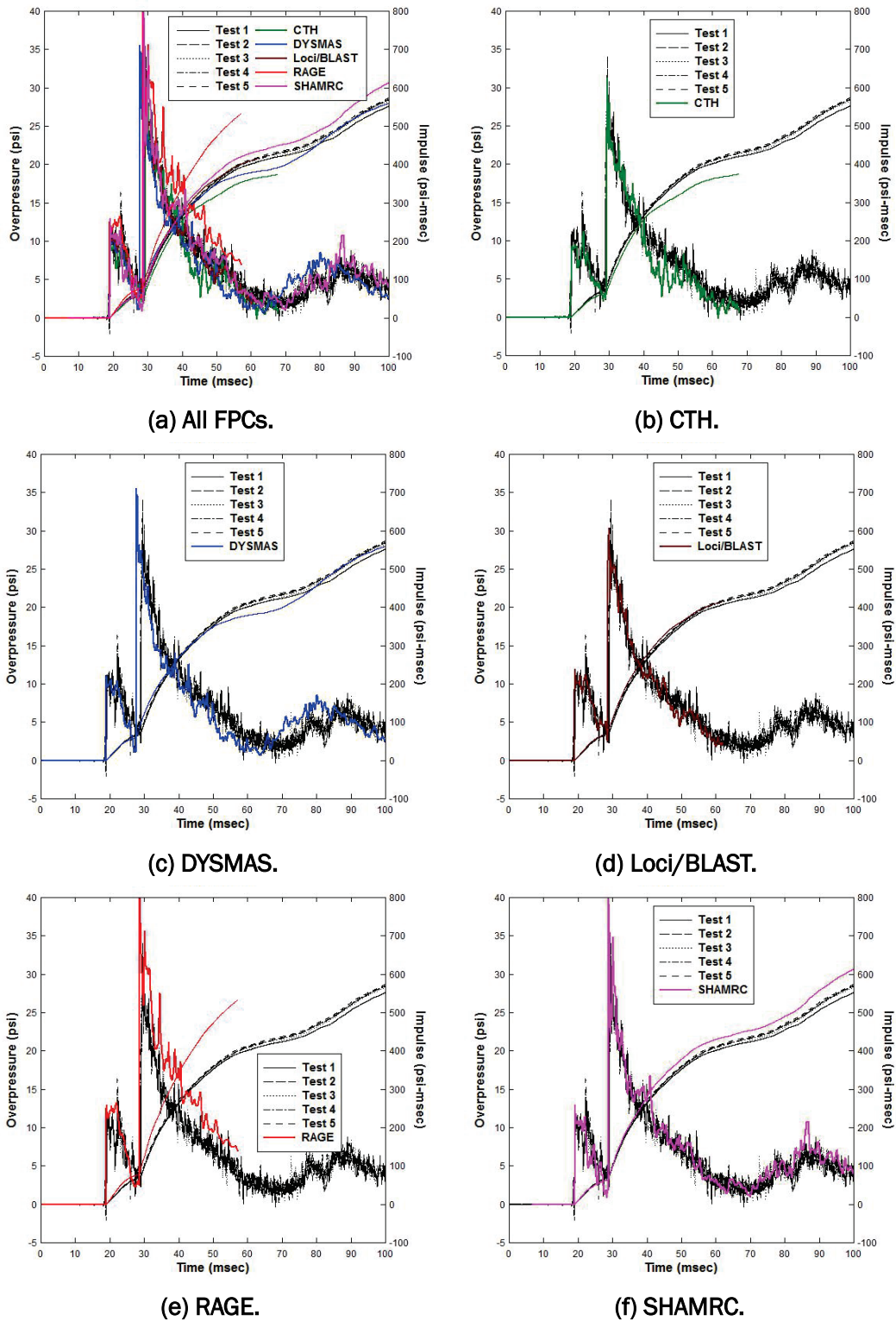
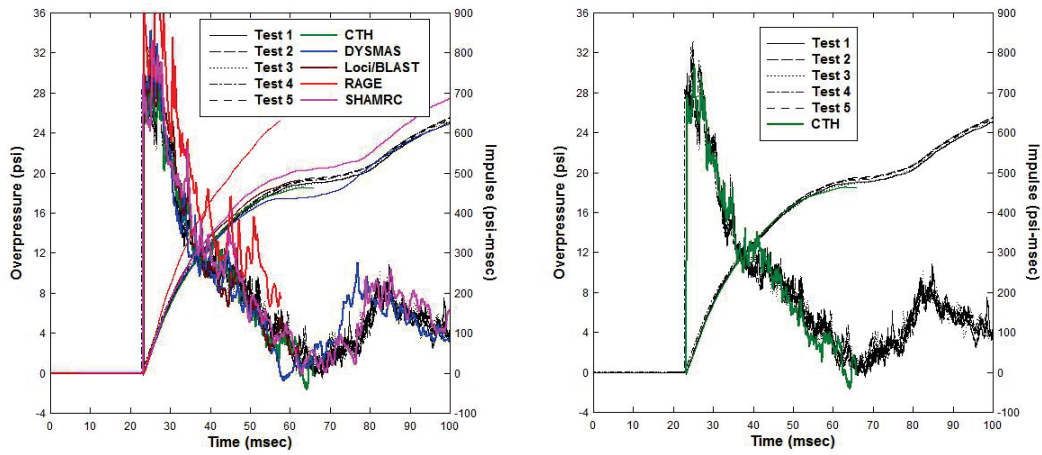
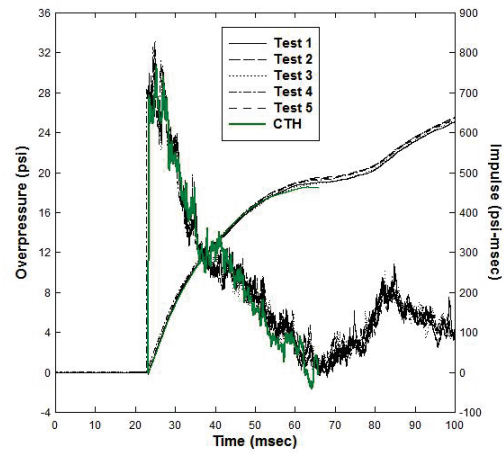


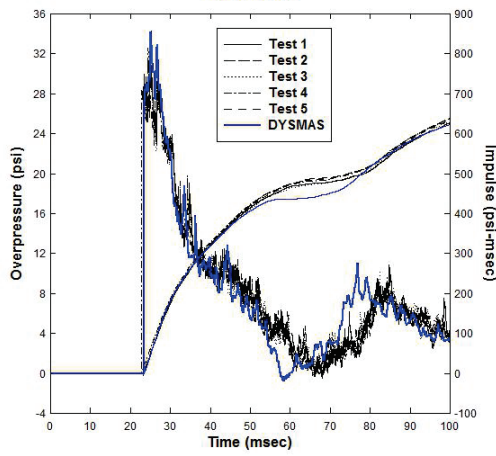
Figure 33. FPC comparisons for target wall gauge P9.



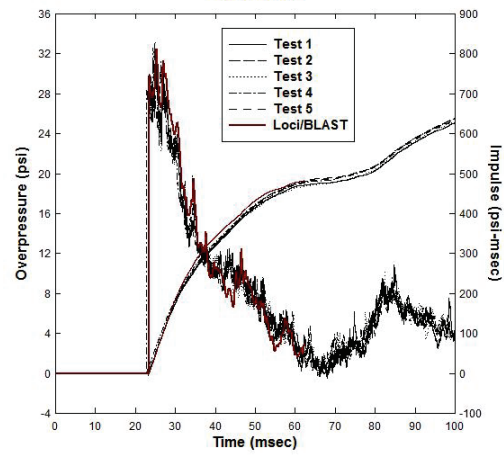
(a) All FPCs.



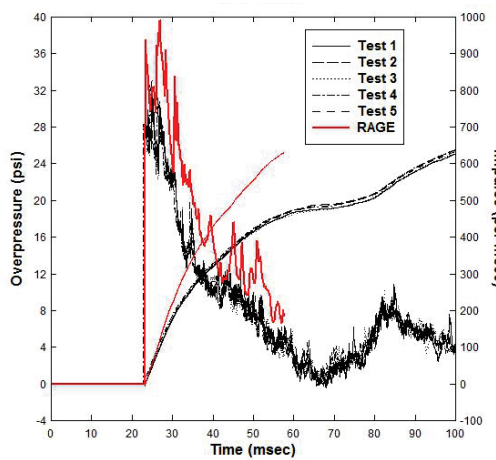
(b) CTH.



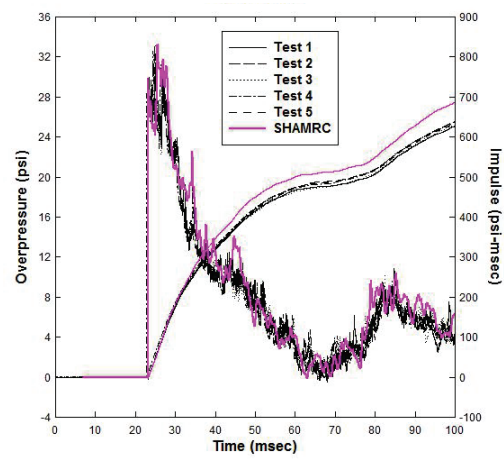
(c) DYSMAS.



(d) Loci/BLAST.



(e) RAGE.



(f) SHAMRC.

3.5 Qualitative assessment of accuracy

A qualitative assessment of code accuracy will be discussed here and subsequently used to rank the performance of the FPCs evaluated in this study. The accuracy assessment is subjective and relies on visual comparisons between the measured and calculated results outlined in the previous sections. Although no quantitative metrics were employed, the qualitative assessment is quite useful as it provides an indication of whether or not a particular code can even be applied to a BLS-type of problem. Furthermore, the three BLS cases considered allow the assessment to cover a range of physical conditions. This is important to gain insight into whether or not a code can provide reasonable predictions of airblast behavior, rather than a “postdictive” response.

The code rankings are based on tiers. Each code is designated to fall into one of three tiers, with codes falling into the first tier being the best performers. It was decided to develop separate rankings for the three different BLS configurations that were modeled. Further, it was decided to subdivide rankings for the last two BLS configurations into interior and target wall gauges. For the 8-ft×8-ft C2SQ configuration, the side-on pressure gauge PR is the interior gauge. For the 8-ft×8-ft C2SQ configuration with a box, the gauges residing on the box are all lumped into the category of interior gauges. A side-by-side comparison of the overall waveform was made for each of the codes in the development of the rankings. It is not possible to assign an ordered ranking for each code (1 to 5) due to differences noted throughout the full time-history of the waveform. Some codes might capture the initial peak well but not the second peak. Conversely, others might overpredict the initial peak but track the measured waveform almost exactly thereafter.

Qualitative rankings for code accuracy are provided in Table 8. These are based on the author’s opinion, and the reader is free to disagree. RAGE was found to perform poorly overall and was placed into the third tier. It is conjectured that there is an issue with the ideal-gas EOS implementation that should be addressed. This is discussed in detail in Appendix D. It was clear from the early 2-DC scoping calculations that RAGE would significantly overpredict the initial peak pressure and subsequently the peak impulse. Given the time constraints on the project, it was decided to move forward with the 3-D calculations with the expectation that the comparisons would be poor. This was somewhat of a less than ideal approach for conducting the analysis with RAGE.

Table 8. Qualitative rankings for code accuracy by tiers.

FPC	GSA Configuration Target Wall	8-ft×8-ft C2SQ Configuration		8-ft×8-ft C2SQ Configuration with Box	
		Target Wall	Side-on Gauge PR	Target Wall	Box Gauges
CTH	1	1	2	1	2
DYSMAS	1	1	2	2	1
Loci/BLAST	1	1	1	1	1
RAGE	3	3	3	3	3
SHAMRC	2	2	1	1	1

For the first case (GSA configuration), the first tier codes were CTH, DYSMAS, and Loci/BLAST. CTH seems to capture the overall waveform the best of the three, with DSYMAS and Loci/BLAST generally under-predicting the arrival time of the second pulse. SHAMRC was placed in the second tier due to the notable overprediction of the initial peak pressure. Otherwise, it replicated the overall waveform exceedingly well. It should probably be considered a close second.

For the second case, a similar ranking is noted for the target wall gauges for all of the same reasons as discussed for the first case. Again, SHAMRC is a close second, only because of the notable overprediction in the initial peak pressure. Otherwise, the calculated waveform correlates well with the measured data. Greater disparities between the calculated and measured data are noted for the side-on gauge PR. Both Loci/BLAST and SHAMRC capture the general structure of the measured waveform as well as the timing of the later time first spike. SHAMRC actually captures the timing of the follow-on spikes exceedingly well, albeit the amplitudes of the spikes are significantly over-predicted. Both CTH and DYSMAS were placed in the second tier due to the drop-off in pressure following the initial peak. It is possible that the tracers resided in mixed cells, which could have affected the results. This might explain the errant, but isolated, differences between the calculated and measured waveforms.

There was a slight switch for the target wall ranking in the third case, where CTH, Loci/BLAST, and SHAMRC fall into the first tier and DYSMAS the second. The slight overprediction of the initial peak pressure and underprediction of the arrival time for the second pulse resulted in DYSMAS being ranked in the second tier. One should note that neither the

CTH nor Loci/BLAST calculations were conducted long enough to capture the second pulse. It is possible that they may have also predicted an earlier arrival for the second pulse. Here, DYSMAS should be considered a close second.

DSYMAS, Loci/BLAST, and SHAMRC all fall into the first tier for comparisons against the box gauges. Both Loci/BLAST and SHAMRC replicate the measured waveforms exceedingly well, at least for the duration of the calculation. There is slightly more disparity between the DYSMAS-calculated waveform and that measured, which is generally related to the timing of the third and subsequent pulses. For CTH, there are noticeable drop-offs in the calculated pressure following the arrival of the reflected shock (second pulse). The drop-offs appear to be pervasive for the front, top, and right face gauges.

3.6 Computational cost

As mentioned earlier, the assessment of code performance entails both accuracy and computational cost. The discussion so far has focused on accuracy, albeit the assessment was subjective and relied on visual comparisons between the measured and calculated results. The focus here is on assessing the cost of conducting a calculation for a BLS-type of problem. The end goal is to move beyond the BLS and address modeling large-scale, real-world environments composed of multiple structures in the blast field. Thus, an assessment of computational cost associated with the BLS modeling should provide an indicator if an FPC can move forward for production computing involving more realistic applications.

A cost comparison for each case is provided in Tables 9 through 11. The tables contain the nominal mesh resolution for reference, the approximate number of cells, the end time of the calculation, the number of processors utilized, and the wall-clock hours (or central processing unit (CPU) time if reported). The total number of processor hours is shown in the last column. This metric is the summation of the number of processors times the wall-clock time (or CPU if specified) over all restarts. The summation is important as it captures changes in the resource requirements. This is best exemplified by a RAGE calculation, where the number of processors utilized grew as the calculation progressed forward in time. CPU times are preferred, since they exclude the expense of reading and writing data; however, the wall-clock times were typically reported by the modelers.

One should also note that the FPC calculations were conducted on different HPC platforms. Processor speeds and memory capacity varied for each of the platforms. Thus, there can be no “apples-to-apples” comparisons as the speed of computation on these platforms differ. Regardless, it is possible to perform a cost assessment on an order-of-magnitude basis as all of the HPC architectures utilized the current state-of-the-art technology. The reader should be able to recognize which FPCs provide a reasonable turn-around time for an analysis, and those that may result in intractable run times. Again, it is reiterated that the end goal is performing production computing involving more realistic applications.

Table 9. FPC computational cost comparison, GSA configuration.

FPC	Mesh Resolution (cm)	Approximate No. of Cells (millions)	Analysis End Time (msec)	No. of Processors	Wall Clock Time (hr)	Total Processor-Hours
CTH	0.5	395	60.5	1024	147	150,528
DYSMAS	1.0	136	62.7	1016	16 ¹	16,256
Loci/BLAST	2.5	52.4	70	200	156.5	31,300
RAGE	0.5 (AMR)	13 - 279	52.6	128 - 1024	429	282,280 ²
SHAMRC (Coarse)	1.0	256	110	64	31	1,984
SHAMRC (Medium-HS)	0.5	1024	110	128 - 256	93.5	20,992

¹ Reported as CPU time.

² Reported in Processor-CPU hours.

Table 10. FPC computational cost comparison, 8-ft×8-ft C2SQ configuration.

FPC	Mesh Resolution (cm)	Approximate No. of Cells (millions)	Analysis End Time (msec)	No. of Processors	Wall Clock Time (hr)	Total Processor-Hours
CTH	0.5	473	67.4	1024	193	197,632
DYSMAS	1.0	166	150	1016	31.9 ¹	32,410
Loci/BLAST	2.5	73.1	70	200	194.9	38,980
RAGE	0.5 (AMR)	39 - 509	57.2	256 - 1536	653	611,490 ²
SHAMRC (Coarse)	1.0	272	110	256	26.6	6,810
SHAMRC (Medium-HS)	0.5	1088	110	256	68.9	17,638

¹ Reported as CPU time.

² Reported in Processor-CPU hours.

Table 11. FPC computational cost comparison,
8-ft×8-ft C2SQ configuration with box.

FPC	Mesh Resolution (cm)	Approximate No. of Cells (millions)	Analysis End Time (msec)	No. of Processors	Wall Clock Time (hr)	Total Processor-Hours
CTH	0.5	473	70	1024	199	203,776
DYSMAS	1.0	166	150	1016	37.5 ¹	38,100
Locj/BLAST	2.5	69.9	70	200	240	48,000
RAGE	0.5 (AMR)	39 - 478	60	256 - 2048	643	661,980 ²
SHAMRC (Coarse)	1.0	272	110	128	52	6,656
SHAMRC (Medium-HS)	0.5	1088	110	128 - 256	101.3	19,808

¹ Reported as CPU time.

² Reported in Processor-CPU hours.

There is one last point to make regarding the SHAMRC calculations. Multiple sets of calculations were conducted for each BLS configuration. Two sets, denoted coarse and medium with half-symmetry (HS), were conducted for the GSA and 8-ft×8-ft C2SQ configurations. Two additional sets of calculations were conducted for the third case (medium fully 3-D and fine half-symmetry). Only those calculations that can be compared across all three BLS configurations are included in the tables. The reader is directed to Appendix E for details on the other SHAMRC calculations.

One would like to use a metric like the grind time to compare expense on a cycle-by-cycle basis (Attaway et al. 1998). The grind time t_{grind} is defined as

$$t_{grind} = \frac{t_{execution}}{N_{cells} N_{cycles}} \quad (1)$$

where $t_{execution}$ is the execution time, N_{cells} is the total number of cells in the problem, and N_{cycles} is the total number of cycles (or time-steps) taken in the calculation. It provides a measure of the CPU time required to perform a calculation for a single cell over one time-step. The grind time is problem dependent, and in the case of transient problems, it can be affected by variable time-stepping. When comparing grind times for different codes, it is necessary that the problem setups be identical (or relatively similar). For this work, that means a comparable physical space encompassing the BLS in each calculation as well as identical approaches for modeling interior

features such as the striker and grill. This is not the case for the BLS modeling effort. Further, code-to-code comparisons based on grind time (or any other computational efficiency measure) should all be performed on the same HPC platform. This is not the case for the BLS modeling effort either. Thus, it is necessary to develop an ad hoc approach to obtain cost comparisons on as consistent a basis as possible.

After reviewing the data in the tables, the decision was made to draw comparisons on a processor-hour (PH) basis scaled to an end analysis time of 100 msec. This measure is defined as

$$PH_{100 \text{ msec}} = \beta (100 \text{ msec}) \left(\frac{PH \text{ at } t_{\text{end}}}{t_{\text{end}}} \right) \quad (2)$$

where the final value of PH and end analysis time (t_{end}) are specified in Tables 8 through 10. The scale factor beta (β) is applied based on symmetry conditions. For a fully 3-D calculation, beta is set to 1. For a half-symmetry calculation, beta is set to 2. The goal is to equate all PH estimates for a fully 3-D calculation. It is assumed that the problem size will grow, and that the number of processors required capturing the increased problem size doubles. The scaled costs are outlined in Table 12. Note the PH value is expressed in terms of processor-kilohours (per 1,000 hr). This was done to simplify comparisons and is in line with the goal of an order of magnitude estimate. The reader should not expect anything more than a rough estimate, given the disparate setups taken by each of the modelers.

Table 12. FPC costs scaled to 100 msec and fully 3-D calculation.

FPC	Processor – K hours to reach 100 msec		
	GSA Configuration	8-ft×8-ft C2SQ Configuration	8-ft×8-ft C2SQ Configuration with Box
CTH	498	586	582
DYSMAS	26	22	25
Locj/BLAST	45	56	69
RAGE	1075	2138	2207
SHAMRC (Coarse)	2	7	6
SHAMRC (Medium-HS)	42	33	36

It is apparent that SHAMRC, DYSMAS, and Loci/BLAST are all cost competitive and fall into the first tier. Both DYSMAS and the SHAMRC (coarse) calculations utilized a 1.0-cm resolution mesh. On this basis, one might rank SHAMRC as the best cost performer for the codes evaluated. The cost for CTH is an order of magnitude greater than any of the first tier codes. Both CTH and the SHAMRC (medium) calculations utilized a 0.5-cm resolution mesh, with CTH requiring about 12 to 16 times more resources. Recall that the PH estimate is a combination of time and processors, with the combination of the two representing the computational resources needed to conduct the calculation.

The RAGE calculations were exceedingly expensive. This is in line with our experience modeling explosive detonations using the SAIC Adaptive Grid Generation (SAGE) code at the ERDC (Archer et al. 2005). The AMR capability in SAGE performs exceedingly well in capturing explosive detonation processes as well as the near field blast behavior; however, run times increase substantially when the physical space being modeled is large. Examples involving a large physical space include both open-air and internal detonations. SAGE (and RAGE) has the capability to map a 1-DS or 2-DC calculation into a 3-D problem setup, thereby reducing the mesh resolution requirements for the latter. Unfortunately, this capability could not be utilized in the BLS modeling that required that all RAGE calculations be 3-D from the start.

4 Summary and Recommendations

An integrated experimental and computational program was conducted to evaluate several FPCs for modeling airblast environments typical of that encountered in the ERDC BLS. The FPCs considered were CTH, DYSMAS, Loci/BLAST, RAGE, and SHAMRC. These codes afforded a range of numerical solvers and EOS options for the modeling effort. The FPCs were evaluated against data generated in the BLS. Three experimental configurations were considered for the validation. These included two empty configurations, with comparisons drawn against reflected pressures measured at the downstream target wall. The third included a box-like structure in the flow field. The structure was instrumented on the exposed sides to provide a more challenging scenario for the model comparisons. The purpose of the integrated program was to assess computational accuracy and cost of the aforementioned FPCs, as well as identify any shortcomings in the physics modeling and areas for future improvement.

A qualitative assessment of accuracy was made based on visual comparisons between the calculated and measured waveforms for the three BLS configurations modeled. Good overall correlation with the measured data was noted for CTH, DYSMAS, Loci/BLAST, and SHAMRC. The relative ranking of these codes based on accuracy is problem dependent, but certainly results from any of these would be considered reasonable. A separate assessment was made based on computational cost. Run times for DYSMAS, Loci/BLAST, and SHAMRC were quite acceptable for production computing. CTH was found to be very expensive, with the computational cost being an order of magnitude greater than that of the other three codes.

RAGE was found to perform poorly overall (in both accuracy and cost). It is conjectured that there is an issue with the ideal gas EOS implementation that should be addressed. This is discussed in Appendix D. The Leidos version of RAGE was utilized in this work, and it is recommended that a follow-on analysis be conducted with the LANL version. This would be helpful to diagnose the issue and possibly pinpoint the source of the problem. The follow-on work could be very limited in scope. A simple 2-DC calculation would suffice and would provide a quick assessment of whether the issue persists in the LANL version.

All of the calculations conducted for this report assumed inviscid flow. Consequently, physical mechanisms such as turbulence and boundary layer effects were not included in the simulations. Review of the user documentation suggests that both Loci/CHEM, a forerunner of Loci/BLAST that has an implicit solver built under the same framework, and SHAMRC have the capability to handle viscosity and/or turbulence. Although the inviscid flow calculations considered here suggest that viscosity has a second order effect, this may not always be the case as the experimental program moves forward. It is recommended that a follow-on analysis that includes viscous effects be conducted with one of the BLS configurations considered here to examine if the solutions change. This would provide an initial validation test of the viscous modeling and provide insight into the computational costs.

The BLS testing considered in the study was based on a single set of driver conditions. It is recommended that extended testing be conducted involving the third BLS configuration (with box). This testing could maintain the same configuration with variations in the driver conditions. This would allow the accuracy of the models to be evaluated over a range of loading conditions. It is further recommended that the testing be extended to consider a two-box configuration. Here the emphasis would be on capturing the diffraction and vortex shedding noted about the first box and subsequent pressure loading on the face of the second box. The spacing between boxes would influence the degree of shock interaction and subsequently the loads induced on the box faces. A methodical approach would be to consider two boxes of the same height and vary the spacing in-between for a fixed set of driver conditions. The driver conditions could then be varied to induce a range of incident shocks conditions. This would allow for the codes to be evaluated over a range of conditions using a relatively simple problem setup.

References

- Archer, B., T. Betlach, M. Clover, E. Dendy, M. Gittings, M. Lumsden, L. McClellan, W. Oaks, D. Ranta, A. Schwendt, C. Scovel, K. Simmons, M. Steinkamp, R. Weaver, and D. Weeks. 2005. *SAGE users manual*. LA-UR-04-2959. Los Alamos, NM: Los Alamos National Laboratory.
- Attaway, S. W., B. A. Hendrickson, S. J. Plimpton, D. R. Gardner, C. T. Vaughan, K. H. Brown, and M. W. Heinsteins. 1998. A parallel contact detection algorithm for transient solid dynamics simulations using PRONTO3-D. *Computational Mechanics* 22:143-159.
- Bessette, G. C., and J. R. Britt. 2011. *Numerical modeling of impulse measurement device tests involving a clay backfill (Tests BM-C-01 through -05)*. ERDC/GSL TR-11-39. Vicksburg MS: U.S. Army Engineer Research and Development Center.
- Crawford, D. A., R. G. Schmidt, and R. J. Butler. 2013a. *Spymaster user's guide, Version 5.3*. Sandia Technical Report. Albuquerque, NM: Sandia National Laboratories.
- Crawford, D. A., A. L. Brundage, E. N. Harstad, K. Ruggirello, R. G. Schmidt, S. C. Schumacher, and J. S. Simmons. 2013b. *CTH user's manual and input instructions, version 10.3*. Sandia Technical Report. Albuquerque, NM: Sandia National Laboratories.
- Crepeau, J., C. Needham, S. Hikida, H. Happ, and R. Bell. 2012. *SHAMRC, Second-order hydrodynamic automatic mesh refinement code, Volume 1: Methodology, Version 8*. Albuquerque, NM: Applied Research Associates, Inc.
- Clover, M. 29 July 2015. Personal communication via e-mail. *RAGE modeling of shock tube problem*.
- Dallriva, F. D., C. F. Johnson, and J. L. O'Daniel. 2016. *Blast load simulator experiments for computational model validation – Report 1*. ERDC/GSL TR-16-27. Vicksburg MS: U.S. Army Engineer Research and Development Center.
- De Groot, A. J., R. J. Sherwood, and J. K. Durrenberger. 2013. *ParaDyn user manual, ParaDyn: A parallel nonlinear explicit, three-dimensional finite-element code for solid and structural mechanics*. LLNL-SM- 644094. Livermore, CA: Lawrence Livermore National Laboratory.
- Doan, L. R., and G. H. Nickel. 1963. *A subroutine for the equation of state of air*. RTD (WLR) TN63-2. Albuquerque, NM: Air Force Weapons Laboratory.
- Gittings, M., R. Weaver, M. Clover, T. Betlach, N. Byrne, R. Coker, E. Dendy, R. Hueckstaedt, M. Kim, W. R. Oakes, D. Ranta, and R. Stefan. 2008. The RAGE radiation-hydrodynamic code. *Computational Science and Discovery* 1:1-71.
- Happ, H., J. Crepeau, S. Hikida, and C. Needham. 2014. *SHAMRC version 8, Volume 2: User's manual*. Albuquerque, NM: Applied Research Associates, Inc.

- Harris, G., A. Luton, T. McGrath, R. McKeown, J. St. Clair, W. Babcock, and A. Wardlaw. 2014. *Overview of the dynamic system mechanics advanced simulation code (DYSMAS)*. NSWC IHSP 14-04. Indian Head, MD: Naval Surface Warfare Center, Indian Head EOD Technology Division.
- Hertel, E. S., and G. I. Kerley. 2006. *CTH EOS package: Introductory tutorial*. SAND98-0945. Albuquerque, NM: Sandia National Laboratories.
- Kitware. 2015. ParaView. <http://www.paraview.org/overview/> (accessed 04 September 2015).
- Lee, E. L., and C. M. Tarver. 1980. Phenomenological model of shock initiation in heterogeneous explosives. *Physics of Fluids* 23(12):2362-2372.
- Luke, E. A. 1999. A rule based specification system for computational fluid dynamics. Ph.D. diss. Starkville, MS: Mississippi State University.
- Luke, E. A., and T. George. 2005. Loci: A rule-based framework for parallel multidisciplinary synthesis. *Journal of Functional Programming* 15(3): 477-502.
- Luke, E. A., and P. Cinella. 2007. Numerical simulations of mixtures of fluids using upwind algorithms. *Computers and Fluids* 36:1547-1566.
- Marcum, D. L. 1998. Unstructured grid generation using automatic point insertion and local reconnection. *The handbook of grid generation*. 18-1. CRC Press.
- McGlaun, J. M., S. L. Thompson, and M. G. Elrick. 1990. CTH: A three dimensional shock physics code. *International Journal of Impact Engineering* 10(1-4):351-360.
- Mord, C. T. 2015. Simulation of the ERDC blast load simulator (BLS) for various test configurations using Loci/BLAST. M.S. thesis. Starkville, MS: Mississippi State University, Dept. of Aerospace Engineering.
- Sandia National Laboratories. 2015. Cubit Toolkit. <https://cubit.sandia.gov/> (accessed 04 September 2015).
- Thompson, D., E. A. Luke, J. C. Newman III, M. Janus, E. Blades, X. Tong, C. Moore, and J. Kang. 2010. *Development of a strategy for simulating blast-vehicle interactions*. TARDEC Report 21200RC. Warren, MI: U.S. Army Tank Automotive Research, Development, and Engineering Center.
- Thompson, D., M. Janus, E. A. Luke, C. Moore, M. Remotigue, X. Tong, R. Weed, and P. Ivancic. 2012a. *Enhanced simulations of blast-vehicle interactions using Loci/BLAST and LS-DYNA*. TARDEC SimBRS WD-34. Warren, MI: U.S. Army Tank Automotive Research, Development, and Engineering Center.
- Thompson, D., E. A. Luke, M. Remotigue, X. Wang, E. Collins, Q. Arnholdus, M. Trcalek, J. Janus, R. Weed, C. Moore, and X. Tong. 2012b. *Multi-fidelity tools for blast analysis in urban environments*. DHS SERRI Report 90028-001. Starkville, MS: Mississippi State University, Center for Advanced Vehicular Systems.
- Thompson, S. L., and L. N. Kmetyk. 1999. *HISPLT: A time-history graphics postprocessor user's guide, Version 4.0*. SAND91-1767. Albuquerque, NM: Sandia National Laboratories.

- Van Leer, B. 1977. Towards the ultimate conservative difference scheme, IV, A new approach to numerical convection. *Journal of Computational Physics* 23(3):276-299.
- Wardlaw, A., A. Luton, J. Renzi, K. Kiddy, and R. McKeown. 2003. *The GEMINI Euler solver for the coupled simulation of underwater explosions*. NSWC IHTR 2500. Indian Head, MD: Naval Surface Warfare Center, Indian Head EOD Technology Division.
- Whirley, R. G., and B. E. Englemann. 1993. *DYNA3-D: A nonlinear, explicit, three-dimensional finite element code for solid and structural mechanics user manual*. UCRL-MA-107254. Livermore, CA: Lawrence Livermore National Laboratory.
- Yarrington, L. 2006. *CTHREZ: User's guide and input instructions, Version 1.03*. Sandia Technical Report. Albuquerque, NM: Sandia National Laboratories.

Appendix A: CTH Modeling

CTH Background

Comprehensive descriptions of the CTH code are provided in Crawford et al. (2013b), Bessette and Britt (2011), and McGlaun et al. (1990). The following is a summary of those descriptions. CTH is a multi-material, Eulerian, large deformation, strong shock wave, solid mechanics code developed at Sandia National Laboratories. It has been in wide use within the DoD community for several decades. CTH falls into a category of structured mesh codes in which the reference mesh is fixed in space and aligned with the major coordinate axes. Three-dimensional (3-D) rectangular meshes, two-dimensional rectangular (2-DR) and cylindrical (2-DC) meshes, and one-dimensional rectilinear (1-DR), cylindrical (1-DC), and spherical (1-DS) meshes are available to the user. CTH also has adaptive mesh refinement. A 3-D mesh is composed of hexahedral cells that can vary in size and aspect ratio along the major coordinate axes. As described by Bessette and Britt (2011), CTH utilizes a two-step solution procedure for the conservation equations. It first takes a Lagrangian step, which allows the reference mesh to deform. The equations of motion are integrated forward in time with the material response updated subject to a constitutive model. The integration is performed explicitly with individual time-steps subject to a Courant-Friedrichs-Lewy (CFL) condition on stability, as well as limits on volume transport between cells. The CTH default CFL values of 0.55 for 3-D and 0.6 for 1-D and 2-D were used for all calculations.

The Lagrangian step is followed by a remap or advection step that maps data (i.e., the volume flux, mass, momentum, energy, and material state data) from the deformed Lagrangian configuration back into the fixed Eulerian frame of reference. In this step, a donor-acceptor relationship is defined where a donor cell is said to advect material to an acceptor cell. First, the volume flux from the donor to an acceptor cell is determined. Then the material mass and internal energy are advected. Finally, the momentum and kinetic energy are advected to the reference mesh. Advection is determined using a second-order accurate scheme attributed to Van Leer (1997). An interface-tracking algorithm is used to reconstruct the locations of material interfaces (as well as free surfaces) based on the volume fraction of materials in the upstream, downstream (acceptor), and donor cells.

CTH supports a wide range of constitutive models appropriate for strong shock, large deformation calculations. It has models for multiphase, elastic, viscoplastic, porous, and explosive materials, with model coefficients provided in a library supplied with the code. The stress response in a material is decomposed into its dilatational and deviatoric behaviors. The dilatational (or volumetric) response is described using an EOS, while a strength model is used to describe the deviatoric (or distortional) response. In the high-pressure regime, SESAME tabular and analytic EOS models are used to replicate the nonlinear behavior of materials. The SESAME table (Hertel and Kerley 2006) is intended to cover a broad density-temperature range so that it can be used in many different applications, e.g., to treat high compressions, large expansions, and high temperatures. SESAME can model solid, liquid, vapor, liquid-vapor, solid-liquid, and solid-solid phase changes. Hertel and Kerley (2006) stated that the SESAME table “allows the use of sophisticated models that are too complicated to be incorporated into analytic formulas. A good tabular EOS gives valid results over a much wider density-temperature range than the analytic EOS models.”

High-explosive detonation can be modeled using programmed burn or several reactive burn models, e.g., the History Variable Reactive Burn (HVRB) model (Hertel and Kerley 2006) developed at Sandia. With the program burn option, “an ideal detonation wave front is made to propagate at a given velocity from initiation points specified by the user” (Hertel and Kerley 2006). In contrast to programmed-burn models, the material decomposition is included in the EOS of reactive burn models, and time evolution of the reaction is described by a rate equation (Hertel and Kerley 2006). Either the Jones-Wilkins-Lee (JWL) analytic (Hertel and Kerley 2006) or the SESAME tabular equations of state can model the high-explosive reaction products (Crawford et al. 2013b).

In the problem development, the user may define material or part geometries using simple primitive shapes, which can be combined (or subtracted) as needed to develop a final geometric entity. As an alternative, computer aided design (CAD) geometry may be inserted using a limited number of file formats (Crawford et al. 2013b), i.e., ASCII versions of a Pro/Engineer tetrahedral or shell mesh, an Exodus tetrahedral or hexahedral mesh, or an STL file. Boundary conditions (BCs) are applied to the borders of the fixed reference mesh. CTH supports several BC types, including reflective or symmetry, transmissive, and outflow (Crawford

et al. 2013b). Transmissive BCs are sound speed absorbing and are typically used to model semi-infinite domains. However, they can be problematic for strong shock interactions where wave speeds exceed the acoustic velocity.

In CTH, artificial bulk viscosity terms (linear and quadratic) assist with the handling of strong discontinuities in stress, such as those found in a shock front. The quadratic term is used to smear a shock front across several cells. The linear term is used to minimize excess noise (“ringing”) in the simulation. A linear term that is too large can cause excessive smearing of the discontinuity (Crawford et al. 2013b).

Within the CTH family of codes, a rezoning program (Yarrington 2006) allows an analyst to modify a simulation at a specified time. The user may change the zoning, orientation, and the number of dimensions. For example, a 1-DS calculation of an aboveground detonation with 0.2-cm cell sizes could be run out until the shock front nears the ground surface. Those results can be rezoned into a 3-D mesh with nominal 1-in. cells, and the calculation continued out to later times. This process allows the analyst to use a much finer mesh for the detonation region and a more affordable mesh size for the subsequent 3-D calculation, resulting in a great savings of time and computer resources versus running the entire simulation in 3-D. Rezoning was not used in this project, due to past problems with the software.

CTH requires all input in CGS units, i.e., centimeter (cm), gram (g), second (sec), and electron volts for temperature (one eV = 11,600 deg Kelvin). Pressures in this unit system are in dynes/cm².

Analysis overview

All of the CTH calculations were run on the Cray XE6 located at the ERDC DoD Supercomputing Resource Center, commonly referred to as Garnet. The Cray XE6 has 4,716 compute nodes with 32 cores per node. Each compute node has a core speed of 2.5 GHz and 64 GB of accessible memory.

A stepwise approach was taken to evaluate the shock environments for this project. This involved a series of 1-DS, 2-DC, and eventually 3-D calculations, with a progressively increasing level of difficulty. Both the SESAME and ideal gas EOSs were used to approximate the properties of

the air. The walls of the BLS were modeled as either rigid or deformable materials. Deformable walls were assigned the properties of lead due to its low wave speed and the desire to achieve a time-step as large as possible. The lead properties were approximated with the Mie-Grüneisen EOS and with an enhanced von Mises yield strength. The elastic parameters were not altered. The striker was modeled in all of the 3-D calculations and in six of the fifteen 2-DC simulations. Other than its nominal 3-in. width, the grill was neither modeled in the 2-DC simulations, due to the axisymmetric geometry, nor in the 3-D calculations, due to the fine mesh resolution required to accurately capture the individual horizontal and vertical 1/8-in.-thick members.

CTH requires input for time-step control, restarts, cell thermodynamics, convection, discards, tracer points, and spatial output. Discards are used to improve the time-step and/or prevent a calculation from stopping due to “material that is acquiring non-physical states.” Spatial output (e.g., pressure, density, or temperature plotted over the computational domain) was saved to Spymaster files (Crawford et al. 2013a). These files were post-processed with either CTH’s SPYPLT software or with the open-source visualization application ParaView (Kitware 2015).

Time-history output locations in CTH are defined with tracer input. Each tracer may be fixed in space or allowed to move. For the BLS simulations, all of the tracers were fixed. As explained in Thompson and Kmetyk (1999), plot variables consist of either point (e.g., pressure, density, temperature), material (e.g., energy, momentum), or global (e.g., time-step, cycle number, mass) information. Approximately 70 variables are available for post-processing. Care must be taken to avoid placing tracers at locations where mixed cells (more than one material per cell) may develop. A mixed cell with air and solid will typically produce undesired output for the user.

Early 1-DS calculations

The 1-DS calculations were conducted for two purposes: (1) to evaluate mesh refinement, and (2) to evaluate the two EOS options for air. Both the SESAME and ideal gas EOSs were used to represent the air. The 1-DS calculations were very cost-effective. For example, a typical run with 0.2-cm resolution, a maximum range of 20 ft, with approximately 3,100 cells, and a simulation time of 20 m/s required less than 40 sec of wall-clock time using 32 cores (or one compute node).

Figure A shows the difference in calculated peak overpressure as a function of range for meshes having cell sizes of 0.2 and 2.0 cm. The source region in the 2.0-cm resolution calculation had a finer mesh (0.2-cm cell size) to ensure consistency in the comparisons. At the 6.6-ft range, the peak overpressure in the finer mesh was 6 percent greater than the coarser one. At the 3.8-ft range, the increase was a 7.5 percent. In Figure A2, the peak overpressure versus range is shown for calculations using the SESAME and ideal gas EOSs for air. At the 6.6-ft range, the peak pressure associated with the ideal gas EOS was 10.9 percent greater and at the 3.8-ft range it was 10.7 percent greater.

Figure A1. Results of 1-DS CTH calculations comparing mesh resolution.

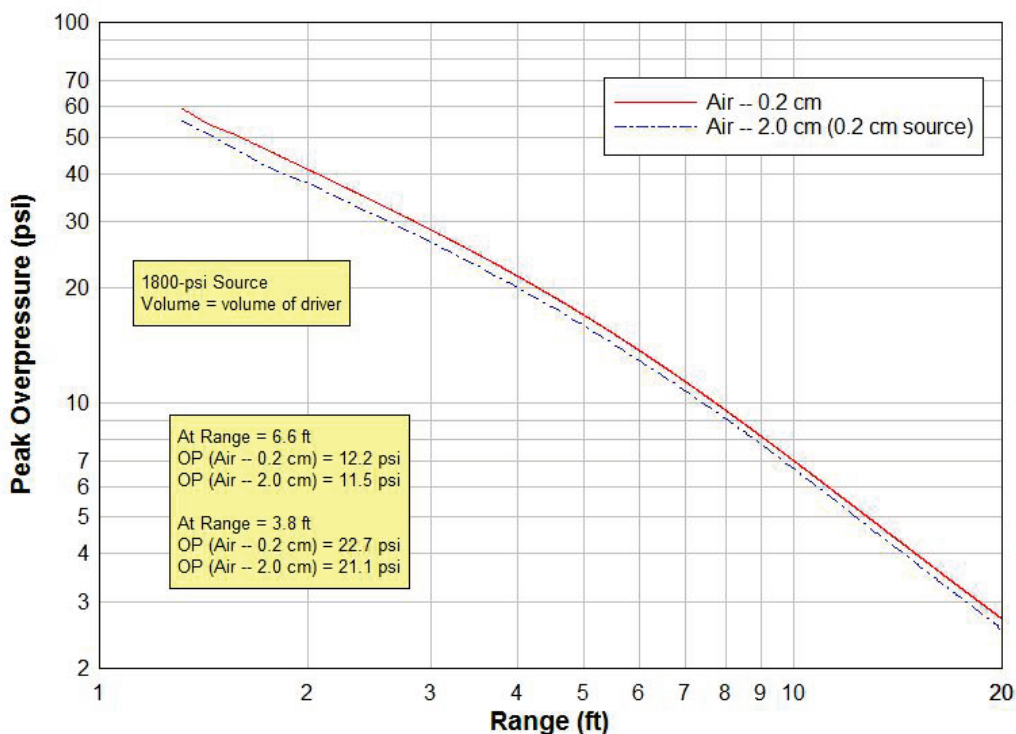
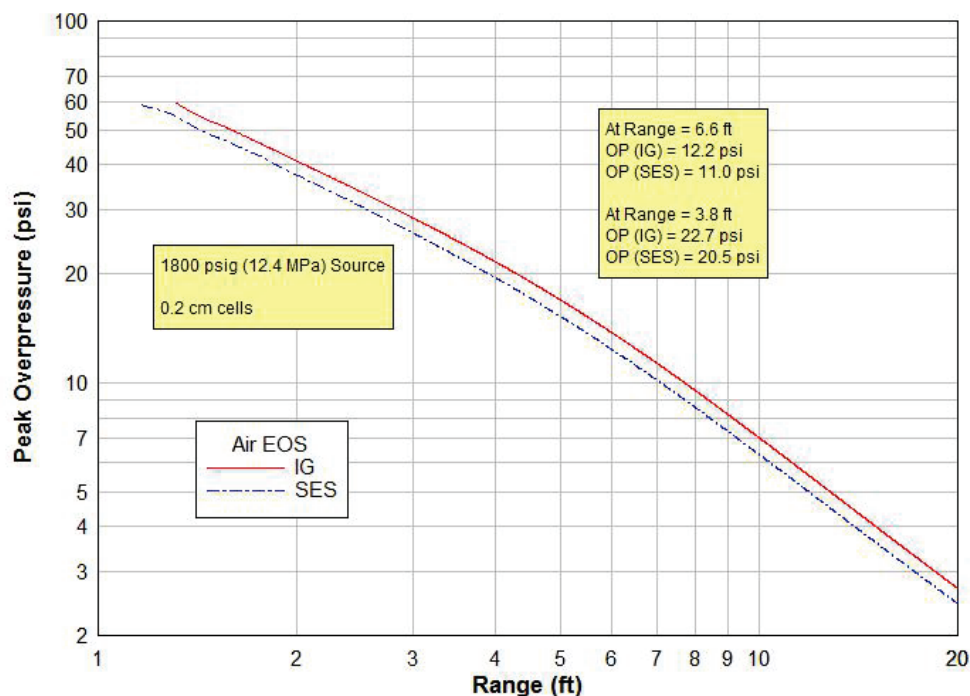


Figure A2. Results of 1-DS CTH calculations comparing EOS options.



Early 2-DC calculations

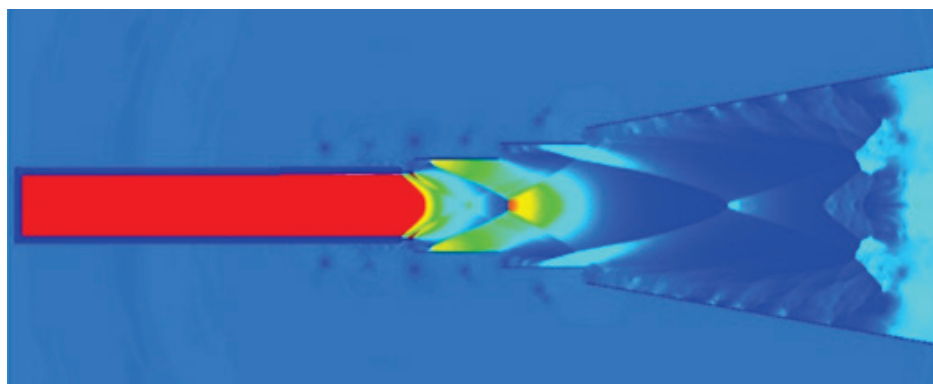
The 2-DC CTH calculations of the GSA configuration (Case 1) were conducted to evaluate (1) the effect of mesh refinement on peak overpressures, (2) different air EOSs, (3) the effect of the striker on downstream pressures, and (4) the planarity of the shock in an axisymmetric geometry. The 2-DC calculations used nominal 0.1-, 0.2-, or 0.5-cm cell sizes. Reflective BCs were applied to the axis of symmetry and transmissive BCs were applied to the three borders of the computational domain. The walls of the BLS were modeled as rigid materials. The air was modeled with either the SESAME or ideal gas EOS. The driver air was assigned an initial pressure of 1,298 psig and an initial temperature of 77°F, and the ambient air initial values of 14.7 psia and 77°F.

Figures A3 through A8 show the results from a nominal 0.2-cm resolution mesh and the SESAME EOS for air. Pressure state plots at 12 msec (a) without and (b) with the striker are shown in Figure A3. The pressure environment between the driver and upstream edge of the CVC-2 section has been significantly perturbed by the presence of the striker. However, the environments from the upstream edge of the cone section to the right edge of the image are qualitatively similar. The expansion of the air in the

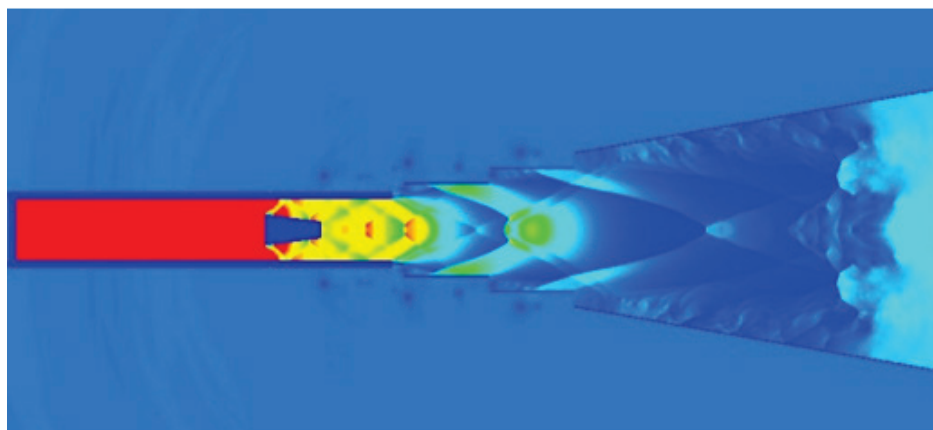
cone section appears to mitigate the heterogeneous state of the pressure field induced by the presence of the striker.

Figure A4 shows the early-time pressure environment at 3, 5, and 7 msec with the striker installed. At 3 msec, the shock has reached the entrance of the cone section with a non-planar front, and high pressure air is venting out of the system. At 5 msec, the initial shock is approximately one-quarter down the length of the cone section and is still non-planar. Within the CVC section, the pressure environment is very heterogeneous and shows multiple reflected shocks. The initial shock at 7 msec is approximately at the center of the cone section and still exhibits some curvature. The complex nature of the environment is still present within the CVC section.

Figure A3. CTH 2-DC pressure state plots at 12 msec, with and without striker.

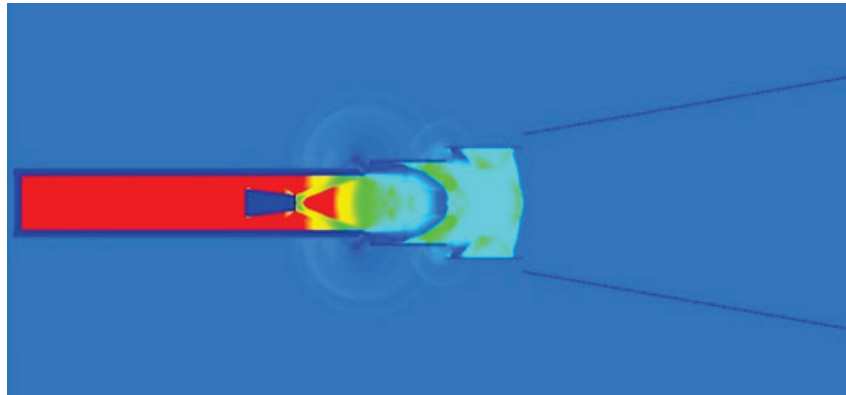


(a) Without striker

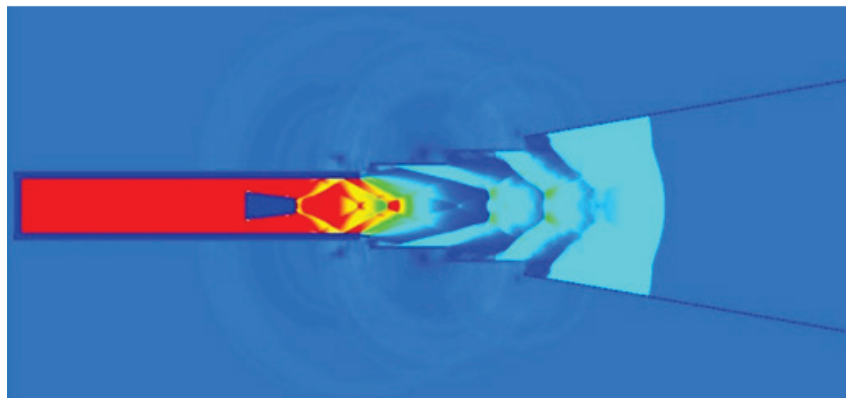


(b) With striker

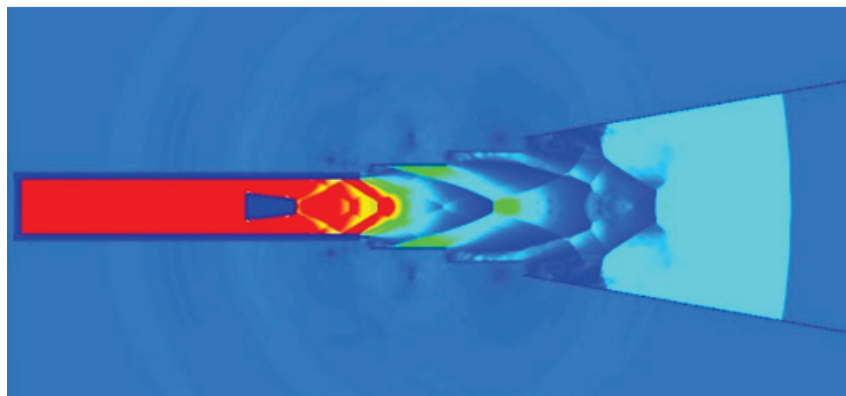
Figure A4. CTH 2-DC pressure state plots at varied times.



(a) 3 msec



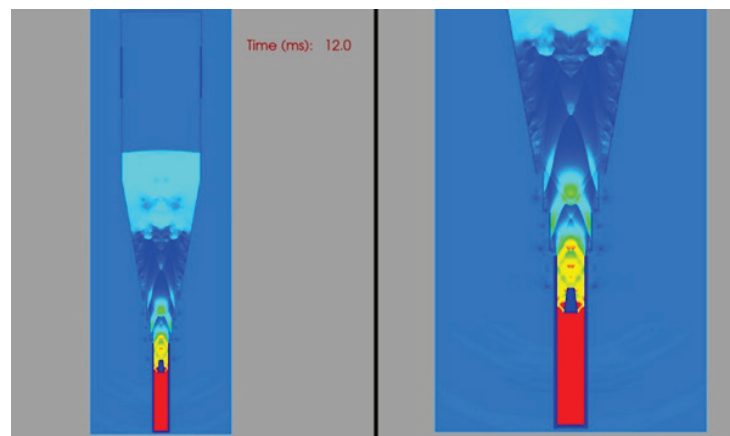
(b) 5 msec



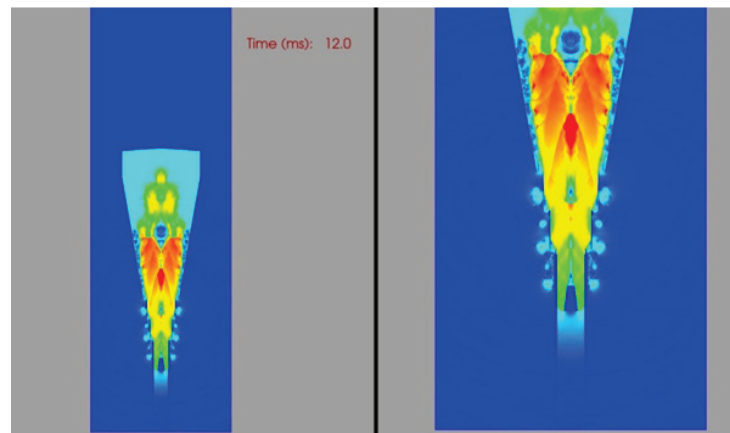
(c) 7 msec

Pressure and velocity magnitude are shown at 12 msec in Figure A5(a) and (b), respectively. Each image shows two views; on the left the entire BLS and on the right the upstream end of the BLS. The initial shock front has entered the TR1 and TR2 sections of the BLS at this time. The pressure environment behind the front is more homogeneous than at the earlier times. However, the velocity magnitude plot exhibits a more complex structure than the pressure. High pressure air escaping from the vents is clearly evident in this image.

Figure A5. CTH 2-DC state plots at 12 msec.



(a) Pressure at 12 msec

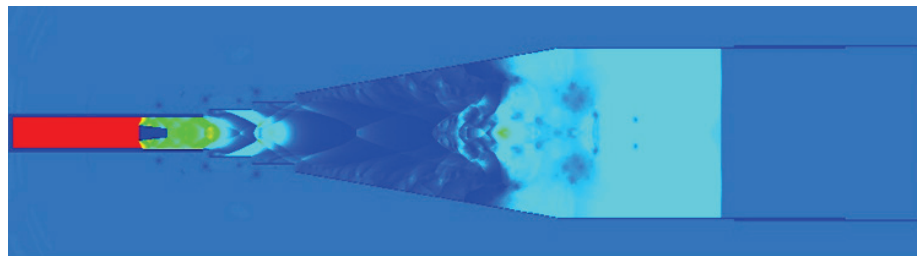


(b) Velocity magnitude at 12 msec

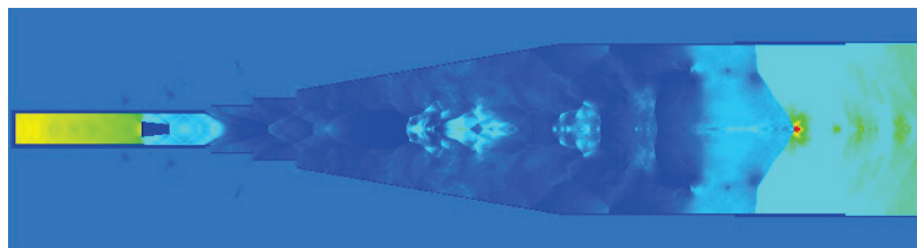
The pressure environment in the BLS at 15 and 27 msec is captured in Figure A6. At 15 msec, the initial shock front is planar, and a mass of air at nominal constant pressure follows the front. At 20 msec (no image provided), the initial shock front reached the bulkhead at the end of the BLS. At 27 msec, the reflected shock front is positioned approximately at the middle of the TR-Cascade section. The reflected front at this time is non-

planar due to the interaction of the front with the mass of air still moving downstream. This image also shows intermittent focusing of higher pressure air along the centerline of the BLS.

Figure A6. CTH 2-DC pressure state plots at later times.



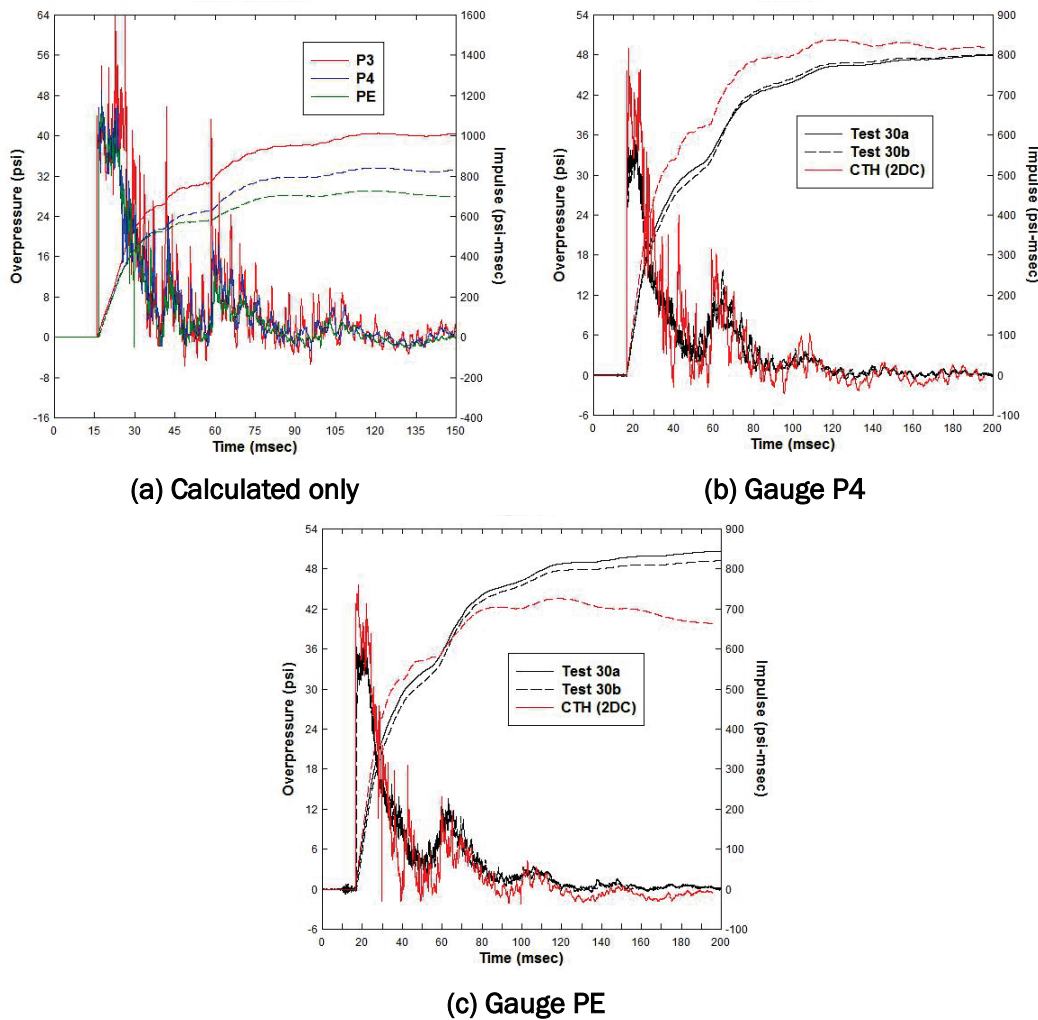
(a) Pressure at 15 msec



(b) Pressure at 27 msec

Figure A7 shows time-history traces at gage locations P3, P4, and PE. Image (a) shows a comparison plot of the traces from the calculation. The P3 trace contains significant noise compared to the other two. This noise is attributed to the tracer location being located in a cell 2.25 in. away from the axis of symmetry. The CTH time-history traces at gage locations P4 and PE are compared to the experimental records in images (b) and (c), respectively. The CTH data were shifted -4.59 msec to match the time of arrival of the experimental records. The peak pressures in the two CTH traces were greater than the measured and the overall impulse was not captured well in CTH.

Figure A7. Gauge comparisons for 2-DC CTH calculation of GSA configuration.



Overview of the 3-D calculations

In general, the 3-D CTH calculations of the BLS were conducted using half-symmetry, a nominal 0.5-cm cell size, the SESAME EOS for air, and deformable walls. There was one exception that utilized the same configuration and resolution; however, the air was modeled as an ideal gas. As described in the main text, three configurations were simulated, the GSA configuration, the 8-ft×8-ft C2SQ configuration, and the 8-ft×8-ft C2SQ configuration with box. Each subsequent configuration added more complexity to the modeling effort.

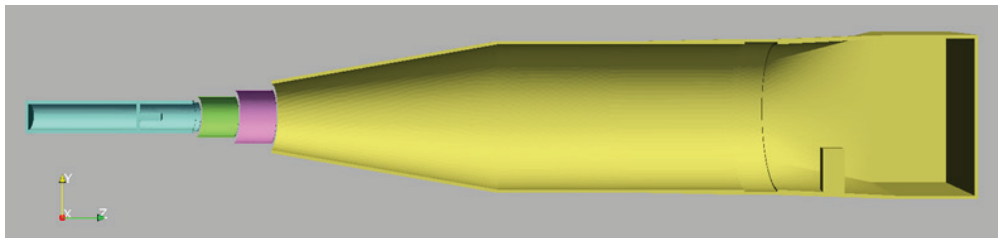
Reflective BCs were applied to the axis of symmetry, and transmissive BCs were applied to the three borders of the computational domain. The BLS

geometry was created in Cubit (a general pre-processing tool; Sandia National Laboratories 2015), and the major components output to individual Exodus files. CTH imports the Exodus files and extracts the volume of each component. It then simply superimposes the prescribed computational mesh on top of the volumes. Figure A8 shows images of the components for the 8-ft×8-ft C2SQ configuration with box. The four colors represent the four volumes imported into CTH. A close-up of the as-modeled striker geometry is shown in Figure A9.

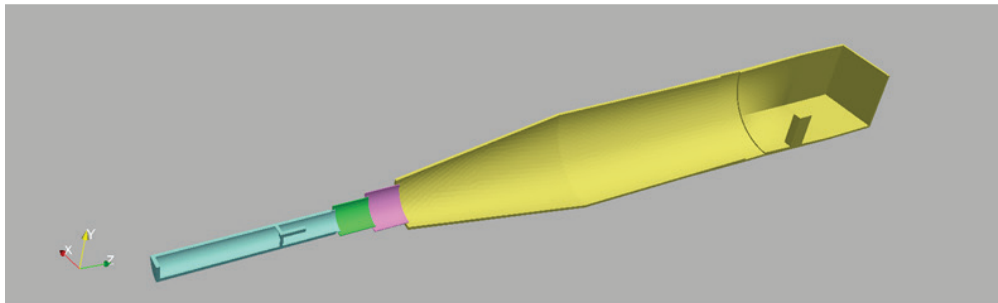
GSA configurations, Tests 30a and 30b

The simulation for the GSA configuration used 395 million cells and required 147 hr of wall-clock time using 1,024 cores. No restarts were required. The resulting pressure environments from the 3-D calculation were not significantly different from the previously described 2-DC results; thus, only the CTH time-history traces for gages P3, P4, and PE are presented herein. These traces were shifted in time -4.59 msec and are compared to the measured data in Figure A10. In general, there was good agreement between the CTH pressure and impulse traces and the experimental results. The one exception was gage P3 (see Figure A10(a)) where the CTH pressures after 40 msec exhibited two excursions above the experimental records, which in turn produced a higher impulse trace after 40 msec. The CTH pressure traces also indicate that the numerical shock front was planar when it reached the bulkhead, as all of the traces had the same time of arrival. Figure A11 compares the 2-DC (0.2-cm resolution) and the 3-D (0.5-cm resolution) pressures and impulses for the P4 and PE gage locations. The oscillations in the 2-DC traces are attributed to the finer mesh.

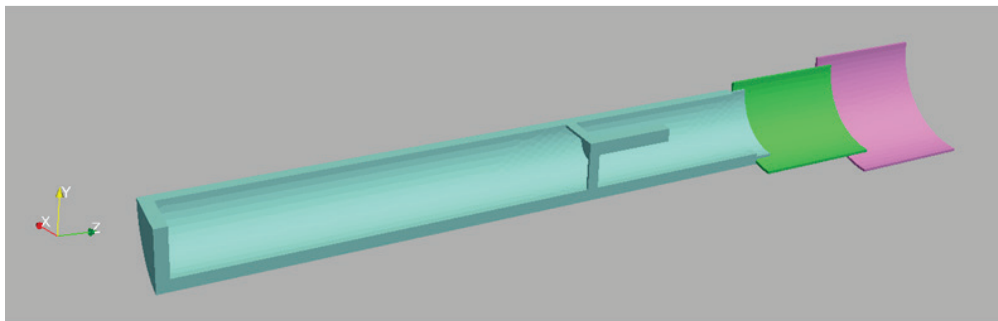
Figure A8. Geometry for the 8-ft×8-ft C2SQ configuration with box.



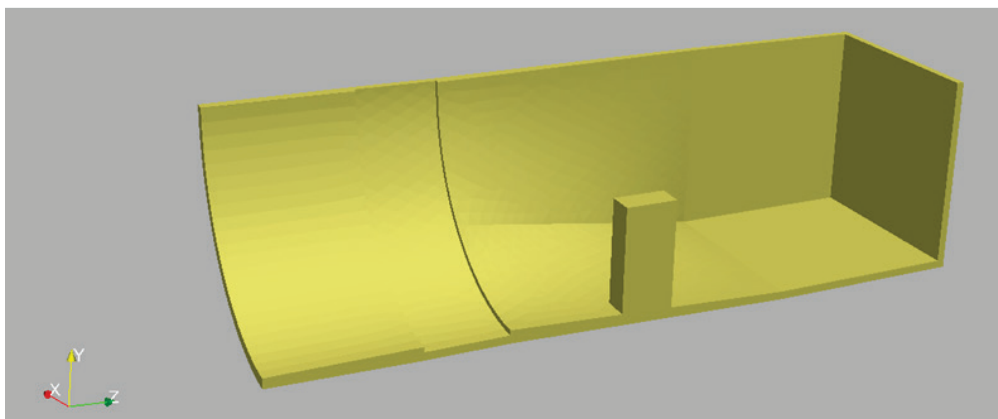
(a) Image of half-symmetry model used in CTH



(b) Quarter-symmetry image of model



(c) Quarter-symmetry image of driver section, striker, CVC-1, -2, and -3



(d) Quarter-symmetry image of instrumented target box

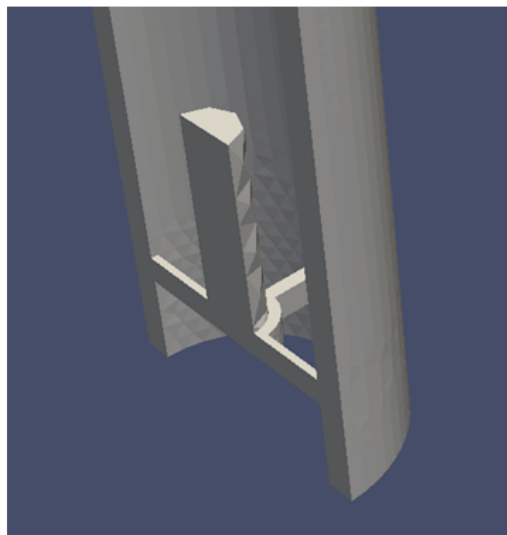
Figure A9. Three views of as-modeled striker geometry.



(a) Downstream view

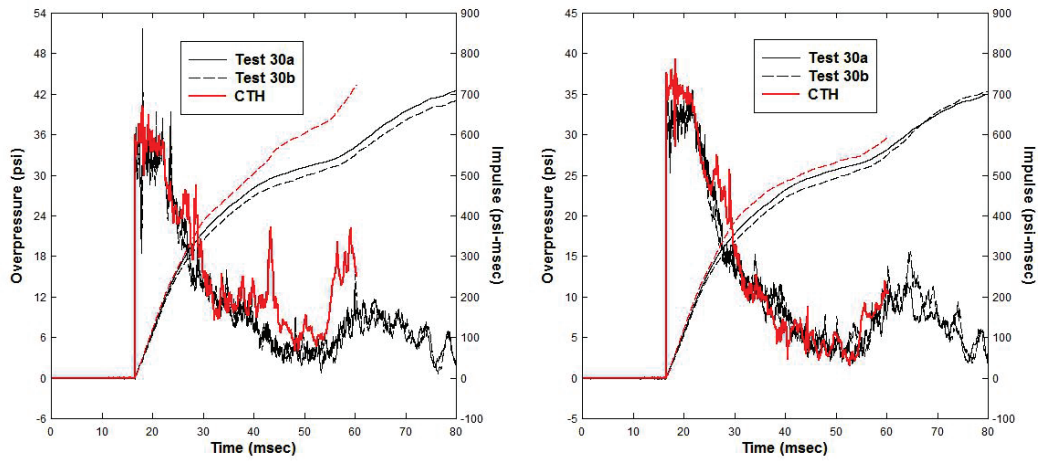


(b) Upstream view



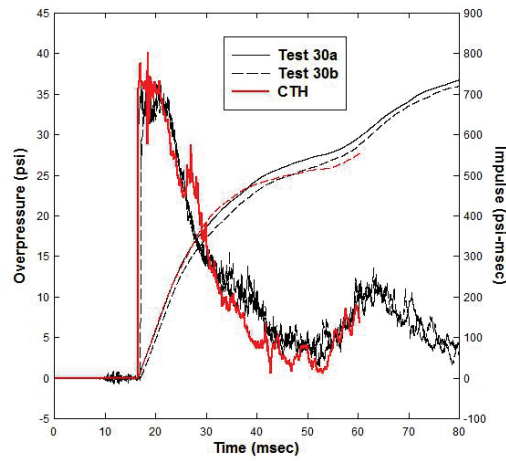
(c) Side view

Figure A10. Gauge comparisons for CTH, GSA configuration.



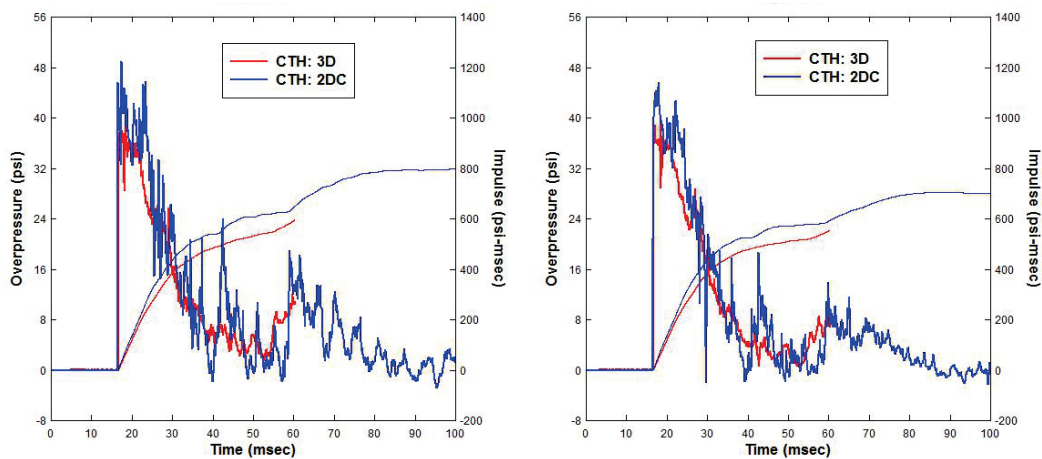
(a) Gauge P3

(b) Gauge P4



(c) Gauge PE

Figure A11. Comparisons from 2-DC and 3-D CTH calculations.



(a) Gauge P4

(b) Gauge PE

Calibration tests with 8-ft×8-ft C2SQ configuration

The CTH calculation of the 8-ft×8-ft C2SQ configuration used 473 million cells and required 193 hr of wall-clock time using 1,024 cores. One restart was required to reach 72 msec of simulation time. Since this simulation used half symmetry, gauge locations on the opposing half were mirrored about the plane of symmetry. The CTH pressure and impulse traces for the target wall gauges are compared with the measured data in Figure A12. The CTH time-histories were shifted -4.80 msec to match the measured arrival time.

With the exception of gauges P7 and P8, there was excellent agreement between the calculations and measured data. The discrepancy for gauge P7 is large; however, the measured pressure-time-history at this particular gauge differs markedly from that measured at the other gauge locations. Although the measurement appears repeatable from test-to-test, one might still consider the data for gauge P7 suspect because it is so out-of-line with the other measurements.

The CTH pressure traces indicate that the numerical shock front was planar when it reached the target wall, as all of the traces had the same nominal TOA. Figure A13 presents the CTH and experimental traces for the side-on overpressure gauge located in the TR2 section of the BLS. The initial pressure traces agree between the TOA and 17 msec, after which the CTH trace falls below the experimental records. At 26 msec, the CTH trace follows the experimental data again. CTH overpredicts the second peak at 40 msec.

Figure A12. Gauge comparisons for CTH, 8-ft×8-ft
C2SQ configuration.

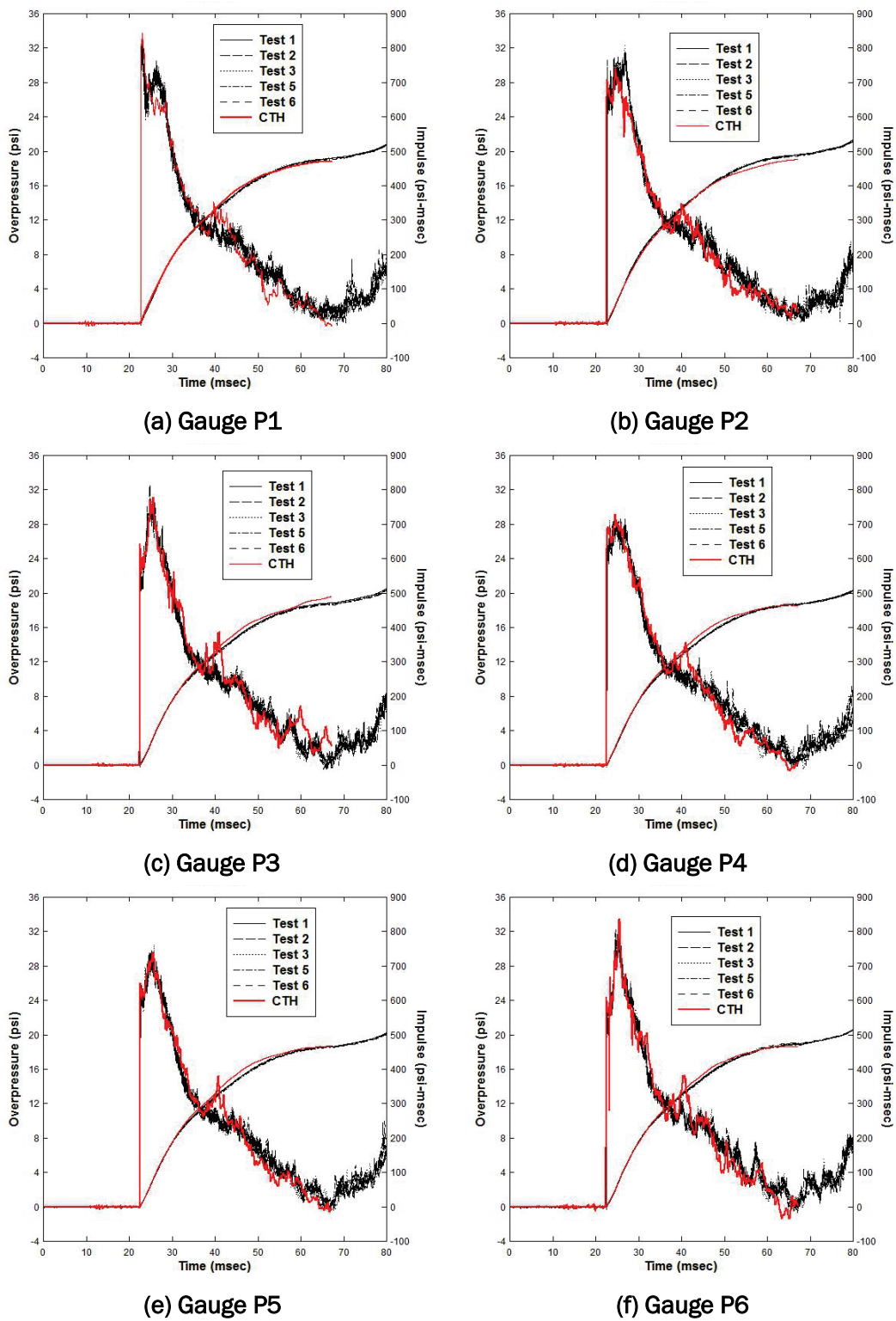


Figure A12. (Continued).

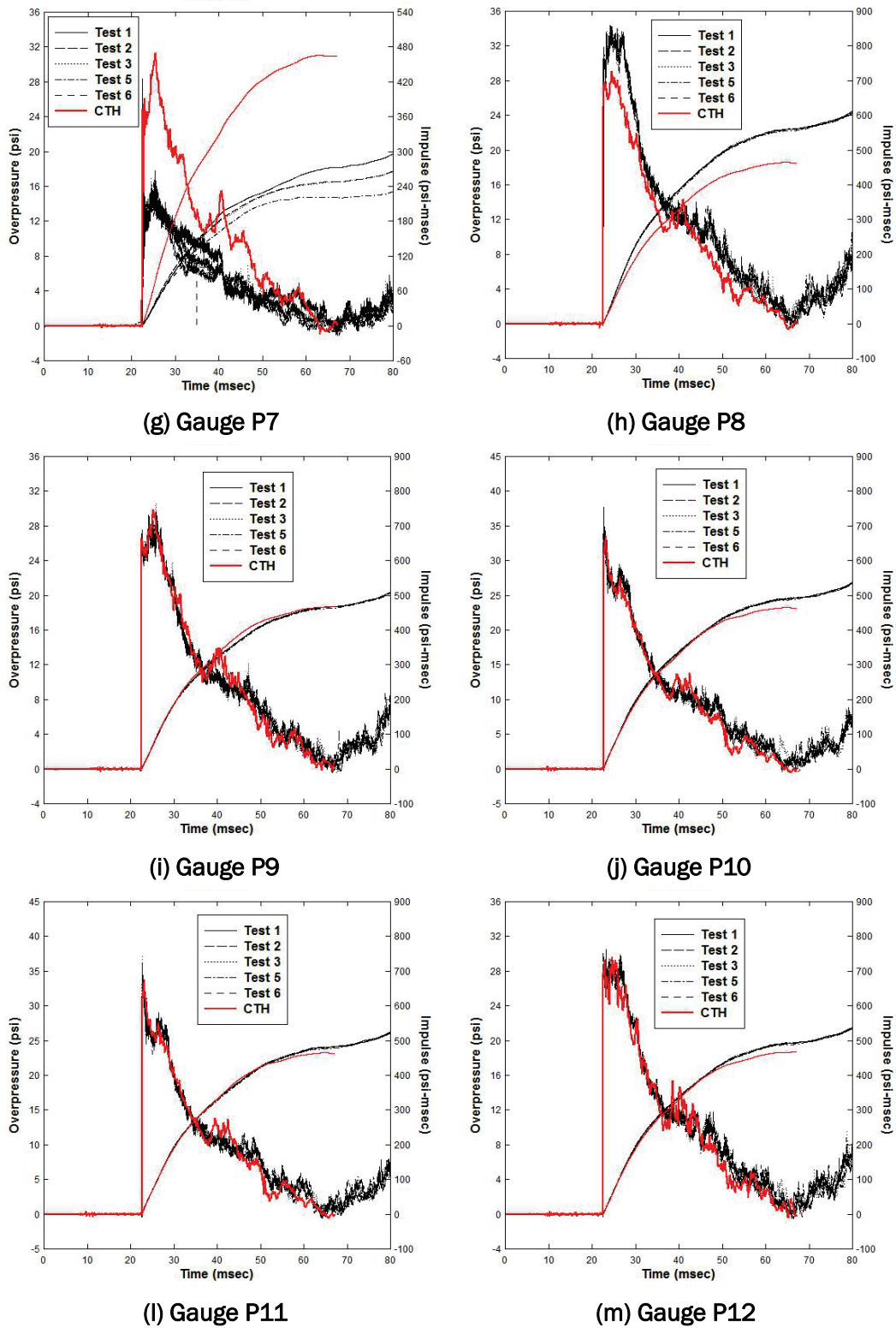
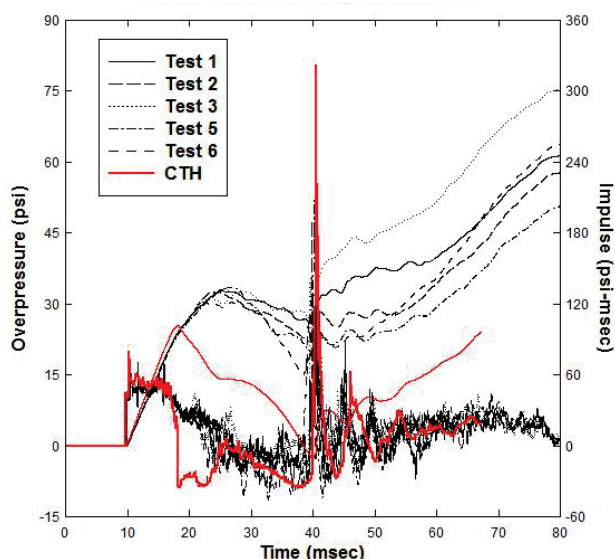


Figure A13. Comparison for CTH at side-on pressure gauge PR.



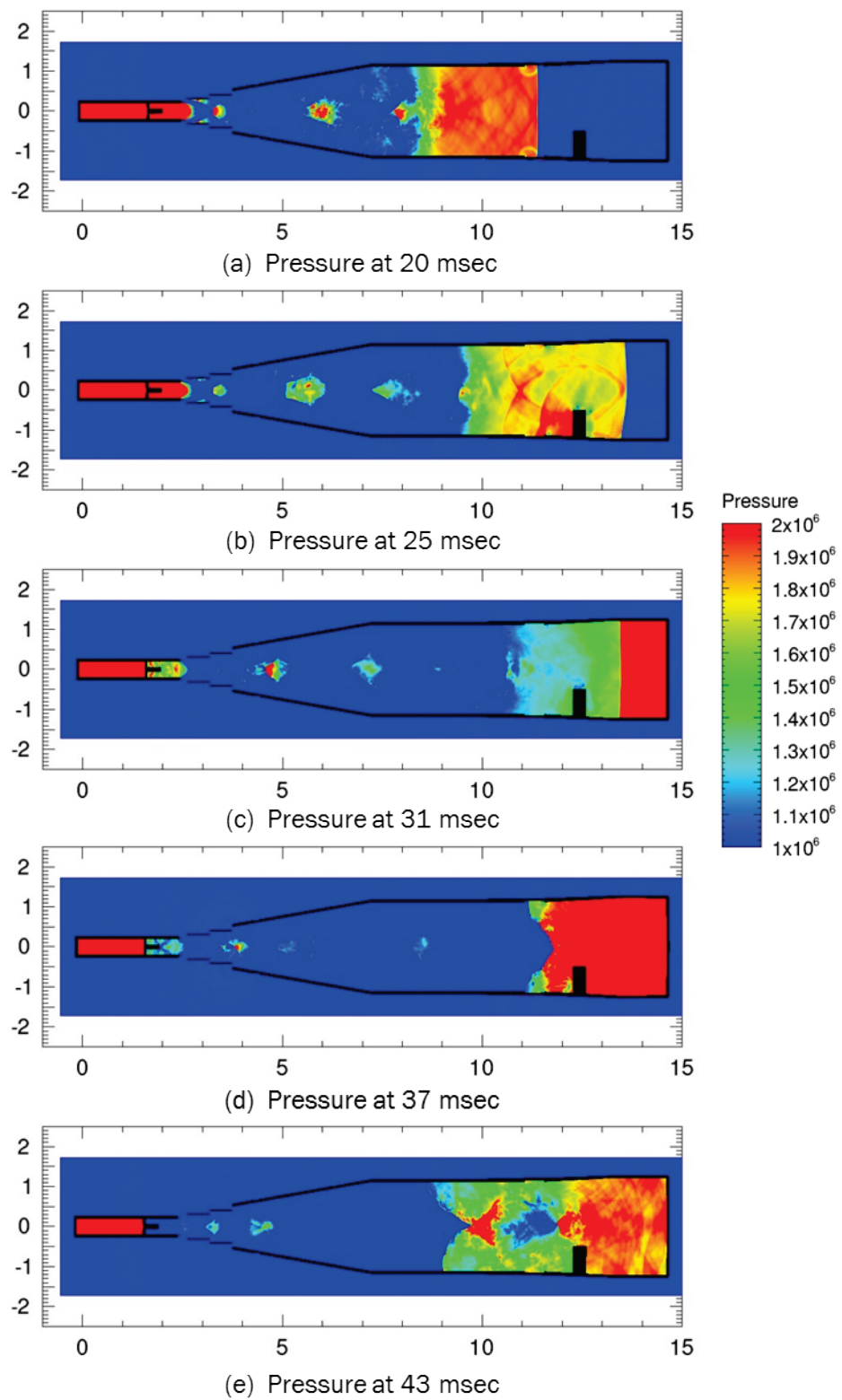
BLS 8-ft×8-ft C2SQ configuration with box

Calculation with SESAME EOS

The CTH calculation of the 8-ft×8-ft C2SQ configuration with box used 473 million cells and required 199 hr of wall-clock time using 1,024 cores. It required two restarts to run the simulation out to 70 msec. The primary objective was to calculate the time-histories for the pressure gauges located on the box structure (see Figure 8(d)). Since this calculation used half symmetry, gauges located on the opposing half of the box were mirrored about the plane of symmetry when possible.

Before showing the time-history traces, the CTH pressure fields between 20 and 43 msec are presented in Figure A14 to give the reader a sense of how the incident and reflected shocks transition with time. The units of pressure in the figure are dynes/cm². At 20 msec, the incident shock is entering the Cascade section of the BLS with a planar front and a relatively homogeneous mass of air at constant pressure behind it (from approximately 8.8 m to 11.3 m). A perturbed pressure field has engulfed the box structure at 25 msec with a reflected shock visible in front of the box. A planar reflected shock is visible moving upstream at 31 msec. At 37 msec, the reflected shock front moving upstream has engulfed the box structure and interacts with the mass of air still moving downstream. This interaction produces a nonplanar front. A complex pressure field both upstream and downstream of the box structure is observed at 43 msec.

Figure A14. CTH pressure state plots, 8-ft×8-ft C2SQ configuration with box.



The CTH pressure and impulse traces from the box gauges are compared to the measured data in Figures A15 to A18. The front face gauge records are plotted in Figure A15, the side gages in Figure A16, the top surface gages in Figure A17, and the back face gages in Figure A18. In addition, the CTH and experimental traces at the P3 and P9 gage locations are compared in Figure A19. All of the CTH time-histories were shifted -4.11 msec to match the measured TOA at gauge PBF1.

Figure A15. Gauge comparisons for CTH, front face.

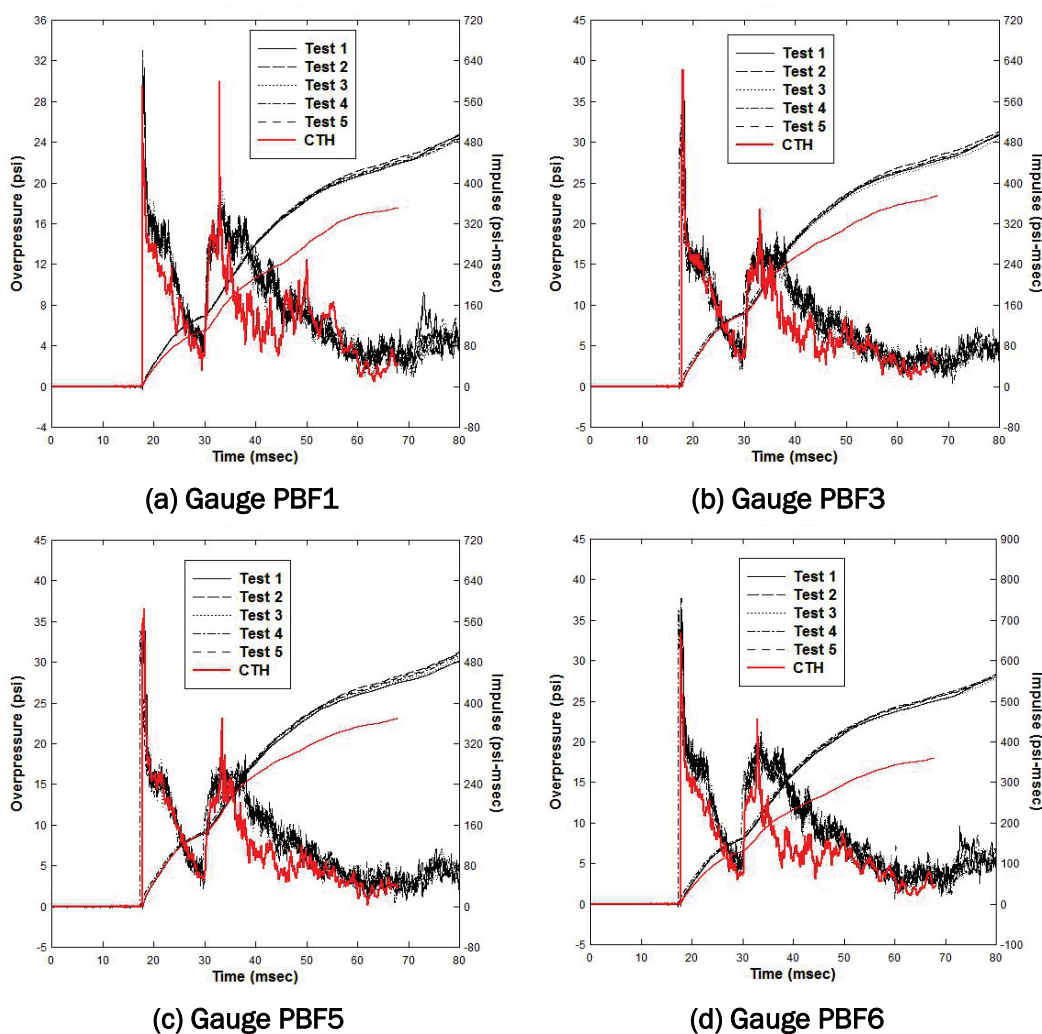
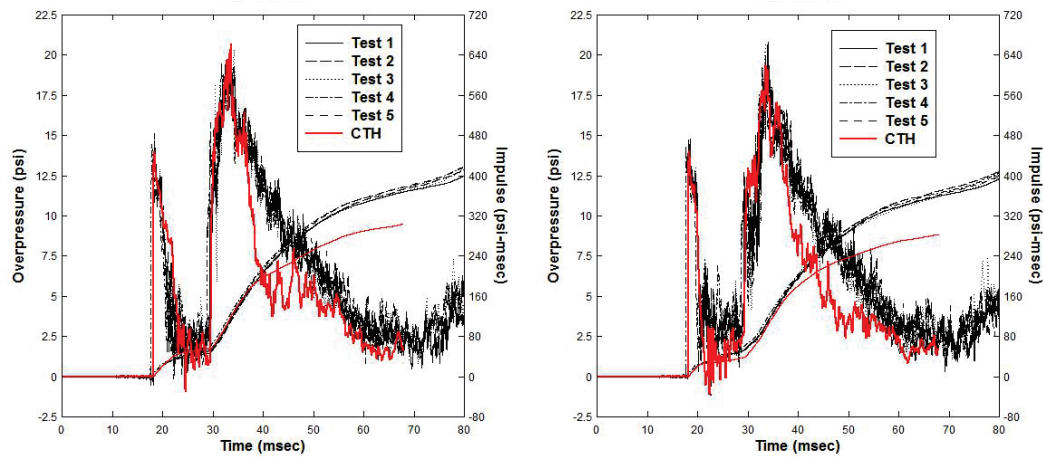
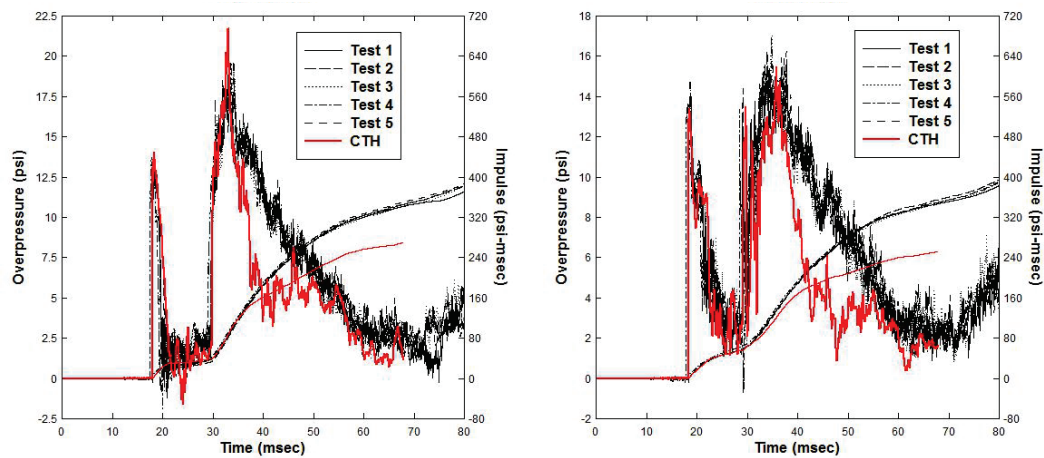


Figure A16. Gauge comparisons for CTH, right face.



(a) Gauge PBR1

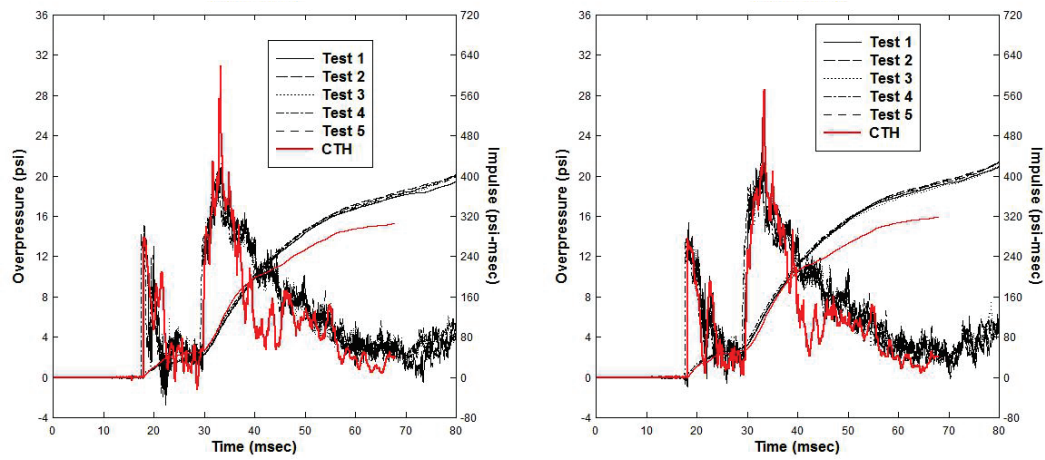
(b) Gauge PBR2



(c) Gauge PBR3

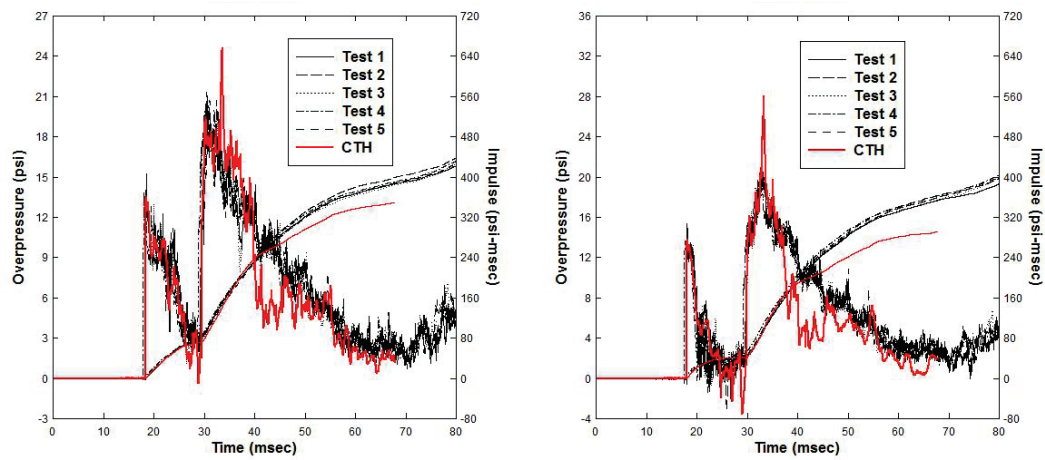
(d) Gauge PBR4

Figure A17. Gauge comparisons for CTH, top face.



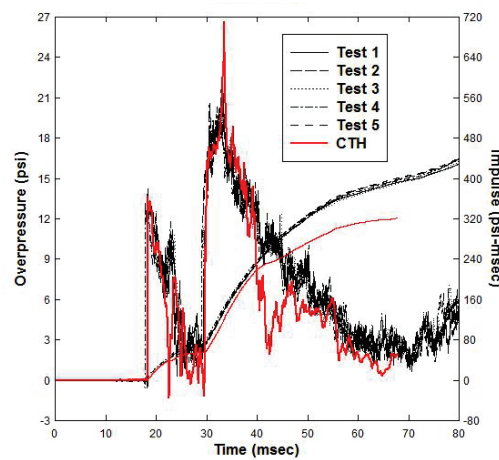
(a) Gauge PBT1

(b) Gauge PBT2



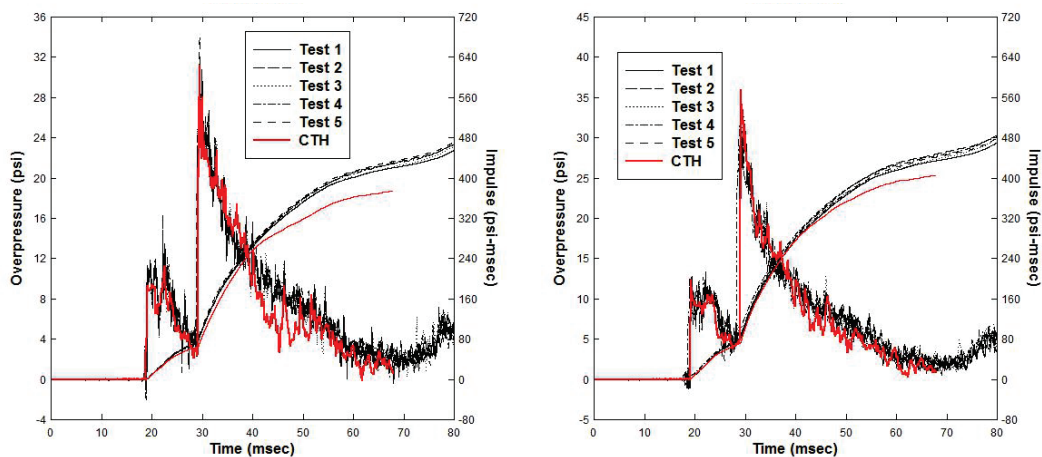
(c) Gauge PBT3

(d) Gauge PBT4



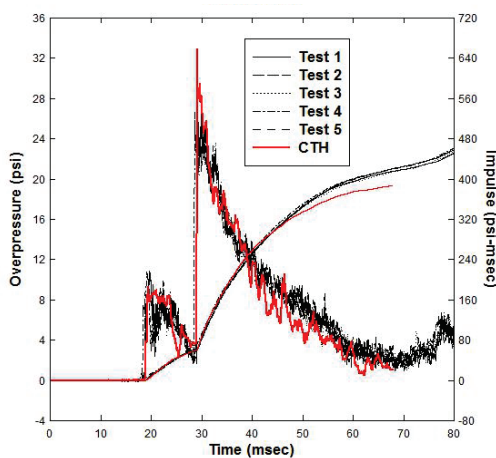
(e) Gauge PBT5

Figure A18. Gauge comparisons for CTH, back face.



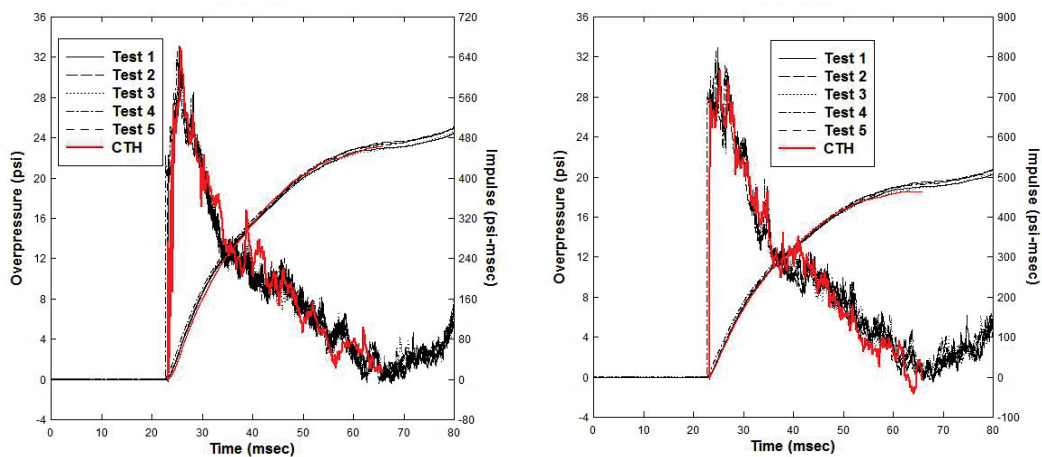
(a) Gauge PBB1

(b) Gauge PBB2



(c) Gauge PBB3

Figure A19. Gauge comparisons for CTH, target wall.



(a) Gauge P3

(b) Gauge P9

The ability of CTH to qualitatively match the measured data for gauges on the box varied from good to poor. In general, very good agreement was observed between the CTH and the experimental traces up to the arrival of the second pressure peak, i.e., the arrival of the reflected shock from the end of the BLS. After that time and for a duration of approximately 10 msec, all of the CTH traces from the front, right, and top face gauge locations fall below the experimental results. After that time, the magnitude of the pressure traces increased and exhibited good agreement with the measurements. The calculated pressure traces on the back face showed better agreement with the measured data than the traces on the other surfaces. Pressure-time-histories for two gauges on the bulkhead at the end of the BLS are plotted in Figure A20. The CTH traces show very good agreement with the experimental results.

The incident pressure fields in the vicinity of the box structure between 22 and 25 msec are shown in an elevation view 1.0 cm off of the symmetry plane (Figure A21) and in a plan view at the gauge PBF3 elevation (Figure A22). The top of each image is downstream of the box. The unshifted TOA of the incident shock on the front face of the box was 21.8 msec. At 22 msec, the reflected shock from the front face is visible in Figure A21(a) and A22(a). At 23 msec (Figures A21(b) and A22(b)), the reflected shock has progressed over the top surface and the side of the box and begins to wrap around the back edges.

The unshifted TOA of the incident shock at the end of the BLS is 27.3 msec. At 31 msec, the reflected shock is approximately halfway between the back face of the box and the end of the BLS. Figures A23 and A24 show the reflected shock impinging on the bottom, back-side of the box at 33 msec. By 35 msec, the shock is wrapping around the top of the box onto the front face.

Figure A20. CTH pressure plots of incident shock around box, elevation view.

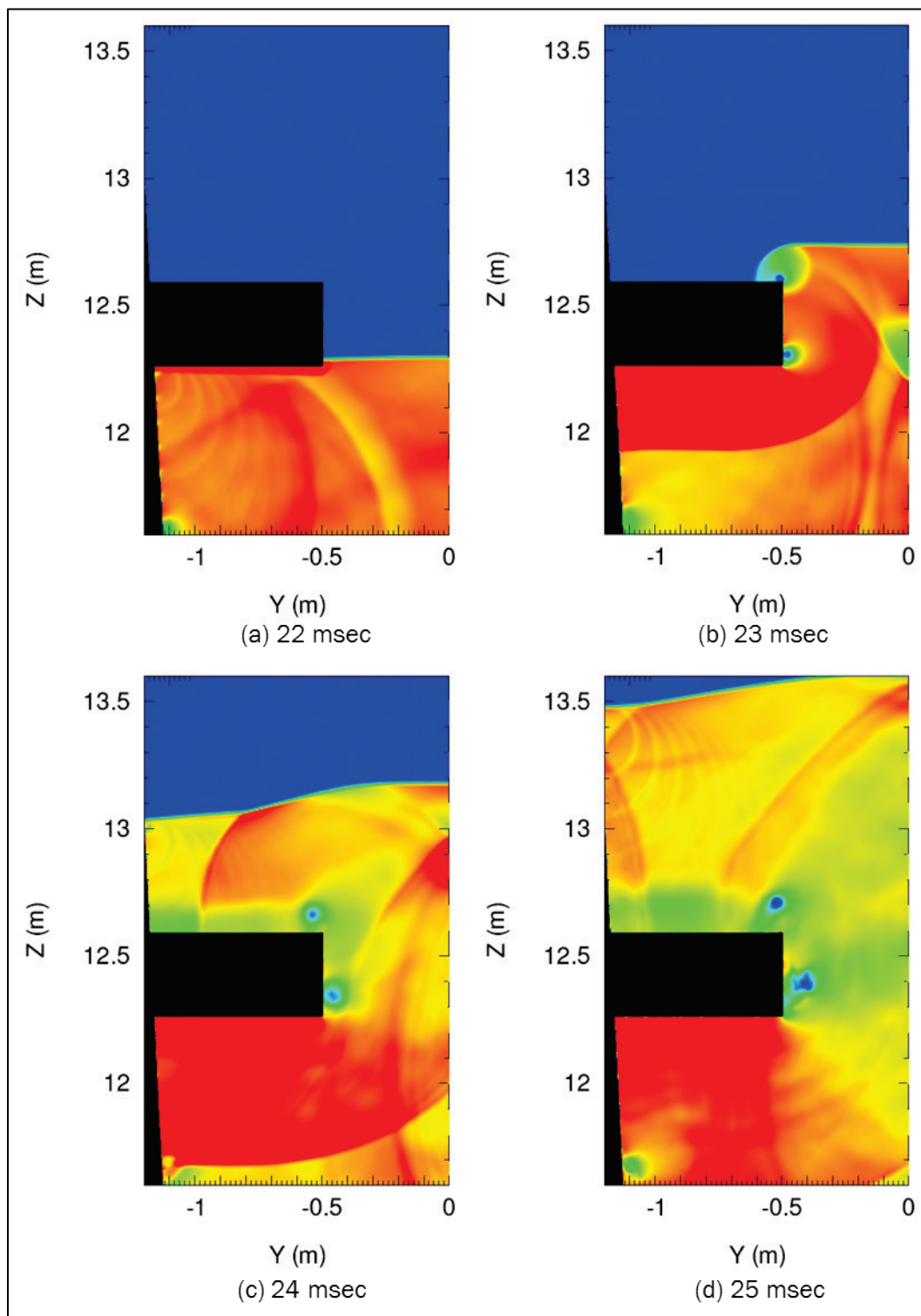


Figure A21. CTH pressure plots of incident shock around box, plan view.

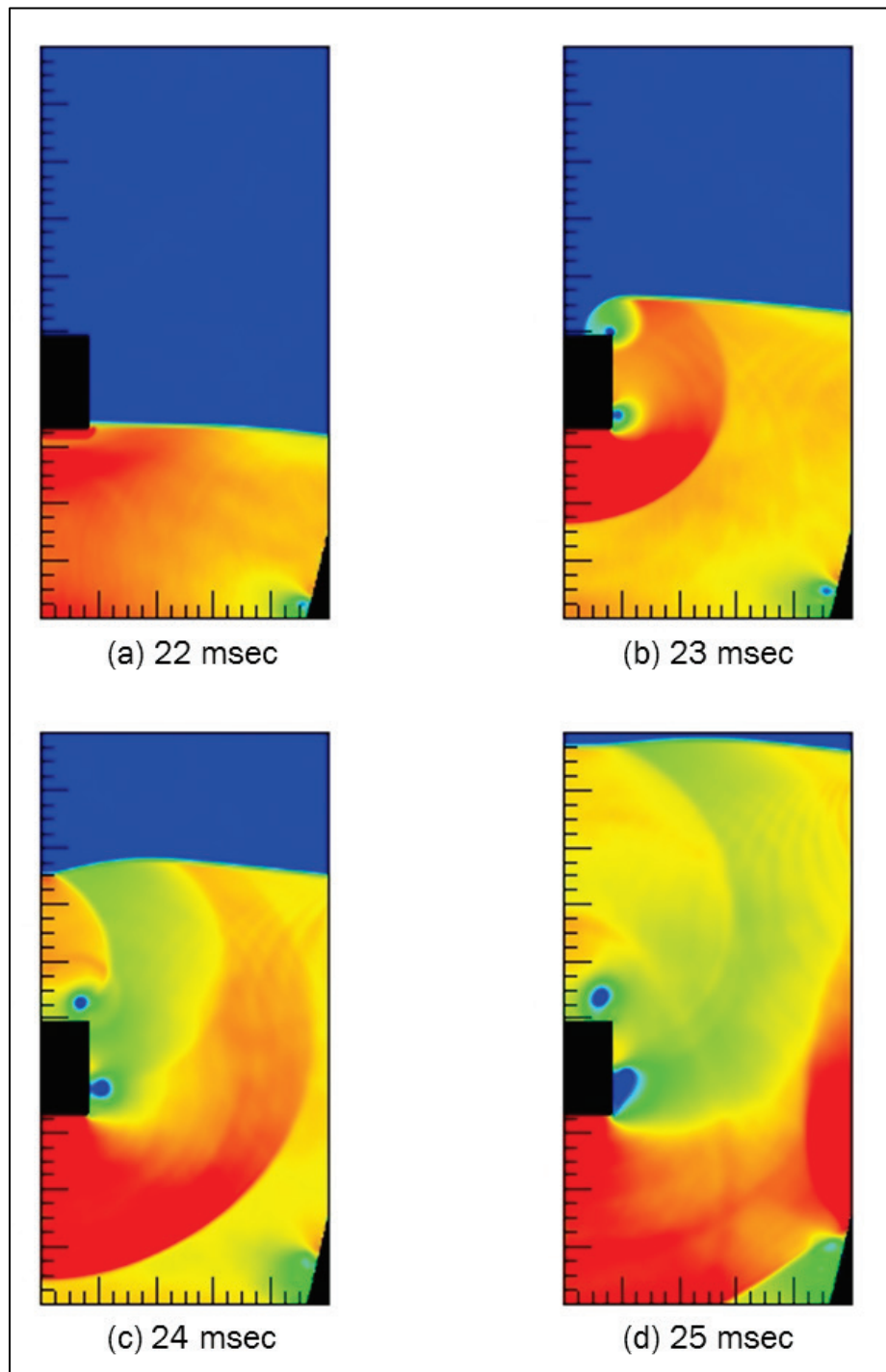


Figure A22. Later-time CTH pressure state plots.

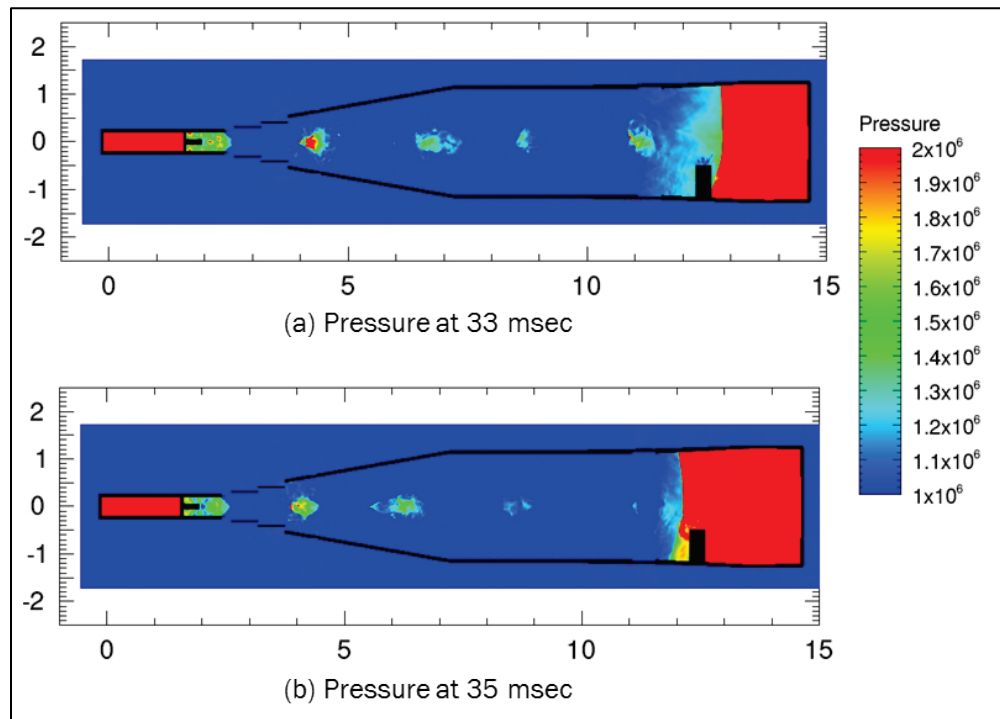
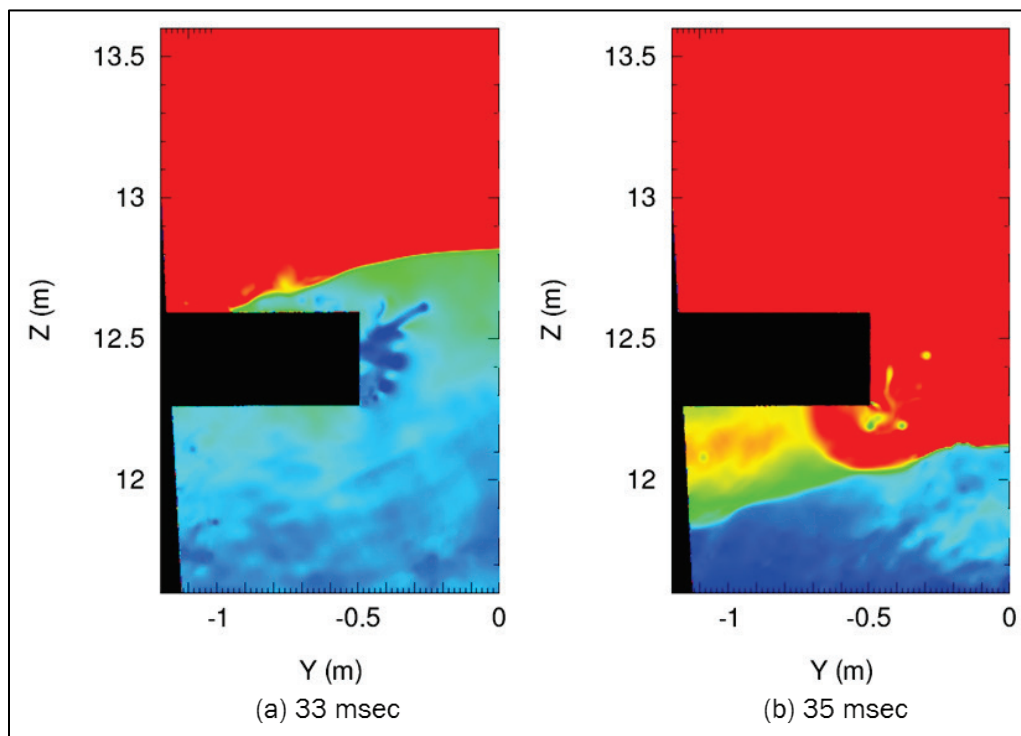


Figure A23. CTH pressure plots of reflected shock around box, elevation view.



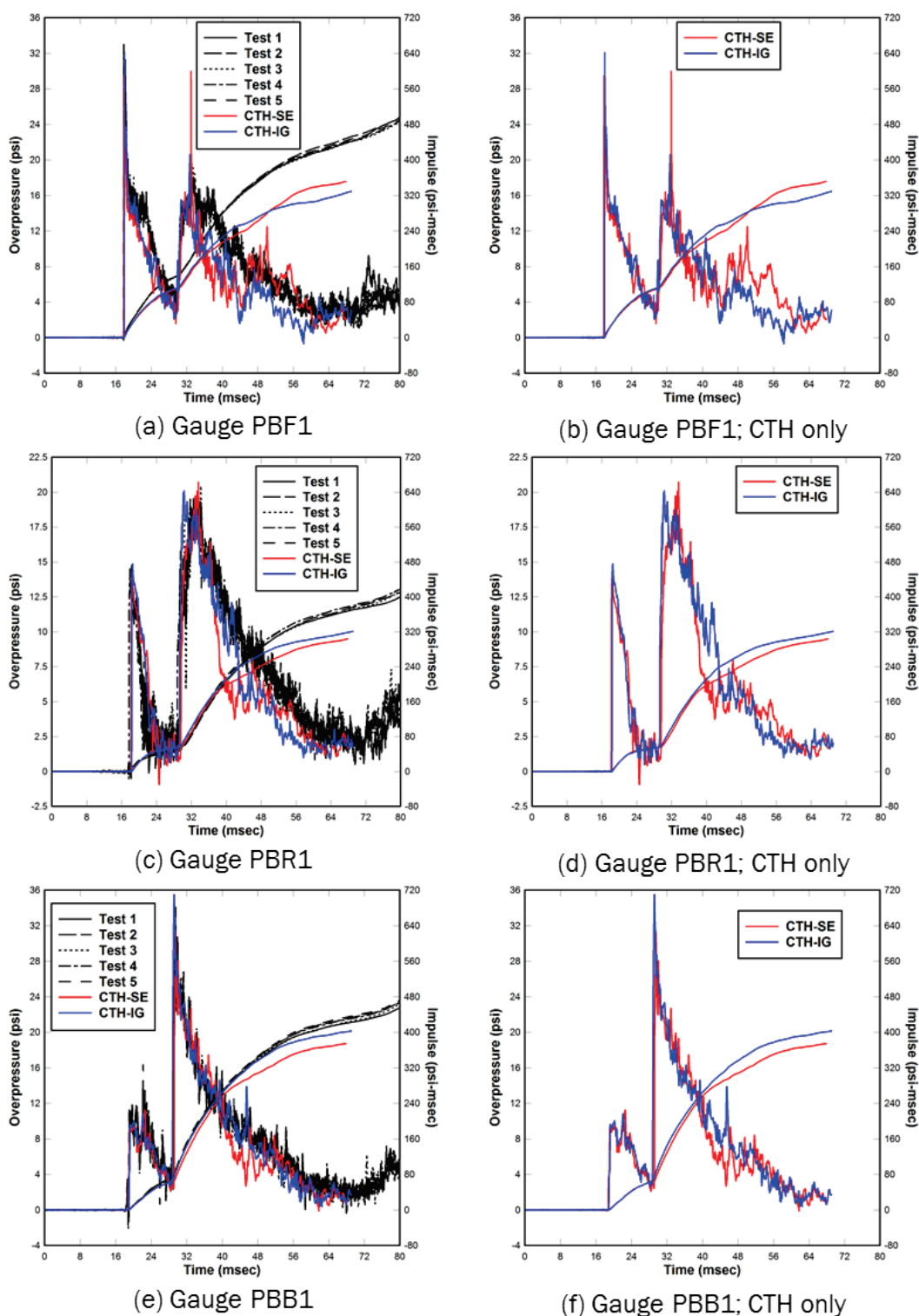
Calculation with ideal gas EOS

This calculation used 473 million cells, required 180 hr of wall-clock time using 1,024 cores, and required two restarts to run the simulation out to 70 msec. The calculation was conducted to see if the ideal gas EOS provided improved pressure and impulse traces from the box gauges. The time-histories were shifted -2.91 msec to match the TOA at gauge PBF1. Figure A24 compares the traces from three gauge locations, one on each of the front, side, and back of the box structure. On the left side of the figure, the CTH waveforms are compared to the experimental results for gauges PBF1, PBR1, and PBB1, while only the CTH waveforms are shown on the right side.

At the PBF1 gauge location (Figures A24 (a) and A24 (b)), the CTH impulse traces were nominally the same up to 36 msec. Between 36 and 45 msec, the ideal gas impulse trace plots above the SESAME trace and after 45 msec it lies below. The simulated impulse traces were well below the experimental results. The simulated pressure and impulse records at the PBR1 gauge location (Figures A24 (c) and A24(d)) matched the experimental results well until 37 msec. After that time, the SESAME pressures drop well below the experimental and a similar drop in pressure is observed in the ideal gas pressures at 42 msec. Both simulation pressure traces track each other after 60 msec. At the PBR1 gauge location (Figures A24(e) and A24(f)), the simulated pressure and impulse records track the experimental results well until 40 msec at which time the SESAME traces fall below both the ideal gas and experimental traces. The ideal gas impulse record begins to diverge from the experimental at 50 msec.

Overall, the ideal gas EOS provided a marginal improvement over the SESAME EOS. Some records exhibited an improved match to the experimental data, and others showed a degraded comparison.

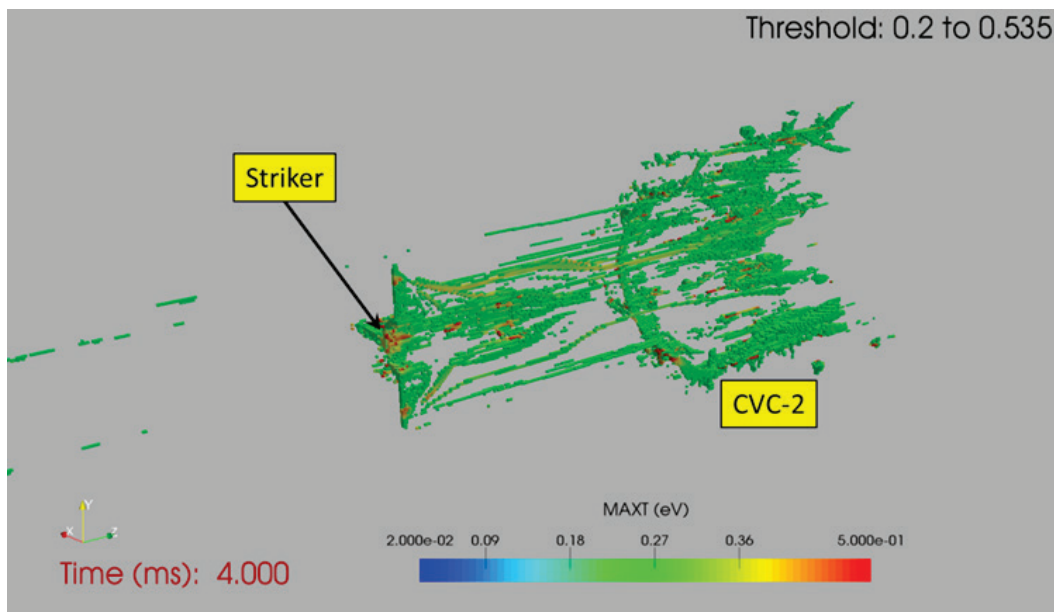
Figure A24. Gauge comparisons between
SESAME and ideal gas EOS.



Lessons learned

The steel walls of the BLS were originally modeled in CTH with a rigid material. This should have maximized the computational time-steps since wave speeds in air would be much larger than steel or any other metal. Early 3-D calculations with the rigid walls suffered from an exponentially decaying time-step. For a 5-msec run, the time-step decayed from 1.0 to 0.2 μsec . Simulations of just the driver and the CVC sections of the BLS were taking 48 hr of wall-clock time using 1,024 cores for an 11 msec run. Various CTH input options were tried to mitigate the decaying time-steps without success, i.e., changing from SESAME to the ideal gas EOS, using different multiple material and temperature models, and removing the striker from the geometry. The cause of the problem was finally recognized after temperatures on the order of 3,100 deg Kelvin (0.27 eV) were observed in the region of the striker (Figure A25). The problem was solved by removing the rigid material and replacing it with a non-rigid material. Given the 1.27-cm-thick walls and the nominal 0.5-cm-sized cells in the mesh, the number of cells through the wall thickness was insufficient for a rigid material. Unfortunately, this problem severely impacted the progress of the CTH modeling effort as it required a significant amount of time to correct.

Figure A25. Temperatures in the region of the striker.



Summary

CTH was used to simulate the blast environment for three configurations of the ERDC BLS. Qualitatively, CTH was able to capture the system responses for each configuration. The calculated time-histories for both the GSA and the 8-ft×8-ft C2SQ configuration matched the experimental records very well. For the 8-ft×8-ft C2SQ configuration with box structure, CTH underpredicted the impulse for all gauges on the box.

The combination of a large length scale and thin BLS walls did not fit well into the strengths of CTH. It is felt the code would perform better for problems involving single or multiple structures in an open-air environment subjected to blast from an explosive source. CTH has a unique capability to handle material strength in its Eulerian solution approach. This capability is not available in typical CFD codes and would be necessary if any simulated structures exhibited elastic or inelastic deformations.

Appendix B: DYSMAS Modeling

DYSMAS background

The coupled code DYSMAS (Harris et al. 2014) was developed by NSWC/Indian Head to simulate underwater explosion (UNDEX) environments and the ensuing marine vessel response resulting from the fluid-structure interaction. The loosely coupled solution approach has three components: an Eulerian code Gemini (Wardlaw et al. 2003) that performs the fluid flow calculation, a Lagrangian code ParaDyn (DeGroot et al. 2013) that performs the structural response calculation, and a coupler that transfers information between Gemini and ParaDyn. This enables DYSMAS to execute calculations that include explicit shock fronts, bubble jets, structural failure, and fluid breakthrough. Included in Gemini are the capabilities to handle compressible and incompressible fluids. Gemini employs a time-split, second-order Godunov scheme to solve the Euler equations. ParaDyn is a 3-D explicit finite element program for analyzing the dynamic response of solids and structures.

DYSMAS is a fluid-structure interaction set of codes that was designed especially for weapon lethality studies, where the explosive charge is detonated in close proximity to the target structure. For such cases, there is strong interaction between the UNDEX loading and the target structure, where the motion of the structure significantly modifies the loading. The suite of codes can be applied to any fluid-structure interaction problem or the individual portions used to simulate their regime alone (e.g., Gemini applied to a fluid problem). DYSMAS has been under continuous development as part of a U.S.-German Project Agreement entitled “Enhanced Undersea Weapons Effectiveness and Ship Survivability through the Application of Validated Computer Codes.”

The Gemini code is an Eulerian solver for the fluid equations of motion and was designed specifically to simulate explosions in water; however, it has been applied to other environments, including explosions in air and soil. The ParaDyn code is an explicit dynamics Lagrangian finite element code that solves the structural equations of motion. The existing interface routines allow Gemini and ParaDyn to exchange information in order for the fluid and structural integration to advance in time. This Eulerian-Lagrangian combination provides a powerful capability that has been extensively validated for complex UNDEX phenomena including explosive

shock propagation, bubble formation and jetting, and fluid-structure interaction. Gemini uses a Cartesian structured mesh (i.e., fixed rectangular cells) and supports setups in varied dimensions (i.e., 1-D, 2-D, or 3-D).

ParaDyn is the parallel implementation of the finite element code DYNA3-D (Whirley and Englemann 1993). DYNA3-D is based on a finite element discretization of the three spatial dimensions and a finite difference discretization of time. The explicit central difference method is used to integrate the equations of motion in time. The central difference method is conditionally stable, and stability is governed by the Courant limit on the time-step. DYNA3-D uses a lumped mass formulation for efficiency. This produces a diagonal mass matrix, which renders the solution of the momentum equation trivial at each step in that no simultaneous system of equations must be solved. The contribution of the element reaction forces and applied loads are accumulated into a nodal force vector, which is then divided by the lumped nodal mass to get the nodal acceleration. This is then integrated forward in time using a central difference approximation to get the nodal velocity and displacement.

The ParaDyn code passes a list of “interface surfaces” to Gemini at the start of a coupled calculation that describes the location of the structure within the fluid domain (i.e., the wetted surface). Each discrete surface is defined solely by three or four nodes specified in the “interface element” section of the ParaDyn input deck. Loads are passed from Gemini to ParaDyn, inducing a response and potential motion of the structure. That new location and state of the structure are then passed back to Gemini for further loading. This coupled treatment occurs at every time-step in the calculation.

Modeling overview

All of the DYSMAS calculations were run on the Air Force Research Laboratory (AFRL) HPC platform Spirit. Spirit has 4,590 compute nodes with 16 cores per nodes. Each compute node has a core speed of 2.6 GHz and 32 GB of accessible memory.

Full 3-D calculations were conducted for all cases considered in the BLS modeling effort. The BLS structure was modeled as a Lagrangian construct, which was then inserted into the Eulerian air domain. The BLS structure was composed of shell elements with a nominal thickness of 0.5 in. The nodal displacements were fixed so that the structure would act

in a completely non-responding fashion. A typical model is shown in Figure B1. Transmitting boundary conditions were applied to all mesh boundaries in the Gemini portion of the calculation. The Eulerian domain extended a moderate distance away from the BLS structure. A uniform cell size was specified throughout the Eulerian domain encompassed by the BLS. A graded mesh was specified beyond the extents of the BLS. The driver gas was represented by a volume of high pressure air that began to propagate at time zero (see Figure B2). The diaphragm and its failure were not modeled. An ideal gas EOS was used to model both the ambient air and the high pressure air contained within the driver section. These were modeled as two separate Eulerian materials in the problem setup. The ambient air was assigned an initial pressure and temperature of 14.5 psia and 77°F, respectively. The driver air was assigned an initial pressure of 1,298 psig and initial temperature of 77°F. The BLS structure was numerically rigid and fixed in space so as to not respond/move. When appropriate, the striker and grill were explicitly modeled within ParaDyn.

A series of calculations were performed to assess the effects of the striker and grill on the flow environment. A simulation was performed without either of those constructs, one with just the striker and one with both the striker and the grill. The striker and grill were modeled with solid elements within ParaDyn and a coupling interface applied to their surfaces to interact with the fluid flow. Both are depicted in Figure B3, shown without the BLS structure. Figure B4 shows the flow field for all three configurations. The top row depicts the configuration without the striker or grill; the second row of images depicts the striker only; and the images on the third row include both the striker and grill. Qualitatively, there is little difference in the pressure field, suggesting that the striker and grill have only a minor effect on the shock and trailing high density gas that propagate down the BLS. A quantitative comparison is provided in Figure B5, which depicts the pressure history calculated near the center of the target wall. Although each construct has an effect on the waveform, the effects are still minor. An approximate 5 percent reduction in peak pressure is seen from each part, and at 30 msec, the striker reduces the impulse by about 5 percent and the grill an additional 2 percent. The arrival times are delayed by each part, approximately 0.2 msec each for both the striker and grill.

Figure B1. Typical DYSMAS model (8-ft×8-ft C2SQ configuration with box shown).

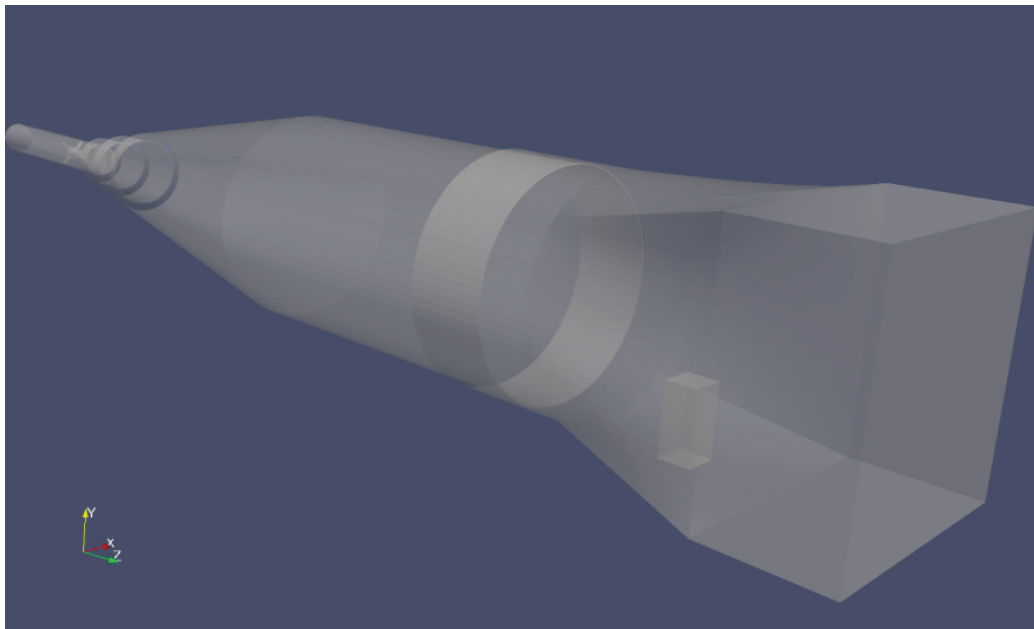


Figure B2. Initial conditions/driver pressure.

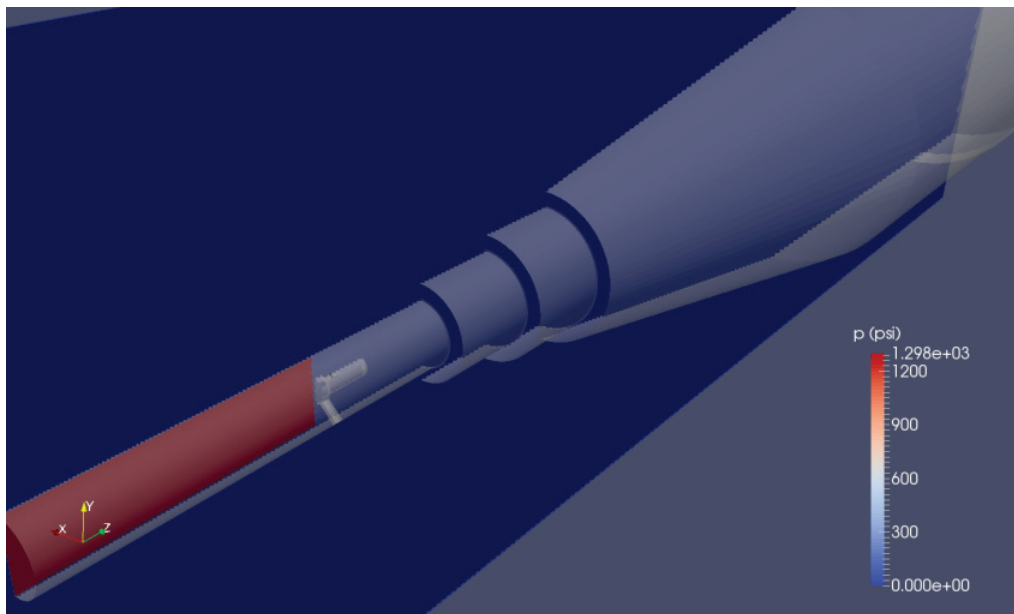


Figure B3. Depiction of striker and grill models.

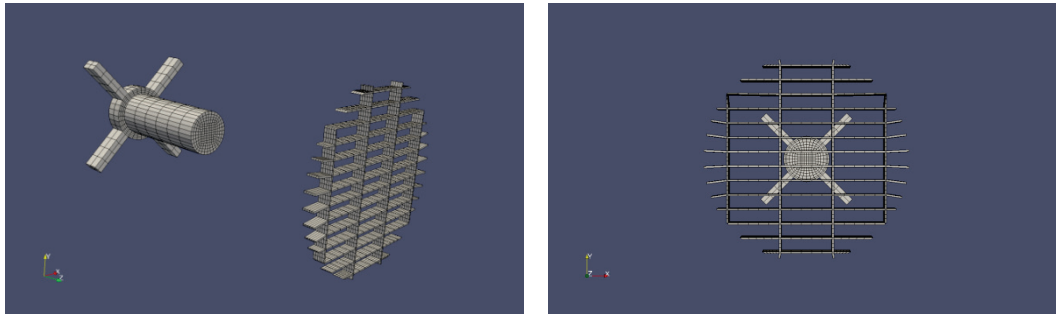


Figure B4. Effect of striker and grill models on the flow field.

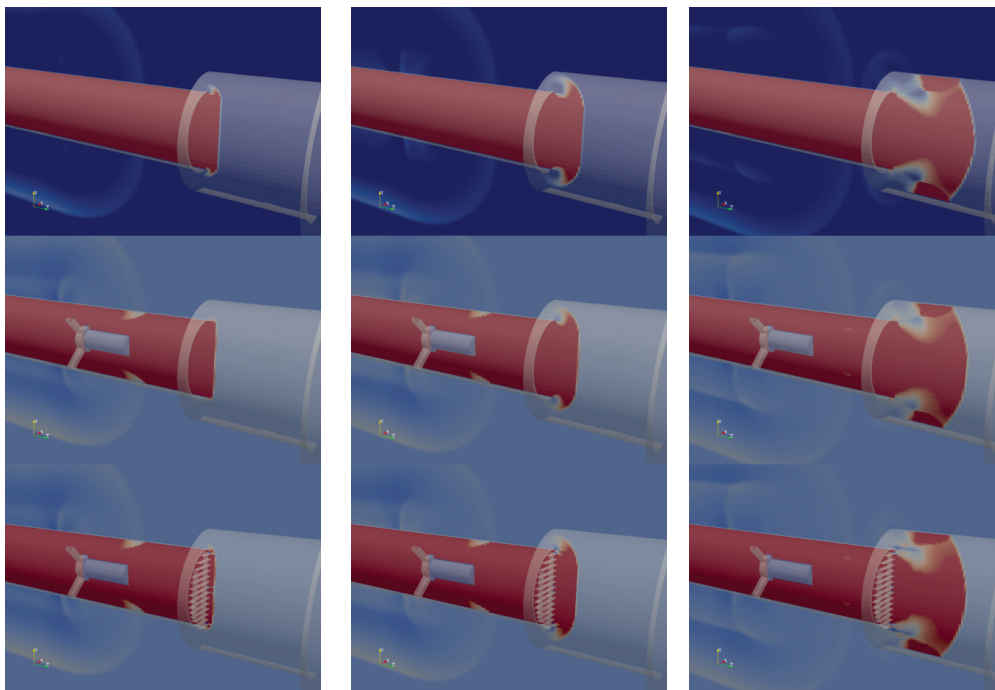
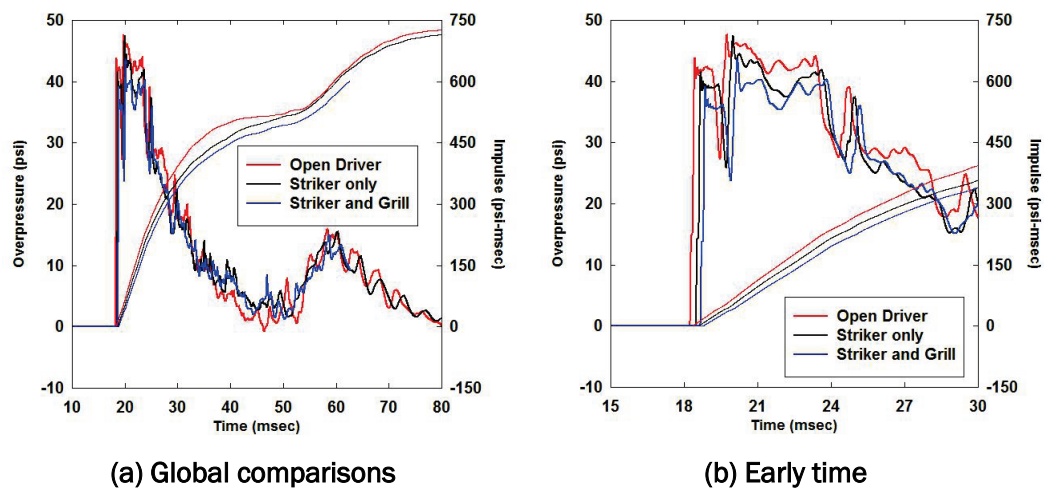


Figure B5. Effects of striker and grill.



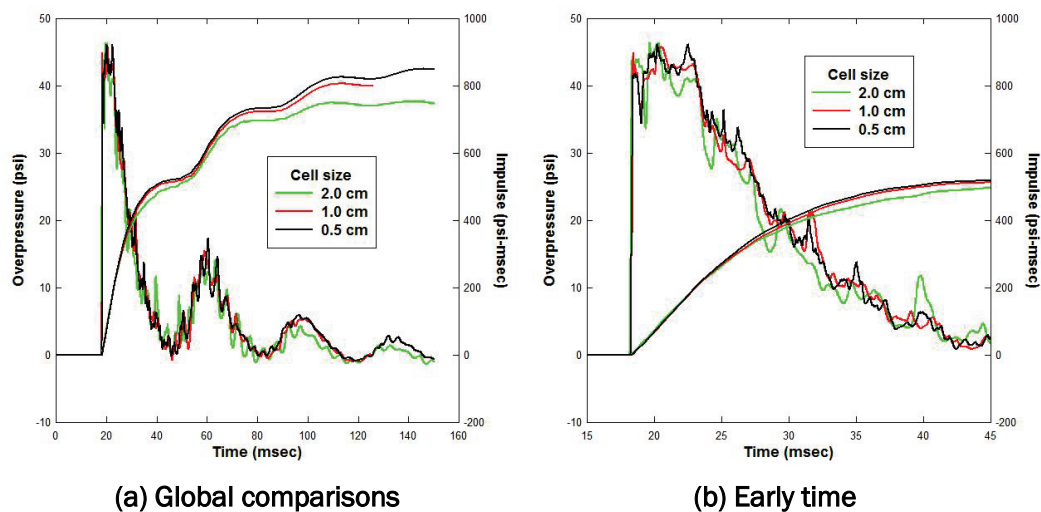
Another set of calculations was performed on one of the initial models with an increasing mesh density within the fluid domain to assess mesh convergence. If grid convergence is obtained, then solutions from the two finest meshes should be identical, and there is confidence that no further refinement is needed. Three mesh densities were used, having a minimum cell size of 2.0, 1.0, and 0.5 cm, respectively. This led to fluid meshes of approximately 18.3 million, 135 million, and 1.0 billion cells. The structural mesh was unchanged throughout this exercise, as altering its mesh density should have very minimal effects on the flow field and behavior due to it being rigid and fixed in space.

Run time statistics are provided in Table B1. Results from the convergence study are provided in Figure B6, which depicts the pressure history and integrated impulse at a single location on the target wall (gauge P5). These results are typical of those at the other gauge stations. Refining the mesh to a 0.5-cm cell size produces a slightly different waveform when observed locally, but the global waveforms match well. There is a 0.85 percent difference in total impulse at 125 msec, indicating the coarser mesh with a 1.0-cm cell size is sufficient to resolve the pressures imparted to the structure within this configuration.

Table B1. DYSMAS run time statistics from convergence study.

Mesh Resolution (cm)	Analysis End Time (msec)	No. Gemini Time-steps	No. Processors	CPU Time (hours)	Approximate Processor-hours
2	150.0	10,252	512	8.51	4,357
1	125.7	14,418	1024	16	16,384
0.5	150.0	28,335	4048	44.13	178,638

Figure B6. Convergence study results.



GSA configuration, calibration tests 30a and 30b

The DYSMAS model of the GSA configuration is depicted in Figure B7. All of the BLS is explicitly modeled, including the vents, Cascade, and target wall. This test included the striker and grill, and this configuration is captured within the model (see Figure B8).

Figure B7. GSA configuration model with slice displaying initial pressure state.

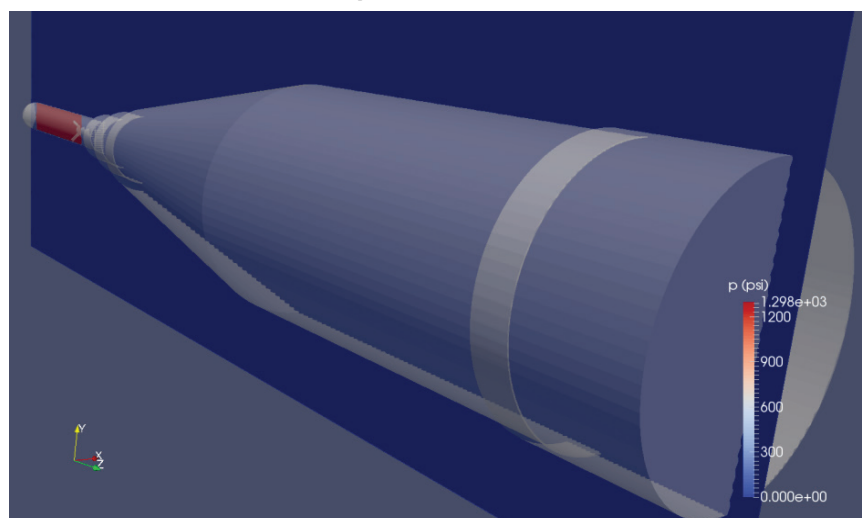
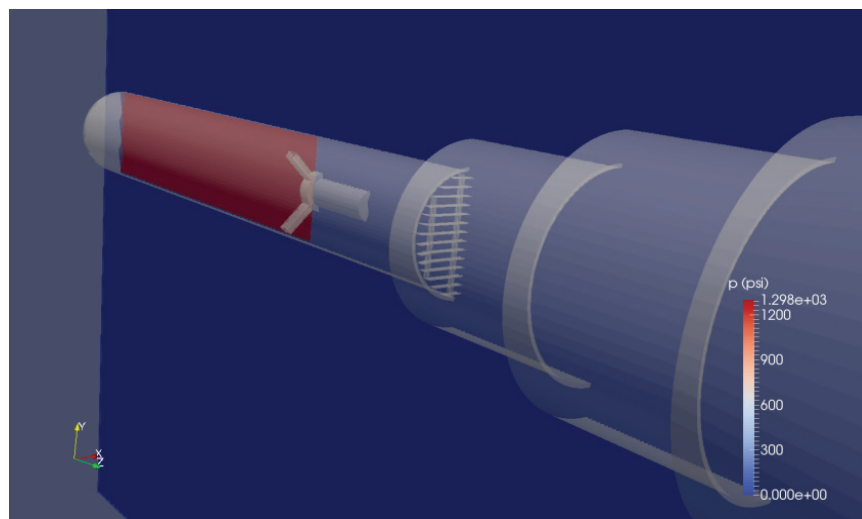
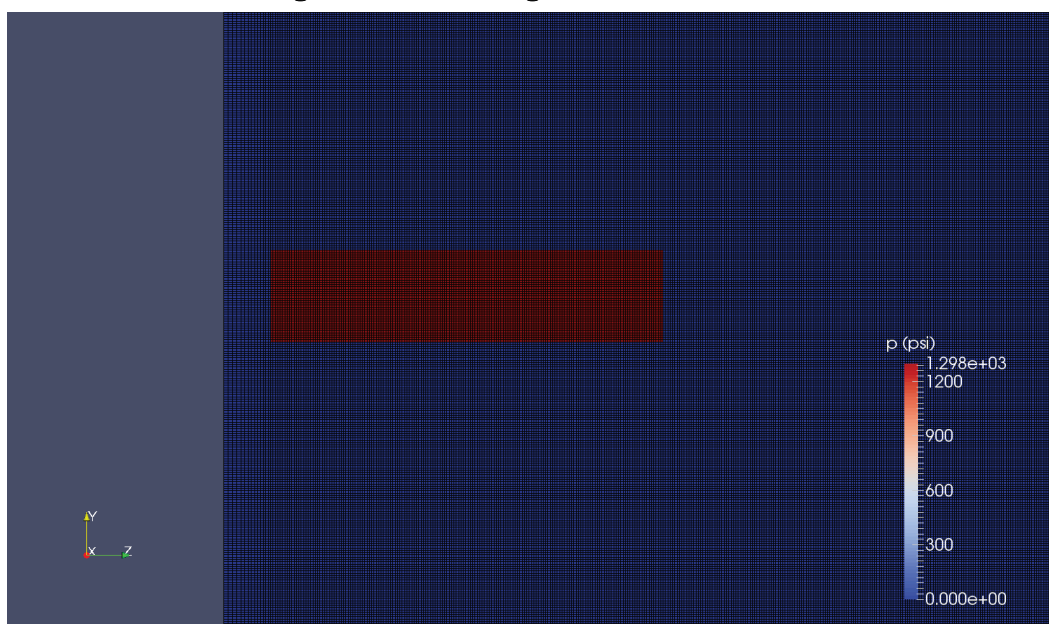


Figure B8. GSA configuration model, close-up of striker and driver pressure state.



A constant cell size of 1.0 cm was used throughout the interior of the BLS model. On the exterior, a graded mesh extended to ± 50.0 cm in the x and y directions and ± 20.0 cm in the z direction along the length of the BLS model. This resulted in a mesh of approximately 136 million cells. A cross section of a portion of the grid superimposed on a contour plot of the initial pressure is provided in Figure B9. The structure model consists of 29,128 shell elements in the superstructure of the BLS and 3,886 solid elements within the striker and grill.

Figure B9. GSA configuration model mesh.



A series of pressure state plots depicting the shock and trailing high density gas flow is provided in Figure B10. They depict the gas leaving the driver, propagating down the BLS, venting from the CVC section, reflecting off the target wall at the downstream end, and flowing back upstream. The time stamps in the individual state plots are given in units of seconds. The shock propagating laterally from the driver section at 1.9 msec is caused by the interaction of the high pressure gas with the surrounding Lagrangian structure at startup of the calculation. While the initial shock propagates in a very planar fashion, there is a considerable amount of heterogeneity in the flow field behind the front, especially at the later times (e.g., see state plots at 27.5 and 40.0 msec).

A comparison of the calculated pressure history at select gauges located on the target wall is provided in Figure B11. The results for gauges P6, P9, and P10 are not included since they are at repeat locations from the center point. All of the gauges exhibit the same basic pattern with small oscillations around the global shock pattern. The most obvious differences occur early-on in the reflected shock history; however, these differences are relatively small indicating that DYSMAS is predicting a planar front interacting with the target wall. Gauge P3, which resides at the center of the target wall, exhibits the greatest fluctuation. The fluctuations in the pressure history generally get smoother as one moves away from the centerline.

Comparisons between the measured and calculated data are provided in Figure B12 for several gauge locations. The calculation was run to 63 msec, which was sufficient to capture the first pulse in the measured data, as well as the initial rise for the second. The calculated results compare well with the measured data at all gauge locations. Note, the calculated results are “as-is” and have not been shifted in time to match the measured shock arrival.

Figure B10. DYSMAS pressure state plots for GSA configuration.

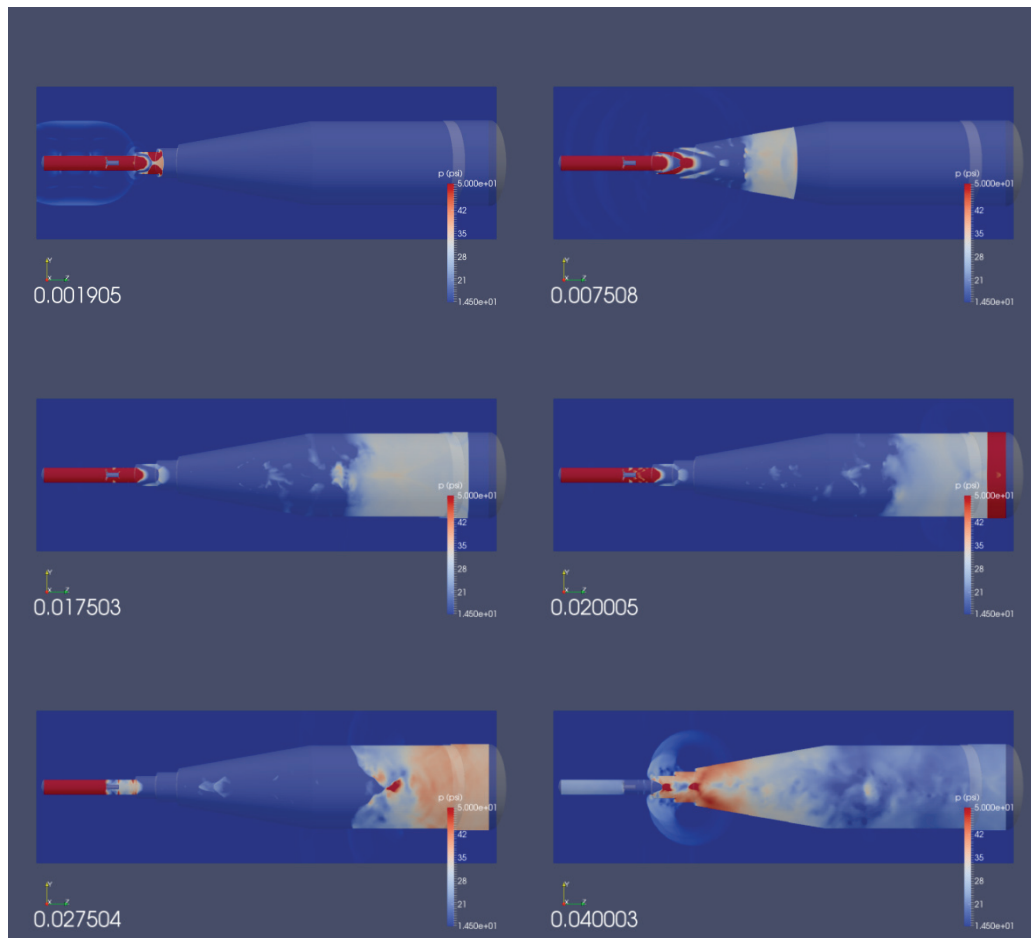
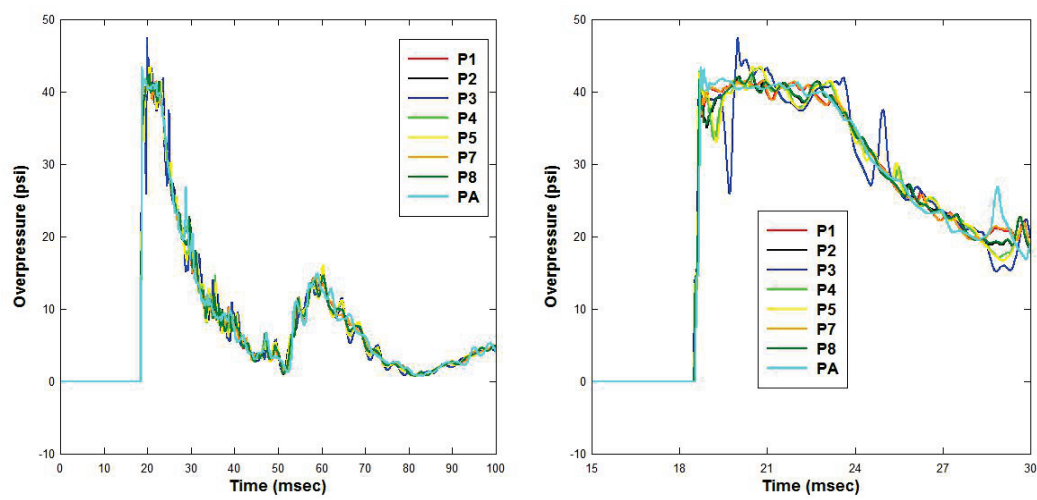


Figure B11. Calculated gauge pressure, GSA configuration.



(a) Global comparisons

(b) Early time

Figure B12. Gauge comparisons for DYSMAS, GSA configuration.

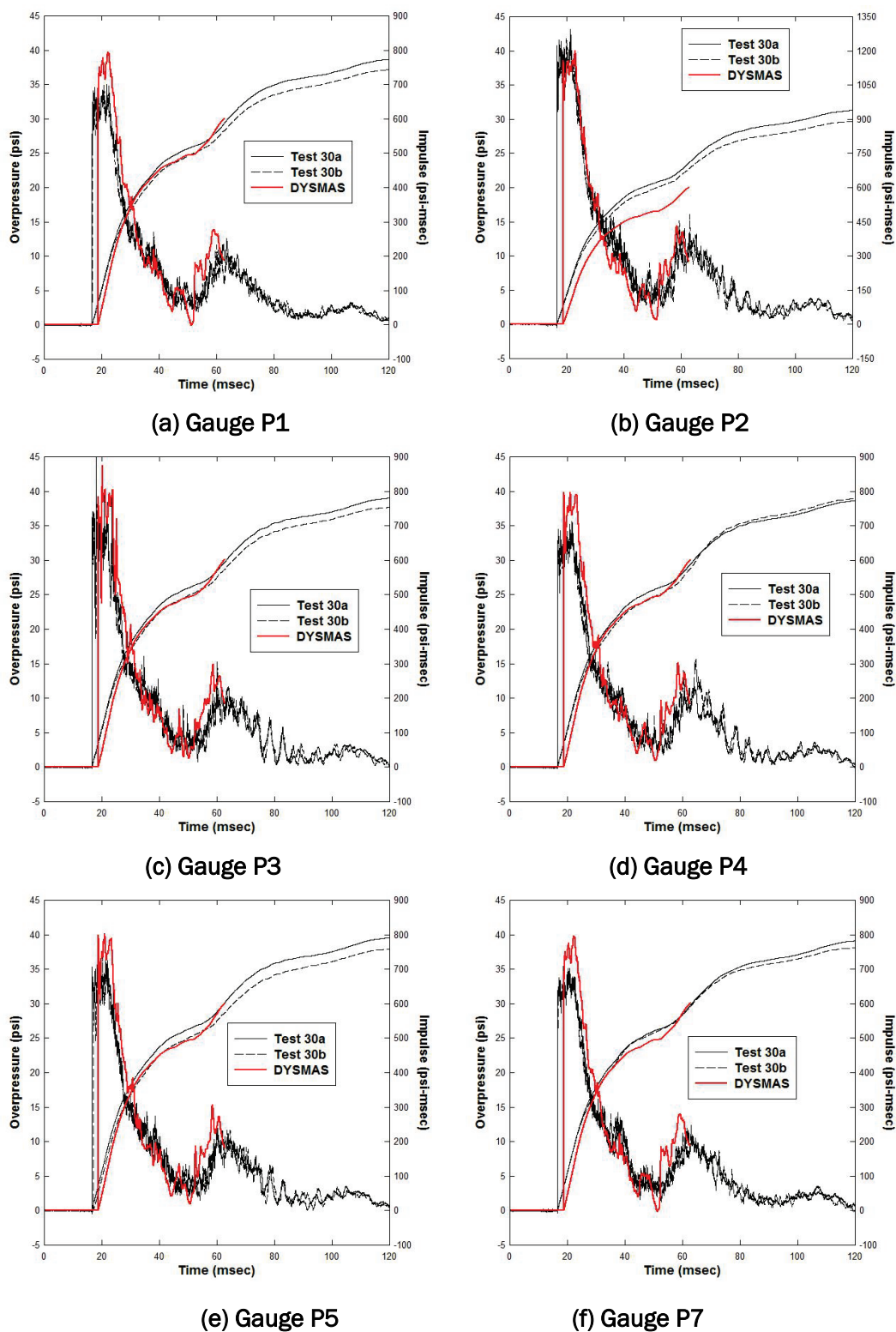
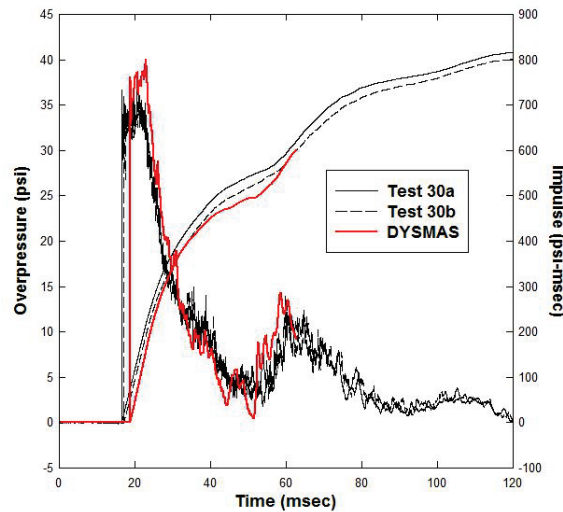


Figure B12. (Continued).



(g) Gauge P9

A 1.0-cm uniform cell size was specified for the region within the BLS, with a graded Eulerian mesh utilized outside. The analysis end time was 62.7 msec. It took 16 hr of CPU time and 1,016 processors to run this calculation to 62.7 msec. In the calculation, 8 processors were allotted to ParaDyn and 1,008 to Gemini. There were approximately 136 million cells in the Gemini mesh. It took 13,370 time-steps in the Gemini portion of the coupled calculation to run the analysis to 62.7 msec.

Calibration tests with 8-ft×8-ft C2SQ configuration

The DYSMAS model for the second case included the striker, grill, and extended section of the BLS. The Eulerian domain contained approximately 165.5 million cells, while the BLS structure consisted of 29,128 shells and 3,886 solid elements. This configuration and a cross section of the pressure field at an early time are shown in Figure B13. A progression through time of the pressure state is provided in Figure B14, which encompasses the high-density gas exiting the driver early-on, the shock and trailing high-density gas propagating down the BLS, reflection off of the target wall, and propagation back upstream toward the vents. The time stamp on each figure is given in units of seconds.

Similar to the first case, this calculation exhibits a clean, planar shock front and more chaotic flow behavior behind the front. By observing the particle velocity along the length of BLS and the density, this heterogeneous behavior can be clearly seen (Figure B15). The contact surface, which

Figure B13. Early time pressure state, 8-ft×8-ft C2SQ configuration.

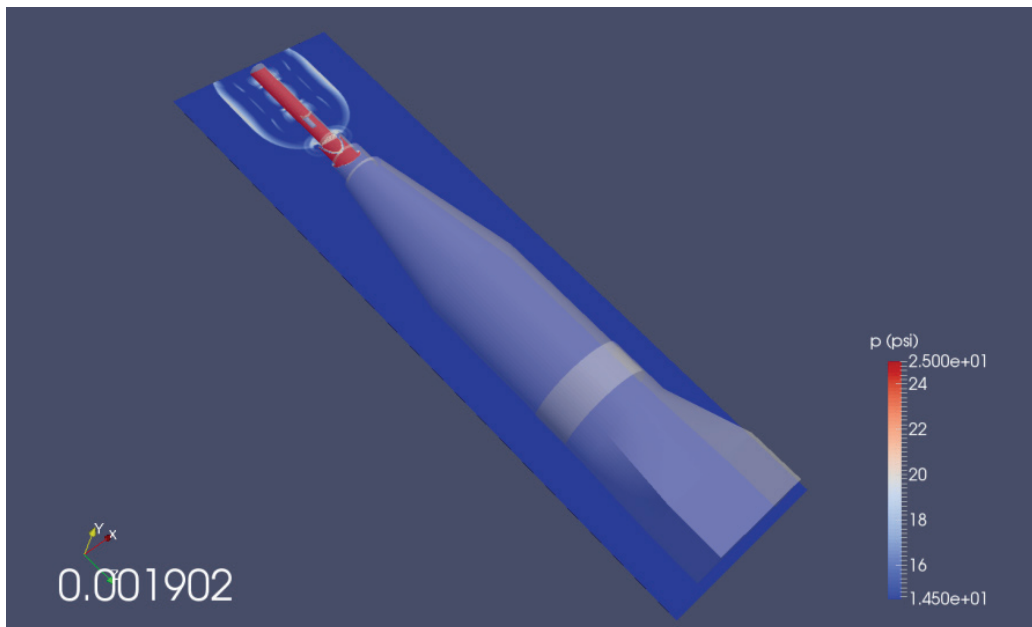


Figure B14. Pressure state plots for 8-ft×8-ft C2SQ configuration.

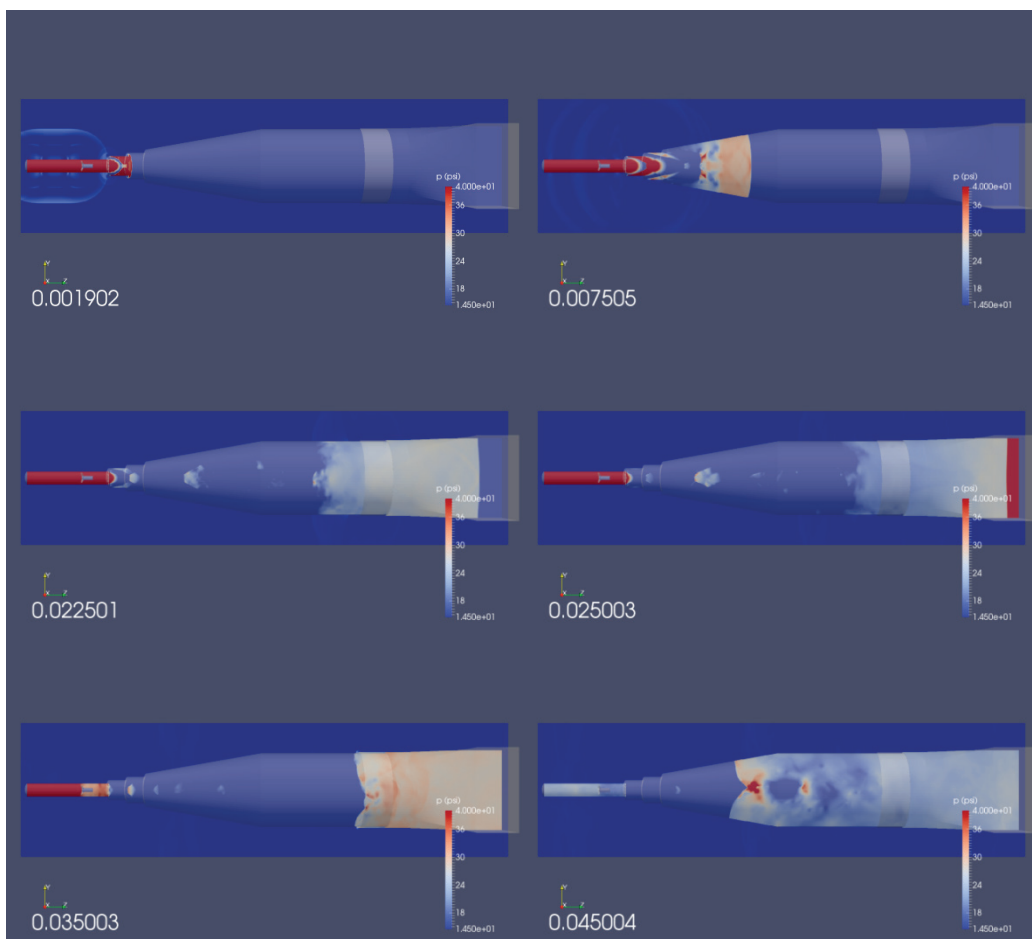
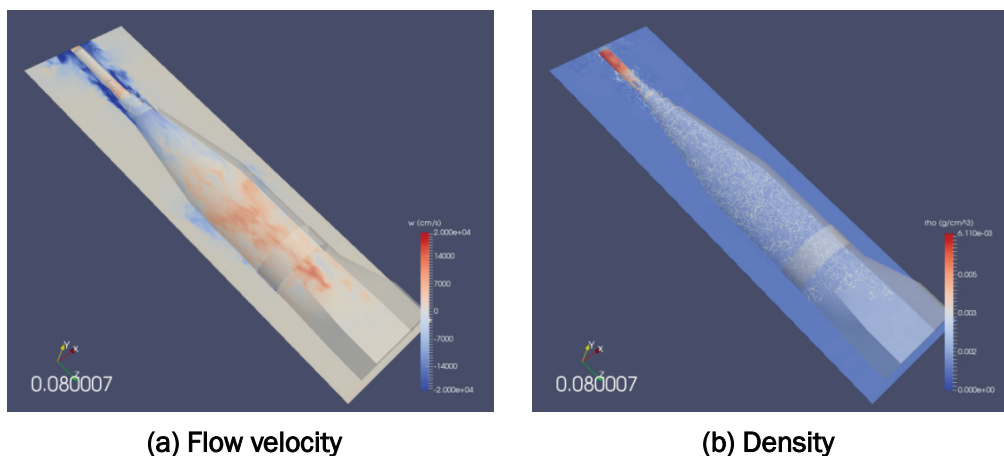


Figure B15. Velocity and density state plots at 80 msec.



is the interface between the driver and downstream gas, follows the shock front but only propagates a limited distance down the tube. The figure indicates that the contact surface extends downstream to the end of the Cascade, but does not go further (determined from additional state plots, not shown); however, the shock front continues onwards as a disturbance propagating through the remaining ambient air.

The calculated pressure histories at various locations on the target wall are shown in Figure B16. The mostly planar nature of the shock front is present, with only slight variations noted in the early reflected shock illustrated in Figure B16(b). Comparisons between the measured and calculated data for the target wall gauges are provided in Figure B17. The calculated results are presented “as-is” and have not been shifted in time to match the measured shock arrival. Overall, one notes good correlation between the calculated and measured waveform, with a slight tendency to overpredict the arrival time (about 1.3 msec later). The only significant disparities are for gauge P7; however, the results from this gauge are suspect when compared with the amplitude and general structure of the waveform at the other gauge locations.

Figure B16. Calculated gauge pressure, 8-ft×8-ft C2SQ configuration.

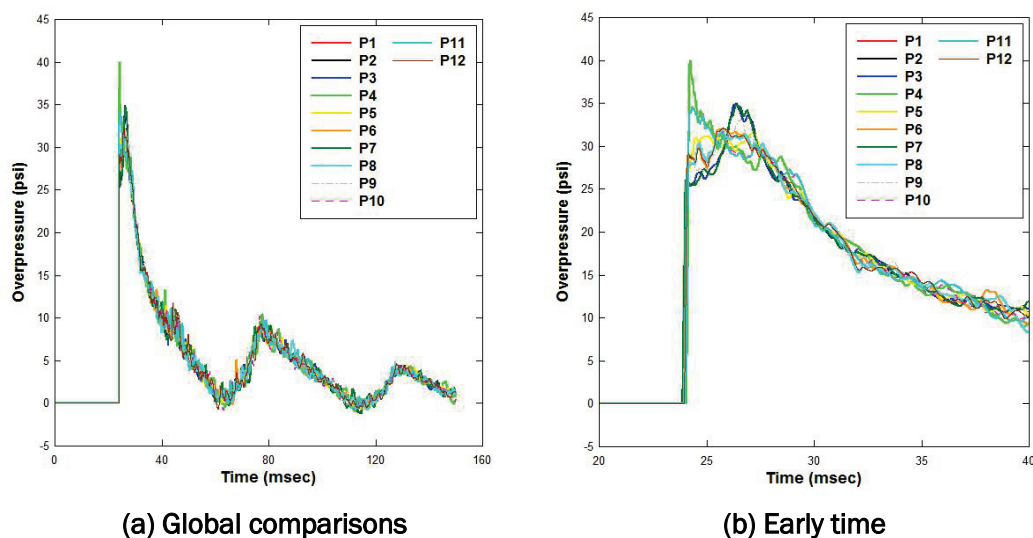


Figure B17. Gauge comparisons for DYSMAS, 8-ft×8-ft C2SQ configuration.

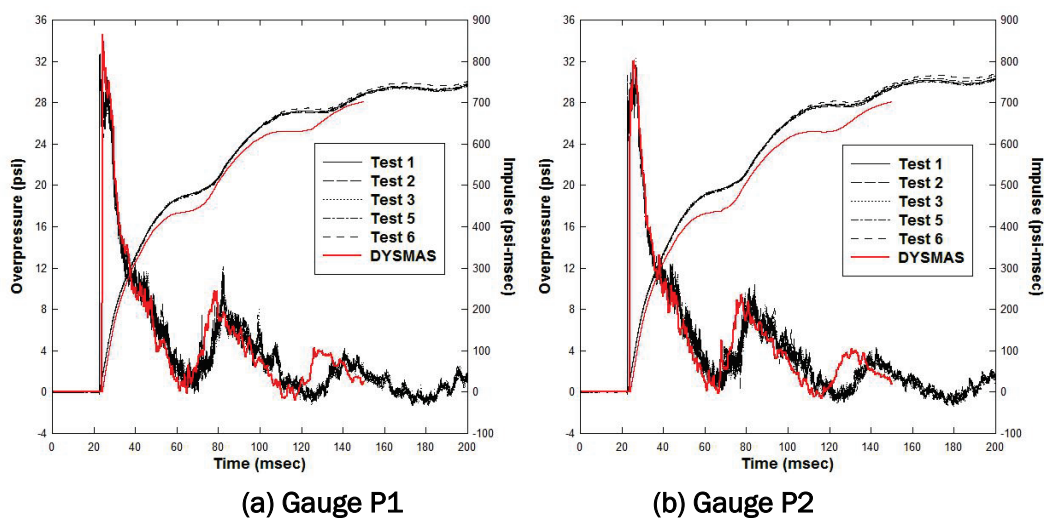
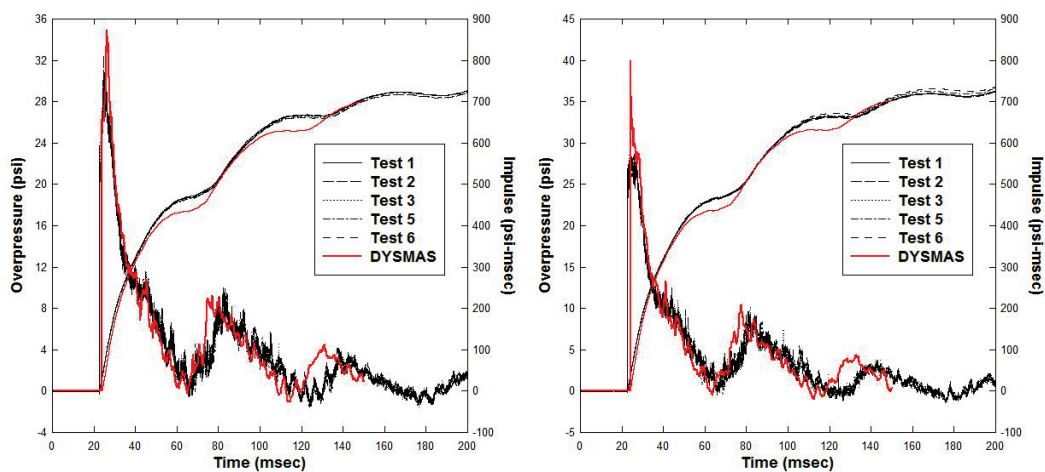
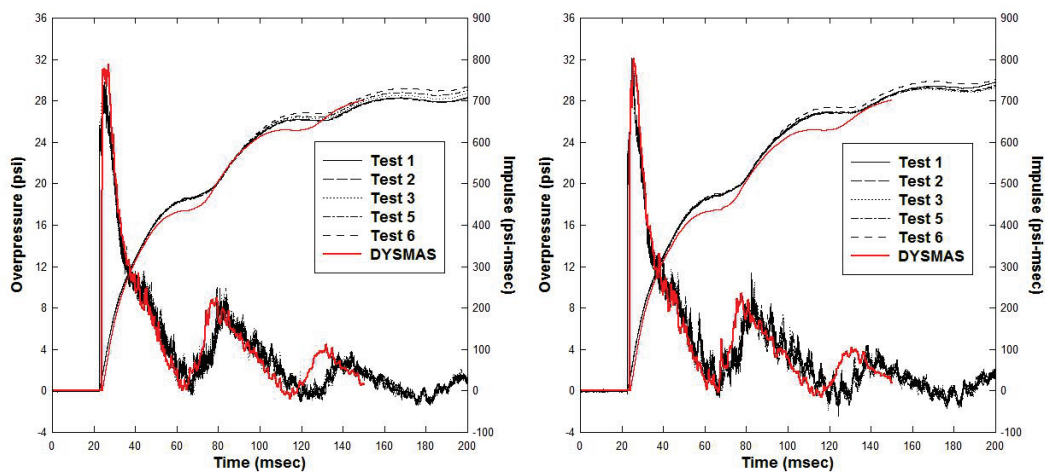


Figure B17. (Continued).



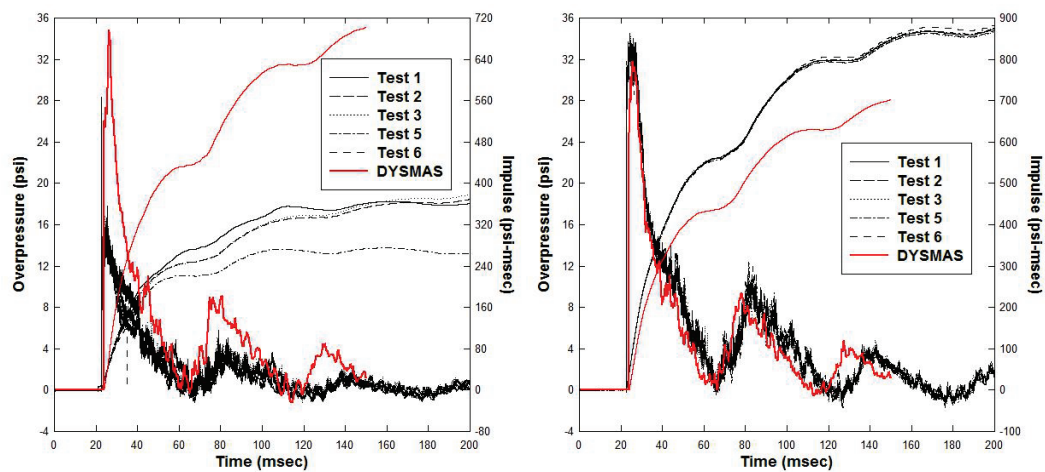
(c) Gauge P3

(d) Gauge P4



(e) Gauge P5

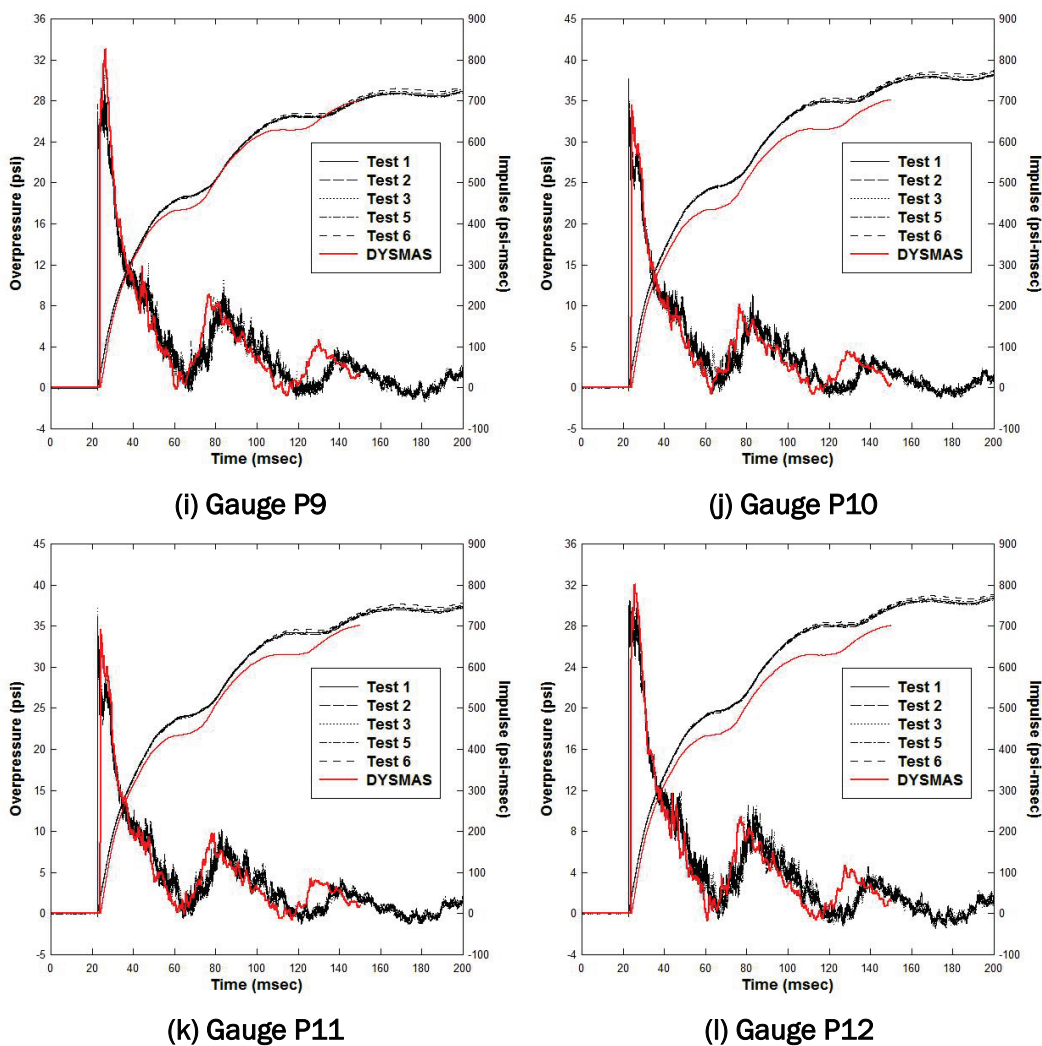
(f) Gauge P6



(g) Gauge P7

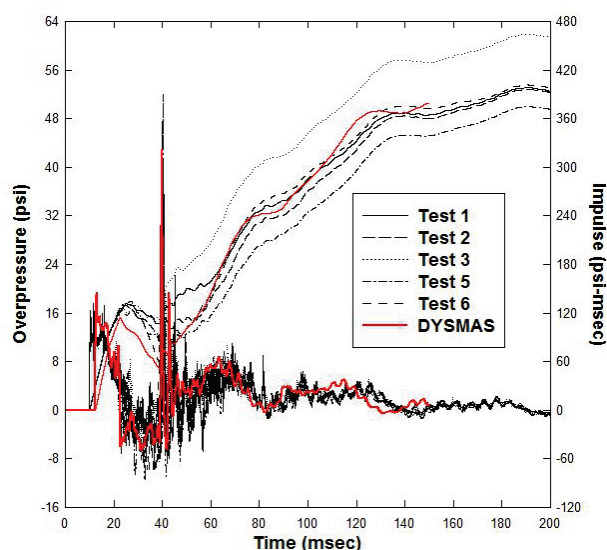
(h) Gauge P8

Figure B17. (Continued).



Comparisons for the side-on gauge PR are provided in Figure B18. The DYSMAS results have been time-shifted by -2.44 msec to match the measured arrival time. This was done to ease comparison of the measured and calculated waveforms. One notes that very good correlation is noted between the two.

Figure B18. Comparisons for gauge PR, 8-ft×8-ft C2SQ configuration.



A 1.0-cm uniform cell size was specified for the region within the BLS, with a graded Eulerian mesh utilized outside. The analysis end time was 150 msec. It took 31.85 hr of CPU time and 1,016 processors to run this calculation to 150 msec. In the calculation, 8 processors were allotted to ParaDyn and 1,008 to Gemini. There were approximately 136 million cells in the Gemini mesh. It took 19,212 time-steps in the Gemini portion of the coupled calculation to run the analysis to 150 msec.

BLS 8-ft×8-ft C2SQ configuration with box

This BLS configuration is the same as in the previous case with the exception of a box structure inserted into the C2SQ section (see Figure B19). As with the previous case, the BLS model included both the striker and grill (see Figure B20). An additional view looking upstream from the calibration plate towards the driver section is provided in Figure B21.

A time sequence of the pressure propagation is shown for the pressure wrapping around the structure in Figures B22 and B23, picturing the pressure inside and overhead views, respectively. The velocity and density plots in Figure B24 illustrate that the contact surface (interface between the driver gas and downstream air) only extends to the end of the Cascade. Thus, the pressure history for gauges residing on the box should be fairly clean and more consistent, as opposed to the box being placed at a location further upstream. The lack of noise in the measured data bears this out.

Figure B19. DYSMAS model of 8-ft×8-ft C2SQ configuration with box.

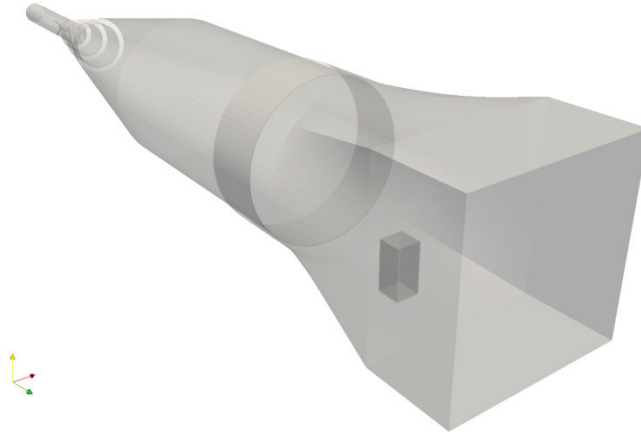


Figure B20. Close-up of striker and grill at the driver end.

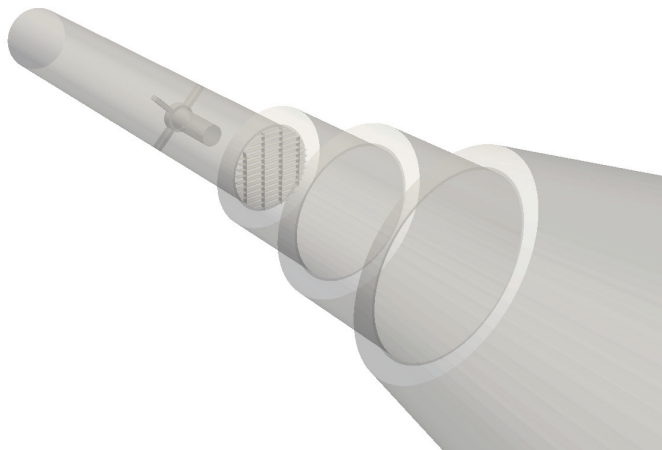


Figure B21. End-on view looking upstream to driver section.

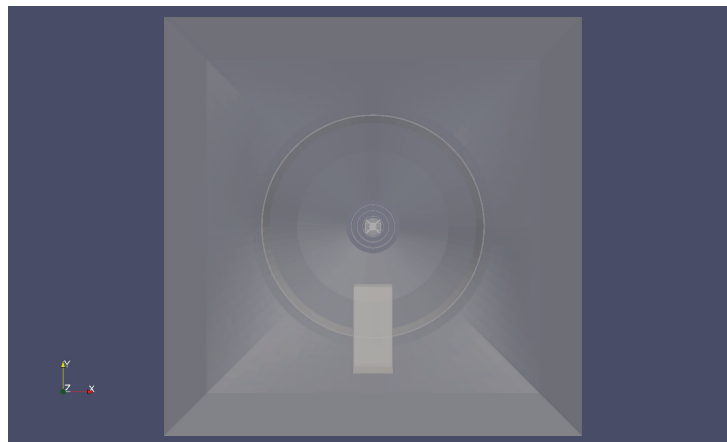
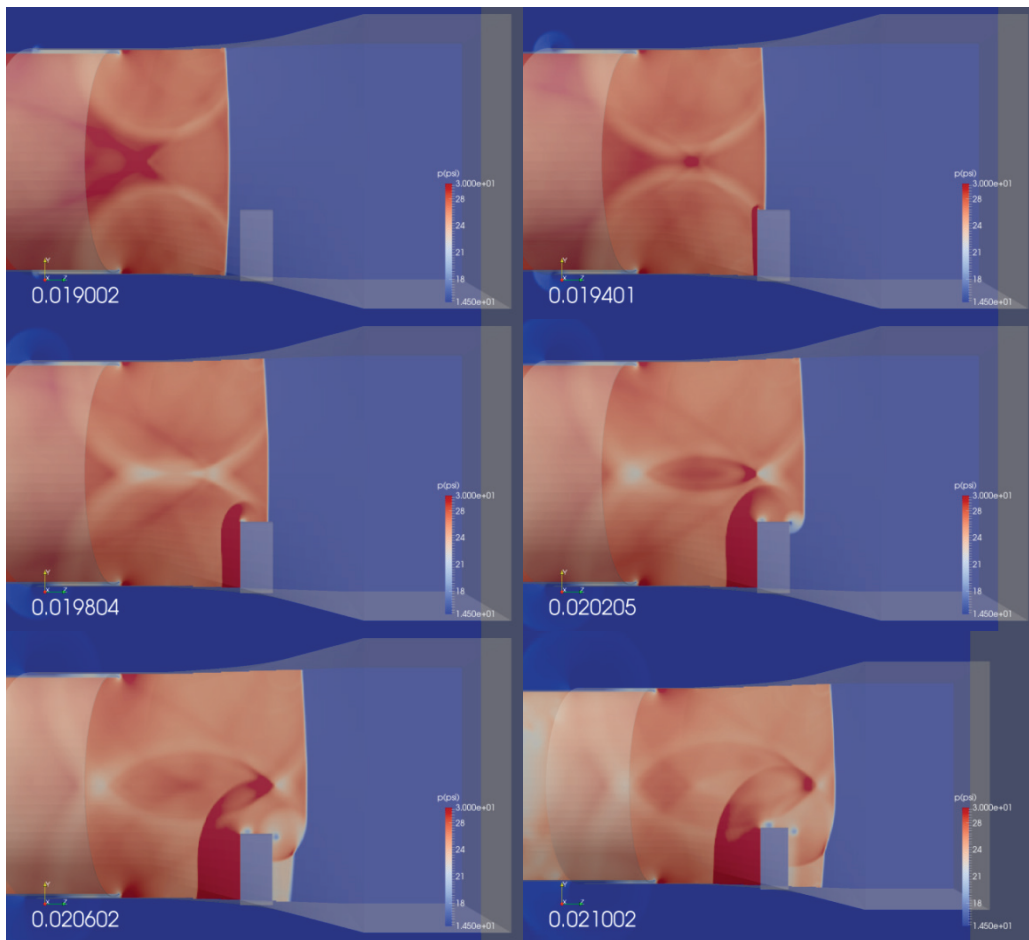


Figure B22. Pressure state plots, 8-ft×8-ft C2SQ configuration with box, elevation view.



The calculated pressure histories for gauges on the box structure are outlined in Figures B25 through B29. These figures provide a global comparison of the calculated results along with a comparison of the early time shock interaction for data on each of the faces (except the right face, which is comparable to that of the left one). In general, one notes good consistency in the calculated results for gauges on each face. There are slight differences for the left and right face gauges due to grid alignment; however, these are negligible. The calculated pressures on each face provide insight into the shock interaction with the box structure. The initial shock distinctly strikes the front face of the box and continues propagating forward in time, wrapping around the structure as seen in the state plots above. Once the shock reflects off the downstream target wall, it again wraps around the structure with a large reflected pressure on the back surface and refracted pressures on the remaining surfaces. This process is also shown in Figure B30, where pressures for the front, back, left side,

and top are plotted against each other. The relative timings are correct for both the initial and reflected shocks, as are the relative peaks with the highest being the first face encountered (front face for the initial shock and back face for the reflected shock) after which the refracted shock front has lower peaks on the side and back faces.

Figure B23. Pressure state plots, 8-ft×8-ft C2SQ configuration with box, plan view.

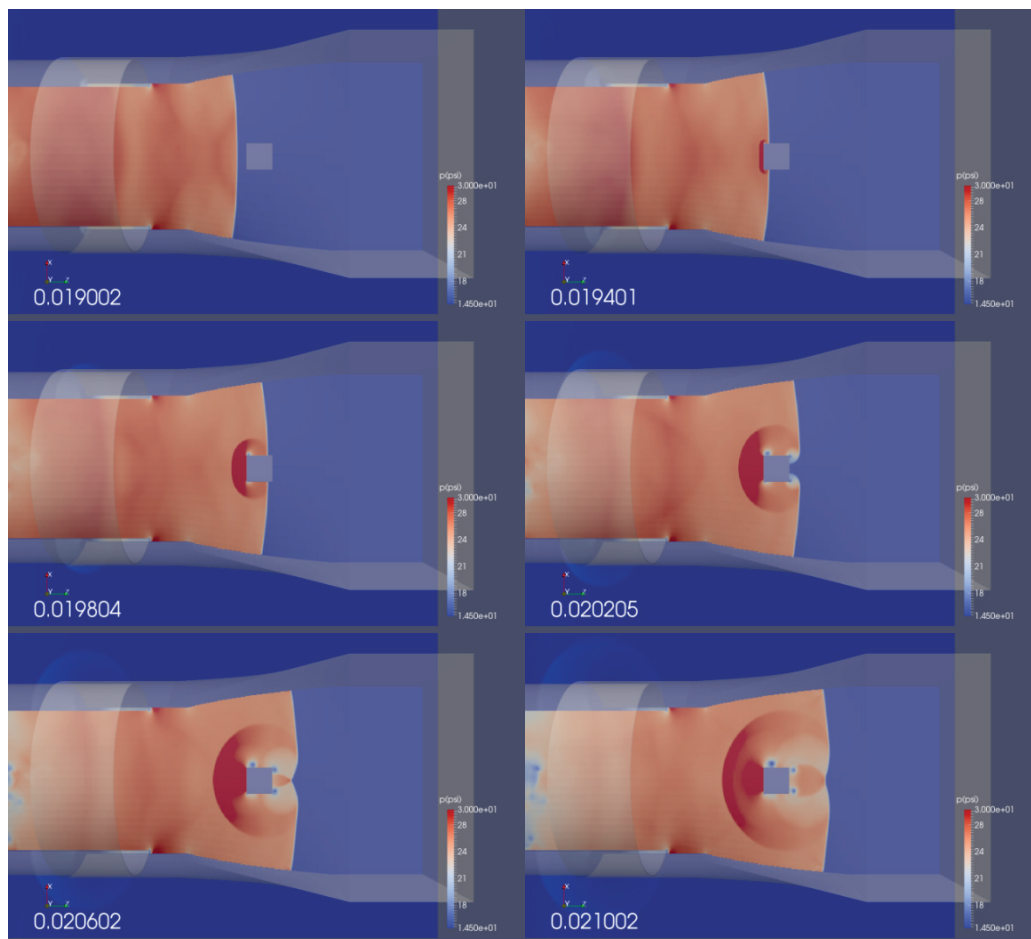
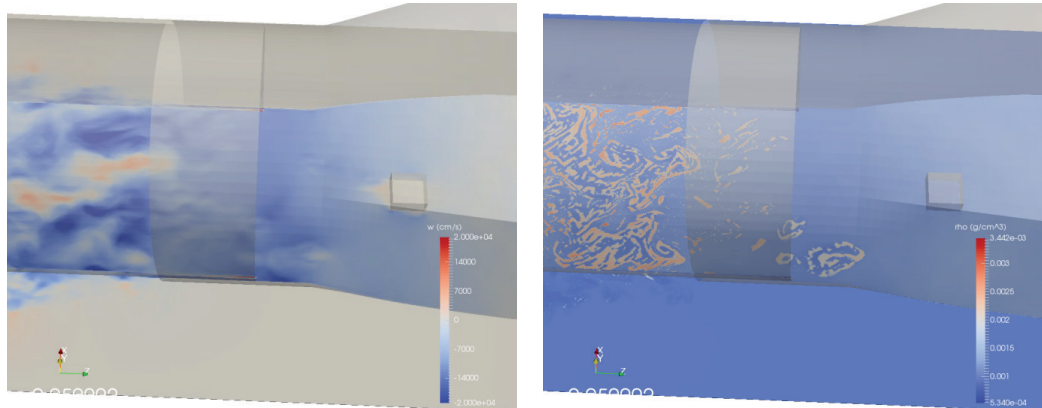


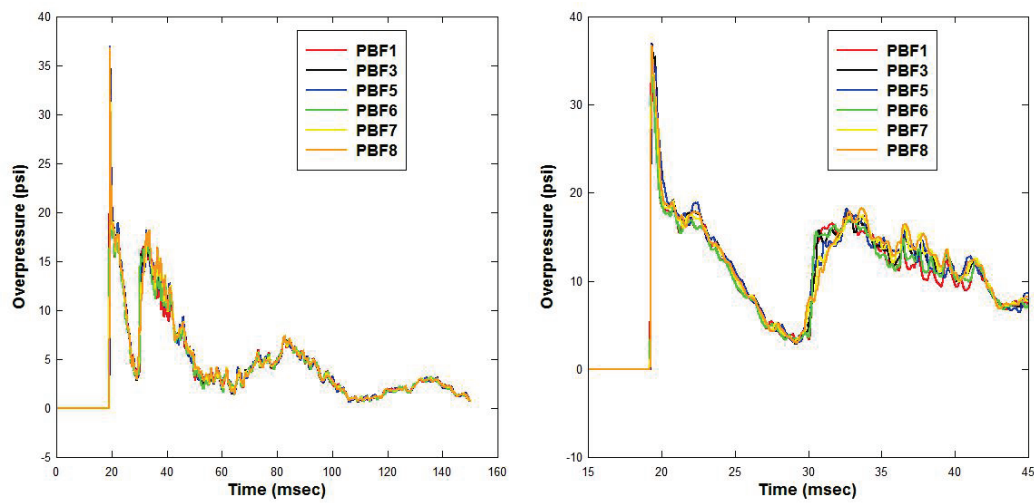
Figure B24. Velocity and density state plots at 50 msec.



(a) Flow velocity

(b) Density

Figure B25. Calculated gauge pressure for DYSMAS, front face.



(a) Global comparisons

(b) Early time

Figure B26. Calculated gauge pressure for DYSMAS, back face.

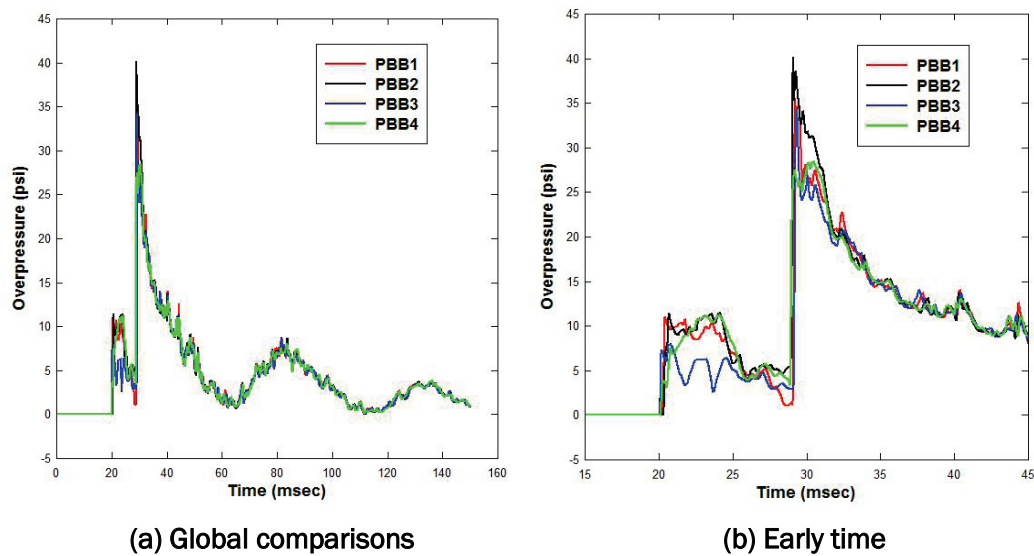


Figure B27. Calculated gauge pressure for DYSMAS, left face.

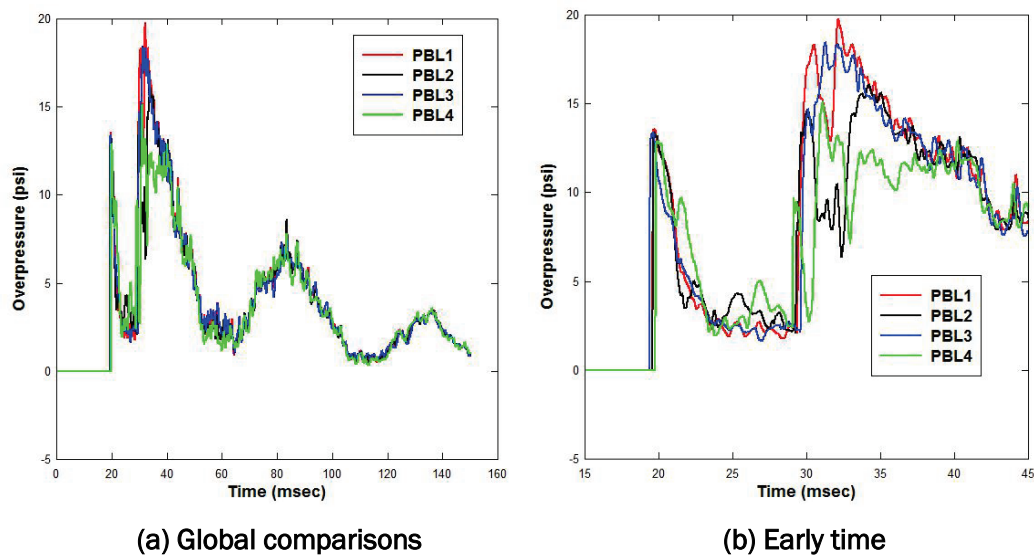
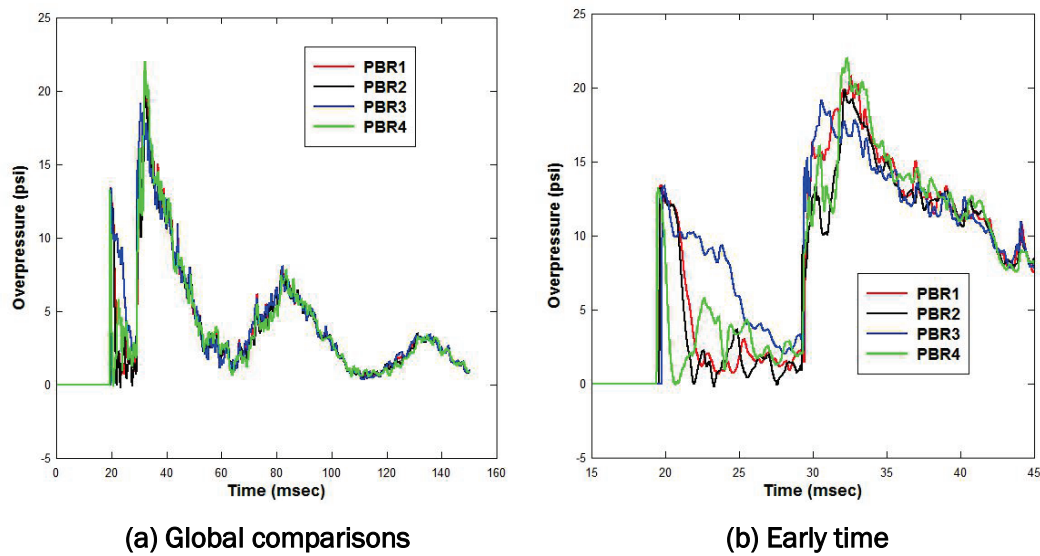


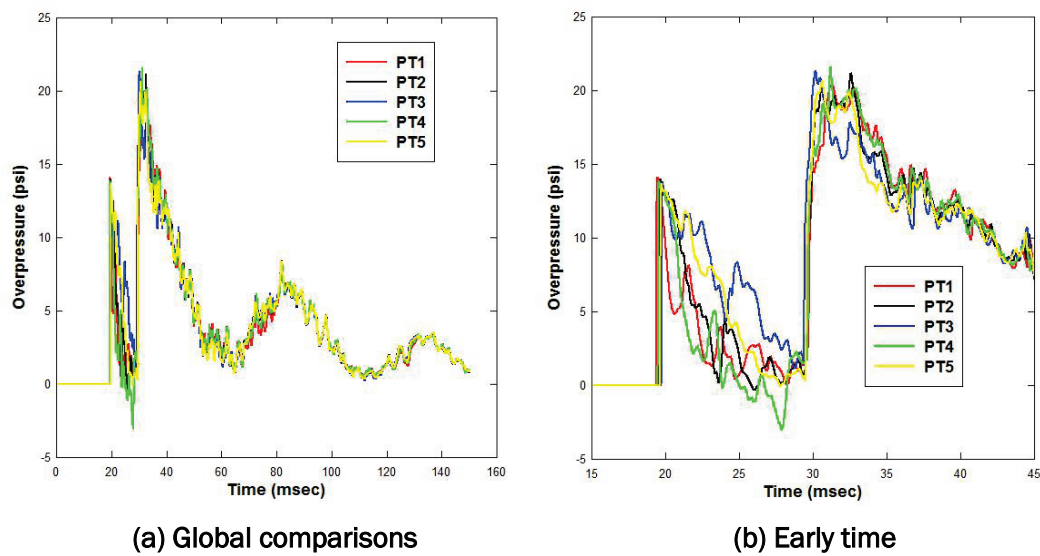
Figure B28. Calculated gauge pressure for DYSMAS, right face.



(a) Global comparisons

(b) Early time

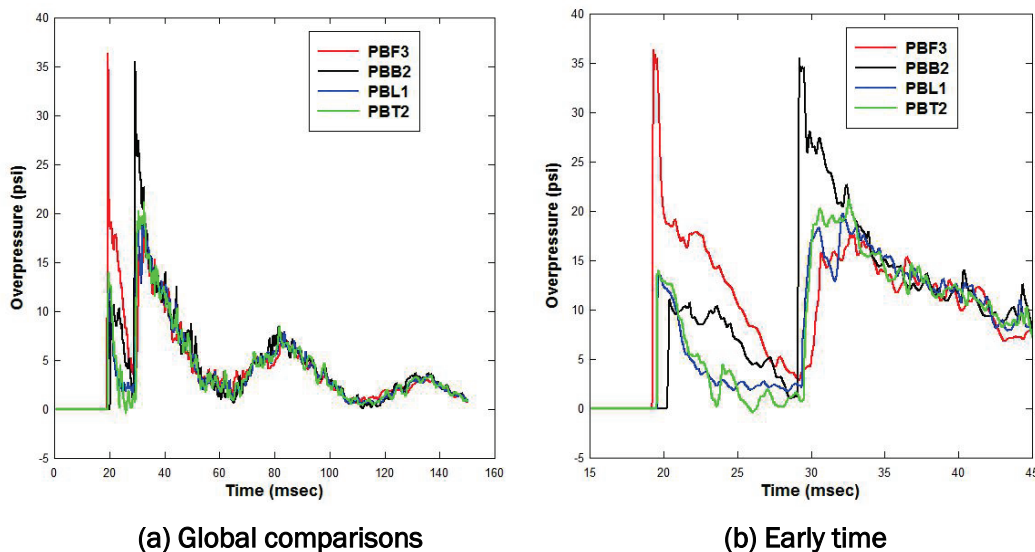
Figure B29. Calculated gauge pressure for DYSMAS, top face.



(a) Global comparisons

(b) Early time

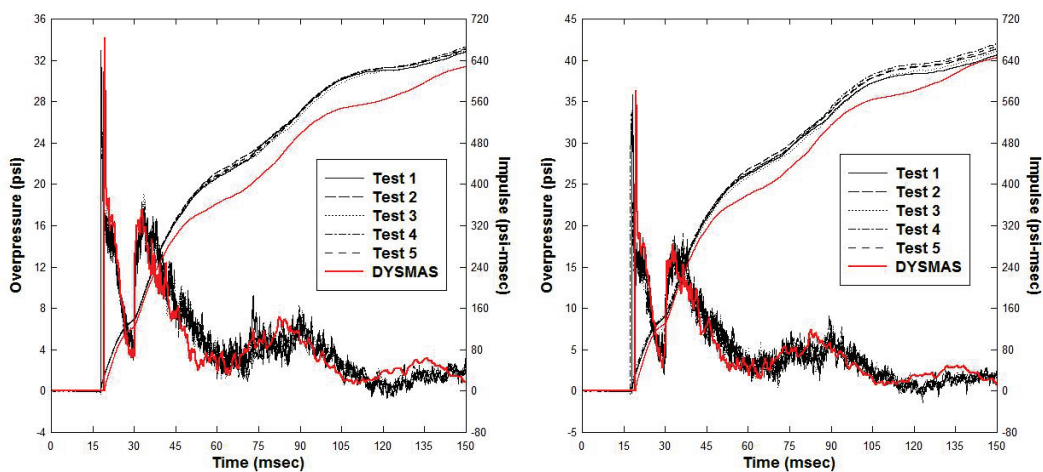
Figure B30. Comparison of calculated gauge pressure on each face.



Comparisons between the measured and calculated data for the gauges on the box structure are provided in Figures B31 through B35. The calculated results are presented “as-is” and have not been shifted in time to match the measured shock arrival. Overall, one notes good correlation between the calculated and measured waveforms with a slight tendency to over-predict the arrival time (about 1.8 msec later). Similar comparisons are provided for the target wall (see Figure B36). Again, good correlation is noted between the calculated and measured data.

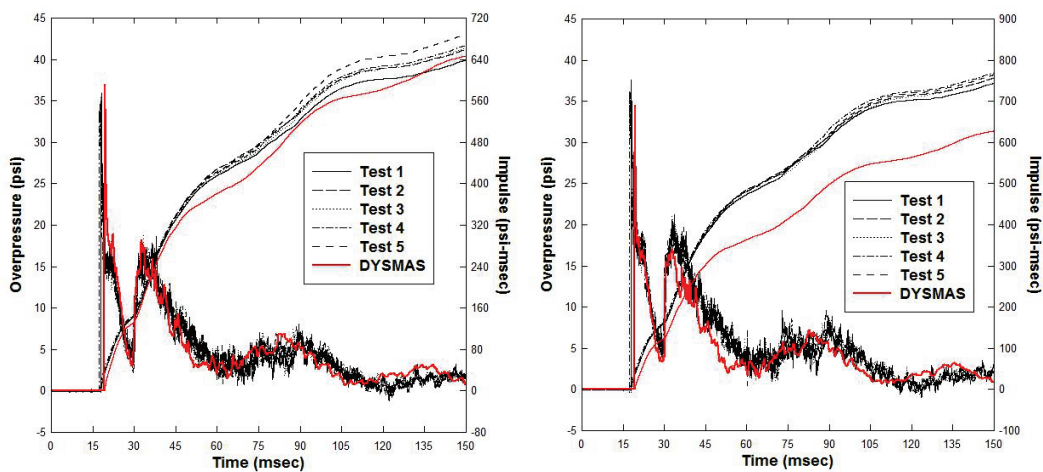
A 1.0-cm uniform cell size was specified for the region within the BLS, with a graded Eulerian mesh utilized outside. The analysis end time was 150 msec. It took 37.48 hr of CPU time and 1,016 processors to run this calculation to 150 msec. In the calculation, 8 processors were allotted to ParaDyn and 1,008 to Gemini. There were approximately 165.5 million cells in the Gemini mesh. It took 19,600 time-steps in the Gemini portion of the coupled calculation to run the analysis to 150 msec.

Figure B31. Gauge comparisons for DYSMAS, front face.



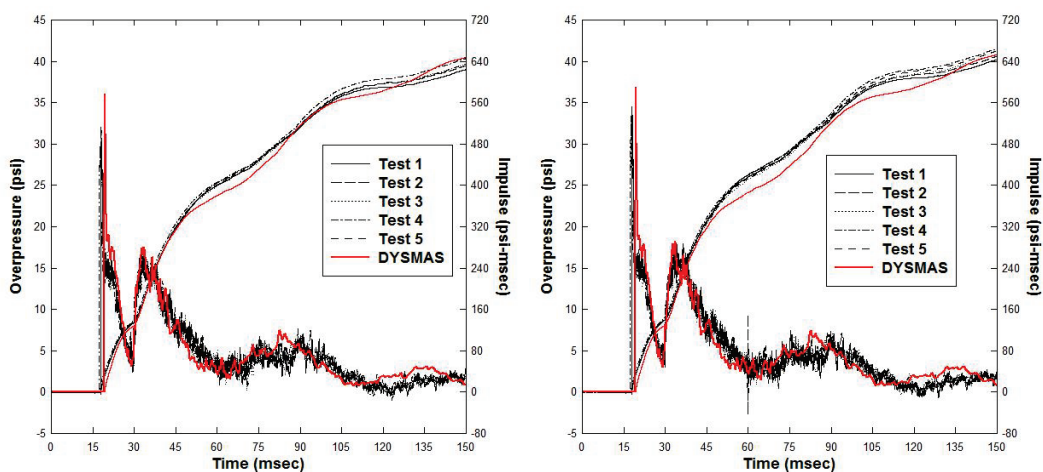
(a) Gauge PBF1

(b) Gauge PBF3



(c) Gauge PBF5

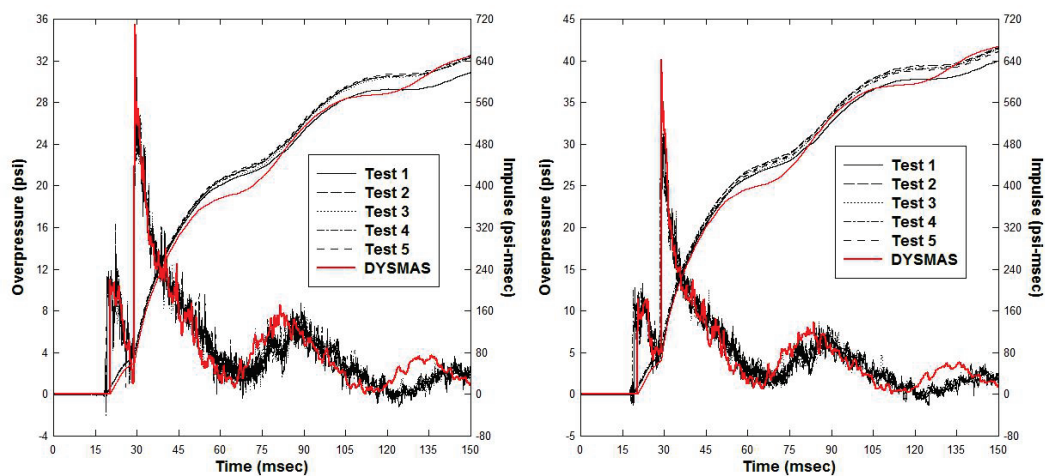
(d) Gauge PBF6



(e) Gauge PBF7

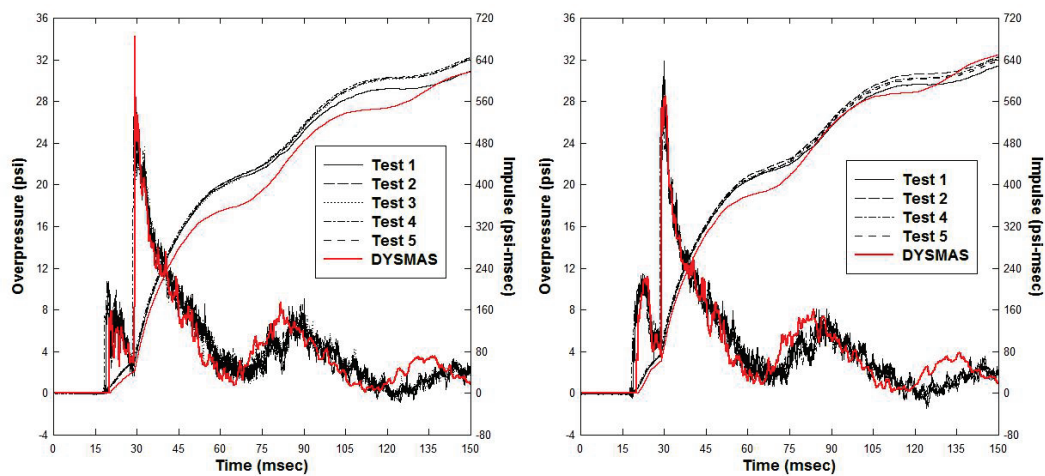
(f) Gauge PBF8

Figure B32. Gauge comparisons for DYSMAS, back face.



(a) Gauge PBB1

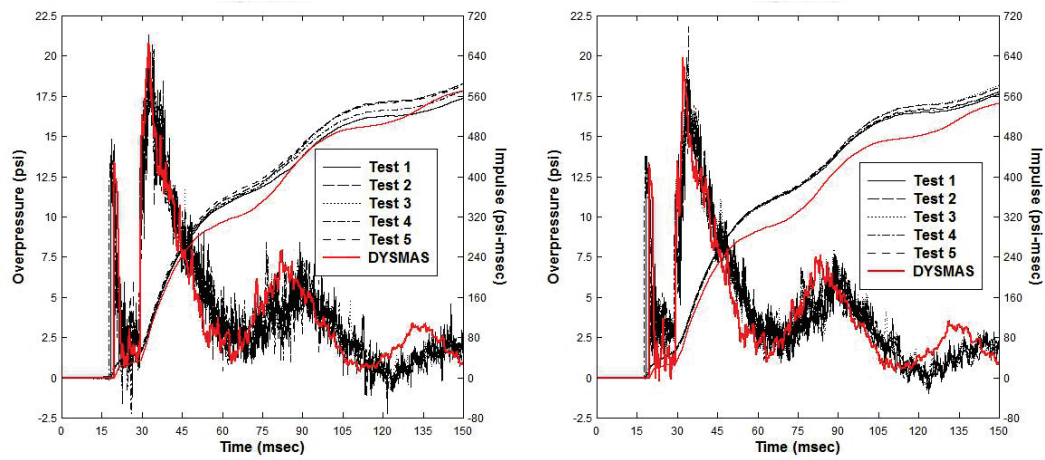
(b) Gauge PBB2



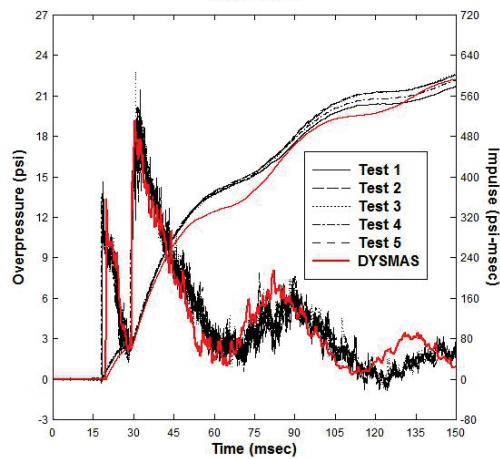
(c) Gauge PBB3

(d) Gauge PBB4

Figure B33. Gauge comparisons for DYSMAS, left face.

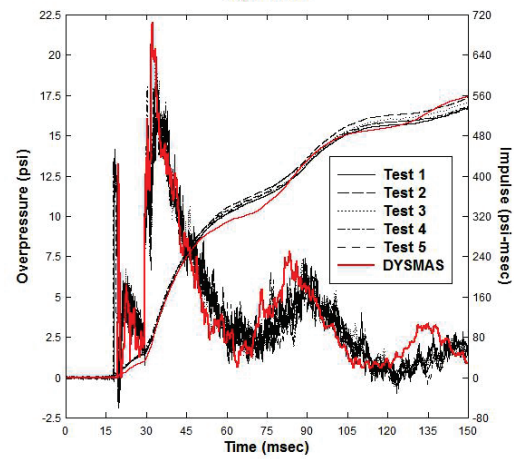


(a) Gauge PBL1



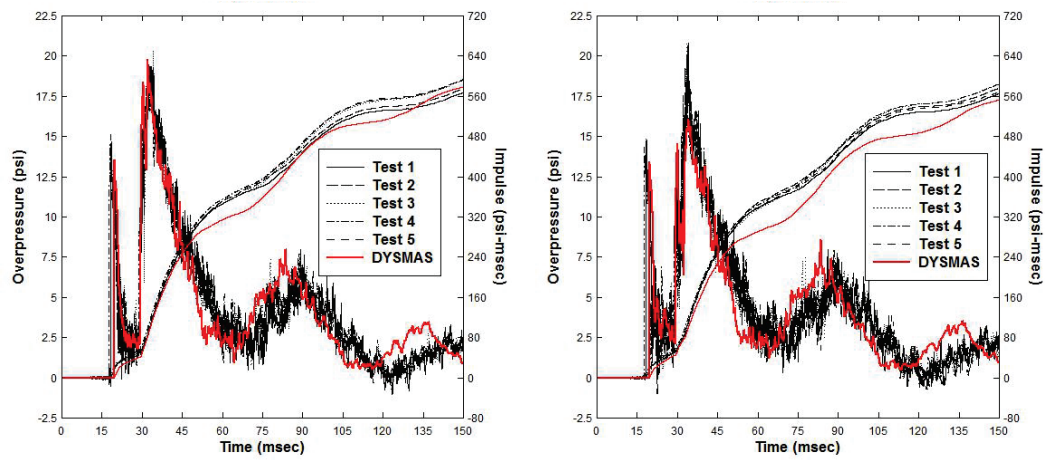
(c) Gauge PBL3

(b) Gauge PBL2

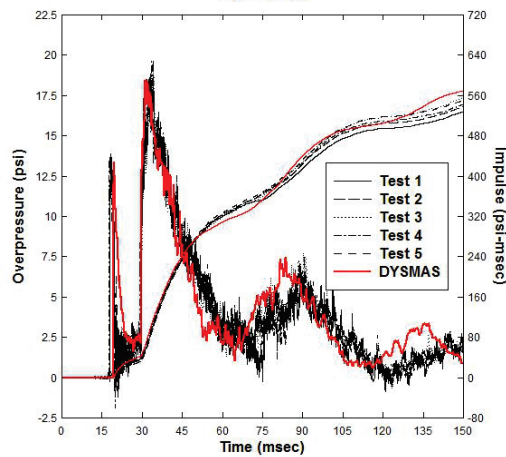


(d) Gauge PBL4

Figure B34. Gauge comparisons for DYSMAS, right face.

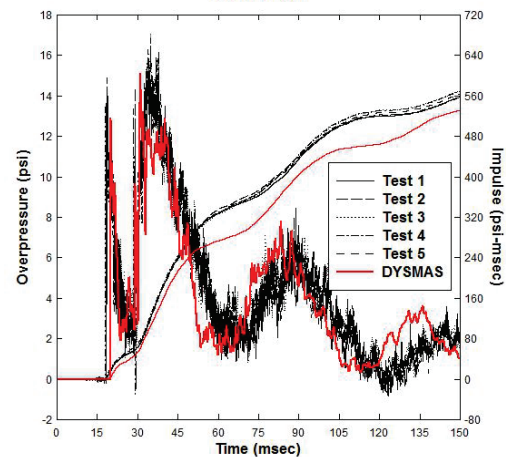


(a) Gauge PBR1



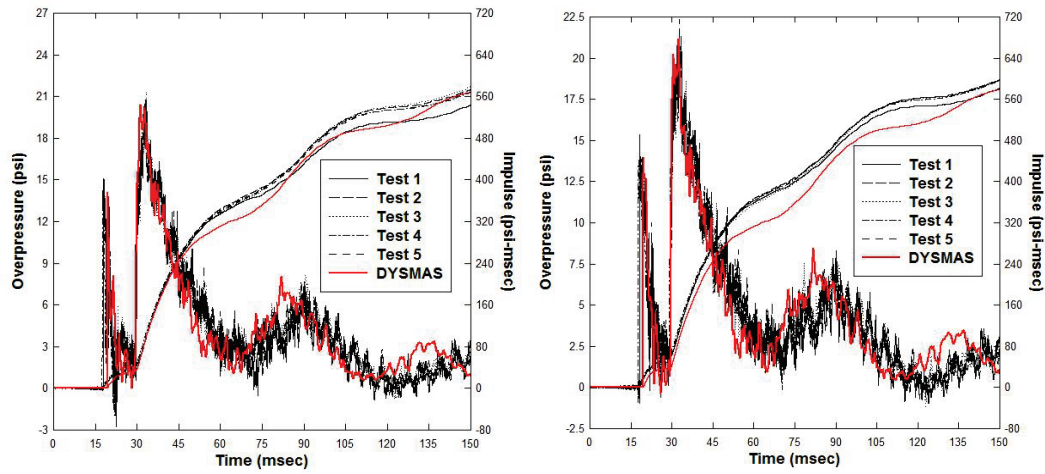
(c) Gauge PBR3

(b) Gauge PBR2



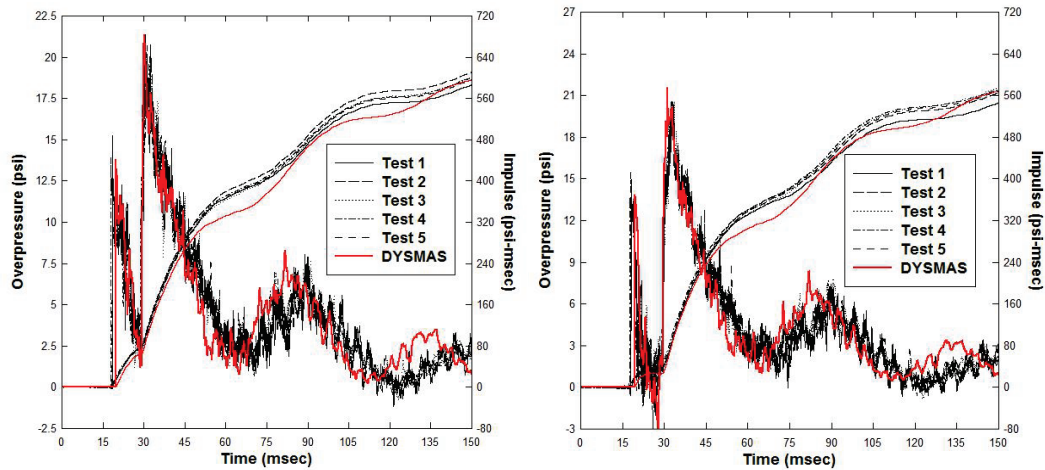
(d) Gauge PBR4

Figure B35. Gauge comparisons for DYSMAS, top face.



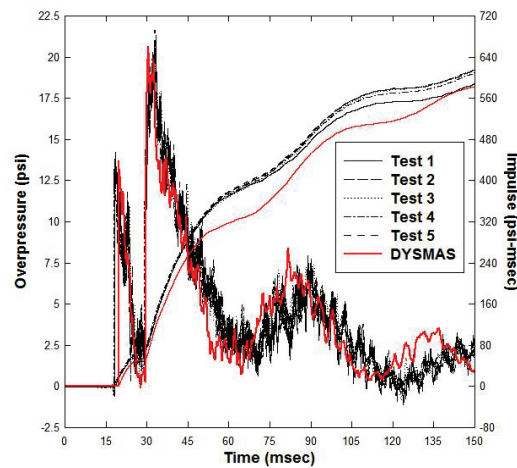
(a) Gauge PBT1

(b) Gauge PBT2



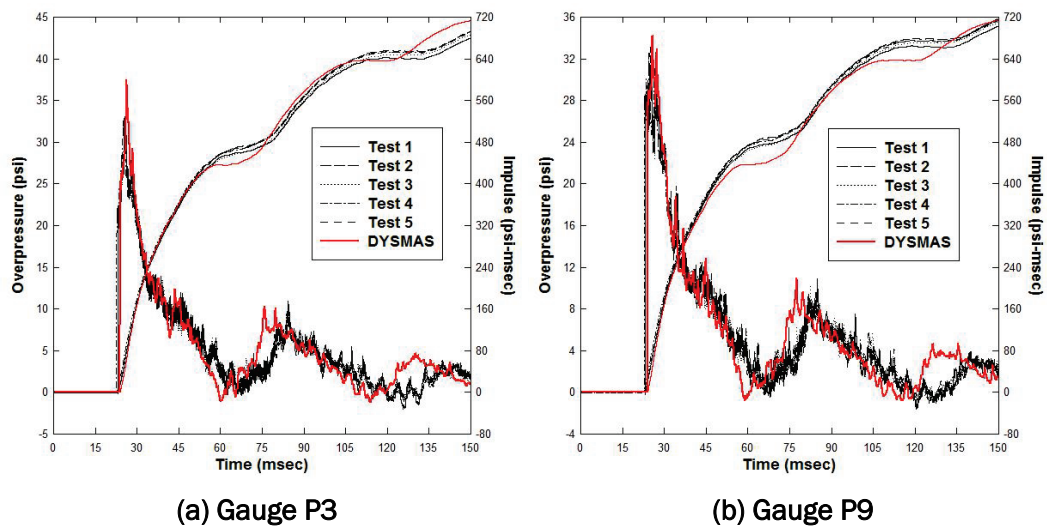
(c) Gauge PBT3

(d) Gauge PBT4



(e) Gauge PBT5

Figure B36. Gauge comparisons for DYSMAS, target wall.



Appendix C: LOCI-Blast Modeling

Loci/BLAST Background

Loci/BLAST is a modern computational fluid dynamics (CFD) code designed to provide accurate simulations for a variety of blast scenarios. Loci/BLAST is based on the Loci/CHEM chemically reacting flow code developed at Mississippi State University (MSU) by Dr. Edward Luke and his co-workers (Luke 1999; Luke and George 2005; Luke and Cinella 2007). Loci/CHEM has been in constant development for more than 15 years and is widely used at the National Aeronautics and Space Administration (NASA) and in the aerospace industry for CFD analysis of aircraft and launch vehicle aerodynamics and chemically reacting flows in rocket motors. Development of Loci/BLAST was initiated under the U.S. Army Tank Automotive Research and Development Engineering Center (TARDEC) Simulation Based Reliability and Safety (SimBRS) program to provide a modern computational tool for analysis of underbody blast effects on military vehicles (Thompson et al. 2010, 2012a). Loci/BLAST was extended to perform simulations of urban blast problems under Department of Homeland Security sponsored Southeast Region Research Initiative (SERRI) funding (Thompson et al. 2012b). Both Loci/CHEM and Loci/BLAST have undergone extensive verification and validation testing over the years and have a proven history of providing accurate and cost-effective solutions for a variety of CFD and blast related problems.

Loci/BLAST has a wide range of capabilities that support large-scale blast analyses. Loci/BLAST is an unstructured cell-centered finite volume code that can utilize generalized grids consisting of a variety of polyhedral cell types (tetrahedra, hexahedra, prisms, etc.). Unlike some other codes used in this research, Loci/BLAST is fully Eulerian (no operator splitting) and uses well-defined, modern unstructured CFD analysis methods such as the Harten-Lax-van Leer-Enfledt (HLLC) approximate Riemann solver to compute fluxes at cell faces and least-squares reconstruction coupled with a nodal Baldwin-Barth limiter to provide second-order spatial accuracy. Explicit time integration is performed using a two-stage second-order Total Variation Diminishing (TVD) Runge-Kutta scheme. The Loci framework on which both Loci/BLAST and Loci/CHEM are based provides facilities for automatic parallelization and cache memory use optimization that makes codes developed using the framework highly scalable and

computationally efficient in parallel computing environments. Loci/CHEM has demonstrated scalability to 10,000 processor class jobs and will scale to larger processor counts with little or no additional code modifications. Other capabilities of Loci/BLAST that support large-scale blast analysis include varied EOS options for energetic materials, a multi-phase soil model, particulate transport models, and both prescribed initiation and reactive burn detonation models. Loci/BLAST can also utilize a unique overset grid capability to reduce the work load associated with generating global grid systems that contain a variety of solid objects of varying shapes and dimensions such as those found in urban blast scenarios.

The Loci framework provides a unique code development paradigm based on principles taken from relational database design and artificial intelligence instead of traditional procedural or object-oriented approaches. Various analysis tasks can be instantiated as a set of rules that operate on prescribed data structures to generate a desired outcome. Codes can then be rapidly developed by compositing rules into a set of queries that perform the desired tasks in the correct order. This reduces the time required to generate complex multi-physics codes because the framework will detect any discrepancies in data transfers between code components and schedule computational tasks to execute in the most computationally efficient manner. Therefore, the time required to implement future code modifications required to support the next phases of the current research will in most cases be shorter than with traditional programming approaches.

Analysis overview

All of the calculations of the ERDC BLS tests using Loci/BLAST were performed by Clayton Mord, a graduate student in Aerospace Engineering at MSU under direction of Dr. Richard Weed and constitutes the bulk of his master's thesis research (Mord 2015). As with the analyses performed with the other codes used in this research, an initial set of 2-D axisymmetric runs were made with the initial BLS configuration to guide problem setup and verify the code could produce a planar shock wave in the test section. These runs were made with a clean flow path that did not include the BLS striker mechanism and the catch grill. Subsequent calculations were run with a variety of mesh configurations until the final grid systems used for the results presented in the following sections were obtained. The grid systems are fully 3-D (planar symmetry is not assumed), model both the

striker assembly as well as the catch grill, and provide an acceptable balance between solution accuracy and total simulation run times. As will be shown in more detail in the following section, the final grid systems consisted of all tetrahedral cells with attention given to gridding around the BLS vent systems, the striker and grill, and finally, the box in the third case involving the 8-ft×8-ft C2SQ configuration. A large plenum was assumed around the BLS to provide a space into which the air flowing through the BLS vents can exhaust and to minimize the effects of waves reflecting off of computational outer boundaries.

Grids were generated for three configurations referred to in this appendix as the GSA configuration, 8-ft×8-ft C2SQ configuration, and 8-ft×8-ft C2SQ configuration with box. The GSA configuration contained all stages of the BLS configuration through the circular section. The second and third cases added the square 8-ft×8-ft test section to the GSA configuration. The grid for the third case was modified to include the box in the C2SQ section.

All analyses were run on the MSU High Performance Computing Collaboratory (HPC) IBM IDataplex and Cray CS300-LC clusters (named Talon and Shadow, respectively). Both systems use multi-core Intel XEON processors for compute nodes. A complete description of both systems is given at <http://hpc.msstate.edu>. Computational grids were generated using the SolidMesh grid generation tools developed by Dr. David Marcum at Mississippi State University (Marcum 1998). SolidMesh provides a GUI-based environment that supports import and manipulation of CAD geometry and grid generation setup. The final volume grids were generated using Marcum's Advancing Front with Local Reconnection 3-D (AFLR3-D) tetrahedral grid generator. All calculations discussed herein were made assuming inviscid flow and used the ideal gas EOS. Although Loci/CHEM has a full viscous flow analysis capability, finer meshes near solid walls would be required to resolve boundary layer and other viscous effects, which in turn, would require switching to an implicit solver instead of the Runge-Kutta scheme to overcome the explicit time-step restrictions inherent in viscous grids. At some point in the next phase of this research, an attempt should be made to quantify viscous effects, but time constraints prohibited any viscous analysis in the current simulations. Pressure-time-histories were extracted at the physical locations of the gauge locations prescribed in the experiments. These were integrated

using trapezoidal integration in a MATLAB program to obtain time-histories of impulse at the various gauge locations.

Problem setup

Overview

The SolidMesh program was used to define the surface geometries and meshes of the three BLS configurations along with computational boundaries and boundary conditions. Only tetrahedral meshes were used to generate the 3-D results presented in this appendix. The final tetrahedral volume meshes were generated using the AFLR3-D program. The surface geometries were defined using a series of drawings and dimensions of the various BLS sections supplied by ERDC. The 2-D pathfinder calculations used both triangular and quadrilateral elements. Initial 3-D simulations for the first case did not include either the striker or the grill; however, following these initial simulations, it was decided to include these in all subsequent 3-D calculations. The procedure used to generate the meshes for both the baseline GSA and the 8-ft×8-ft configurations, as well as the modeling of the striker mechanism and grill are described in the following sections. A description of the 2-D axisymmetric and initial 3-D calculations for both the GSA and 8-ft×8-ft configurations are given in Mord (2015). For this report, only the final 3-D BLS geometries and meshes are discussed.

Creation of baseline meshes

The 3-D GSA configuration was created by revolving lines about the x-axis to form a set of surfaces with radial symmetry. The 8-ft×8-ft configuration was derived from the GSA model. The 8-ft×8-ft configuration differs from the GSA version only after the Cascade. Therefore, the geometry for the symmetric portion of the BLS inner surface was created from a set of lines revolved around the x-axis. The non-symmetric components (C2sQ and SQ1) were developed as separate surface entities and merged with the revolved line components to form the final BLS model. The two sections of the model are separated by a small gap of 0.4 in. This distance was taken from photographs of measurements from the BLS and is therefore consistent with the BLS experiments. The outlines of the final GSA and 8-ft×8-ft configuration wall geometries along the plane of symmetry can be seen in Figures C1 and C2.

Figure C1. GSA configuration geometry.

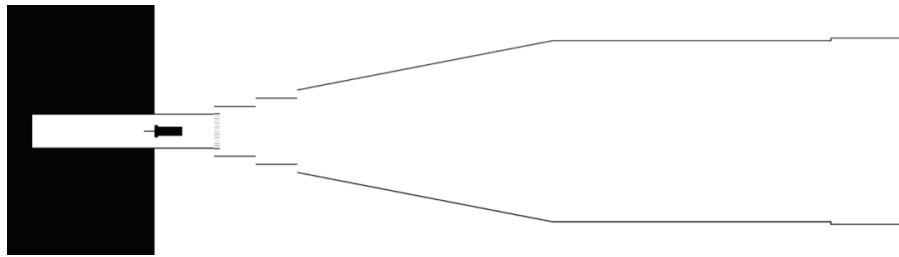
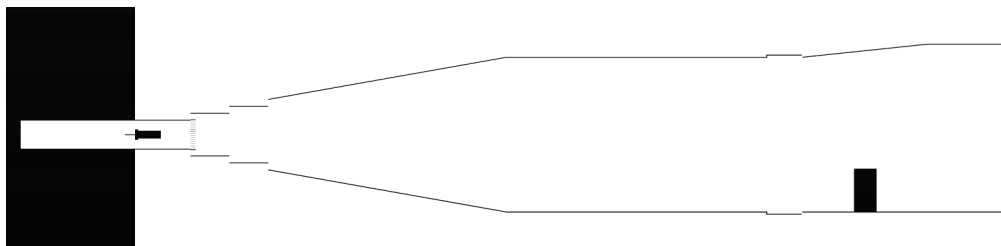


Figure C2. BLS 8-ft×8-ft C2SQ configuration geometry with box.

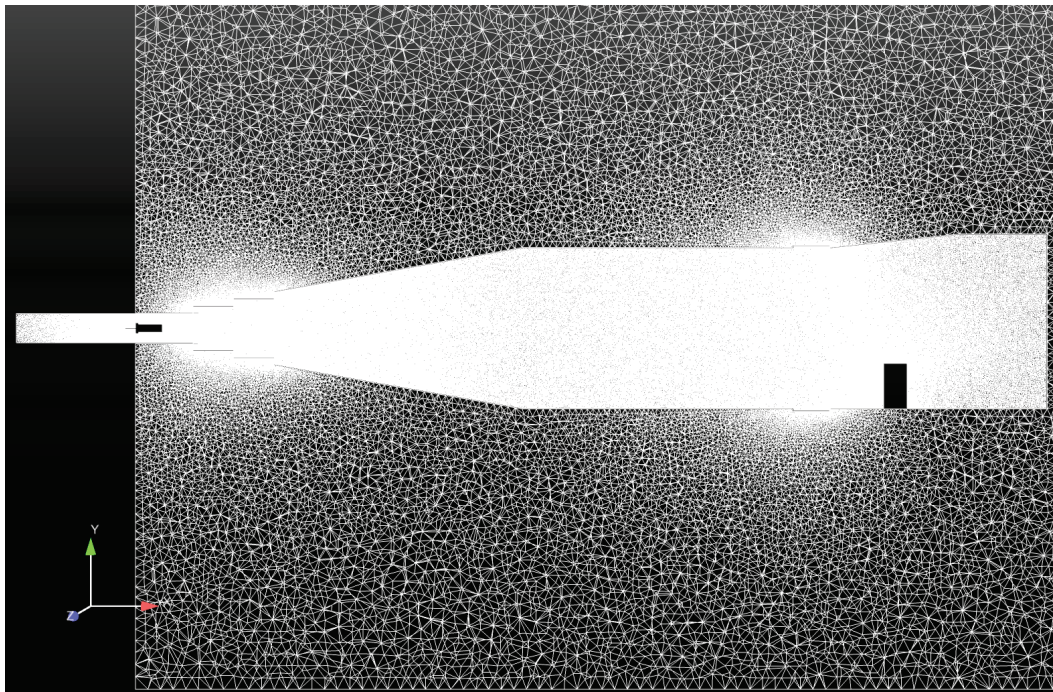


The final BLS mesh in both configurations had a maximum mesh resolution of 1.0 in. throughout. The extent of the computational grid for the 8-ft×8-ft configuration with box is seen in Figure C3. The outer mesh boundaries were extended beyond the surface of the BLS to provide a large region into which the air moving through the vents can exhaust and to place the computational boundaries at a sufficient distance from the BLS to eliminate any potential spurious reflections from the boundary surfaces. The point spacing was reduced to 0.5 in. around the vents and Cascade to accurately capture the flow around the edges associated with each. This spacing was chosen because the walls of the BLS were modeled as 0.5-in. thick; therefore, this was the coarsest spacing that would accurately capture the flow around the edge. For the final meshes, no planar or axial symmetry is assumed so all three meshes are fully 3-D.

Modeling the striker mechanism and grill

The grill and striker were both modeled as separate entities to simplify grid generation. Modeling these as separate bodies made the overall grid generation easier with the added bonus that both the grill and striker could be added or removed without compromising the rest of the BLS.

Figure C3. BLS 8-ft×8-ft C2SQ configuration with box, mesh in Z=0 plane.



The striker geometry was modeled using a variety of methods. The section with arms was made using trimmed circular surfaces. The needle was made as a thin cylinder without a point. The point could have caused trouble with the grid size, so it was not modeled. The spring mechanism on the other side of the striker was also modeled as a solid cylinder due to the complexity of making a helical spring. The point spacing around the striker was defined as 0.125 in. because a small distance between the striker arms and the wall of the CVC section was required, and 0.125 in. was already the required spacing of the grill; theoretically, a point spacing of 0.125 in. was the smallest value that could be used without significantly slowing down the calculation. The mesh around the striker along with the driver, grill, and initial vents along the plane of symmetry can be seen in Figure C4. A close-up view of the mesh around the striker is shown in Figure C5. Figure C6 shows the mesh at the striker face looking upstream.

The grill surface geometry was developed by first creating the front face of the grill as a composite surface composed of many smaller surfaces. This group of small surfaces was then copied to form the back face of the grill. Finally, all the surfaces that connect the two faces were defined. The spacing around the grill was restricted to the 0.125-in. thickness of the grill walls. This is similar to how the spacing around the vents was defined; the

flow will move past the forward and backward faces of the grill in one cell. Also, the grill was spaced one cell width away from the BLS inner wall because of issues that occurred with attempts to physically attach the grill to the wall. The mesh around the grill can be seen in Figure C7.

Figure C4. Driver section, computational grid showing striker, grill, and vents.

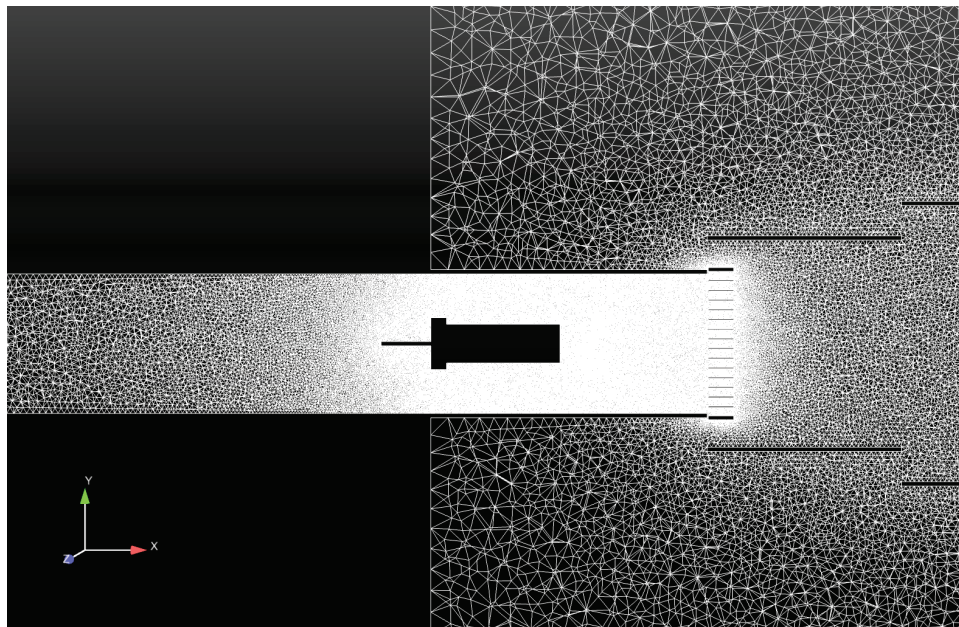


Figure C5. Close-up of computational grid around the striker mechanism.

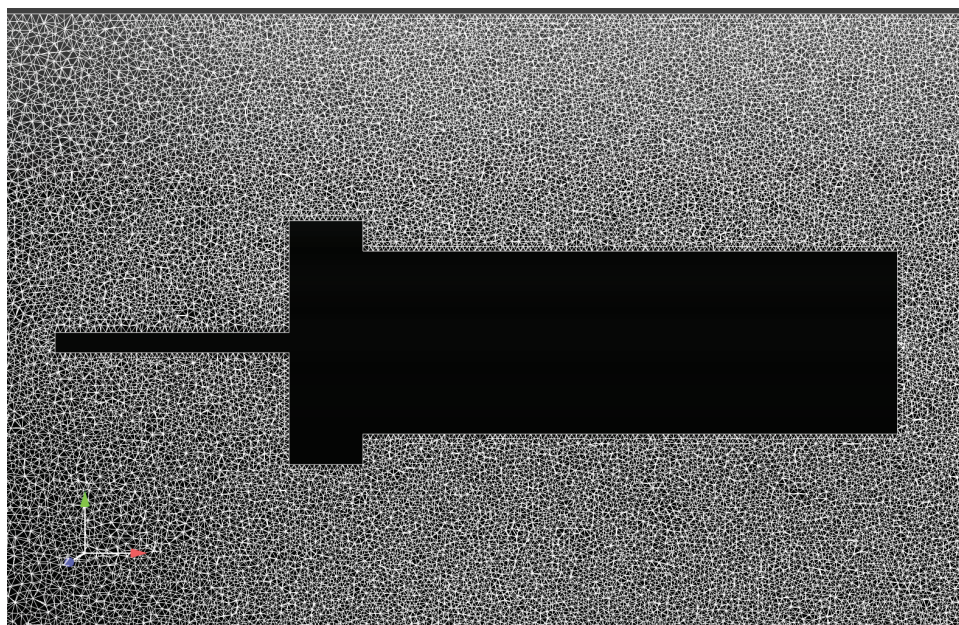
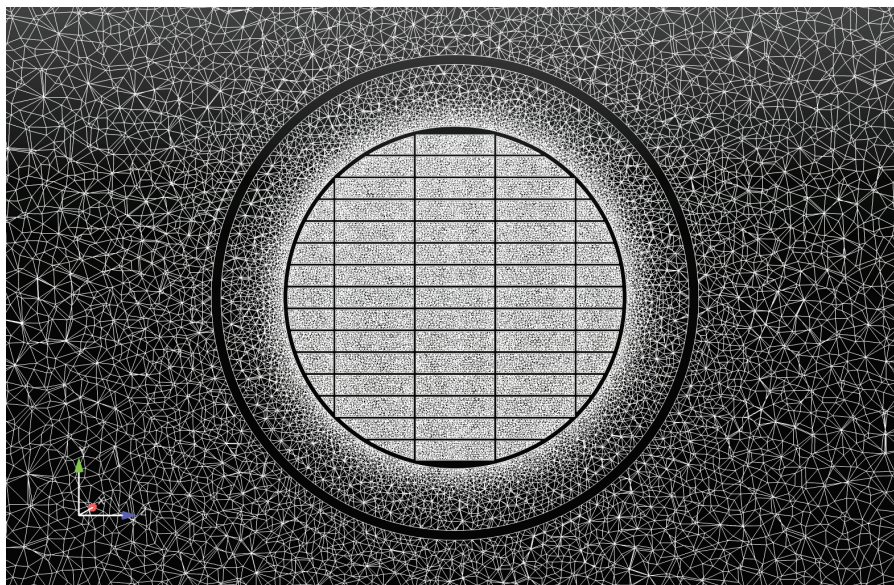


Figure C6. Cross section of computational grid around the striker mechanism.



Figure C7. Computational grid around grill looking toward driver section.



Case specific mesh modifications and sizes

The mesh used in the initial GSA configuration calculations was reduced from 101 million to 52.4 million cells for the final run. It included the addition of the models for the striker and grill that were neglected in the original mesh. The side-on pressure gauge and its mounting rod were not modeled. Instead, a Loci/BLAST data probe location was specified that corresponded to the location of the side-on gauge.

The computational mesh for the 8-ft×8-ft C2SQ configuration (no box) consisted of 73.1 million cells. The mesh was generated using the geometry initially developed for the 8-ft×8-ft configuration with box and had further refinements around the striker and catch grill. An attempt was made to model the side-on gauge assembly used in the 8-ft×8-ft C2SQ configuration without box tests; however, the mounting rod for the gauge was not included due to problems with modeling the attachment of the rod to the disk and the entire assembly to the BLS wall. Instead, the side-on gauge disk was fixed in space and floats in the flow path. This helped reduce the complexity of the mesh in the region around the gauge and also reduced the overall size of the mesh at the expense of some uncertainty in the results due to neglecting the mounting rod.

For the third case, the box was formed by first creating the five wetted surfaces of the box and then trimming the four vertical faces of the box with the BLS floor. The point spacing around the target box was chosen to be 0.5 in. A close-up view of the mesh around the box is shown in Figure C8. This mesh contained approximately 69.9 million cells.

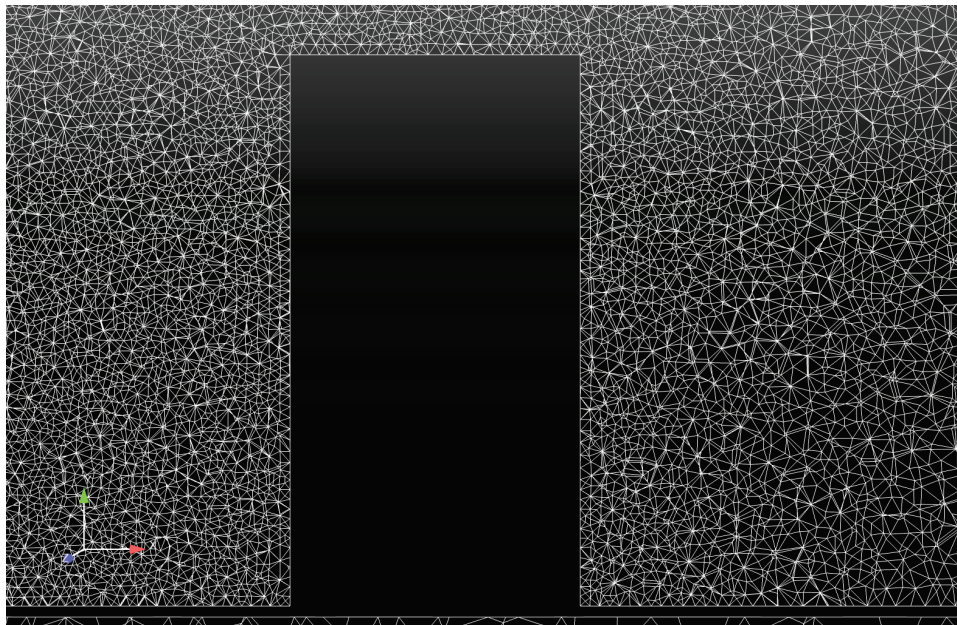
Initial conditions

An initial absolute pressure of 1312.7 psi (1298 psig) was specified for the driver section. Driver and ambient temperatures were set to 77°F. Ambient pressure in all other regions of the mesh was set to 14.7 psi. Initial values of density were computed from the specified pressure and temperature using an ideal gas EOS.

Boundary conditions

A second-order reflecting boundary condition in which values in ghost cells used to implement the boundary condition are obtained by reflecting adjacent interior values is imposed on the exterior boundary surfaces, the BLS walls, the striker assembly, and the catch grill.

Figure C8. Computational grid along plane of symmetry, around box.

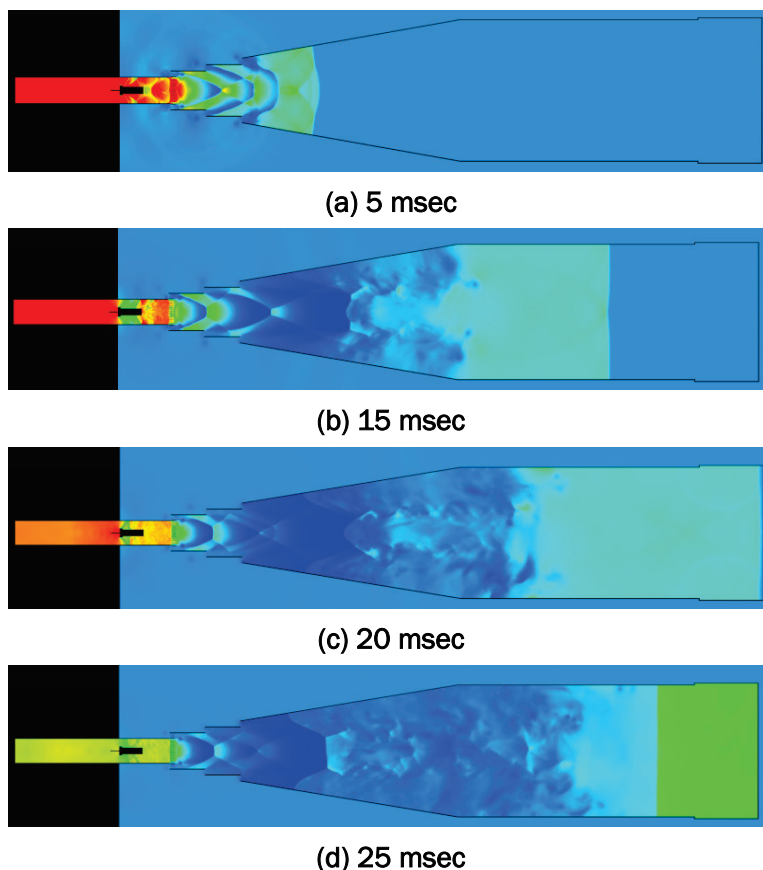


GSA configuration, calibrations Tests 30a and 30b

The GSA configuration simulations were run on the MSU HPC Shadow cluster using 200 processors. The full simulation consisted of several runs with restarts and ran to a simulation time of about 70 msec. Total wall clock time for the simulation was 156.53 hr. Loci/BLAST computes a gross estimate of parallel efficiency, which averaged around 88 percent for the GSA configuration simulations on Shadow.

The results for this case were first analyzed to verify that a planar shock front was formed in the test section. Pressure contours along the plane of symmetry and the magnitude of the gradient of the density field that provides Schlieren-like images were used to visualize the formation, the movement of the planar shock wave, and the complex flow field through the driver, striker, grill, and CVC sections. These images were generated using the Ensight 3-D visualization tool. Pressure contours normalized by the maximum reflected pressure at the end plate at select times are shown in Figure C9. At 5 msec, the shock front has exited the CVC section and is about one-quarter the distance into the conical section.

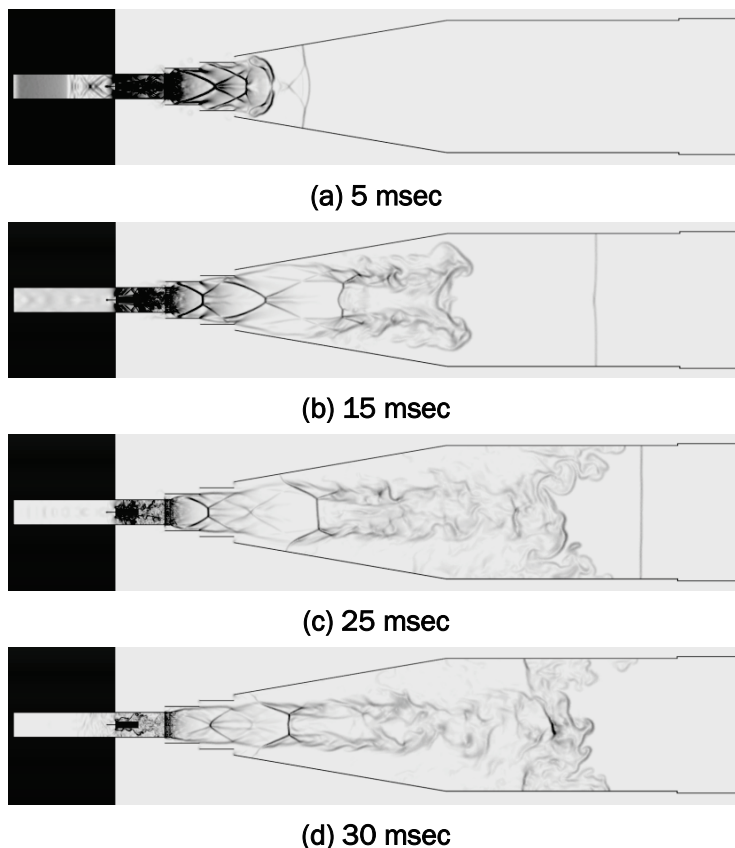
Figure C9. GSA configuration pressure contours.



The shape of the shock front is slightly bulged along the centerline and is normal to the BLS wall. High-pressure gas is still moving through the striker and grill. The flow field through the vent system is extremely complex with multiple oblique shocks being formed. At 15 msec, the shock front is about three-quarters the way down the constant area section. A planar shock front is clearly seen at this time. At about 20 msec, the shock front has reached the target wall and is reflected back. At 25 msec, the reflected shock is moving upstream and has reentered the constant area section. The reflected shock continues to move upstream until it interacts with the residual driver gases.

The Schlieren-like images shown in Figure C10 give an alternative view of the complexity of the flow field during all phases of the calculation. In particular, the interaction of the oblique shocks generated by the flow through the vents is clearly seen. At 5 msec, the oblique shocks around the vents are clearly distinguished. A planar shock in the constant area section is seen at 15 msec. The oblique shocks from the vents are merging into barrel-like shock structures that are moving into the conical section. At

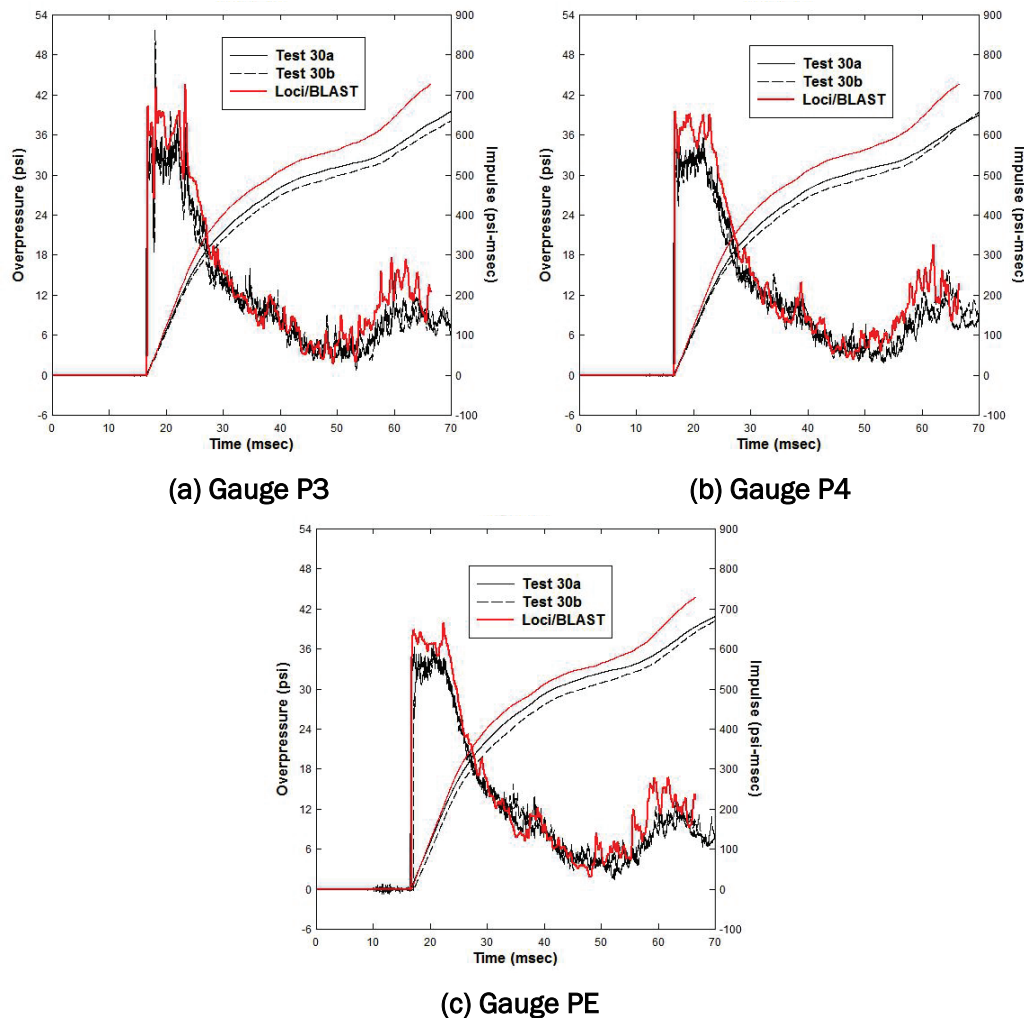
Figure C10. Density gradient magnitude contours, GSA configuration.



25 msec, the reflected shock is seen to be moving upstream and is about to interact with the high-pressure driver gas moving downstream. At 30 msec, the reflected shock has interacted with the driver gas and lost all structure. The resulting flow field at this time is highly complex and most likely consists of areas of highly turbulent flow with localized vortices. Since this simulation is inviscid, the turbulent nature of the flow field and any shock-boundary layer interactions are not captured. Therefore, the actual flow field will be different.

Next, the Loci/BLAST results were compared with the measured data at the P3, P4, and PE gauge locations (see Figure C11). The computed results were time shifted by -3.4 msec to match the measured arrival time. As seen in the figures, Loci/BLAST tends to overpredict the initial peak pressure. There are also small differences after 50 msec. These differences show up in the computed impulse, where the second peak is slightly overpredicted. Even with these differences, one notes good overall agreement with the measured data. The differences are probably due to variations in mesh densities in the areas around the gauge locations.

Figure C11. Time-shifted gauge comparisons for Loci/BLAST, GSA configuration.

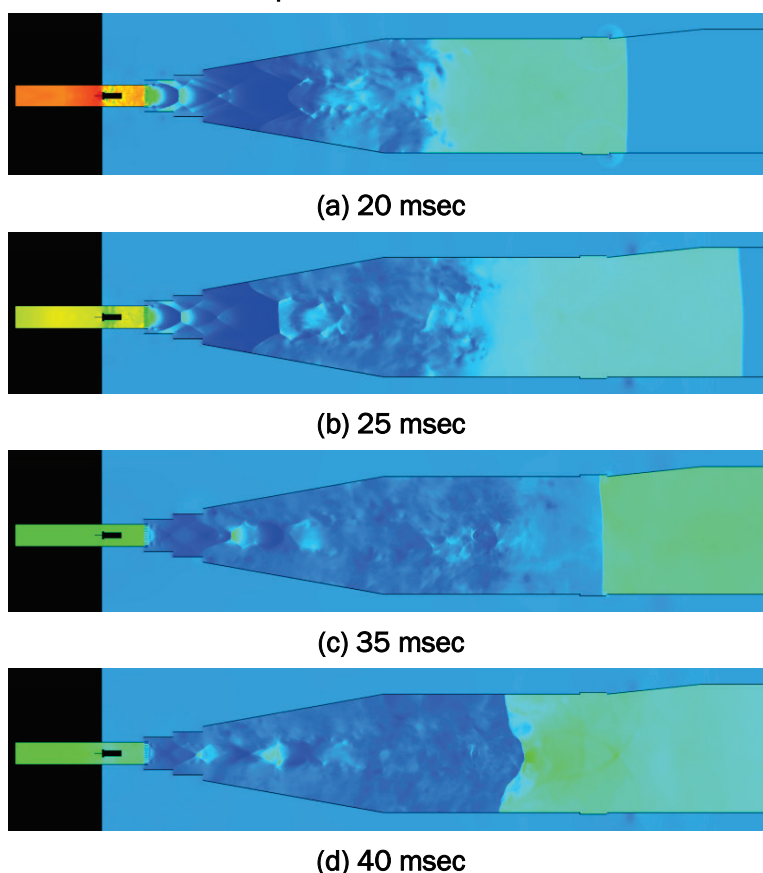


Calibration tests with 8-ft×8-ft C2SQ configuration

The Loci/BLAST calculation for this case was run on the MSU HPC Shadow Cluster using 200 processors. As previously stated, two additional geometric components were added to the GSA configuration for this case. The first is the addition of the C2sQ and SQ1 sections. The second is an approximate model of the side-on pressure gauge assembly. The analysis of this case consisted of a series of restarts that were terminated at a simulation time of about 70 msec. Total wall clock time for the simulation was 194.94 hr. The average parallel efficiency estimate was 88 percent. As in the GSA simulation, visualization of pressure contours and density gradient magnitude along the plane of symmetry were used to track the movement of the planar shock through the BLS and to examine shock

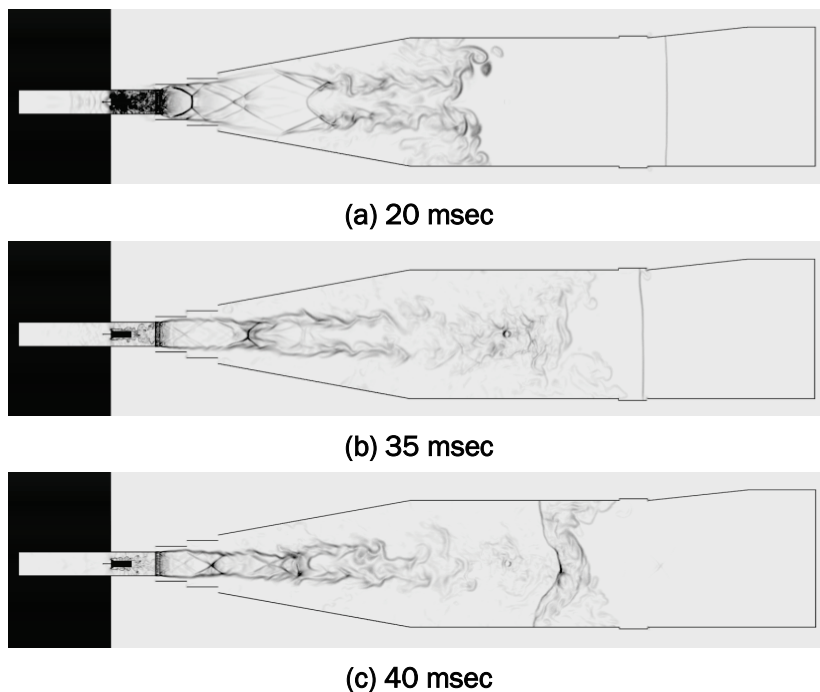
interaction with the driver gas. Pressure contours at select times are shown in Figure C12. Results at previous times were identical to the GSA simulation results. At 20 msec, the planar shock is seen to have moved through the Cascade and into the C2SQ transition section. The shock wave is approaching the back end of the SQ1 section at 25 msec. The reflected shock wave is moving upstream at 35 msec and has exited the C2SQ transition section. At 40 msec, the reflected wave has moved into the GSA section and is interacting with the driver gas moving downstream.

Figure C12. 8 ft×8 ft C2SQ configuration pressure contours.



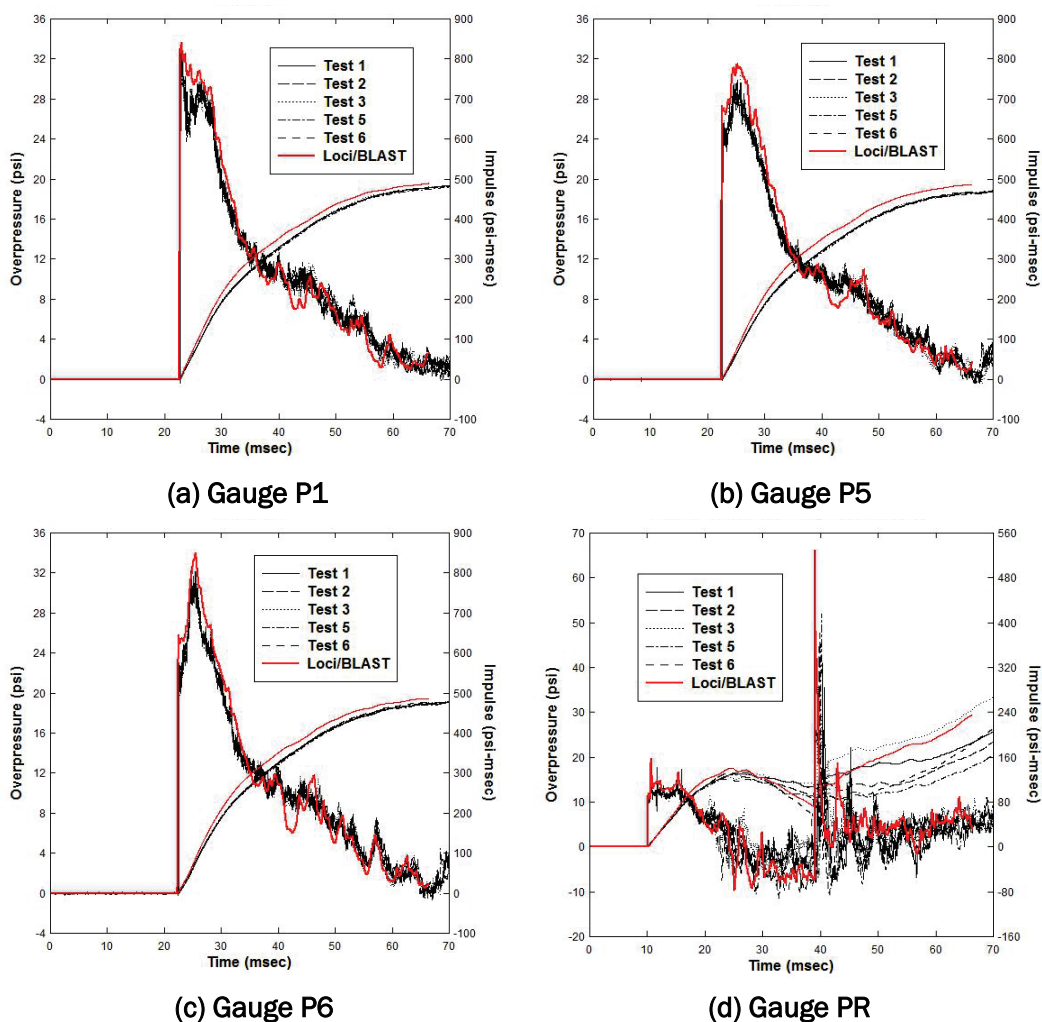
Schlieren-like images are shown at select times in Figure C13. As with the first case, these images illustrate the complexity of the flow field particularly when the reflected shock interacts with the driver gas. The incident shock wave at 20 msec and the reflected wave at 35 msec are clearly seen. At 40 msec, the reflected wave is being eaten away by the driver gases along the BLS centerline. The existence of density gradients downstream of the interaction again indicates the complexity of the flow field in this region.

Figure C13. Density gradient magnitude contours, 8-ft×8-ft C2SQ configuration.



The calculated pressure-time-histories and corresponding impulse are compared with measured data in Figure C14. The computed results were time shifted by -3.6 msec to match the measured arrival time. Comparisons are made for the P1, P5, P6, and PR (side-on) pressure gauge locations. The Loci/BLAST results for gauges P1, P5, and P6 are in excellent agreement with the measured data. The initial peak pressure and rise time are very close to that measured. The computed waveforms at these gauges are almost identical to the experimental results except for small variations in the pressure oscillations. The integrated impulse also compares well. Similar results are also obtained for the side-on gauge PR. The biggest anomaly is the large overprediction of the pressure spike around 40 msec. Other than this anomaly, Loci/BLAST is seen to provide an accurate prediction of the waveform for the side-on gauge.

Figure C14. Time-shifted gauge comparisons, 8-ft×8-ft C2SQ configuration.

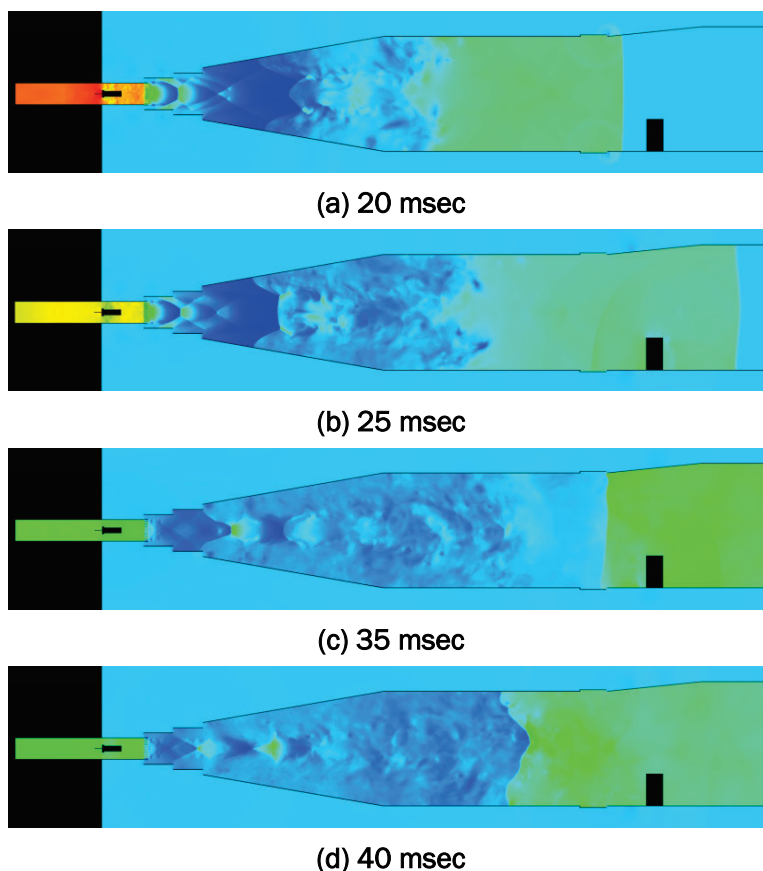


BLS 8-ft×8-ft C2SQ configuration with box

The Loci/BLAST calculation for this case was started on the MSU HPCC Talon system. When the Shadow system became available, it was restarted on Shadow and run out to a simulation time of around 65 msec. The calculation ran for 47.5 hr on Talon using 192 processors and 214.2 hr on Shadow using 200 processors for a total run time of 261.7 hr. However, the XEON processors used on Shadow are at least twice as fast (probably more) as the processors used on Talon, and the time required to run the entire problem on Shadow is estimated to be about 238 to 240 hr of wall clock time. The average parallel efficiency was about 88 percent on Shadow.

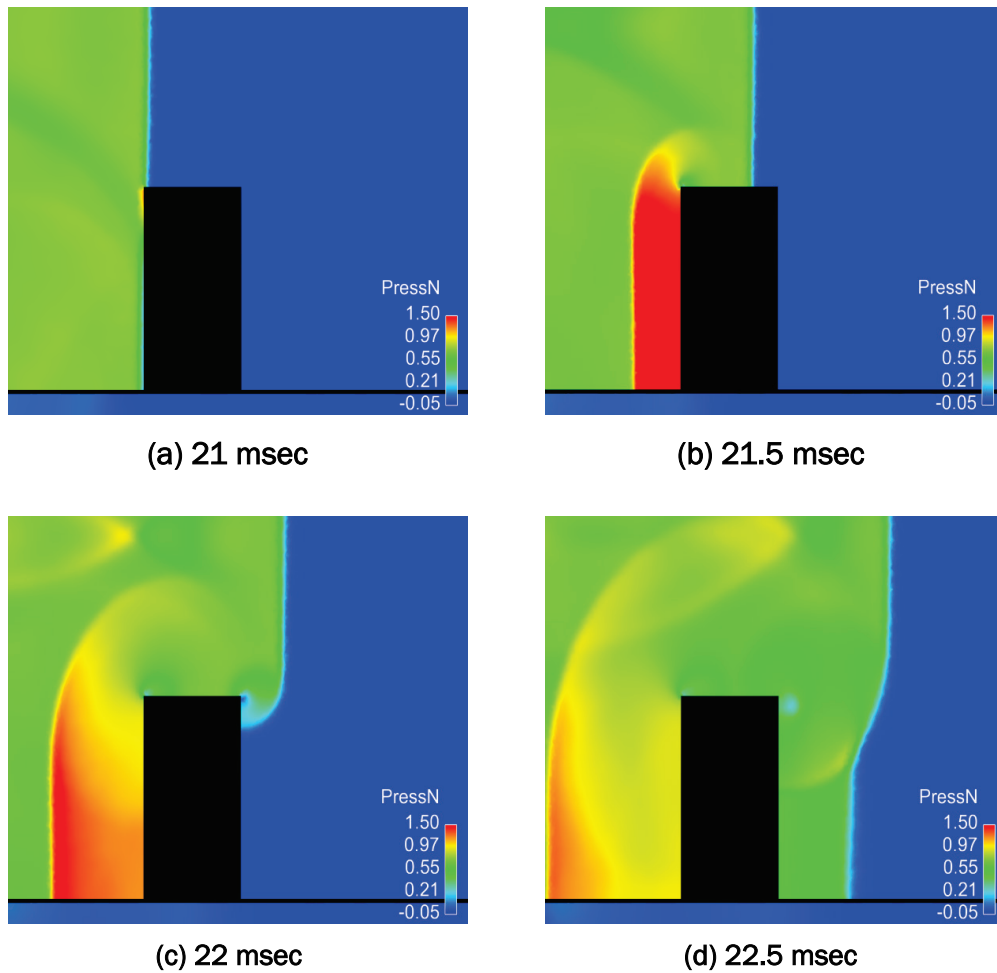
As with the other test cases, pressure contours and density gradient magnitude contours were plotted to track the shock movement through the BLS and to visualize the complex flow field around the box when both the incident and reflected shock waves intersect and pass over it. The pressure contours are for pressures normalized by an estimate of the peak reflected pressure on the face of the target at pressure gauge PF3. Figure C15 shows the pressure contours at select times. Comparison with the results from the second case suggests that the box had little effect on the location of the incident and reflected shock at the same simulation times.

Figure C15. Pressure contours, 8-ft×8-ft C2SQ configuration with box.



The Schlieren-like images for this case showed similar results for the incident and reflected waves as seen in the second case. In order to get a more detailed view of the interaction of the incident and reflected shock waves with the box, close-up views of the pressure contours were made for times during which the incident and reflected shocks passed over the box. The images for the incident shock wave are shown in Figure C16. The pressure in the figure has been normalized, based on the peak pressure on the front

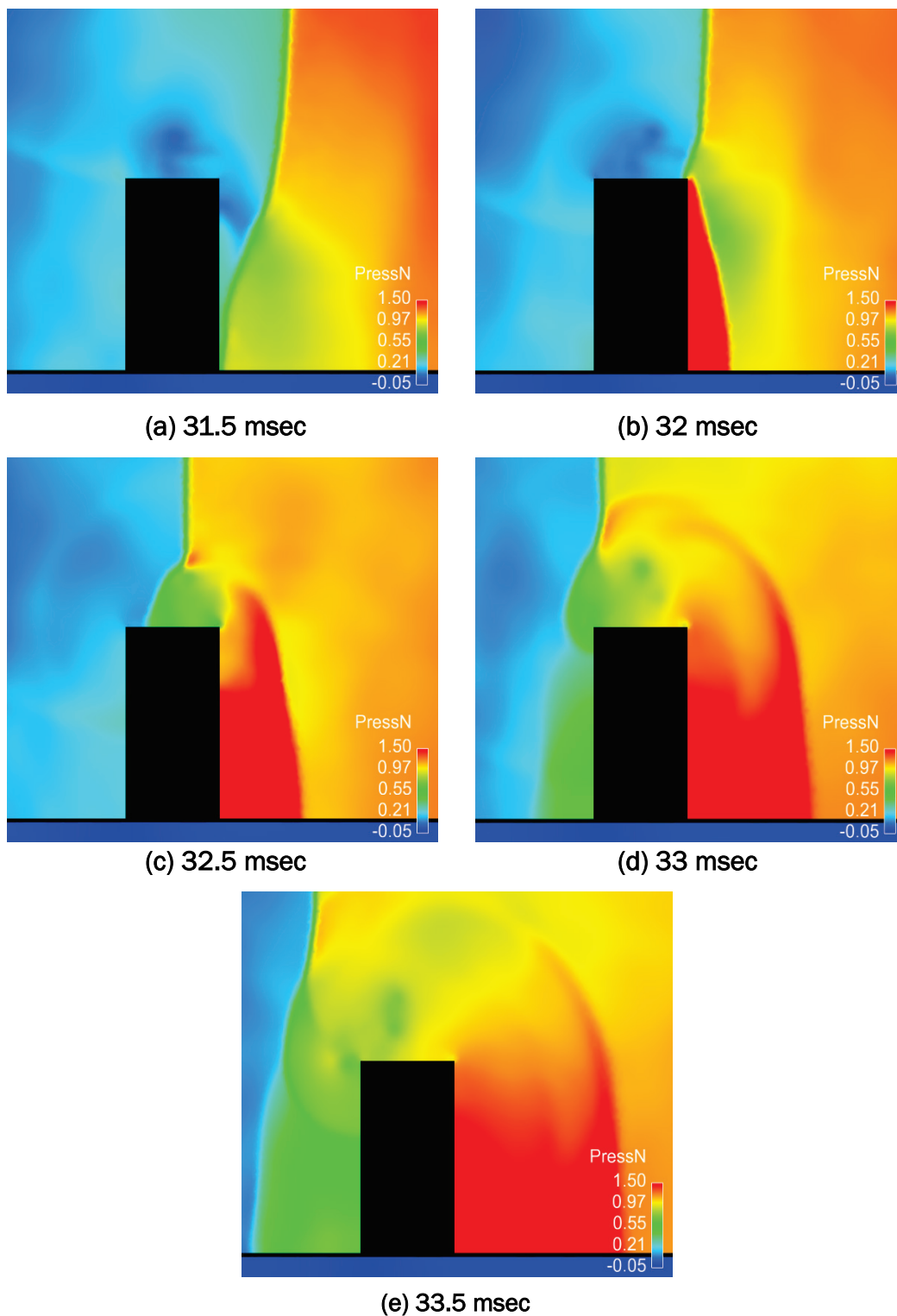
Figure C16. Contours of incident shock pressure around box.



face (specifically with respect to gauge PBF3). The passage of the shock over the box along with the reflection off of the front face and reformation of the shock after it passes the back face of the box are clearly seen. The shock front moves around the box reaching the top edge of the back face around 22 msec. After passage, the bottom half of the shock lags the upper part with a noticeable bend around the upper back edge of the box. The reflected wave from the front face is seen to rapidly move upstream and begin to lose strength as it moves toward the driver.

Similar images were generated for the interaction of the primary reflected wave with the box. Figure C17 shows the pressure contours in the vicinity of the box at select times. The pressure in the figure has been normalized based on the peak pressure on the front face (specifically with respect to gauge PBF3). As with the incident shock interaction, the primary reflected shock also produces a secondary reflected shock that moves downstream

Figure C17. Contours of reflected shock pressures around box.



from the back face of the box. As the primary reflected wave moves over the box it assumes a bow-like shape due to interaction with the box. It eventually returns to a more planar shape as it moves upstream out of the

transition region until it begins to interact with the driver gas, after which it loses a coherent shape.

Computed pressure-time-histories and resulting impulse were compared against the measured data at several gauge locations on the front, back, top, left, and right side faces of the box. In addition, comparisons were drawn against P3 and P9 gauges located on the target wall. The computed results were time shifted by -3.1 msec to match the measured arrival time. The results for front face gauges are shown in Figure C18. The correlation with the measured data are excellent. The computed waveform shapes are similar to that measured for all gauges except PBF6, where Loci/ BLAST is seen to slightly overpredict the incident peak pressure. Overall, the secondary shock at 30 msec is accurately captured with only minor differences noted after 50 msec.

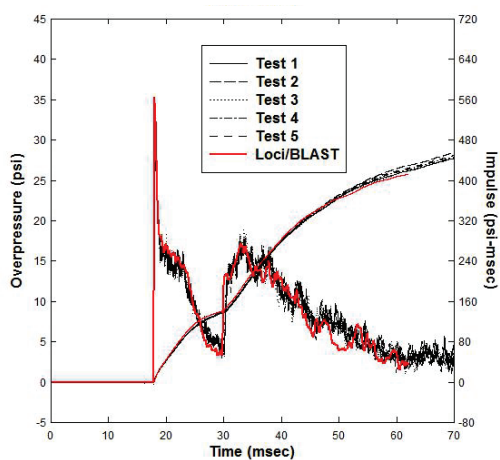
The results for the back face gauges are shown in Figure C19. The correlation with the measured data are also excellent. As with the front face gauges, the overall waveforms are accurately predicted with the largest variation seen in the results for PBB2 and PBB4 where the peak pressure is slightly overpredicted; however, this has little effect on the integrated impulse.

The results for the left face gauges are shown in Figure C20. The excellent correlation with experimental data seen in the front and back face results are repeated for PBL1 and PBL2. There are no comparisons for PBL3 and PBL4. Following the analysis, it was found that these gauges were misplaced in the model. The setup assumed symmetry of the gauge positioning for the right and left sides; however, this was not the case in the experimental setup where the third and fourth gauges were asymmetric for the two sides.

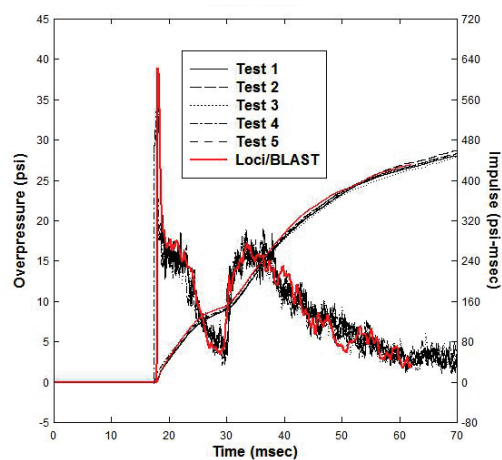
The results for the right face gauges are shown in Figure C21. All of these gauges were correctly placed in the model and match the locations in the experimental setup. Once again, the computed waveforms are similar to the measured ones.

Figure C22 provides a comparison for the gauges on the top face. Once again, good correlation is noted with the measured data. Peak pressures are extremely close for all gauges along with the impulse.

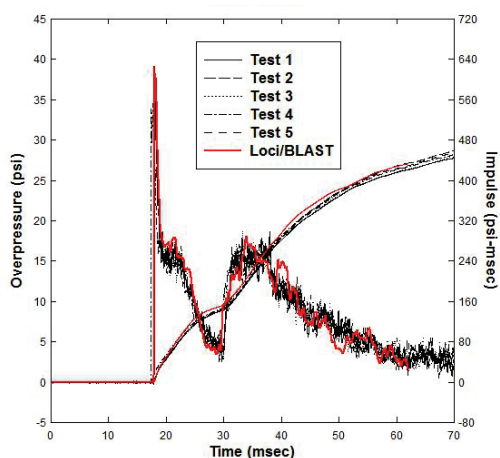
Figure C18. Time-shifted gauge comparisons for Loci/BLAST, front face.



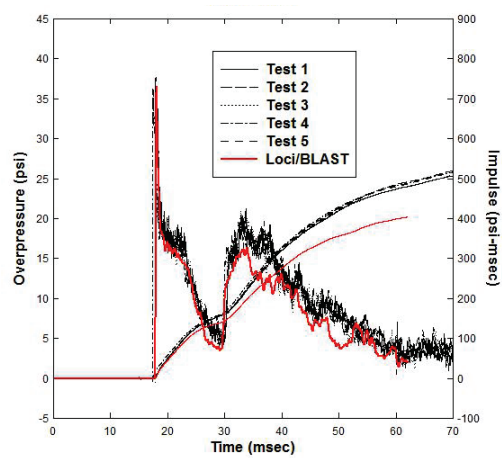
(a) Gauge PBF1



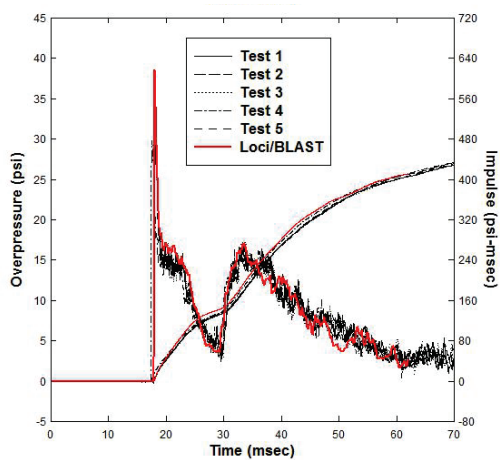
(b) Gauge PBF3



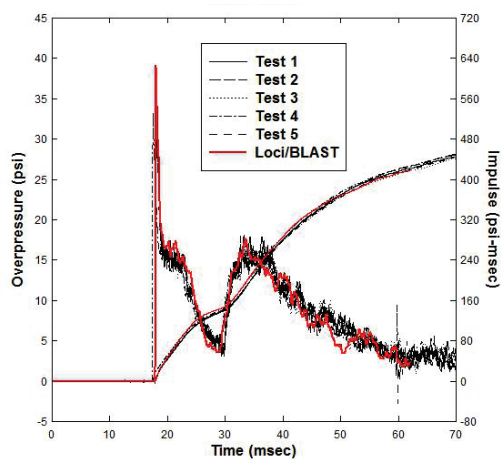
(c) Gauge PBF5



(d) Gauge PB6

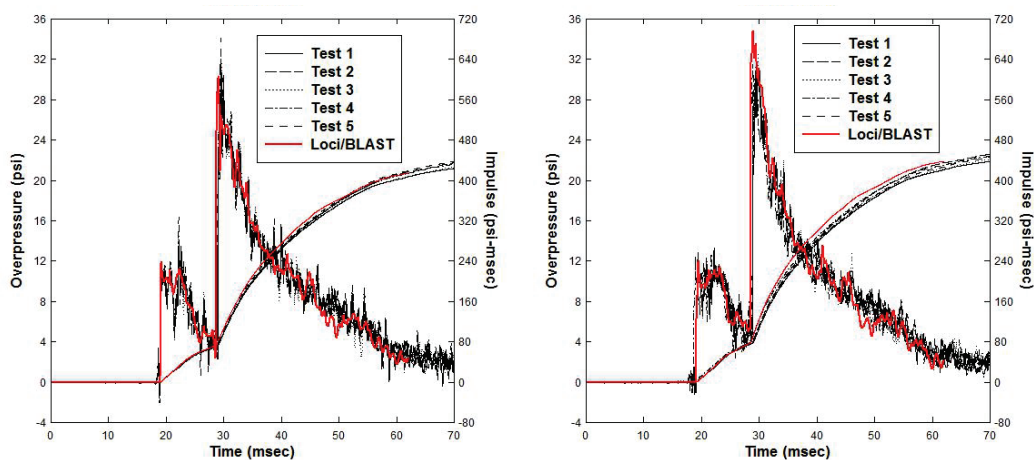


(e) Gauge PBF7



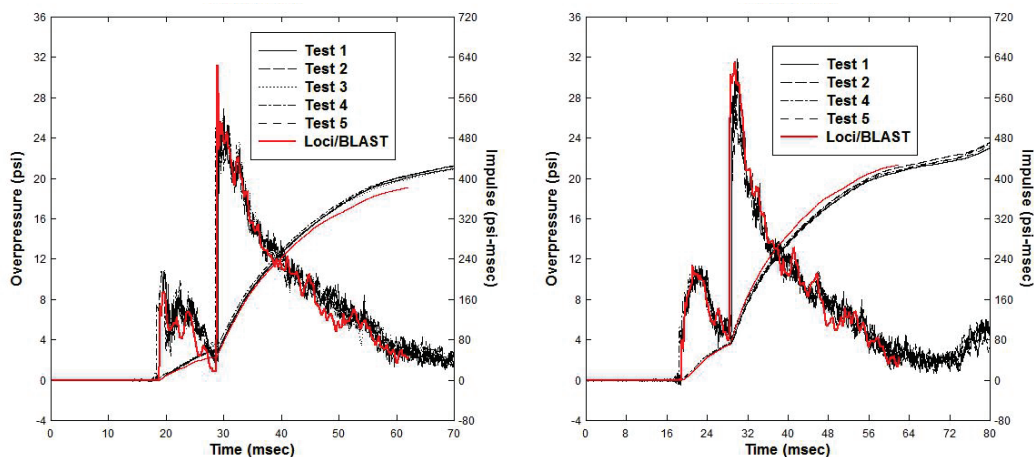
(f) Gauge PBF8

Figure C19. Time-shifted gauge comparisons for Loci/BLAST, back face.



(a) Gauge PBB1

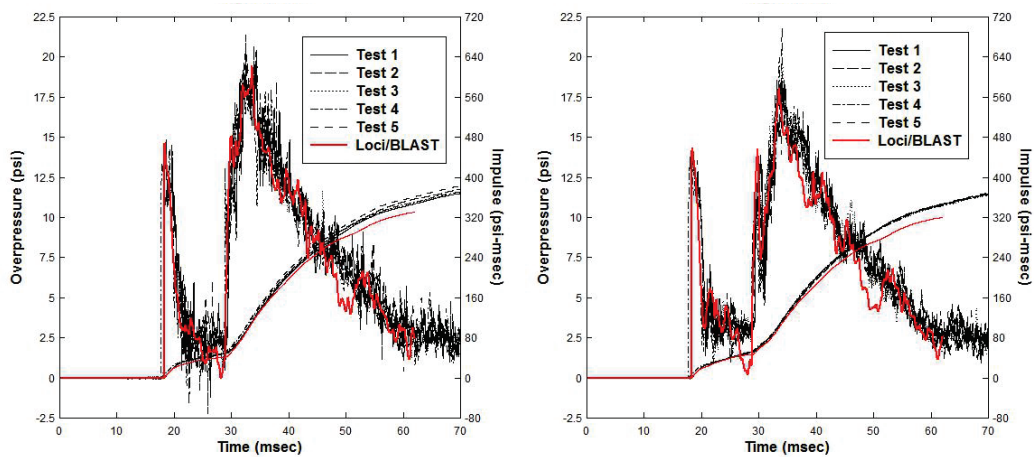
(b) Gauge PBB2



(c) Gauge PBB3

(d) Gauge PBB4

Figure C20. Time-shifted gauge comparisons for Loci/BLAST, left face.



(a) Gauge PBL1

(b) Gauge PBL2

Figure C21. Time-shifted gauge comparisons
for Loci/BLAST, right face.

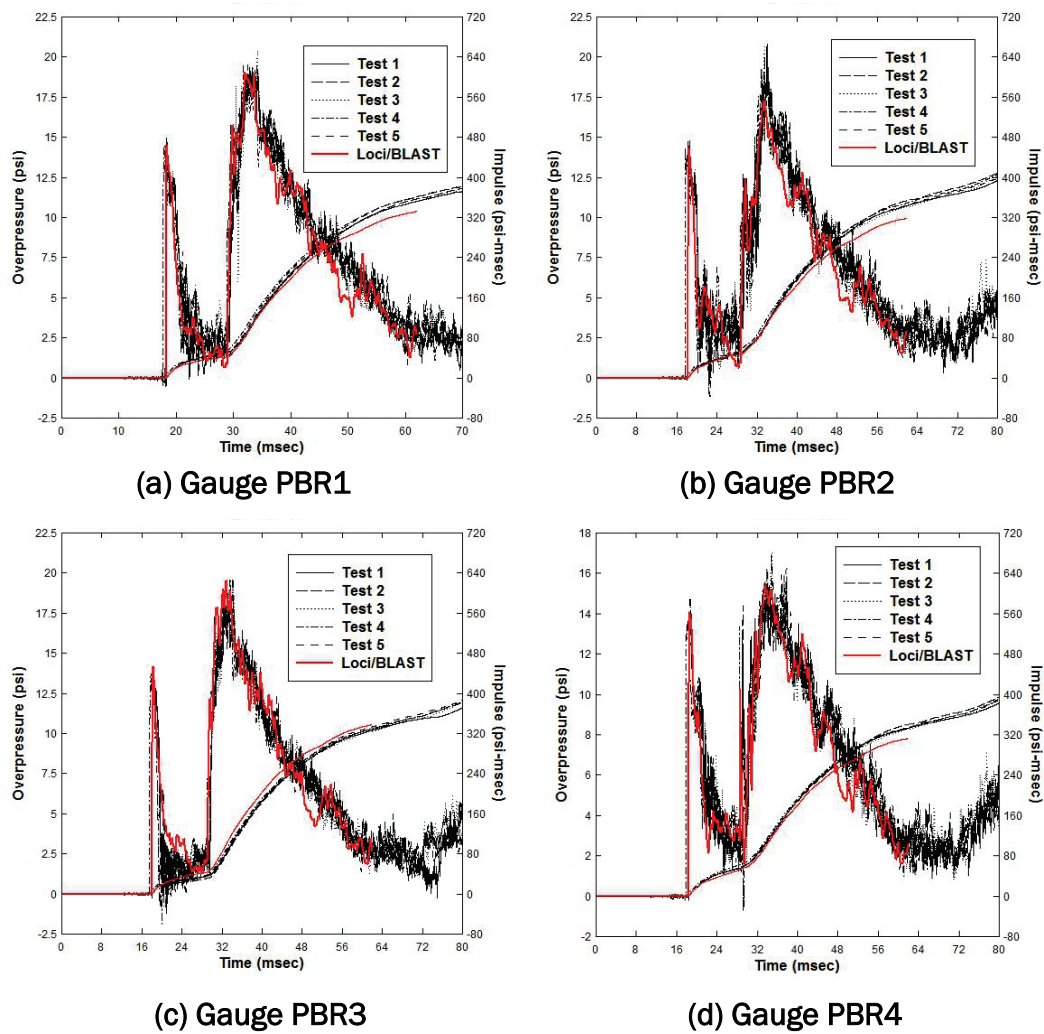
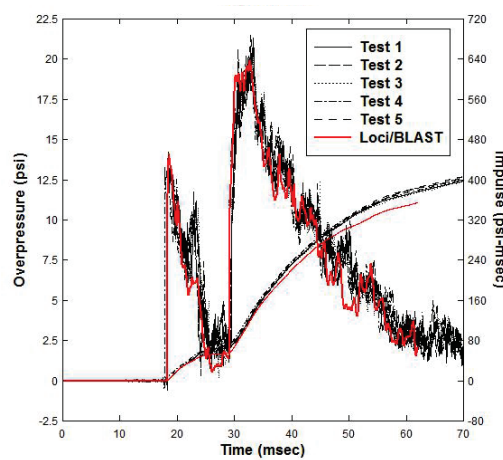
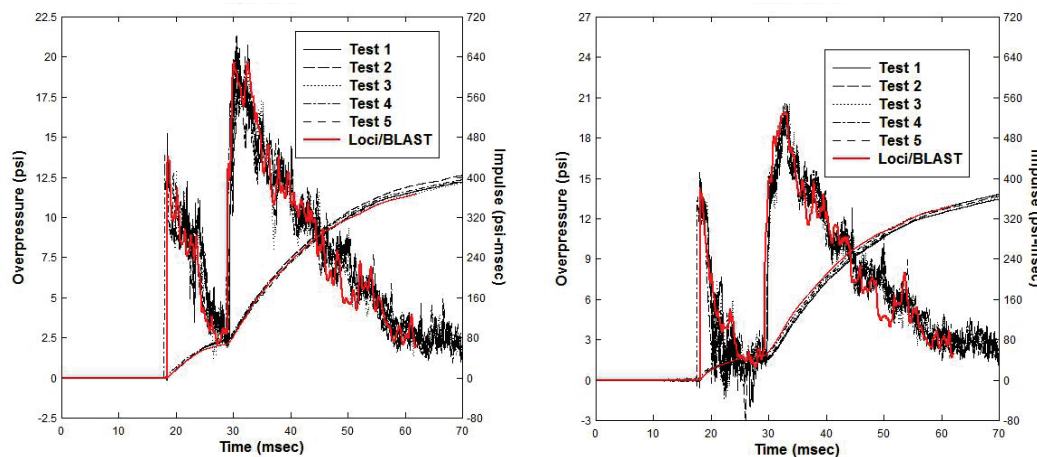
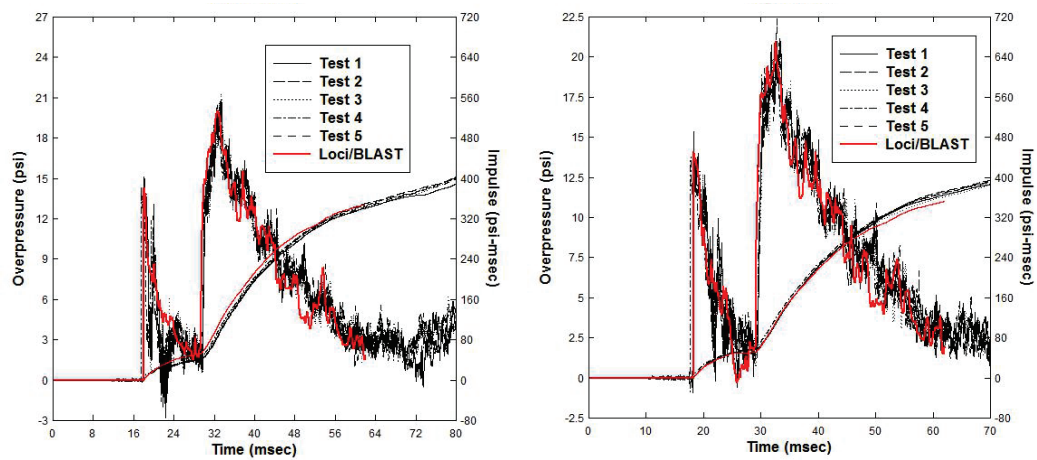
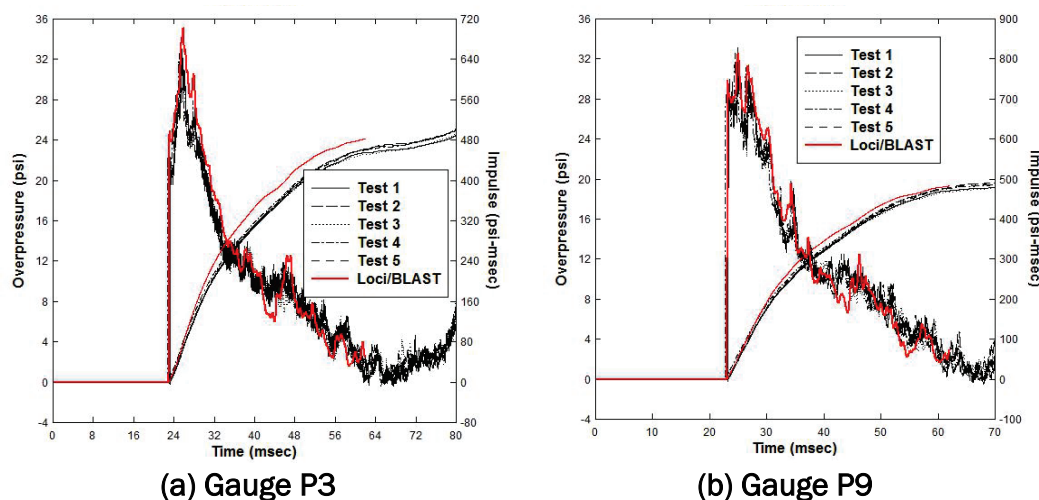


Figure C22. Time-shifted gauge comparisons
for Loci/BLAST, top face.



Finally, the comparisons for gauges P3 and P9 are shown in Figure C23. The computed results for the P3 gauge overpredict the peak pressure but still captures the measured waveform with good accuracy. The results for the P9 gauge are in much better agreement than the P3 gauge. Again, the measured waveform shape is accurately reproduced.

Figure C23. Time-shifted gauge comparisons for Loci/BLAST, target wall.



Conclusions and recommendations

The MSU Loci/BLAST code was used to successfully simulate the 3-D flow fields in the ERDC BLS for three different experimental configurations. Correlations were made with measured pressure-time-histories and impulse values at a variety of gauge locations. In general, the quality of the comparisons ranged from very good to excellent. In particular, the results for the 8-ft×8-ft C2SQ configuration with box demonstrated that Loci/BLAST can accurately reproduce both incident and reflected planar wave interactions with the box. In most cases, the calculated waveforms were similar to the measured ones. These results indicate that Loci/BLAST is an excellent candidate for future BLS analyses and related airblast analyses.

Based on these results, the following recommendations have been made. The grid size used in the current simulations varied from about 50 to 70 million cells. A much larger mesh needs to be generated and run on the ERDC HPC systems to quantify the improvements in accuracy that can be obtained by a much finer mesh. This will also allow us to investigate the parallel scalability of Loci/BLAST and Loci/CHEM for both BLS analyses

and large-scale airblast problems. Since all the simulations in the current research were inviscid and neglected important viscous effects such as turbulence and shock-boundary layer interactions, a viscous analysis should be attempted in the next phase of this project. The excellent correlations obtained with the inviscid solutions indicate that these effects might be secondary for the current test cases. However, viscous effects still need to be examined to quantify under what circumstances they become important.

Appendix D: RAGE Modeling

RAGE background

The Radiation Adaptive Grid Eulerian (RAGE) code was developed by Leidos, formerly Science Applications International Corporation (SAIC) (Gittings et al. 2008). There was no user manual available for RAGE; however, there was a draft manual and example problem set available for a companion code, the SAIC Adaptive Grid Eulerian (SAGE) (Archer et al. 2005). SAGE has been in use at ERDC for many years, and there is considerable in-house experience modeling high explosive events with this code. This provided a launching point for running RAGE. Fortunately, both SAGE and RAGE shared a common set of input commands and structure. This made the transition from running SAGE to RAGE fairly seamless. The ensuing discussion of RAGE draws upon that in Gittings et al. (2008) and Archer et al. (2005), as well as our past experience with SAGE at ERDC.

One should note that there are actually two versions of RAGE, one maintained by Leidos and the other by Los Alamos National Laboratory (LANL) (Clover 2015). The Leidos version of RAGE was utilized for all calculations discussed herein. The development path for the code base appears to have split in the 2006 time frame. All calculations discussed herein were conducted on the ERDC HPC platform Garnet using Version 20110102.000, which was installed by Leidos at the onset of this project. Garnet is a Cray XE6 that has 4,716 compute nodes with 32 cores per node. Each compute node has a core speed of 2.5 GHz and 64 GB of accessible memory.

RAGE is a multidimensional, massively parallel code that uses a two-shock or single-intermediate-state approximate Riemann solver in the shock capturing. Both minmod and modified van Leer slope limiters are available for use in calculating gradients across cell faces. The latter sets the flux limiter to 1.5 and has the benefit of reducing ringing behind the shock front. RAGE has the ability to handle multi-material cells and a robust adaptive mesh refinement (AMR) capability. The AMR capability was of great interest in this work, as a fine resolution is desired when modeling shock propagation.

All RAGE calculations are conducted on a structured block mesh composed of rectangular cells, i.e., a mesh of fixed spacing along the Cartesian

axes. The number of cells assigned to a particular axis can vary; however, the cell count must be even to support AMR. The code supports 1-D, 2-D, and 3-D problem setups, all within the same architecture. It uses an h-adaptive approach in the mesh refinement, where cells are split and/or joined uniformly based on an indicator. All mesh adaption is conducted subject to a 2-to-1 refinement rule. This rule requires that the level of refinement not differ by more than one level between adjacent cells. This rule applies to both refinement and unrefinement. The mesh adaption is continuous in both space and time, with cell adaption triggered based on changes in state data, e.g., velocity or pressure, between cells or via estimates of the first-order truncation error (Gittings et al. 2008). Details on the indicator thresholds were not available. Based on our personal experience with the code, it appears the refinement strategy is geared towards shock-following.

For structured Eulerian codes, boundary conditions are applied to the mesh extents, rather than individual materials. The available documentation indicated that only reflective boundary conditions are supported. Further discussion with Leidos indicated that outflow boundary conditions were available as well; however, these were not suited to the particular setup chosen for the BLS, which involved the use of rigid materials (Clover 2015). Thus, the analysis setup relied on reflective boundaries at the mesh extents. This boundary condition type can lead to artificial reflections from the mesh extents that can affect the solution later in time. The only way to avoid this is to extend the mesh well beyond the physical bounds of the BLS. This helps mitigate any artificial reflections at the cost of additional computations on the extended mesh.

Materials are inserted into the mesh to develop the problem setup. This generally takes the form of overlaying primitive objects (blocks, cones, and spheres for 3-D problems) to build up a desired geometry. The order of the overlay process determines whether a material is inserted (added) or masked (cutout). The walls of the BLS were modeled as rigid (non-responding) materials. The surrounding air was modeled as a hydrodynamic material. It should be noted that RAGE supports geometry import from a CAD package; however, this capability was not utilized for the calculations discussed herein.

The Leidos version of RAGE used in these analyses does not have a material interface reconstruction algorithm. The consequence is that increased

resolution may be needed to ensure that the thin shell of the BLS structure is captured in the modeling. Meeting this resolution requirement can lead to excessively long run times that are intractable for 3-D analyses. It is not just a matter of resolving the shell thickness, but also the need to resolve the shell along the full length of the BLS (about 40 ft) as well as shocks traversing the extended mesh outside the BLS. The AMR capability is helpful to efficiently partition the refined regions initially; however, as the calculation progresses, the number and complexity of the shock reflections increase resulting in growth of the overall problem size. It is up to the analyst to achieve a balance between the desired mesh resolution, available computational resources, and turnaround time for the analysis.

There are two approaches for dealing with the issue of capturing the thin shell of the BLS with an acceptable resolution. The first is to modify the location of the shell structure so that the material interfaces are aligned with the cell boundaries. The second is to artificially increase the thickness of the shell structure to allow more cells to span its thickness while at a lower level of resolution. Both options were investigated; however, one should note that the ability to carry out the former is difficult given the conical nature of several BLS sections.

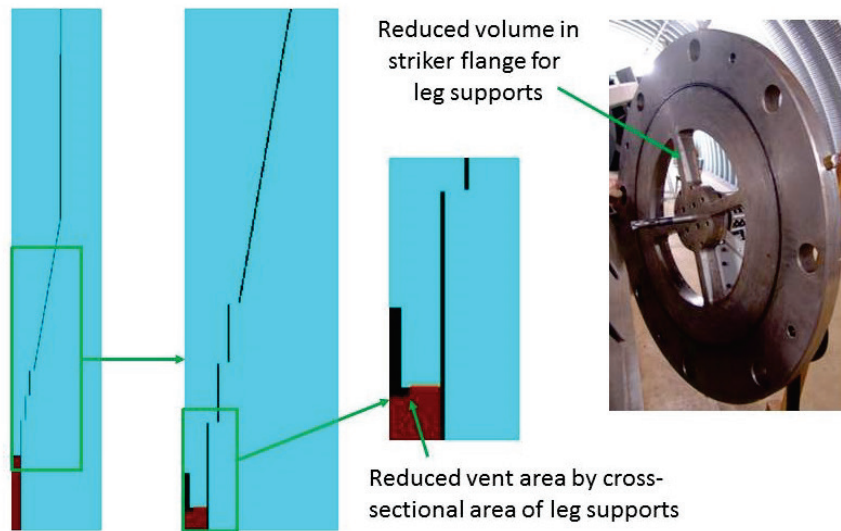
RAGE has several EOS modeling options suitable for airblast applications. These include SESAME tables for air and an extensive EOS library that covers a range of conventional explosives. The options for modeling the explosive process are limited to an ignition and growth model (Lee and Tarver 1980), which transitions the explosive from its initially unreacted to fully reacted states both described using a Jones-Wilkins-Lee (JWL) EOS. RAGE also supports an ideal gas EOS. Both the SESAME and ideal gas EOS options were of interest for the BLS modeling.

RAGE requires that all data be in the centimeter-gram-second (CGS) system of units. With this system of units, pressure is in units of dynes/cm², density in g/cm³, velocity in cm/s, and temperature in electron-volts. For presentation purposes, the RAGE results are typically cast in English units to maintain consistency with the overall report write-up. There are select circumstances where the data are presented in CGS units, mainly due to limitations in modifying plot ranges. The units will be clearly defined when this occurs.

GSA configuration, calibration Tests 30a and 30b

The initial RAGE modeling involved a series of 2-D cylindrical (2-DC) calculations. The first set of calculations involved a resolution study, while the second looked at the sensitivity of various modeling options on the predictions. The problem setup used for the 2-DC calculations is shown in Figure D1. The image represents only a small portion of the computational grid. Only the axisymmetric components of the BLS can truly be modeled in a 2-DC calculation. Consequently, neither the grill nor leg supports in the striker flange can be properly modeled. It was felt that the opening (or vent) area in the striker flange should be preserved. To do so, the diameter of the ring support at the base of the striker mechanism was artificially increased to maintain an equivalent opening area.

Figure D1. RAGE model setup for 2-DC calculations involving the GSA configuration.



The computational grid extended well beyond the BLS to minimize any effects from artificial reflections at the mesh boundaries. The initial cell size h_o was set to 64 cm for all calculations discussed herein. When invoking the AMR capability, the user must also specify the maximum level of resolution (MLOR). Once these input data are specified, one can then determine the size of the finest cell in the mesh h_{MLOR} as follows.

$$h_{MLOR} = \frac{h_o}{2^{(MLOR-1)}} \quad (D-1)$$

For the 2-DC calculations, the mesh extended out 40 cells in the axial and lateral directions with the origin defined at the base of the driver. Thus,

the mesh encompassed a physical space that was 2,560 cm by 2,560 cm (40 times h_o in either direction), with the longitudinal axis of the BLS aligned with the axis of revolution in the problem setup. The extended mesh was thought sufficient to avoid any reflections that might originate from the mesh boundaries and affect the solution later in time.

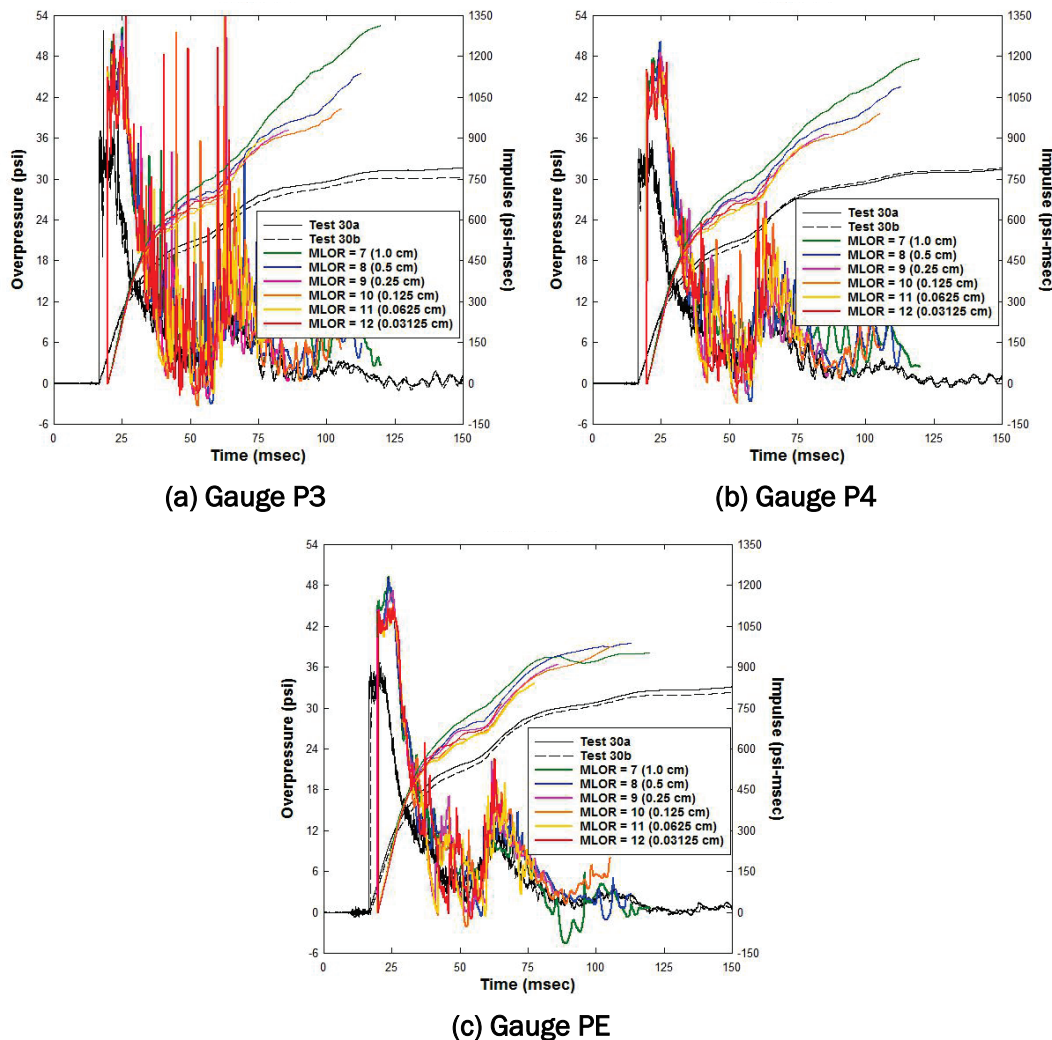
The walls of the BLS were modeled as rigid (non-responding) materials. The outer shell thicknesses of the CVC sections depicted in Figure D1 were artificially increased to a thickness of 0.79 in., about 1.6 times the true thickness. A trial-and-error approach was taken in determining the increased shell thickness. A set of scoping calculations was conducted using a MLOR of 9 (0.25-cm cell size) and the true shell thickness. The thickness was increased in 0.1-in. increments, until it was determined that the shell structure was adequately captured in the model. The choice of a starting MLOR of 9 was subjective, but seemed reasonable based on experience with other Eulerian codes and their requirements for resolution through the thickness of a material. Increasing the CVC shell thickness to 0.79-in. results in a decrease in vent area; this is on average 7.5 percent for each vent. This reduction should have no effect on the peak pressures for the target wall gauges; however, it could potentially affect the late-time blow-down of the gas, and hence the impulse.

The shell thickness for the driver and other downstream sections was increased slightly more to about 1.2-in. thick. The artificially increased thickness for these other sections should have no effect on the calculations since they have no vents and only serve to contain the gas in the BLS.

The material surrounding the BLS structure was composed of air. Only a single air material was specified throughout; however, the initial conditions varied by region to match those specified in the test. Here, the pressure of the driver gas was set to 1,298 psig and was assumed to be at an ambient temperature of 77°F. The remainder of the air both inside and outside of the BLS was set to ambient conditions (14.7 psia, 77°F). The air was modeled as an ideal gas having a ratio of specific heats (gamma γ) of 1.4, which is reasonable for the range of conditions considered here. The air for all calculations was modeled as an ideal gas. It was desired to also consider a SESAME EOS for real air; however, it was found that run times with this EOS were intractable. It was decided that all modeling would rely solely on an ideal gas EOS.

A mesh convergence study was conducted. The results are shown in Figure D2 for three gauge locations, P3, P4, and PE. The radial distance from the BLS centerline for these gauges was 2.25, 13.2, and 30 in., respectively. The gauges selected provide a good indication of the influence of radial offset on the data. In practice, the measured (and calculated) results were generally consistent across the target wall. The resolution for each calculation is denoted in parentheses, along with the MLOR. Overall, one notes that the calculated TOA is slightly larger than measured (on the order of 20 percent) with the initial peak pressure being significantly over-predicted (on the order of 35 to 40 percent). In turn, this leads to a notable overprediction in the impulse.

Figure D2. Comparison of 2-DC RAGE results for GSA configuration.



The calculated results at gauge P3 are exceedingly noisy. This gauge is near the centerline of the BLS (2.25-in. offset). The BLS walls and any symmetry planes in a calculation act as perfect reflectors, and it is conjectured that this idealization induced ringing in the solution due to the axisymmetric nature of the problem setup. The ringing in the calculated result diminishes with increased radial distance from the centerline. Thus, the results for gauges P4 and PE provide the greatest insight on the influence of mesh resolution. It is clear that only marginal improvements in the impulse are noted with increasing resolution. A sub-millimeter resolution is certainly more than adequate to capture the shock propagation. Thus, one must conclude that the overprediction is due to some other factor in the problem setup.

A sensitivity study was conducted next to further investigate the problem setup. The results of the study are outlined for gauge PE in Figure D3. These results are typical of those noted at the other gauge locations. All calculations are based on a MLOR of 9 (0.25-cm cell size). They utilized the mock-up striker mechanism depicted in Figure D1, unless stated otherwise. Also, the modified van Leer limiter was used throughout, unless stated otherwise.

The first variation considered the influence of the flux limiter (see Figure D3(b)), where the less accurate minmod slope limiter was specified. This did not influence the calculated results. The next variation did not include any striker mechanism in the setup, thus focusing on the influence of the striker assembly on the downstream flow field (see Figure D3(c)). Here, a slight increase in the peak reflected pressure was noted when the striker was omitted from the setup. Recall, the grill is not included in the 2-DC model. Thus, one might infer that the grill may lead to a constriction in flow, and hence a reduction in the gauge pressures measured downstream. As an aside, it is useful to review an earlier test that did not have a grill (see Figure D4). The TOA for Test 24 in the figure was time-shifted to match that for Test 30a. There were issues triggering the measured data in the earlier testing. Although the measured TOA from these earlier tests is suspect, the general shape of the pulse is not. It is clear that the two sets of data compare well, suggesting that the grill does not significantly influence the measured data. One can then infer that the grill would not affect the calculations, had it been included in the problem setup.

Figure D3. Results from 2-DC sensitivity study.

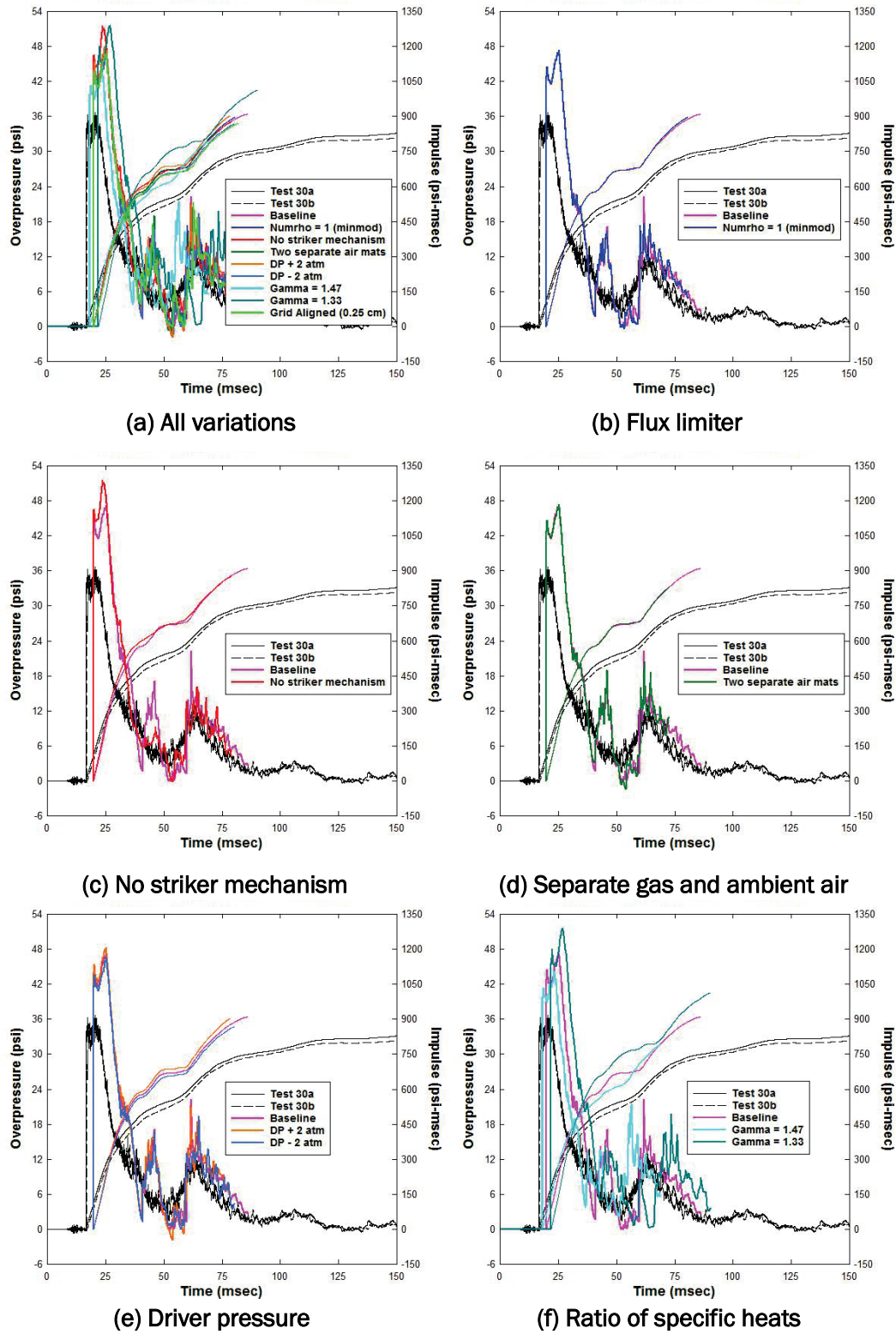
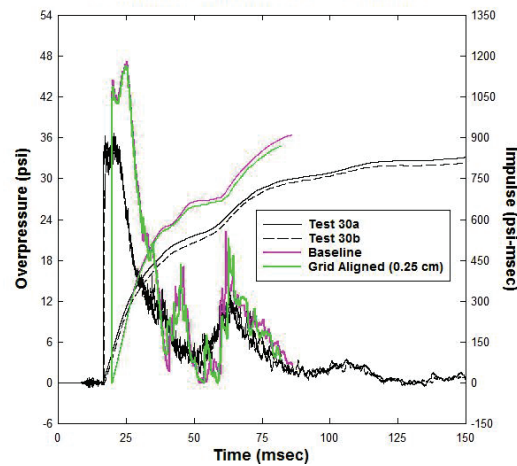
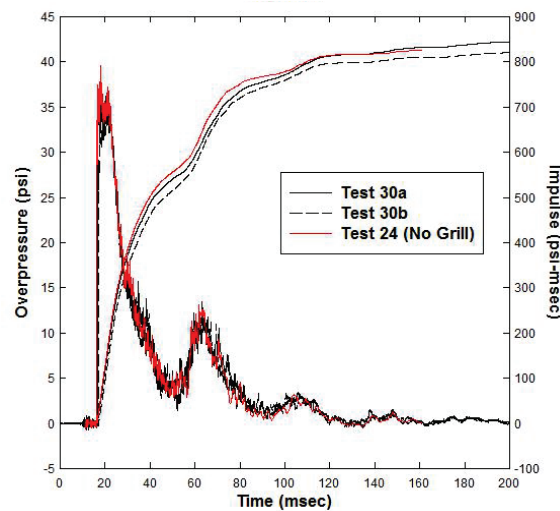


Figure D3. (Continued).



(g) Grid aligned BLS structure

Figure D4. Comparison of gauge PE measured data with and without grill.



Further variations considered the air modeled as two separate materials, ambient air and the compressed driver gas (see Figure D3(d)); variations in the initial driver pressure as ± 2 atmospheres (± 29.4 psi) as shown in Figure D3(e); variations in gamma by ± 5 percent as shown in Figure D3(f); and modifying the location of the BLS outer shell structure so it was aligned on cell boundaries (see Figure D3(g)). Note that it is not possible to align the conical segments along the cell boundaries as they are non-orthogonal entities. The results were fairly insensitive for all cases except for variations in gamma.

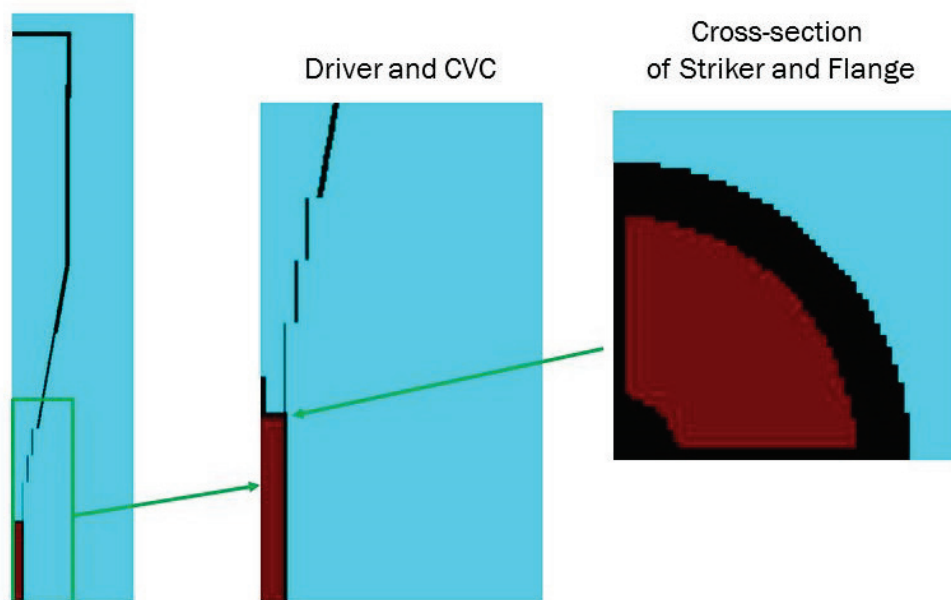
One should note that the ratio of specific heats, or gamma, is assumed constant throughout the entire domain, regardless of the changing conditions. In reality, one can expect some variation in gamma; however, it should be reasonably small for the limited range of conditions considered here. The bounding cases for gamma used in the sensitivity study are not applicable to the case at hand; however, they do indicate that even with these unrealistic choices, the initial peak pressure is still significantly overpredicted.

There are other possible causes for the differences between the calculated and measured results. These include modeling (or lack of) diaphragm rupture and the reduced venting area in the CVC (necessary to conduct the calculation). The driver gas is assumed to be at a uniform pressure. When the calculation starts, the driver gas instantaneously flows downstream with no impedance. It is possible that the process of rupture and lack of uniformity in the initial flow may have some effect; however, it is doubtful that the effect would be as great as observed in these calculations. Thus, the reasoning for the overpredictions is at present unknown.

Although the GSA configuration is predominately axisymmetric, the emphasis is on 3-D modeling as this provides a better indication of a code's performance for handling realistic applications. Thus, all further calculations involved modeling the BLS configurations in 3-D. Note, symmetry conditions about the longitudinal axis were considered to reduce the run time. The 2-DC sensitivity study suggests that RAGE will overpredict both the peak pressure and impulse in the 3-D setup. Given the time constraints on the project, it was necessary to proceed forward with the 3-D calculations with the expectation that both the peak pressure and impulse would be overpredicted.

The 3-D problem setup for the GSA configuration is outlined in Figure D5. Quarter symmetry was assumed with symmetry planes about the vertical and horizontal planes along the longitudinal BLS axis. The figure depicts only a portion of the mesh. The actual mesh extended out along the cardinal directions (30 cells along the x-and y-axes and 40 cells along the z-axis). As with the 2-DC setup, the origin was defined at the base of the driver. The initial cell size was 64 cm, resulting in a grid encompassing a 1920-cm \times 1920-cm \times 2560-cm region of physical space. The extended mesh was thought sufficient to avoid any reflections that might originate from the mesh boundaries and affect the solution later in time.

Figure D5. RAGE 3-D problem setup for GSA configuration.

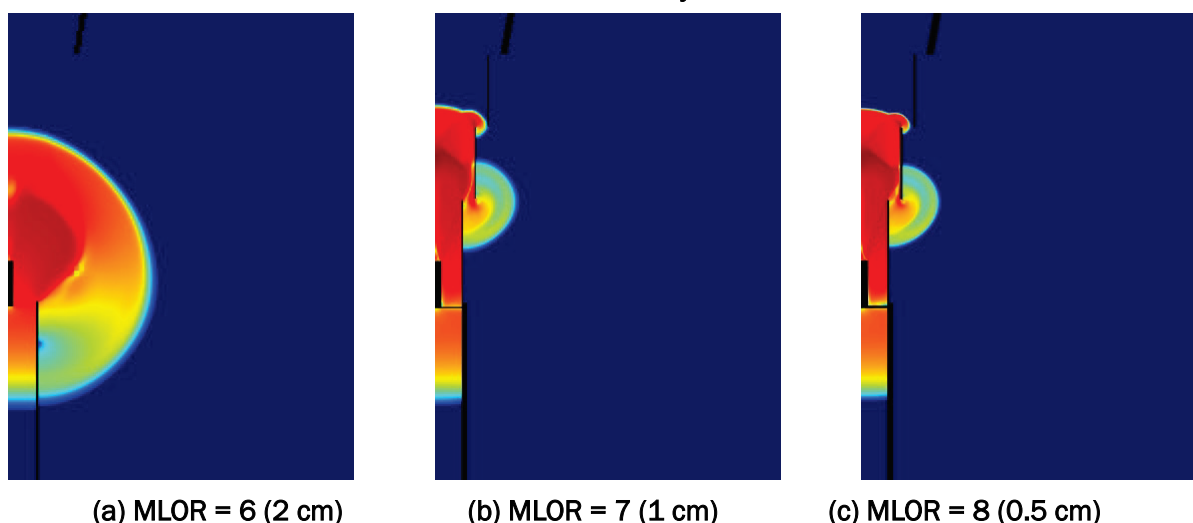


The walls of the BLS were modeled as rigid (non-responding) materials. The outer shell thickness of the CVC sections was artificially increased to a thickness of 0.79 in., about 1.6 times the true thickness. The plot in Figure D5 suggests that the shell thickness for CVC-1 is less than the others. This is not the case; rather the appearance of a thinner shell is a plotting artifact only. The shell thickness for the other downstream sections was increased even more. As discussed earlier, it was necessary to artificially increase the shell thickness in order to reduce the resolution requirements and ensure tractable run times. The artificially increased thickness for the downstream sections is not an issue, as they contain no vents; however, the increased thickness of the CVC shell effectively reduces the vent area by about 7.5 percent on average. This may have some effect on the blow-down later in time and hence the final peak impulse.

The surrounding air was modeled as a hydrodynamic material. The air was modeled as an ideal gas, having a constant gamma of 1.4. The pressure of the driver gas was 1,298 psig. It was assumed to be at an ambient temperature of 77°F. The remainder of the air both inside and outside of the BLS was set to ambient conditions (14.7 psia, 77°F). More detail was added to the mock-up of the striker mechanism, with the legs of the flange included in the model. Again, no attempt was made to include the grill as it could not be adequately resolved.

A sensitivity study looking at refinement level was initially conducted to assess potential bleed-through in the CVC section for the 3-D problem setup. The findings are illustrated in Figure D6, which depict the resultant velocity field at 2 msec as a function of the MLOR. The minimum cell size is denoted in parentheses. The initial cell size is 64 cm. The MLORs considered were 6, 7, and 8; resulting in minimum cell sizes of 2.0, 1.0, and 0.5 cm, respectively. It is clear that the minimum acceptable resolution for the 3-D analysis is 1.0 cm.

Figure D6. Example of bleed-through at 2 msec in 3-D RAGE analyses.



Spatial plots of the resultant velocity field at select times are provided in Figure D7. The scale for the plots on the right-hand side is cast in terms of cm/s. The scale range could not be modified using the post-processing tools supplied with RAGE. The times selected for the plots represent important events in the shock propagation problem. By 5 msec, the shock front has traversed the CVC section and has entered into the GSA cone. By 10 msec, the front has entered into the constant area section. A nearly planar front is achieved by 15 msec. The front impinges on the target wall at about 20 msec, after which it is reflected. The reflected shock interacts with any residual high density gas propagating downstream, resulting in a highly complex shock environment.

Comparisons between the measured and calculated data are provided in Figure D8. The calculated results have been shifted in time by -3.15 msec to match the measured arrival time. The time shifting was done to ease comparisons of the waveforms. The measured data were fairly consistent

Figure D7. Velocity field for 3-D RAGE calculation,
GSA configuration.

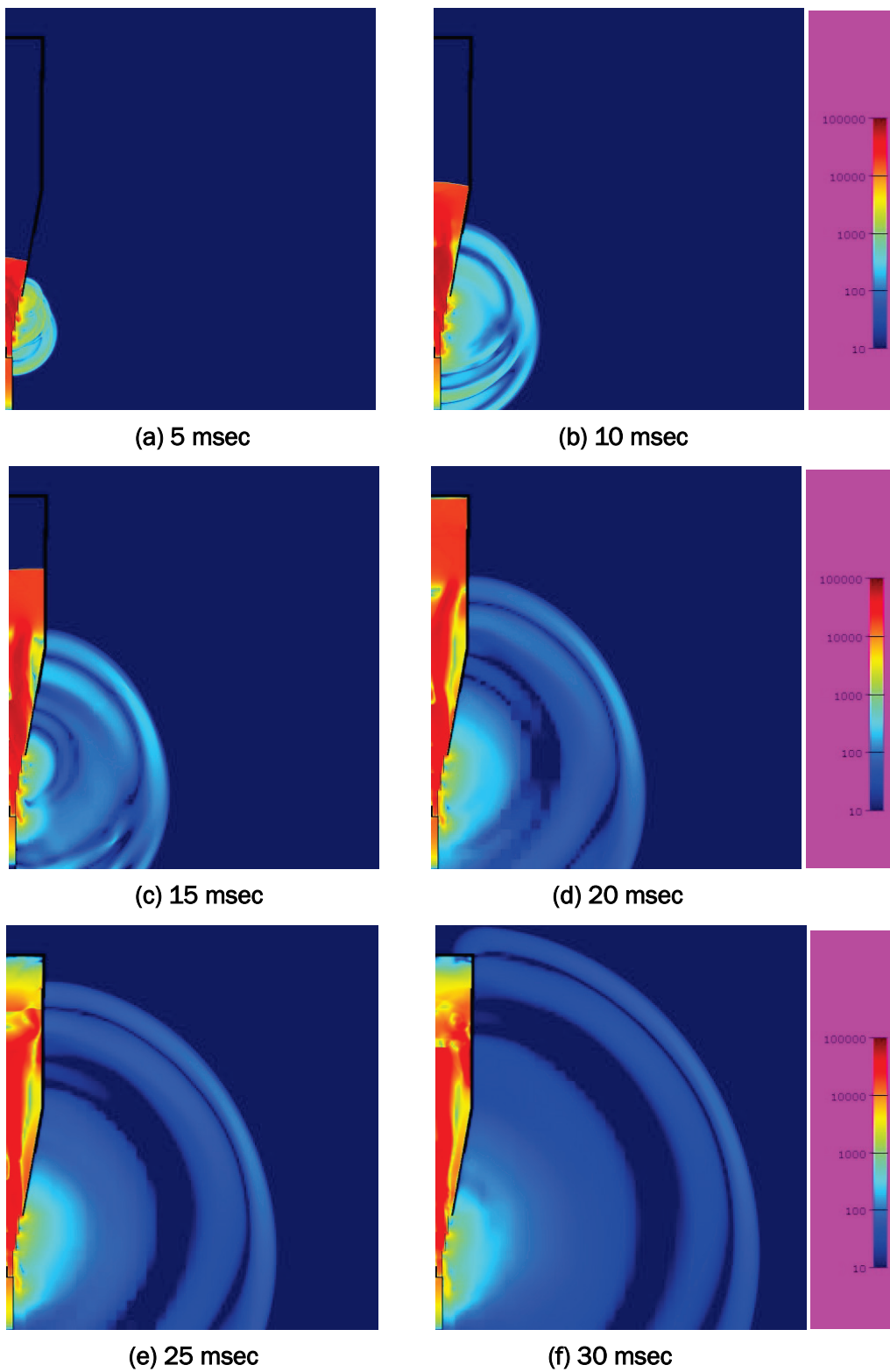
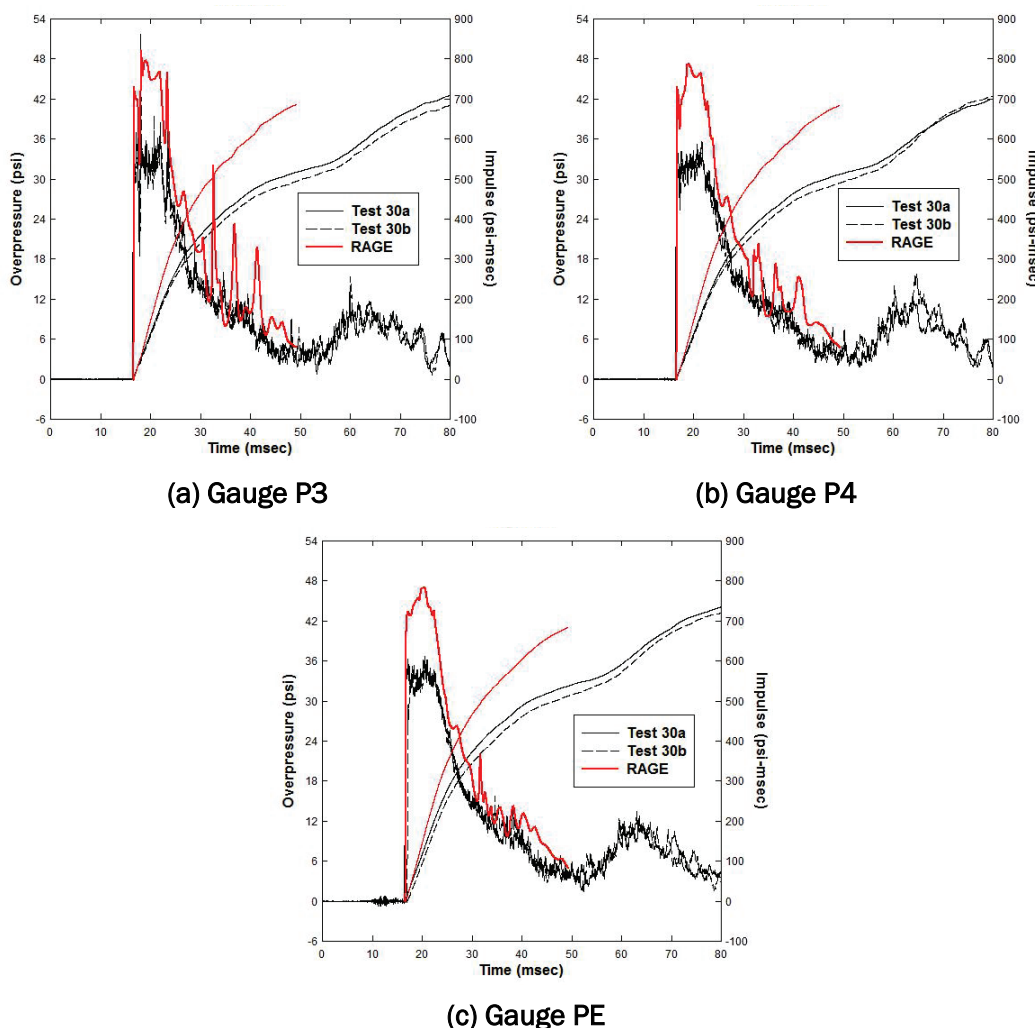


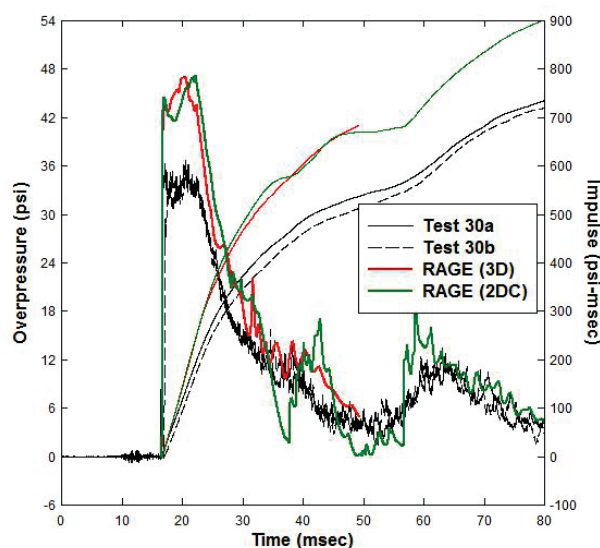
Figure D8. Time-shifted gauge comparisons for RAGE, GSA configuration.



across the target wall, indicating that the incoming shock front was fairly planar with edge effects having little influence on the reflected pulse (at least over the time frame of interest). In all cases, RAGE significantly overpredicts the peak pressure by about 35 to 40 percent. In turn, this leads to a significant overprediction of the impulse. The degree of overprediction is exaggerated by the relatively long duration of the initial pulse. As noted in the 2-DC calculations, there is a significant amount of ringing in the calculation. The ringing diminishes with increasing radial offset of a gauge.

It is worthwhile to compare the 2-DC and 3-D RAGE results. Comparisons at gauge PE are provided in Figure D9. These are typical of those at the other gauge stations. The MLOR was held fixed for the duration of both

Figure D9. Comparisons of 2-DC and 3-D RAGE calculations for gauge PE.



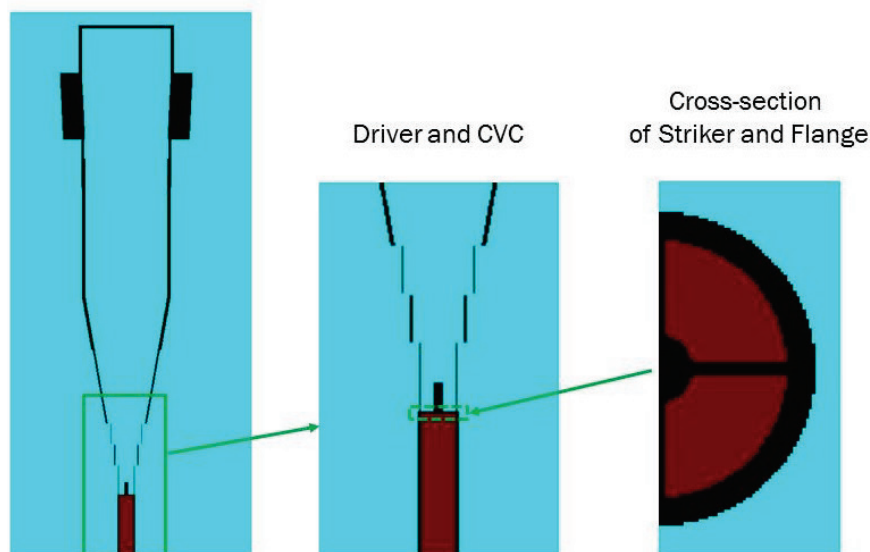
the 2-DC and 3-D calculations. Overall, one notes excellent agreement between the 2-DC and 3-D calculations.

The 3-D RAGE calculation was conducted over a series of restarts out to a final analysis time of 52.6 msec. The output from each calculation was reviewed to obtain timing data. The calculation was run at a MLOR of 8 (0.5 cm) for the entire calculation. Over the duration of the calculation, the number of cells in the problem grew from 13.4 to 279 million. The number of processors required grew from 128 at startup to 1,024 by the end of the calculation. The total number of wall-clock hours to conduct the entire calculation was 429 hr. It took approximately 282k processor-CPU hours for the calculation to reach 52.6 msec. This is defined as the CPU time multiplied by the number of processors, with the quantity summed for all restarts. This is a very expensive calculation.

Calibrations tests with 8-ft×8-ft C2SQ configuration

The problem setup for the second case is depicted in Figure D10. This model is an extension of the GSA setup that includes the C2SQ and SQ1 sections. The longitudinal axis of the BLS ran along the z-axis in the model, with the origin at the base of the driver. Half symmetry was assumed, with a reflecting plane about the y-axis. The initial cell size was 64 cm. The number of level zero cells along the x, y, and z-axes were 60, 30, and 40, respectively. Thus, the grid encompassed a 3,840-cm × 1,920-

Figure D10. RAGE 3-D problem setup for 8-ft×8-ft C2SQ configuration.



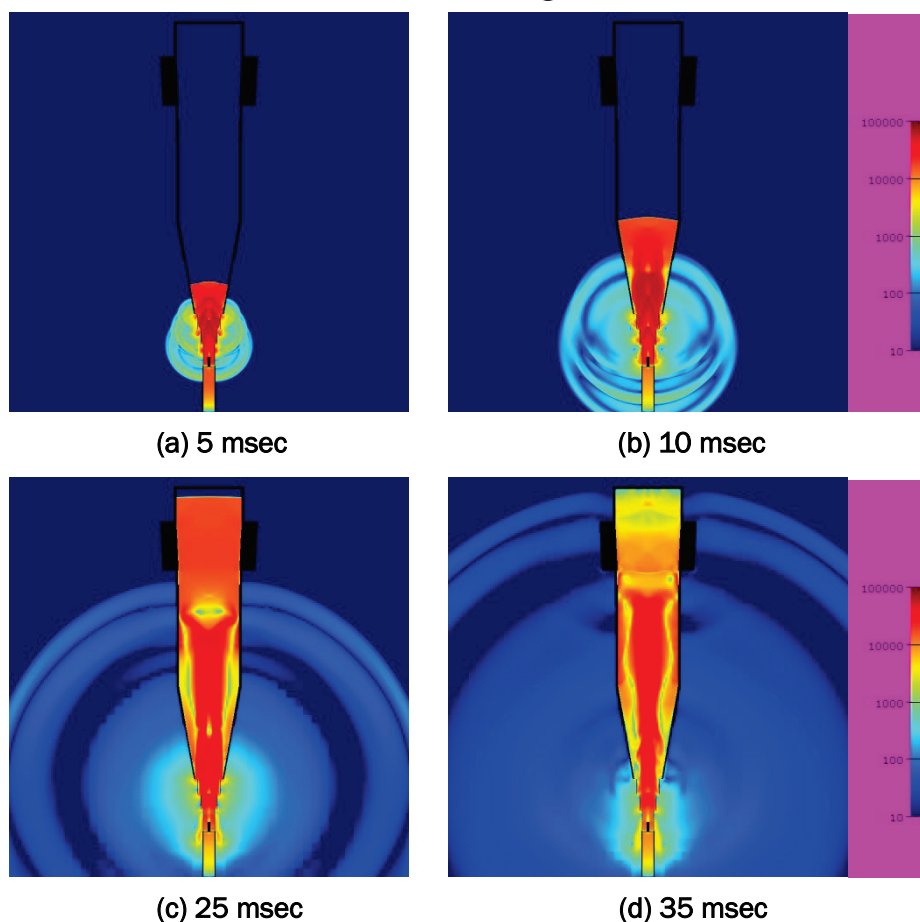
cm × 2560-cm region of physical space. The model depicted in Figure D10 was built up with overlaid primitive objects. The C2SQ transition section posed some challenges, and it is likely that the curvature in the corners is sharper than indicated in the photographs of Section 2. A CAD model import would have been preferred; however, there was no documentation (nor example) for the model import.

The same general approach for the problem setup from the first case was taken here, where the BLS structure was treated as a rigid material, and the ambient air and compressed gas were modeled as an ideal gas having a ratio of specific heats of 1.4. The conditions for the ambient air were based on an average of that specified in the testing. The initial driver gas pressure was set to 1,298 psig and was assumed to be at an ambient temperature of 60°F. The remainder of the air both inside and outside of the BLS was set to ambient conditions (14.7 psia, 60°F). As with the previous case, the CVC shell thickness has been artificially increased from 0.5 to 0.79 in. The plot in Figure D11 suggests that the shell thickness for CVC-2 is larger than the others. This is not the case; rather the appearance of a thicker shell is a plotting artifact only. The shell thickness for the other downstream sections was increased more. This is most obvious in the C2SQ section. This transition section was built up via a series of overlaid primitive objects. The thickness was exaggerated to avoid gaps being induced in the model. The artificially increased thickness of the downstream sections should have no effect on the solution, as they contain no vents; however,

the increased thickness of the CVC shell effectively reduces the vent area by about 7.5 percent on average. This should not affect the initial peak pressure, but could potentially affect the later time impulse due to a reduction in the rate of gas venting.

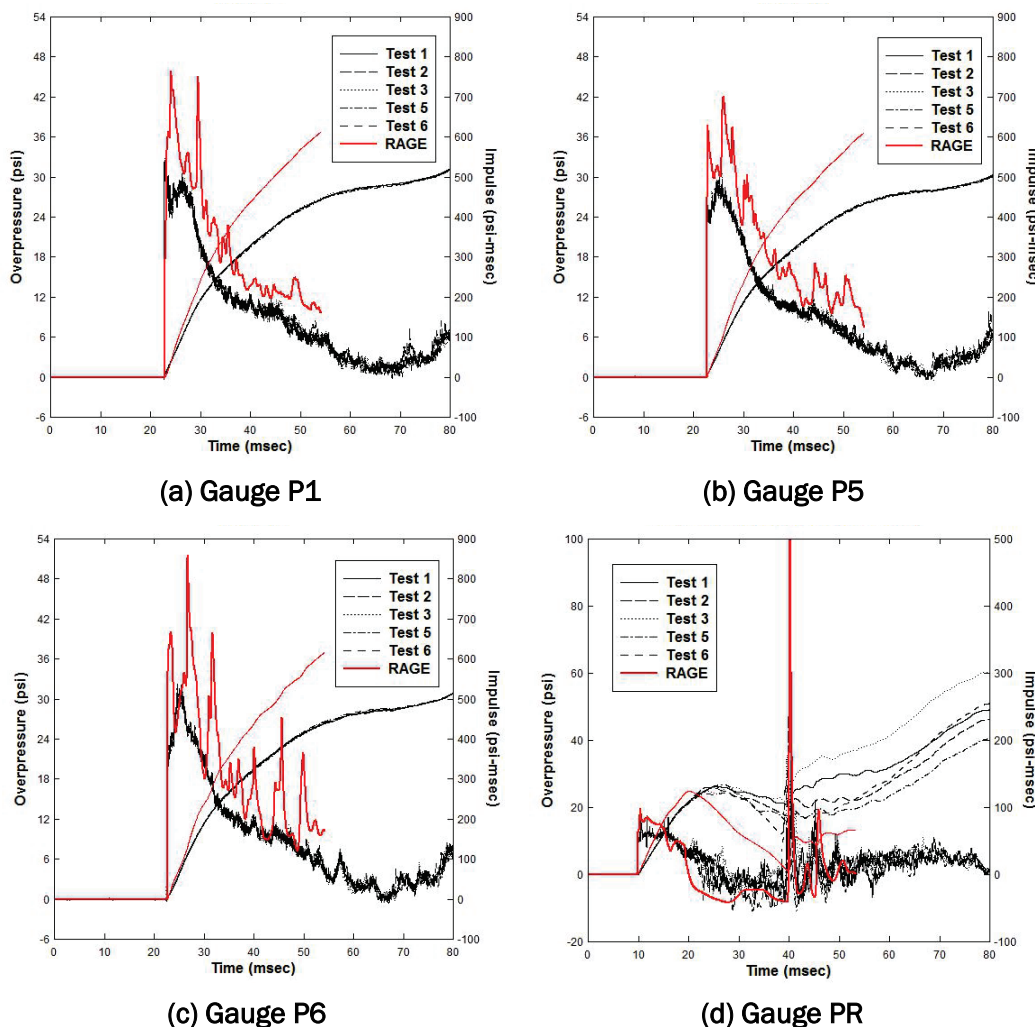
Spatial plots of the resultant velocity field at select times are provided in Figure D11. The scale for the plots on the right-hand side is cast in terms of cm/s. The scale range could not be modified using the post-processing tools supplied with RAGE. The times selected for the plots represent important events in the shock propagation problem. By 5 msec, the shock front has traversed the CVC section and has entered into the GSA cone. By 10 msec, the front has entered into the constant area section. The front impinges on the target wall at about 26 msec, after which it is reflected. The reflected shock interacts with any residual high-density gas propagating downstream, resulting in a highly complex shock environment.

Figure D11. Velocity field from RAGE calculation, 8-ft×8-ft C2SQ configuration.



Comparisons between the measured and calculated data are provided in Figure D12 for select gauge locations. The figure contains comparisons for three gauges on the target wall (P6, P5, and P1) along with the side-on pressure gauge PR. The radial distance of the target wall gauges from the BLS centerline was 10.625, 24.5, and 46.72 in. for gauges P6, P5, and P1, respectively. Thus, the gauges selected provide a good indication of the influence of radial offset on the data. It is important to note that the measured data were fairly consistent across the target wall, indicating that the incoming shock front was fairly planar (at least over the time frame of interest). The calculated pressure-time-histories for the target wall gauges were shifted in time by -2.93 msec to match the measured arrival time.

Figure D12. Time-shifted gauge comparisons for RAGE, 8-ft×8-ft C2SQ configuration.



Similarly, the calculated side-on gauge data were shifted by -3.79 msec to match the measured arrival. The time shifting was done to ease comparisons of the waveform.

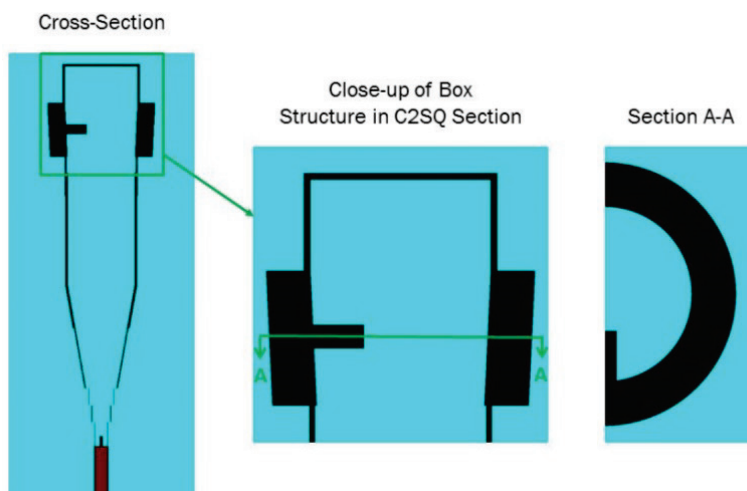
RAGE significantly over-predicts the initial peak pressure for the target wall gauges (on the order of 40 to 45 percent). In turn, this leads to a significant overprediction in the impulse. The initial side-on pressure at gauge PR is also overpredicted, but to a much lesser extent. The decay rate behind the initial peak predicted by RAGE is higher than measured. Further, one notes a longer negative phase duration in the RAGE calculation as compared with the measured data. On a positive note, the timing of the subsequent spikes is captured well by RAGE.

The RAGE calculation was conducted over a series of restarts out to a final analysis time of 57.2 msec. The output from each calculation was reviewed to obtain timing data. The calculation was run at a MLOR of 8 (0.5 cm) for the entire calculation. Over the duration of the calculation, the number of cells in the problem grew from 38.5 to 509 million. The number of processors required grew from 256 at startup to 1,536 by the end of the calculation. The total number of wall-clock hours to carry out the entire calculation was 653 hr. It took approximately 618k processor-CPU hours for the calculation to reach 57.2 msec. This is defined as the CPU time multiplied by the number of processors, with the quantity summed for all restarts. This is also a very expensive calculation.

BLS 8-ft×8-ft C2SQ configuration with box

The problem setup for the third case is depicted in Figure D13. This model is identical to that used for the second case, with the exception of an instrumented box placed in the C2SQ section. The BLS structure and box were treated as rigid materials; the ambient air and compressed gas were modeled as an ideal gas having a ratio of specific heats of 1.4. The conditions for the ambient air were based on an average of that specified in the testing. The initial driver gas pressure was set to 1,298 psig and was assumed to be at an ambient temperature of 60°F. The remainder of the air both inside and outside of the BLS was set to ambient conditions (14.7 psia, 60°F). As with the previous cases, the CVC shell thickness was artificially increased from 0.5 to 0.79 in. The shell thickness for the other downstream sections was increased more. This is most obvious in the C2SQ section. This transition section was built up via a series of overlaid

Figure D13. RAGE problem setup for 8-ft×8-ft C2SQ configuration with box.



primitive objects. A box was inserted into the model along the base of the C2SQ section. Since a plane of symmetry was employed in the problem setup, it was only possible to collect information on one side of the box (right face) for comparison with the measured data.

Spatial plots of the resultant velocity field at selected times are provided in Figure D14. The scale for the plots on the right-hand side is cast in terms of cm/s. The scale range could not be modified using the post-processing tools supplied with RAGE. Comparable results were noted with the previous case for times leading up to initial interaction with the box. For brevity, they have not been included here. The plots in Figure D14 focus on interaction of the incident and reflected shocks with the box. They provide an overall view of the BLS. The plots in Figures D15 through D17 provide a close-up view of the region about the box. Independent state plots of the density, pressure, and velocity state are provided at select times. The scale for the density plots is in g/cm³; the scale for the pressure plots is in dyne/cm²; and the scale for the velocity magnitude plots is in cm/s. It is instructive to cross-reference between the overall and close-up views of the flow state when analyzing the data.

Figure D14. RAGE velocity field, 8-ft×8-ft
C2SQ configuration with box.

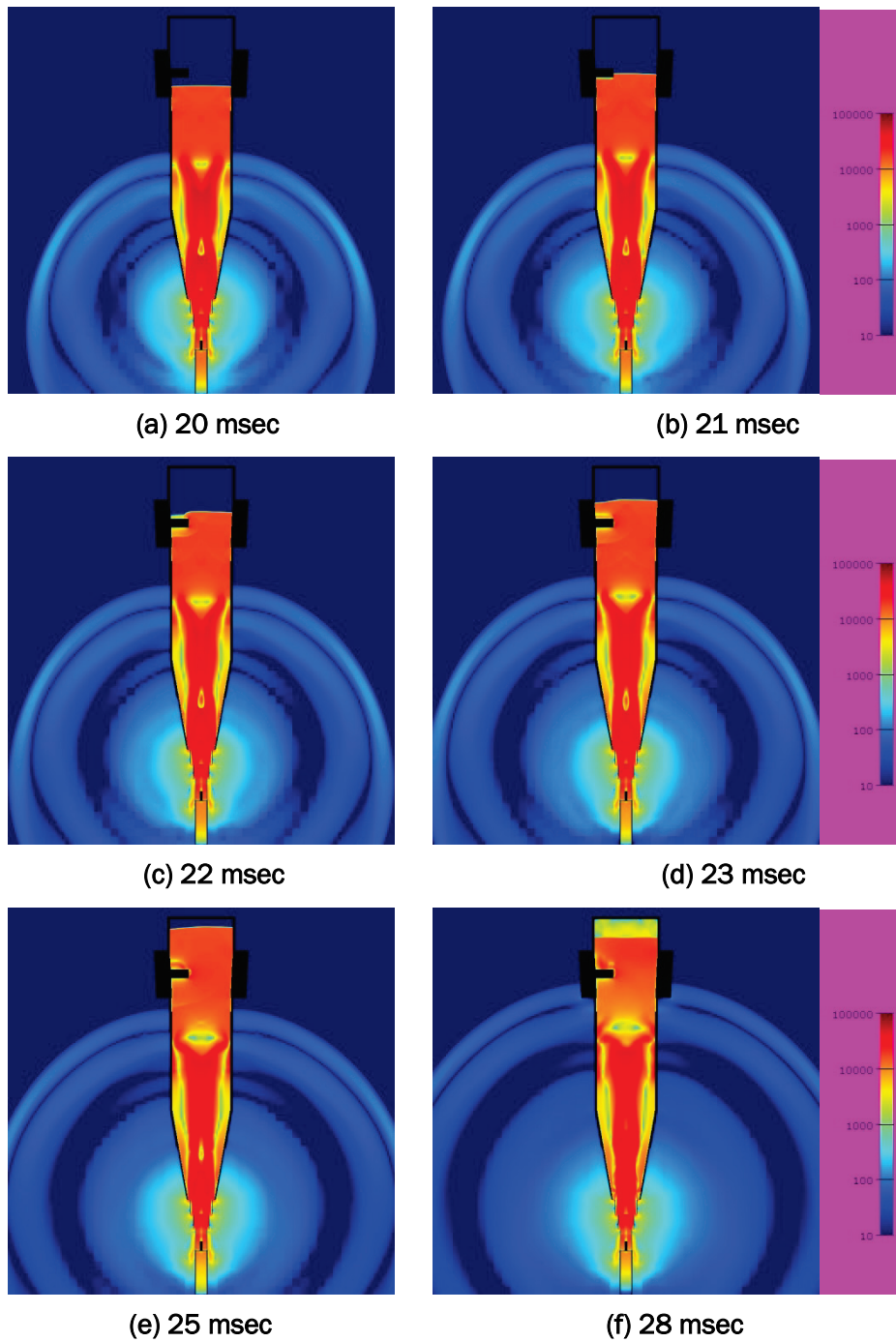
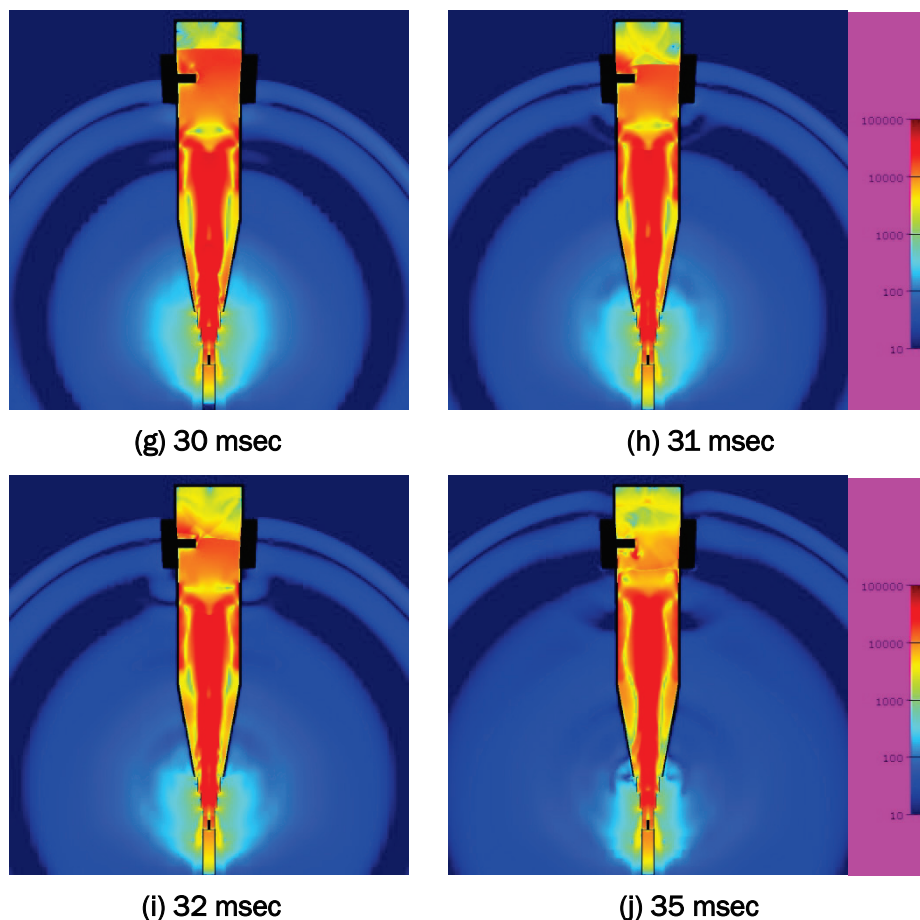


Figure D14. (Continued).



In Figure D14 at 20 msec, the incident shock front is about to impinge on the box. By 22 msec, the front has traversed the box and is diffracting about the back side. The process of front face reflection, passage across the top surface, and diffraction about the rear of the box is best illustrated in the detailed state plots. After traversing the box, the front recombines downstream to form an almost planar front again by 25 msec. It reflects from the target wall at about 26 msec. The reflected shock then travels upstream and interacts with the back face of the box at about 31 msec. The reflected shock is no longer planar as it travels toward the back face of the box, as it is affected by the residual pressure and temperature state of the air in the region between the box and target wall. By 35 msec, the reflected shock has traversed the box and passed into the Cascade section. Although it has recovered much of its planar structure, this will be short-lived as it continues moving upstream. It will eventually interact with the residual gas flow, which will cause it to lose much of its structure.

Figure D15. Flow state around box at 21 msec.



(a) Density

(b) Absolute pressure



(c) Resultant velocity

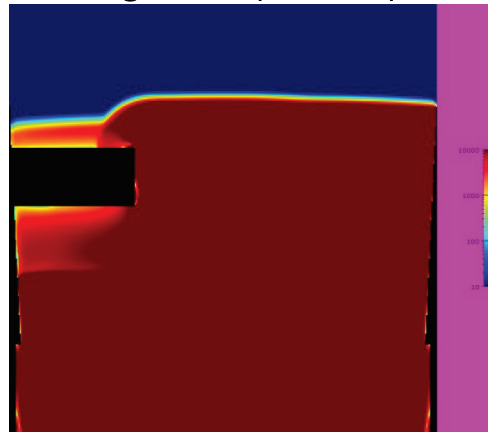
Figure D16. Flow state around box at 22 msec.



(a) Density

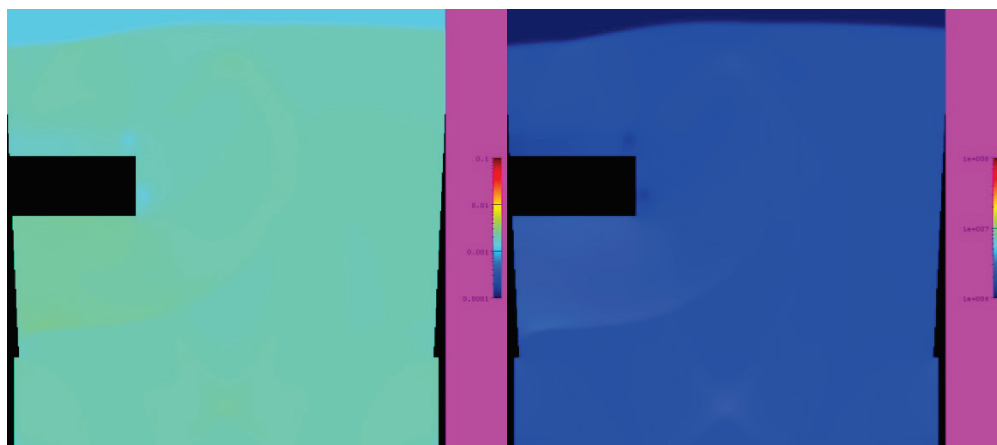
(b) Absolute pressure

Figure D16. (Continued).



(c) Resultant velocity

Figure D17. Flow state around box at 23 msec.



(a) Density

(b) Absolute pressure



(c) Resultant velocity

Comparisons between the measured and calculated data are provided in Figures D18 through D21 for the gauges positioned on the box. Comparisons for the gauges located on the target wall are provided in Figure D22.

Overall, RAGE tends to overpredict the peak pressure for both the incident and reflected shocks, which in turn, leads to a substantial overprediction in the impulse. This is readily apparent for the front face gauges (see Figure D18), with less of a disparity noted for gauges on the other faces.

Figure D18. Time-shifted gauge comparisons for RAGE, front face.

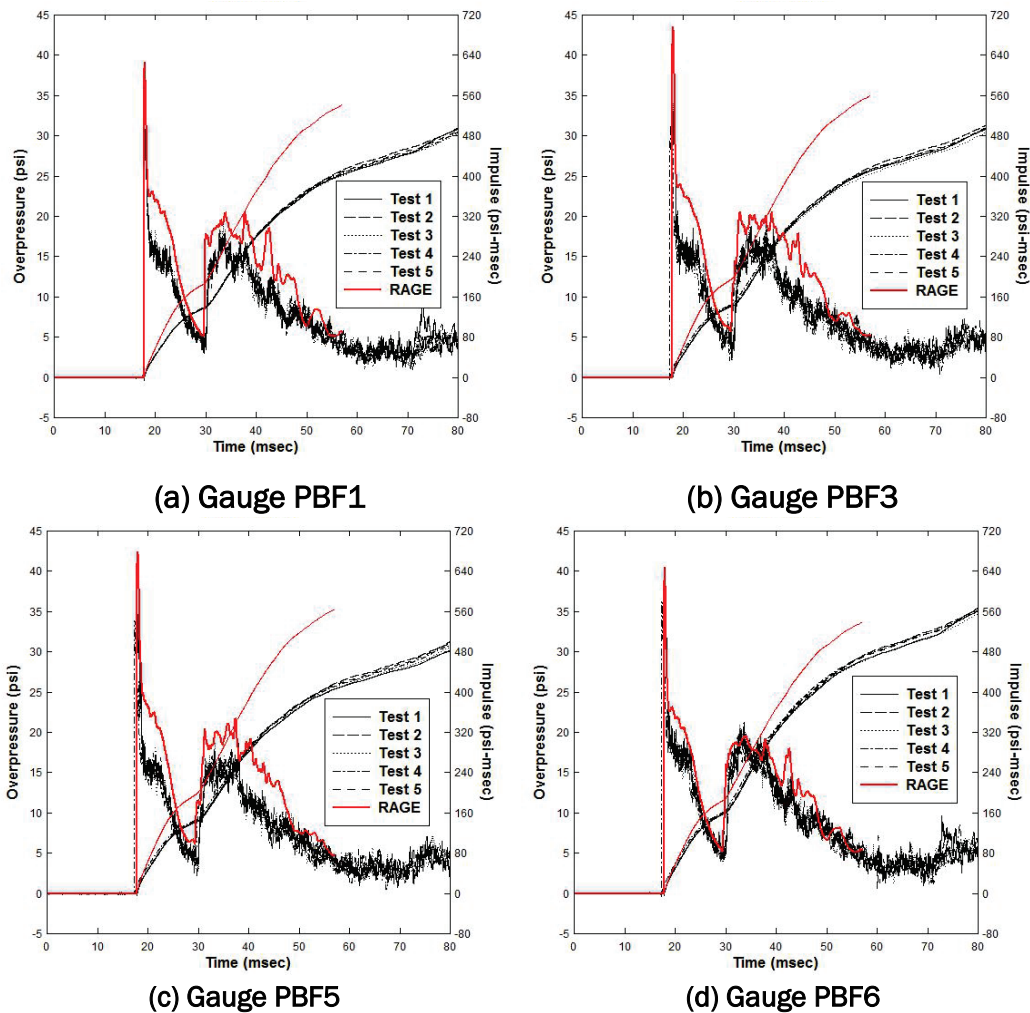
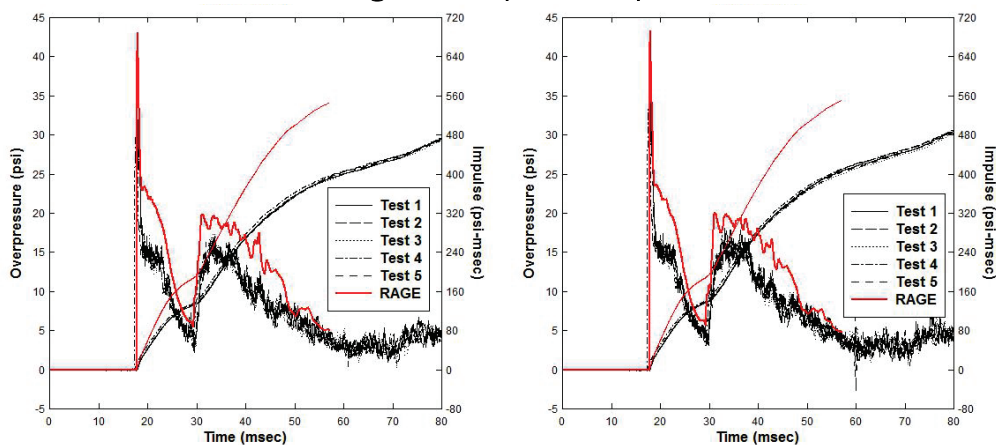


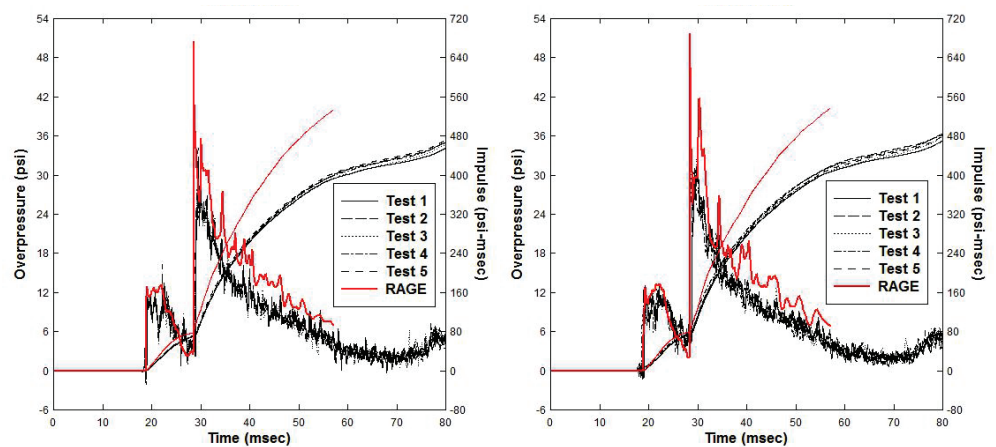
Figure D18. (Continued).



(e) Gauge PBF7

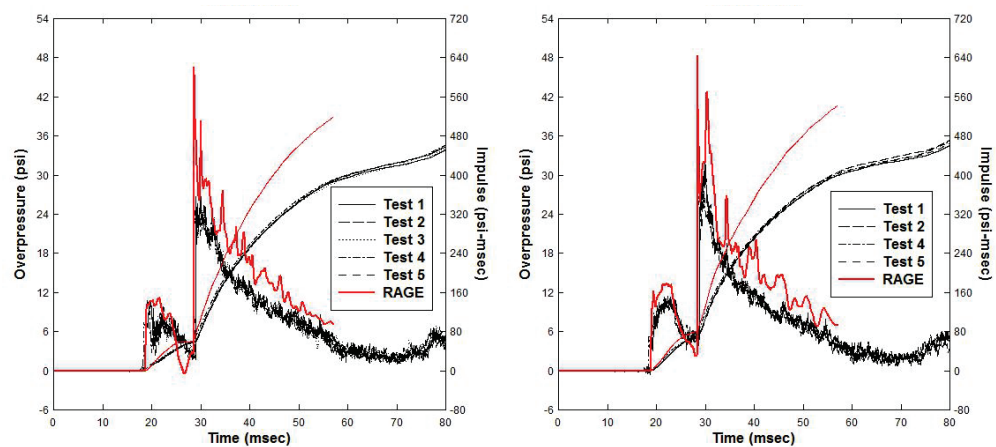
(f) Gauge PBF8

Figure D19. Time-shifted gauge comparisons for RAGE, back face.



(a) Gauge PBB1

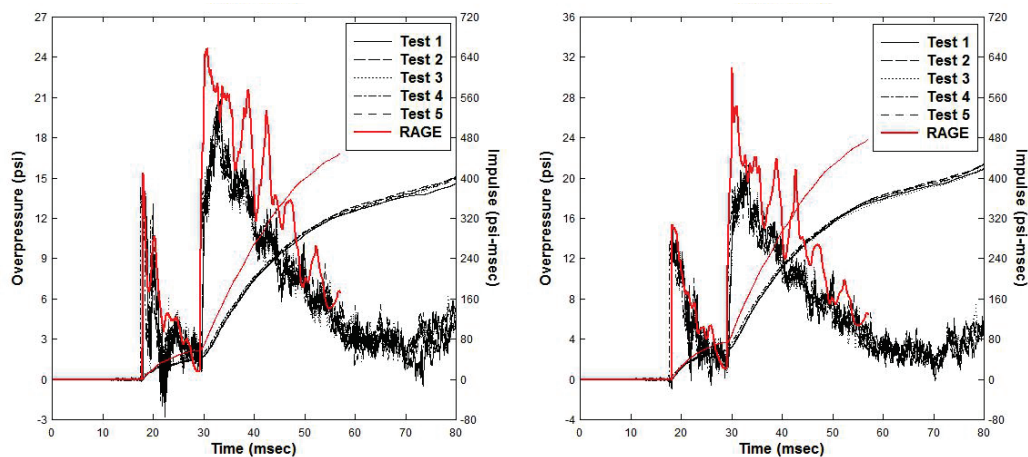
(b) Gauge PBB2



(c) Gauge PBB3

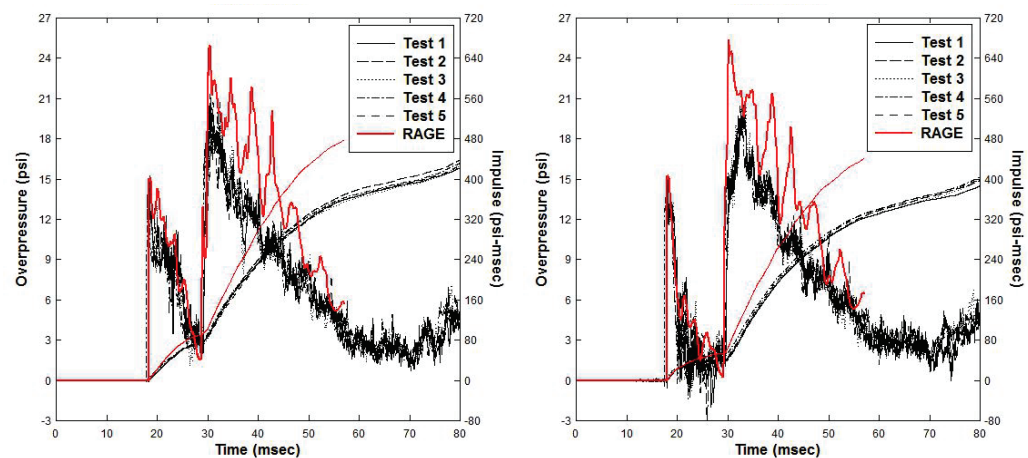
(d) Gauge PBB4

Figure D20. Time-shifted gauge comparisons for RAGE, top face.



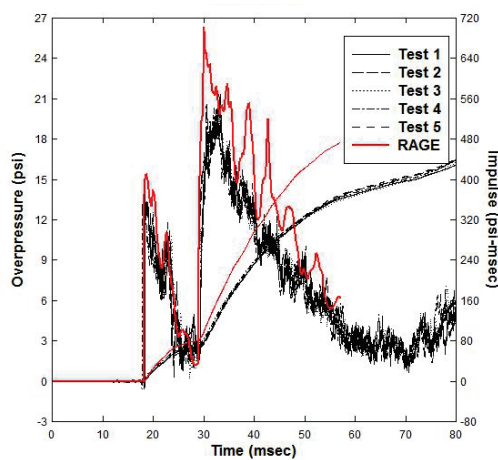
(a) Gauge PBT1

(b) Gauge PBT2



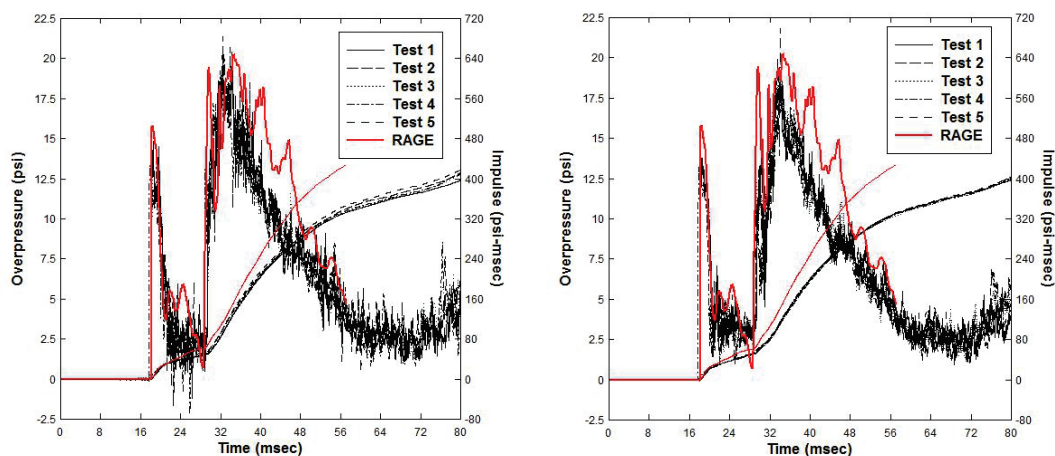
(c) Gauge PBT3

(d) Gauge PBT4



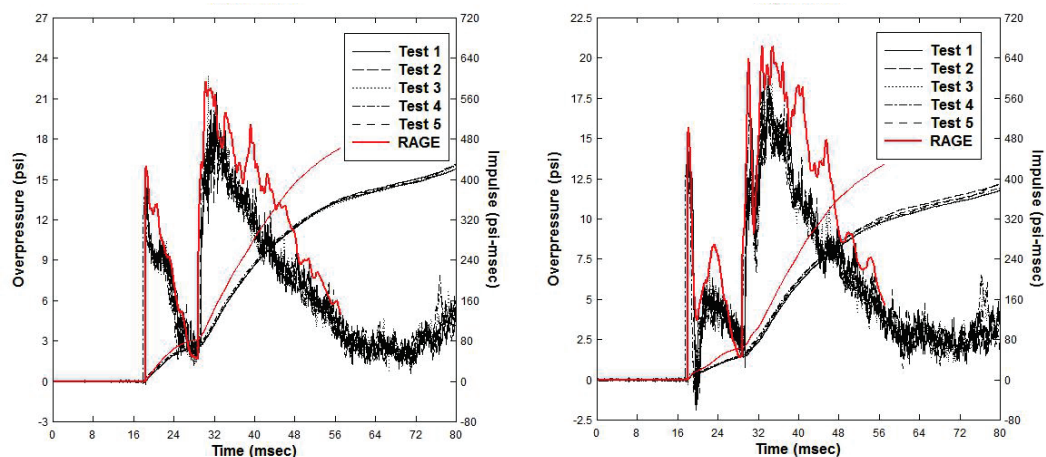
(e) Gauge PBT5

Figure D21. Time-shifted gauge comparisons for RAGE, left face.



(a) Gauge PBL1

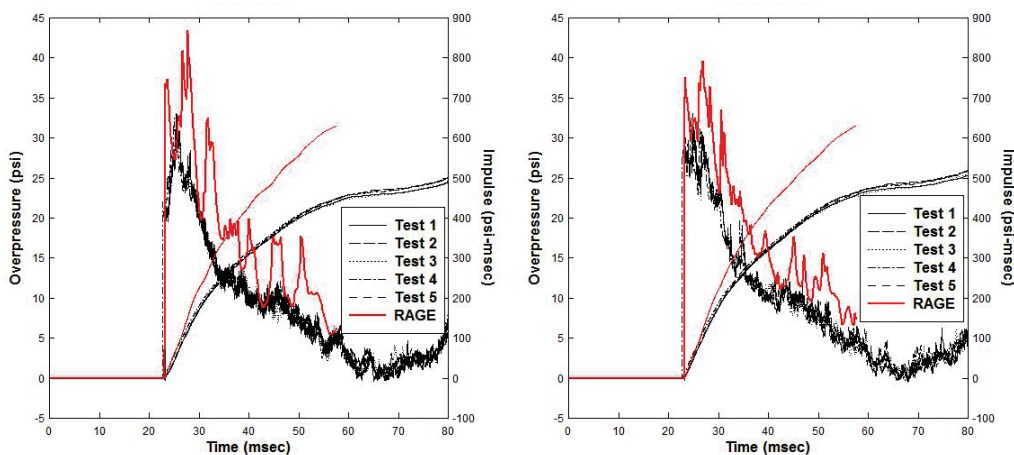
(b) Gauge PBL2



(c) Gauge PBL3

(d) Gauge PBL4

Figure D22. Time-shifted gauge comparisons for RAGE, target wall.



(a) Gauge P3

(b) Gauge P9

Not only is the peak pressure overpredicted, but the initial rate of decay from the peak is generally less than observed. In turn, this adds to the overprediction noted in the impulse, as this is simply the integration of the pressure-time-history. Although there are disparities in the peaks and rate of decay, one notes reasonable correlation with the timing of the peaks and general structure of the waveforms. For example, when reviewing the comparisons for the front face gauges, one notes two distinct peaks in the calculations with the difference in arrival of the two peaks correlating well with the measured data. Similar observations apply for the comparisons for the two gauges on the target wall.

The RAGE calculation was conducted over a series of restarts out to a final analysis time of 60 msec. The output from each calculation was reviewed to obtain timing data. The calculation was run at a MLOR of 8 (0.5 cm) for the entire calculation. Over the duration of the calculation, the number of cells in the problem grew from 38.6 to 478 million. The number of processors required grew from 256 at startup to 2,048 by the end of the calculation. The total number of wall-clock hours to conduct the entire calculation was 643 hr. It took approximately 662k processor-CPU hours for the calculation to reach 60 msec. This is defined as the CPU time multiplied by the number of processors, with the quantity summed for all restarts. This, too, is a very expensive calculation.

Conclusions and recommendations

Overall, RAGE tended to significantly overpredict the initial peak pressure of the arriving shock. Furthermore, the initial rate of decay from the peak was less than that observed. The combined effect led to integrated impulses that were significantly greater than those observed (ranging from 20 to 45 percent overprediction depending on the gauge). Despite the disparities in the peaks and rate of decay, one did note reasonable correlation with the timing of the peaks and general structure of the waveforms. This was most evident in the comparison for the third case, where multiple peaks were discerned on gauges on the different sides of the box.

The reason for the tendency toward overprediction is unclear. The early 2-DC mesh resolution and sensitivity study did not expose any “first order” influences on the calculations. This is troubling in that the calculations appeared relatively insensitive to wide variations in the parameters considered. It is conjectured that the roots of the problem are related to the use of an ideal gas EOS. The SAGE code has been used extensively at

ERDC for modeling airblast resulting from explosive detonations (both ideal and non-ideal) with great success. The initial BLS calculations were conducted using SAGE while RAGE was being installed on the ERDC HPC platform Garnet. The results for the two codes were quite similar, with SAGE also exhibiting a tendency for overprediction for the BLS modeling. The setup for the early SAGE calculations was comparable to that used in the RAGE modeling. It also treated the air using an ideal gas EOS with a constant gamma of 1.4. The version of SAGE in use at ERDC is much older, dating back to the 2004 time frame. This suggests that this issue of overprediction may be unique to BLS-type of problems involving air states in relatively low pressure regimes. It also suggests that this has been an unrecognized issue up to this point.

Of course, one can never discount the potential for user error. Our experience at ERDC has been exclusively based on modeling explosive detonations. The BLS experiments represent a vastly different class of problems. There were discussions with Leidos regarding the BLS problem setup. Leidos provided many constructive suggestions, in particular, focusing on alternative options in the hydrodynamic treatment as well as alternate setups to improve run times. These suggestions were generally implemented into the RAGE modeling, with the exception of modifying the BLS layout to ensure edges were aligned on cell boundaries. This really is not possible given that many BLS sections are conical in nature. Furthermore, one cannot align the circular sections in a 3-D setup. For these reasons, it was decided to artificially increase the BLS shell thickness to overcome any difficulties with capturing it in the modeling.

It is recommended that a follow-on analysis be conducted with the LANL version of RAGE. This would be helpful to diagnose the issue and possibly pin-point the source of the problem. The follow-on work could be very limited in scope. A simple 2-DC calculation would suffice and would provide a quick assessment of whether the issue persists in the LANL version.

It is also recommended that the user manual be updated to reflect the current version of the code. This work drew upon the 2005 user manual for SAGE, which is only an incomplete draft. It would be helpful to update the user documentation and develop a corresponding set of example problems. The example problems would illustrate the code's features and provide a means for independently testing installations on new HPC platforms.

Appendix E: SHAMRC Modeling

SHAMRC Background

The Second-order Hydrodynamic Automatic Mesh Refinement Code, or SHAMRC, is a government-owned fluid dynamics suite of codes developed and maintained by Applied Research Associates (ARA). It is able to solve 2-D as well as 3-D problems using a finite-difference scheme and can be run either in serial or parallel processing environments. Some of the applications for which the code is used include high explosive detonations, nuclear explosive detonations, structure loading, airblast, thermal effects, munitions blast and fragmentation, shock tube phenomenology, dust and debris dispersion, and atmospheric shock propagation. The code employs a structured Eulerian grid that can make use of adaptive mesh refinement (AMR) for dividing the computational domain into smaller grids at several levels of refinement to provide high-resolution results. Other capabilities of the code include multiple geometries, non-responding and responding structures, two-phase flow with non-interactive and interactive drag-sensitive particles, several atmosphere models, multiple materials, a large material library, HE detonations, a K- ϵ turbulence model, water and dust vaporization, and a predictive metal and gaseous afterburn model. SHAMRC is second-order accurate in space and time and is fully conservative of mass, momentum, and energy.

SHAMRC is better described as a suite of codes as it is composed of multiple programs that are used for setting up, running, and post-processing each calculation (Crepeau et al. 2012; Happ et al. 2014). The main programs that are used for achieving this are listed and explained here. Whenever the users want to accomplish any of these, they must first call SHAMRC to generate the source code (referred to as “make”) and eventually execute it (simply called “run”). This makes sure that the code is tailored and optimized specifically for the problem at hand.

1. KEEL – generate initial computational grid
2. SHARC – solver that advances grid conditions in time
3. PULL – plot conditions in computational grid at various times
4. STASRT/STAPLT – process, plot, and extract station (gauge) data

This appendix covers all of the calculations that were performed for the three different BLS configurations using SHAMRC.

Problem setup

All of the SHAMRC calculations were run on the ERDC HPC platform Garnet. Garnet is a Cray XE6 that has 4,716 compute nodes with 32 cores per node. Each compute node has a core speed of 2.5 GHz and 64 GB of accessible memory. Three different BLS configurations were considered in this modeling effort, i.e., the GSA configuration, the 8-ft×8-ft C2SQ configuration, and the 8-ft×8-ft C2SQ configuration with box. For simplicity, these will be referred as the first, second, and third cases, respectively.

Although the GSA configuration could have been modeled in 2-D due to its axis-symmetric geometry, all three cases were modeled in 3-D. However, since all three cases were symmetric with respect to the BLS centerline, at least a one half-symmetry model was considered for each case. For these half-symmetry models, reflective boundary conditions were specified on the plane of symmetry. All other boundaries, including the ones for the fully-3-D models, were specified as transmissive, i.e., flow can exit the mesh through these boundaries but it is not allowed to flow back into the grid.

The mesh used for the three cases was flat, i.e., it did not involve any type of AMR nor was any grading applied. Therefore, the cell size was fixed throughout the computational domain. The cell size was selected so that it would be less than the smallest dimension in the problem. Not taking into account the diaphragm-catch grill at the end of the CVC-1 component, the smallest dimension in the BLS was 0.5 in. (1.27 cm), which corresponded to the diameter of the striker as well as the thicknesses of the outer BLS shell for several sections. For this reason, the largest cell size considered in any of the analyses presented herein was 1.0 cm. Other resolutions considered include a 0.5-cm cell size for each of the three cases, and a 0.25-cm cell size for the case having the box in the flow.

Table E1 summarizes relevant information about the grid resolution and problem size for each case. Additionally, it includes a “Nomenclature” row used for identifying each model considered. Three mesh resolutions were considered and are referred to as the coarse, medium, and fine meshes. The corresponding cell sizes were 1.0, 0.5, and 0.25 cm, respectively.

Table E1. Summary of models considered for the three BLS configurations.

Case	1		2		3			
Nomenclature	Coarse	Medium (HS)	Coarse	Medium (HS)	Coarse	Medium	Medium (HS)	Fine (HS)
Cell size (cm)	1.0	0.5	1.0	0.5	1.0	0.5	0.5	0.25
Half-symmetry?	No	Yes	No	Yes	No	No	Yes	Yes
Total cells (millions)	256	1024	272	1088	272	2176	1088	8704

Models that make use of half-symmetry are denoted with “(HS).” Half-symmetry was not used in any of the coarse-meshed models, as computational time was manageable, and results could be obtained in a relatively short amount of time. For problems having smaller cell sizes, half-symmetry was essential for reducing the computational cost.

Only one material was specified in the input files of all models, i.e., air. All of the solid components of the BLS, including the walls, were defined as “islands.” An island, in SHAMRC jargon, refer to a non-responding structure in the mesh. These rigid structures have no momentum or energy associated with them, and their density is equal to one. Because of these properties, all of the solid components that were modeled were entirely reflective. Additionally, all island/solid geometries were constructed by using 3-D simple entities, such as cylinders, rectangular cuboids, cones, and tetrahedrons.

For air, two different initial conditions were specified in all cases. First, a constant density and pressure atmosphere model was set for the ambient air, which used a density of 1.225×10^{-3} g/cm³ and an internal energy of 2.044×10^9 ergs/g. Secondly, a pressure of 8.94939×10^7 dynes/cm² (1,298 psi) and a density of 1.082×10^{-1} g/cm³ were set for the compressed air in the driver. The density corresponded to air at a pressure of 1,298 psi and a temperature of 66°F. Additionally, three different equations of state were considered, a Doan-Nickel version, a fixed gamma law (ideal gas), and a tabular air from Los Alamos National Laboratory (SESAME tables). A comparison between these is made in this appendix for the BLS having a GSA-configuration and using a cell resolution of 1.0 cm. Based on recommendations by an experienced SHAMRC user, the Doan-Nickel EOS was selected for use on all cases.

Tracers, or stations in SHAMRC jargon, were placed throughout the mesh at the specified gauge locations and then adjusted slightly to account for mesh resolution. This was done to avoid issues with mixed cells being partially filled with air and “islands.” As a general rule, stations residing on a wall were offset by 1.5 times the resolution level of each model. For meshes composed of 1.0, 0.5, and 0.25-cm cells, the spatial offsets were 1.5, 0.75, and 0.375 cm, respectively. This condition positioned stations at least one cell away from their corresponding wall. All tracers were fixed in space, with material allowed to impinge upon and flow through their location.

Time offset

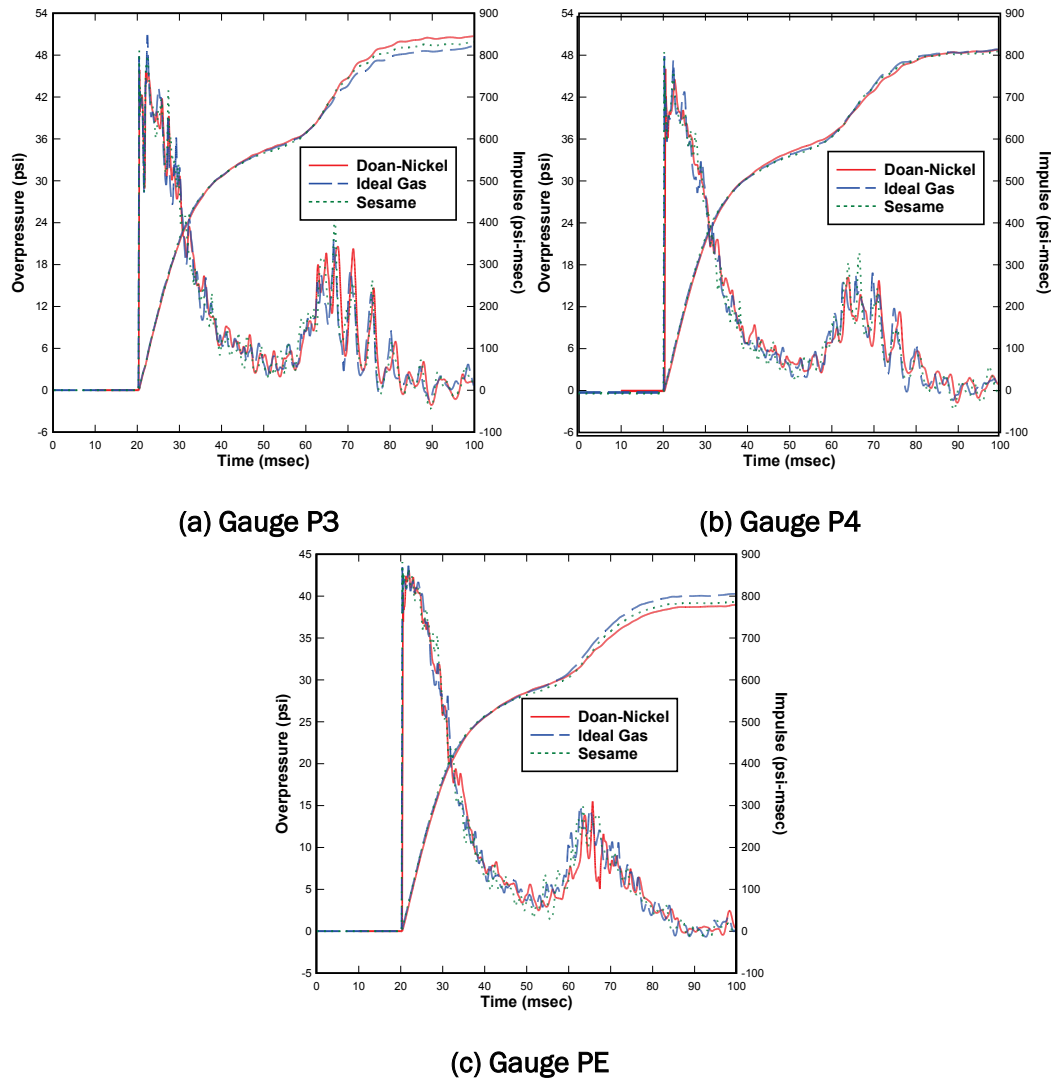
When compared with the measured data, all of the incident pressure pulses in the calculated results show a lag in the time of arrival, usually about 3.0 to 4.0 msec. The reason for the difference in arrival times is unknown at this time. To ease comparisons, the calculated arrival times are shifted throughout to match the measured data. The amount of time offset is also affected by the mesh resolution. The time offsets applied for each calculation are noted in the ensuing discussion.

EOS selection

SHAMRC has several EOS options. Of these, only three appeared appropriate for modeling the air in the BLS: (a) fixed gamma law, (b) Doan-Nickel real air, and (c) tabular air from LANL SESAME tables. The first one, the fixed gamma law, is commonly known as the ideal gas law. This EOS assumes a constant gamma of 1.4 for air. The second one, the Doan-Nickel, was developed by Larry Doan and George Nickel (1963) and is based on the fact the gamma value of air, which is the ratio between the specific heat at constant pressure and specific heat at constant volume, will vary from a value of 1.4 when incident pressures go beyond 300 psi. The third one is based on the SESAME EOS library developed by Los Alamos National Laboratory.

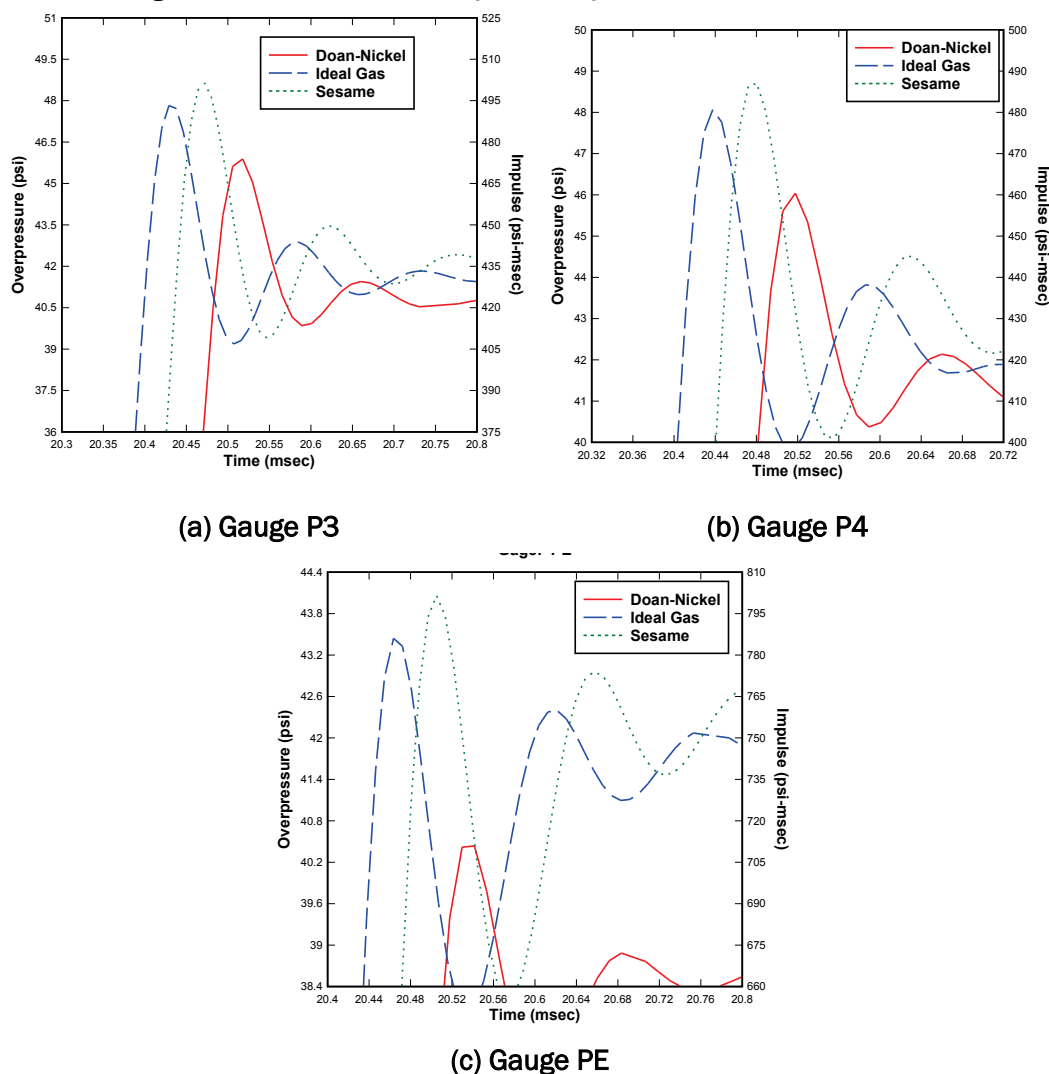
These three EOSs were tested using the BLS GSA configuration, which is the first case out of the three different experimental configurations. The mesh size for these numerical tests was fixed at 1.0 cm. Figure E1 compares the results obtained from these EOSs for three gauges located on the BLS target wall: P3, P4, and PE. As seen in the figure, there is no significant difference in the shape of the calculated pressure pulse, although

Figure E1. Influence of EOS on calculated result, GSA configuration.



there are slight differences in the magnitude of the pressure at specific time-steps. These slight differences in the pressure are enough to make the integrated impulses deviate from each other after about 60 msec, which is the time at which the pressure wave reflects from the target wall for the second time. However, the deviations do not exceed 3 percent by the time the numerical analysis was concluded at 100 msec. It is interesting to note that there is no consistency in regard to which EOS will produce the highest impulse at the end of the pressure-time records. For gauge P3, the highest impulse is attributed to the Doan-Nickel EOS, while the lowest one corresponds to the ideal gas EOS. This trend is exactly the opposite for gauge PE. For gauge P4, all three EOS produce almost the same integrated impulse. Another interesting observation is presented in Figure E2, which shows zoomed views of the initial peak pressures calculated for Gauges P3,

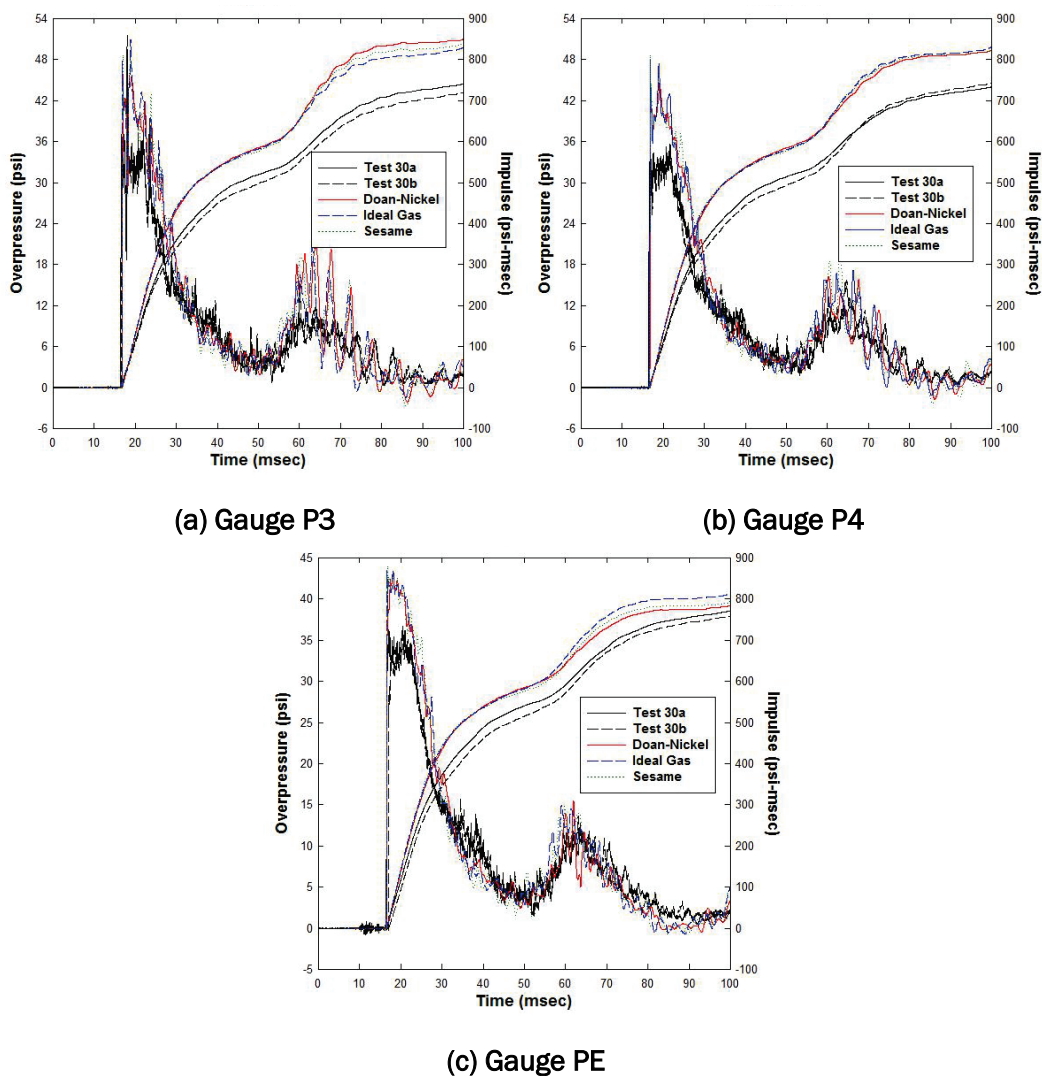
Figure E2. Calculated initial pressure peaks as a function of EOS.



P4, and PE. Note that in all three records, the EOS having the earliest time of arrival is the ideal gas followed by the SESAME and Doan-Nickel EOS (in that order). Moreover, a similar behavior can be seen for the initial pressure peak. In this case, the highest pressure is always produced by the SESAME EOS, followed by the ideal gas and then the Doan-Nickel EOS.

Comparisons with the measured data are provided in Figure E3. At first, it is obvious that, although the shape of the pressure-time records agree, the initial calculated pressure peak and impulse are both overpredicted for each EOS. Following the initial pressure pulse, during the pressure decay and second reflection, the computed pressures agree with the measured data. Since none of the EOS provided a best estimate to the measured data, additional criteria were considered to select one EOS to be

Figure E3. EOS comparisons with measured data, GSA configuration.



used in the validation calculations. Considering that the driver pressure of 1,298 psi will produce an incident pressure above 300 psi close to the driver, the Doan-Nickel EOS seemed like a good choice. Moreover, the use of this EOS was recommended by an experienced SHAMRC user.

GSA configuration, calibration Tests 30a and 30b

The first of the three BLS configurations that was tested was the GSA configuration. Two numerical models were run in SHAMRC for this case, with comparisons made with measurements on the target wall. The time offsets applied to the calculated data for each model considered are outlined in Table E2. Time offsets were applied to each gauge. The time offsets for the two models are comparable.

Table E2. Time offsets for GSA configuration models (in msec).

Gauge	Coarse	Medium (HS)	Gauge	Coarse	Medium (HS)
P1	-3.64	-3.64	P6	-3.83	-3.80
P2	-3.83	-3.77	P7	-3.86	-3.85
P3	-3.77	-3.76	P9	-3.79	-3.79
P4	-3.83	-3.79	P10	-3.82	-3.82
P5	-3.79	-3.79	PE	-3.86	-3.84

With regard to the computational resources that were used for both models, the coarse model was run for 31.0 hr using 64 processors while the half-symmetric “medium” model was started on 128 processors and eventually increased to 256 processors. The 128 processors were used for 23.0 hr while the 256 processors were used for 70.5 hr. Both models were run up to 110 msec.

Comparisons between the measured and calculated data are provided in Figure E4. Disregarding the magnitudes of the calculated pressure and integrated impulse, the overall shape of the pressure-time records agree. The general shape of the waveform is composed of an initial peak that occurs at about 16 to 17 msec, and a second peak of less amplitude that occurs around 60 msec. These two pressure spikes cause the integrated impulse to be composed of two noticeable “bumps.”

In general, the initial calculated pressure peak is higher than that measured by as much as 50 percent. This overprediction causes the impulse from the numerical results to be greater than that measured. During the first pressure decay, at usually about 30 to 40 msec, the calculated pressure briefly goes below the experimental values and then returns to similar values. This underprediction is seen as well during the pressure decay following the second reflected pressure pulse. Another observation seen during the second pressure pulse of some records (e.g., P3, P4, and P6) is that multiple pressure reflections in one of the calculated results cause the integrated impulse to deviate from the other calculated one. There is no consistency in regards to which of the two models will end up having the highest impulse. However, there is a tendency that the impulse of the numerical results will be overpredicted by as much as 10 to 20 percent. An exception to this trend is gauge P2 (Figure E4(b)). The initial calculated peak pressure correlates well with that measured, resulting in excellent comparisons with the integrated impulse.

Figure E4. Time-shifted gauge comparisons for SHAMRC, GSA configuration.

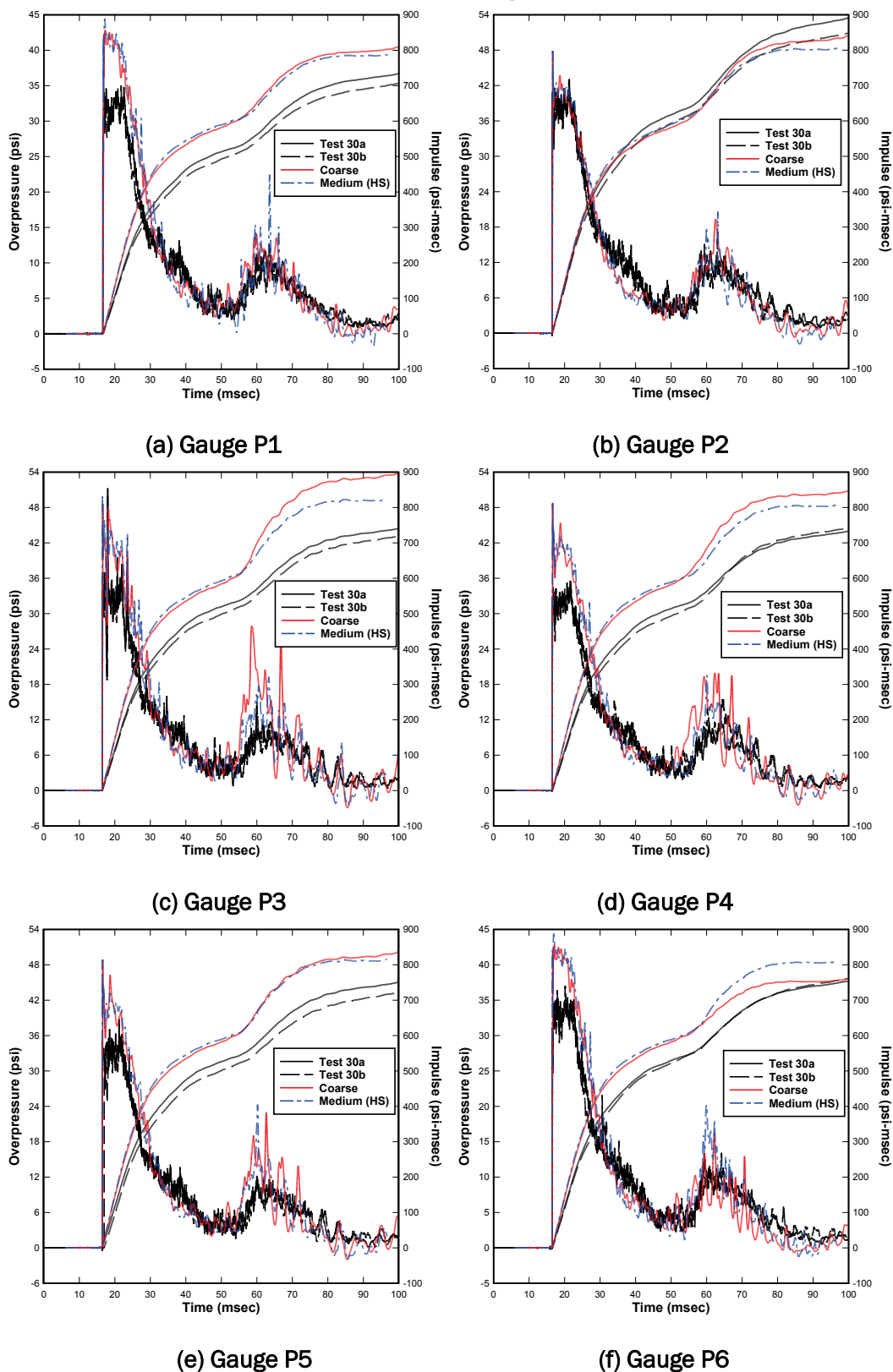
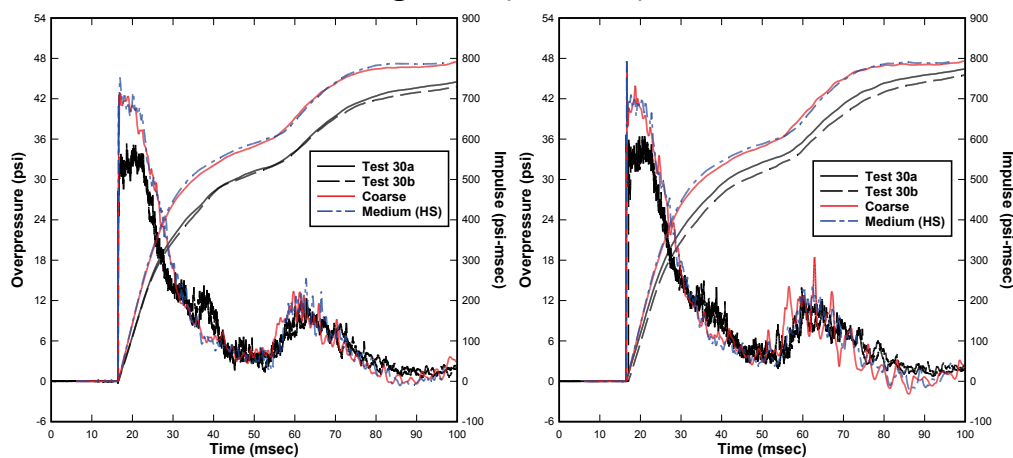
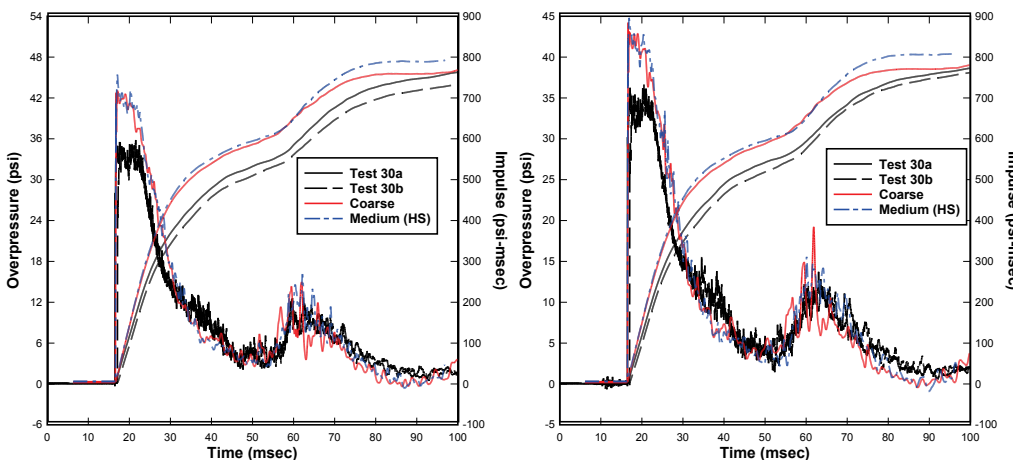


Figure E4. (Continued).



(g) Gauge P7

(h) Gauge P9



(i) Gauge P10

(j) Gauge PE

A series of pressure contours are presented in Figure E5 showing the pressure wave as it traverses the BLS and reflects from the target wall. The legend at the top of the figure shows the pressure magnitude in dynes/cm². Note that the pressure front becomes planar once it leaves the conical section. However, a mismatch in the radial dimensions of the Cascade sections seen at 20 msec makes the portion of the pressure front farther from the BLS centerline lag. This, in turn, affects the measured TOA for gauges having the largest radial distance from the BLS centerline.

Figure E5. Pressure contours from SHARMC calculation,
GSA configuration.

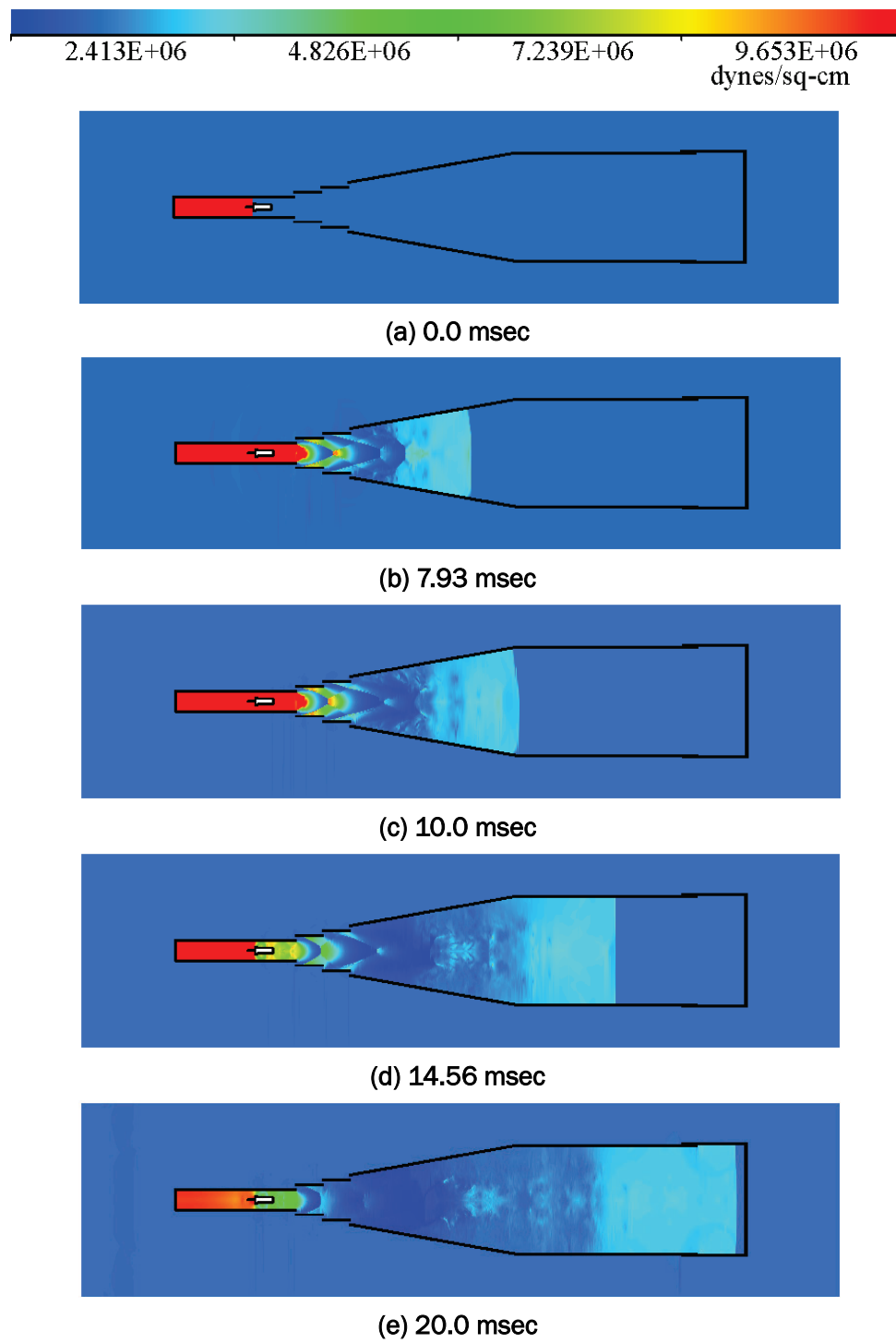
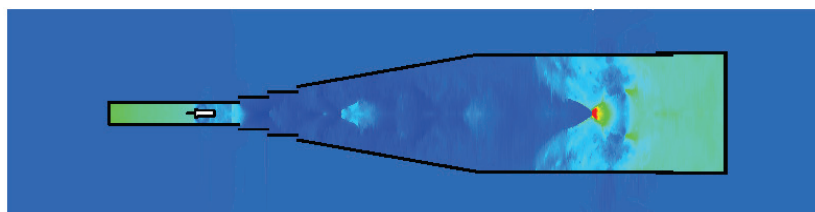
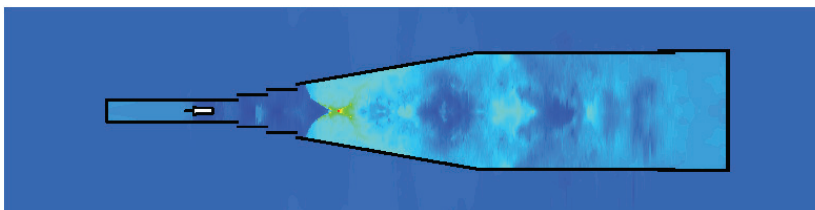


Figure E5. (Continued).



(f) 30.0 msec



(g) 40.0 msec

Calibration tests with 8-ft×8-ft C2SQ configuration

Similar to the GSA configuration, two models were run for this second case. The first was a fully-3-D mesh with a 1.0-cm resolution. The second involved a half-symmetry mesh with a 0.5-cm resolution. In the tables and figures of this section, these two runs are identified as “Coarse” and “Medium (HS)”, respectively. For the coarse model, 256 processors were used for a total wall time of about 26.6 hr. For the half-symmetry medium model, 256 processors were used for about 68.9 hr.

As mentioned before, the numerical results obtained for this case had a later time of arrival than that measured. Because of this, the calculated pressure-time-histories were shifted to match the measured values. Table E3 outlines the time shifts applied to each gauge. In general, the offsets for the coarse models are less than those for the medium one. The reason for this, as mentioned in the setup section of this appendix, is that the stations in the coarser model were spatially offset twice the distance (1.5 vs. 0.75 cm) than those in the medium model. This positioned the gauges in the coarse model closer to the driver resulting in slightly earlier times of arrival.

Table E3. Time offsets for 8 ft×8 ft C2SQ configuration models (in msec).

Gauge	Coarse	Medium (HS)	Gauge	Coarse	Medium (HS)
P1	-3.43	-3.95	P8	-3.36	-3.87
P2	-3.30	-3.83	P9	-3.40	-3.93
P3	-3.32	-3.81	P10	-3.57	-4.07
P4	-3.39	-3.91	P11	-3.57	-4.08
P5	-3.36	-3.88	P12	-3.43	-3.96
P6	-3.35	-3.87	PR	-3.87	-4.06
P7	-3.37	-3.87			

Comparisons between the calculated and measured data are provided in Figure E6. Except for a few gauges, these comparisons are not very different from the results that were presented for the first case. First, the shape of the pressure-time records is dominated by two pressure pulses, which correspond to the first and second interaction of the pressure wave with the gauges on the target wall. Second, the two pressure pulses are “echoed” in the integrated impulses as the shape of these can be explained as having two curvilinear sections. Third, the initial peak pressure tends to be over-predicted, causing the impulse to be overpredicted as well. A noticeable difference with respect to the first case is that the calculated pressures following the first pressure decay are in better agreement with the experimental data.

There were two gauges on the target wall whose behavior differed markedly from the other gauges. The measured data for gauge P7 is suspiciously low as compared to the other gauges, suggesting an anomalous measurement at this gauge location. For gauge P8, the calculated pressure and impulse matches the measured data until the first pressure decay, where the pressure is slightly lower, resulting in an underprediction of the impulse.

Figure E6. Time-shifted gauge comparisons for SHAMRC,
8-ft×8-ft C2SQ configuration.

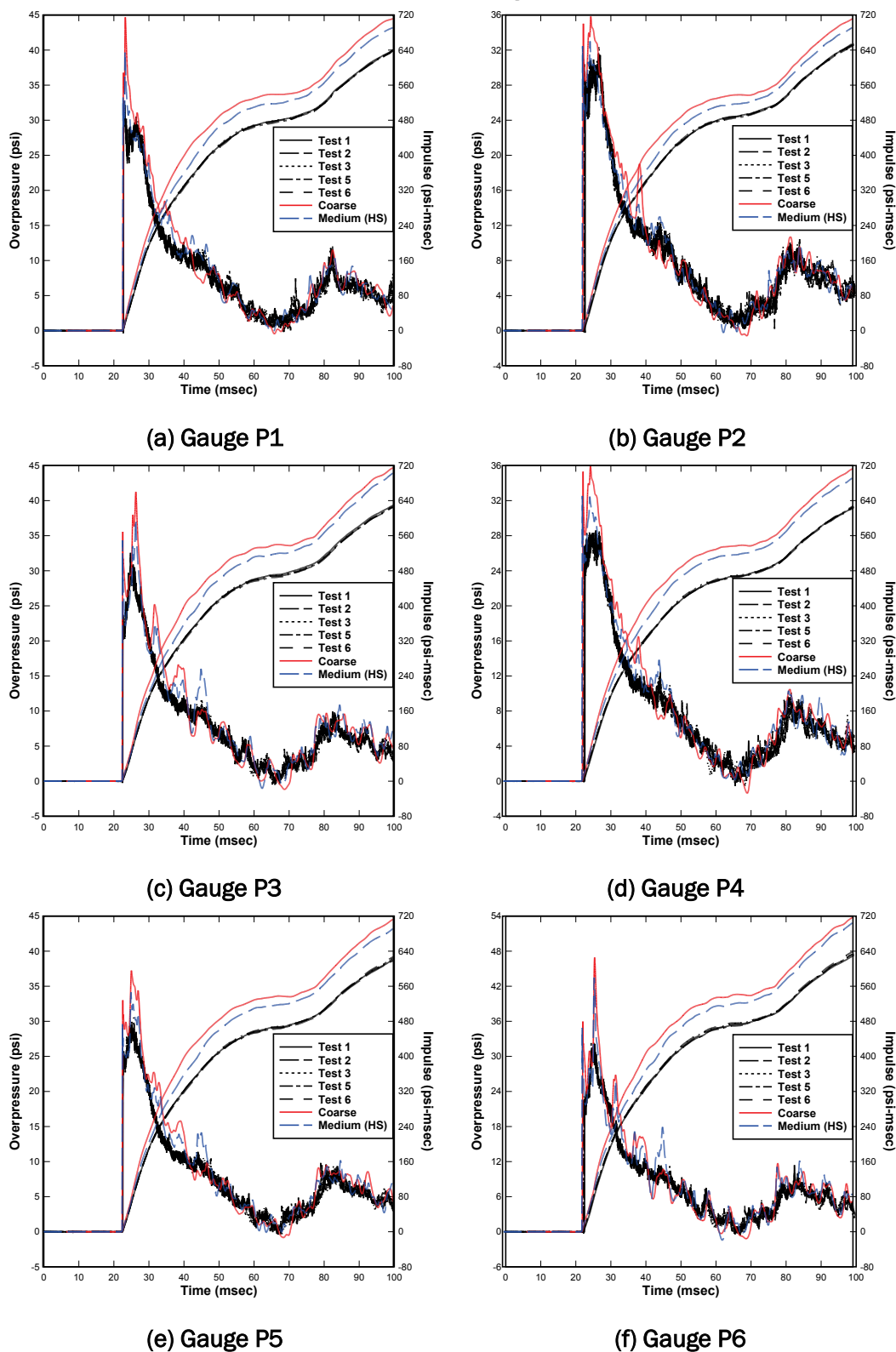
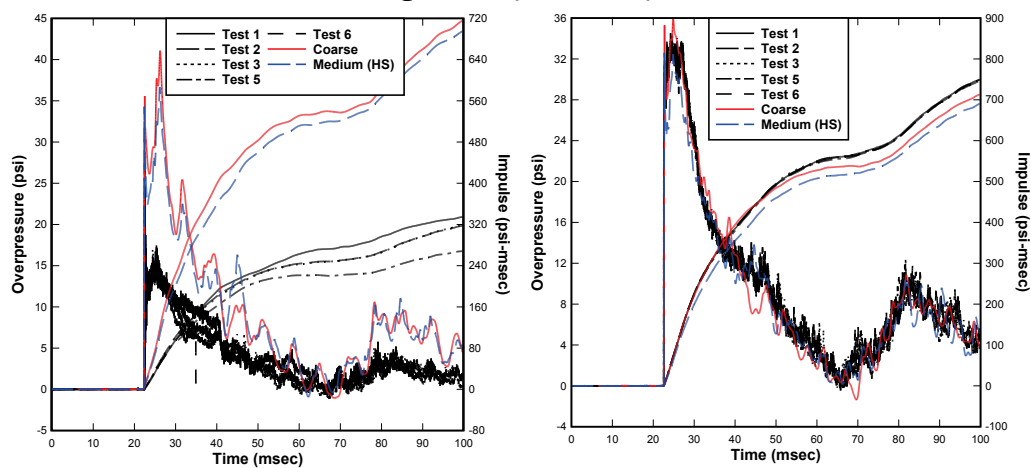
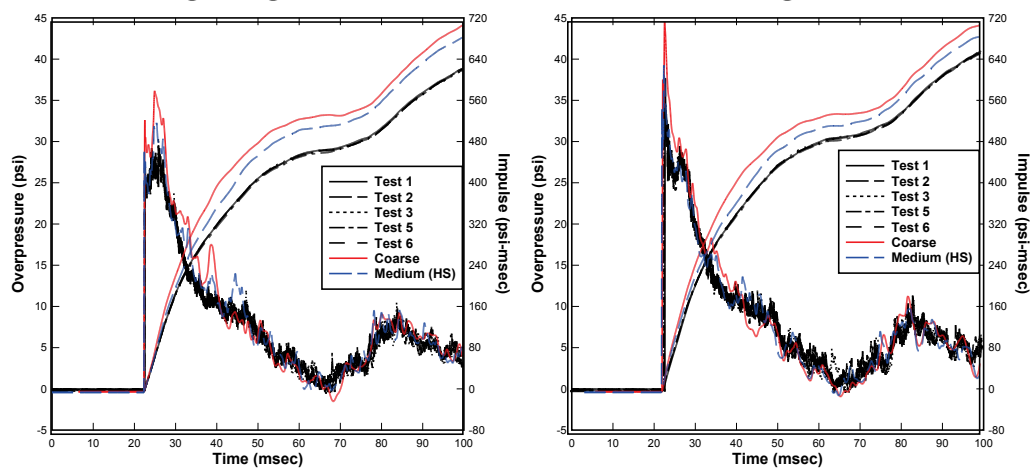


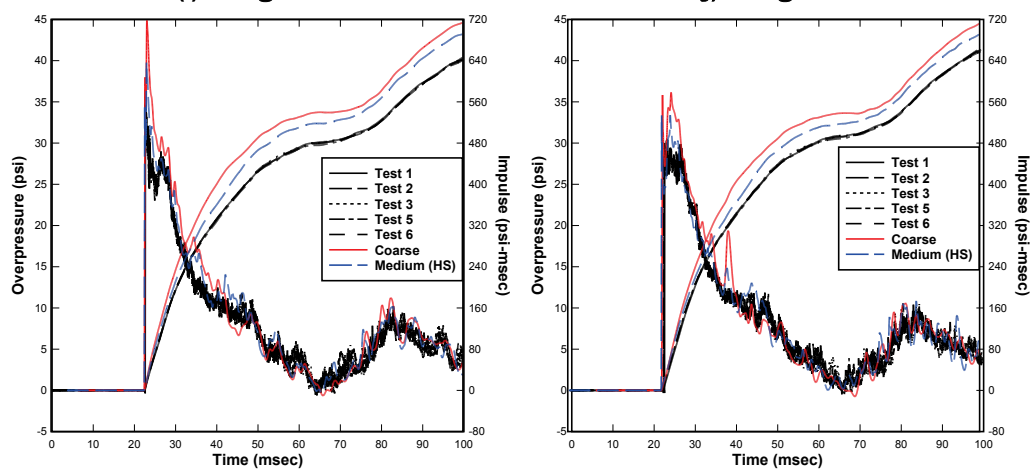
Figure E6. (Continued).



(g) Gauge P7



(i) Gauge P9



(k) Gauge P11

(l) Gauge P12

Comparisons between the calculated and measured data for the side-on pressure gauge PE are provided in Figure E7. The same trends noted previously apply here. That is, there is an overall tendency of overprediction in the calculated results. Given that this is a side-on gauge, there is a noticeable difference in the shape and frequency of secondary reflections when compared to the other gauges. The calculation appears to capture the timing of these secondary reflections; however, there are notable differences in the amplitudes of the peaks.

Figure E7. Comparisons for side-on pressure gauge PE.

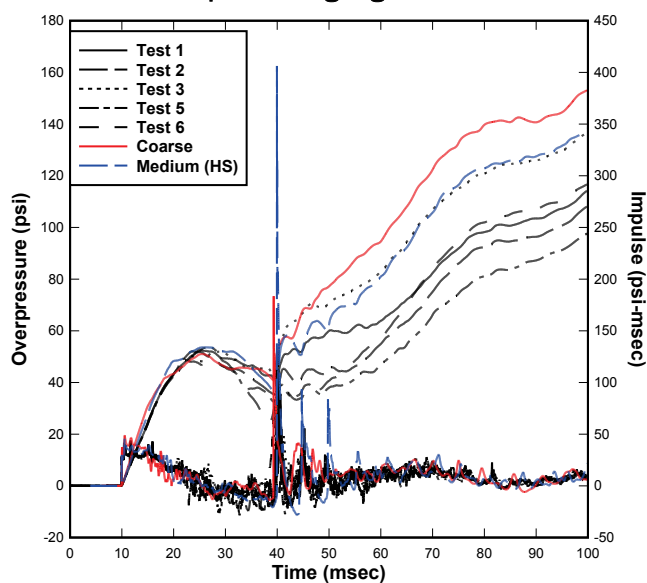
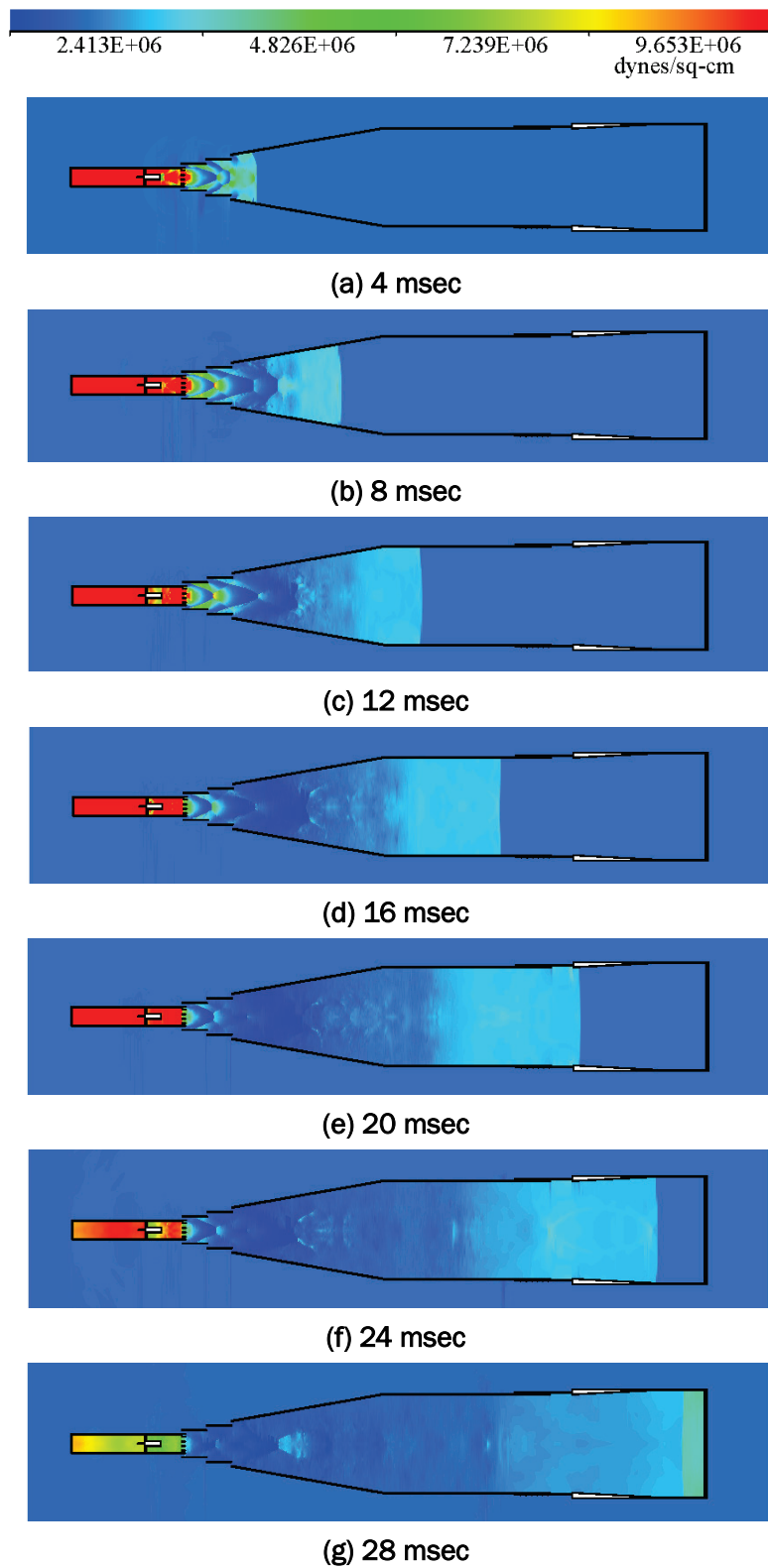


Figure E8 shows pressure contours of the compressed air front traveling from the driver to the target wall of the BLS. The contours at time zero are not included, as they were not radically different from what was shown for the first case. One main difference between these contours and the ones shown earlier is that it takes more time for the pressure front to reach the end-wall, given that the overall length of the BLS is greater for this case. Another difference is the inclusion of the grill at the location of the first vent. However, it is not clear from these images if the grill induces significant turbulence into the flow as it traverses the grill.

Figure E8. Pressure contours from SHAMRC calculation,
8-ft×8-ft C2SQ configuration.



BLS 8-ft×8-ft C2SQ configuration with box

The third case had the same configuration as the second with the only difference being an instrumented box placed in the C2SQ section. Four models were considered for this case. They included two fully-3-D models having resolutions of 1.0 and 0.5 cm, and two half-symmetry models having resolutions of 0.5 and 0.25 cm. Each of these models required varying computational resources. The first model (coarse, fully-3-D) utilized 128 processors for a total of 52 hr of wall clock time. The second model (medium, fully-3-D) was initially run for 23.5 hr using 128 processors, but the number of processors had to be increased to decrease the computational time. The model was restarted using 256 processors for 47 hr, after which it was restarted again using 512 processors for 48 hr. The third model (medium, half-symmetry) was started on 128 processors for 47.75 hr and restarted with 256 processors for 53.5 hr. The fourth model (fine, half-symmetry) was started on 4,096 processors for 176.3 hr, which advanced the simulation to about 45.0 msec. The number of processors was doubled to 8,192 for about 42.1 hr, which progressed the simulation time to 58.58 msec. Finally, the number of processors was increased to 16,384 for 29.5 hr, which carried the calculation out to a little over 60.0 msec. Given the excessive cost of the fine meshed calculation, it was decided not to continue it any further.

The times for which the numerical results were shifted to match the measured TOA are summarized in Tables E4 and E5. There is no consistency in which of the four models required the largest time offset, but the one that required the smallest offsets was the coarse model. Moreover, the medium fully-3-D and half-symmetric models required identical time offsets for most of gauges, which was expected given that the cell sizes of both problems were equal. Gauges PBR1 and PBR2 do not have a time offset recorded for the medium model, nor are they included in the pressure-time plots because they were incorrectly positioned in the model.

Table E4. Time offsets for gauges on the target wall (in msec).

Gauge	Coarse	Medium	Medium (HS)	Fine (HS)
P3	-2.97	-3.22	-3.20	-3.14
P9	-3.06	-3.30	-3.30	-3.23

Table E5. Time offsets for gauges on box (in msec).

Gauge	Coarse	Medium	Medium (HS)	Fine (HS)
PBB1	-2.97	-3.47	-3.48	-3.42
PBB2	-3.06	-3.48	-3.50	-3.44
PBB3	-3.24	-3.49	-3.51	-3.44
PBB4	-3.31	-3.51	-3.51	-3.45
PBF1	-3.30	-3.49	-3.49	-3.44
PBF3	-3.32	-3.50	-3.50	-3.47
PBF5	-3.28	-3.50	-3.50	-3.47
PBF6	-3.31	-3.49	-3.49	-3.45
PBF7	-3.39	-3.49	-3.52	-3.48
PBF8	-3.30	-3.50	-3.50	-3.47
PBL1	-3.30	-3.51	-3.51	-3.47
PBL2	-3.32	-3.50	-3.48	3.44
PBL3	-3.30	-3.50	-3.50	-3.44
PBL4	-3.29	-3.49	-3.49	-3.42
PBR1	-3.29	N/A	-3.48	-3.42
PBR2	-3.30	N/A	-3.50	-3.45
PBR3	-3.30	-3.48	-3.48	-3.48
PBR4	-3.31	-3.50	-3.50	-3.45
PBT1	-3.32	-3.51	-3.51	-3.46
PBT2	-3.30	-3.50	-3.48	-3.45
PBT3	-3.29	-3.48	-3.48	-3.43
PBT4	-3.30	-3.50	-3.50	-3.44
PBT5	-3.33	-3.52	-3.52	-3.45

Comparisons between the calculated and measured data are provided in Figures E9 through E14. The first set of records show the gauges located on the target wall (see Figure E9). The behavior seen in these plots is not

too different from that of the cases discussed earlier, where the initial peak pressure is overpredicted in the calculations, causing the integrated impulse to be higher than that measured.

The comparisons for gauges located on the back face of the box are provided in Figure E10. The shapes of these records differ from the ones shown for gages P3 and P9 as they are facing downstream, away from the driver. The first peak observed in the records is attributed to the first interaction of the pressure wave as it travels over the box. The second is attributed to the reflected wave that is travelling upstream. Overall, the pressures and impulses are overpredicted in the calculation. An exception to this is gauge PBB3 in which the duration of the first pressure pulse in the calculation is shorter than that measured, resulting in better correlation with the measured impulse. Additionally, gauge PBB4 displays the biggest difference in the integrated impulse due to a high peak pressure exhibited in the second pressure pulse in the plot.

The comparisons for gauges located on the front face of the box are provided in Figure E11. These results are reminiscent of all the gauges previously shown that were positioned on the target wall. That is, almost all these records show overpredictions in the calculated pressures as well as in the integrated impulse. The obvious exception to this overprediction is gauge PBF6, whose measured impulse is 11 to 12 percent higher than the calculated results. This is caused by a lower calculated pressure associated with the second, reflected pressure pulse.

Figure E9. Time-shifted gauge comparisons for SHAMRC, target wall.

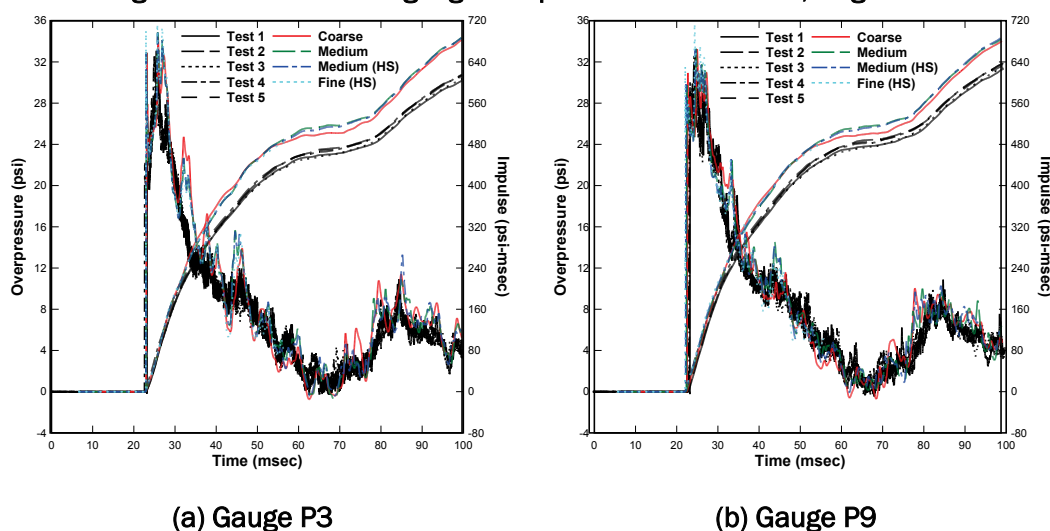


Figure E10. Time-shifted gauge comparisons for SHAMRC, back face.

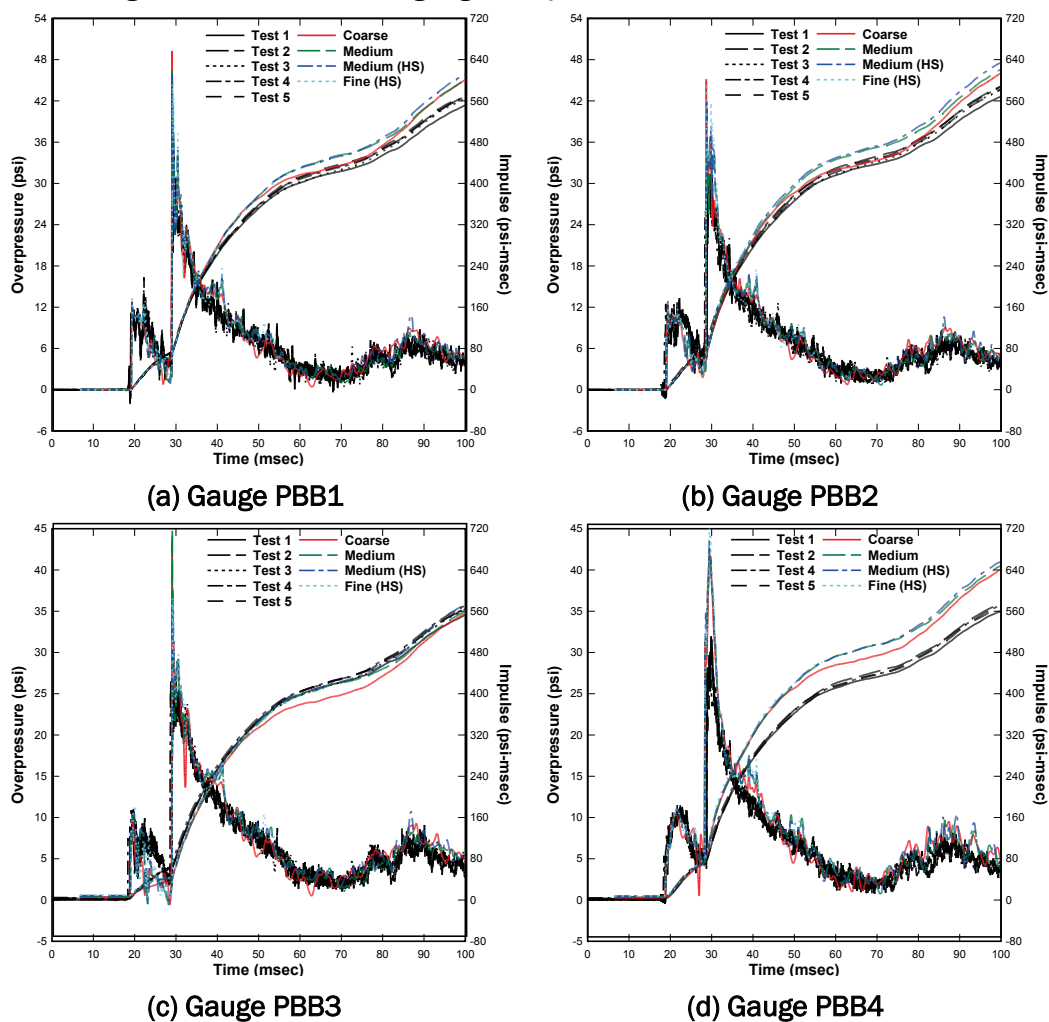
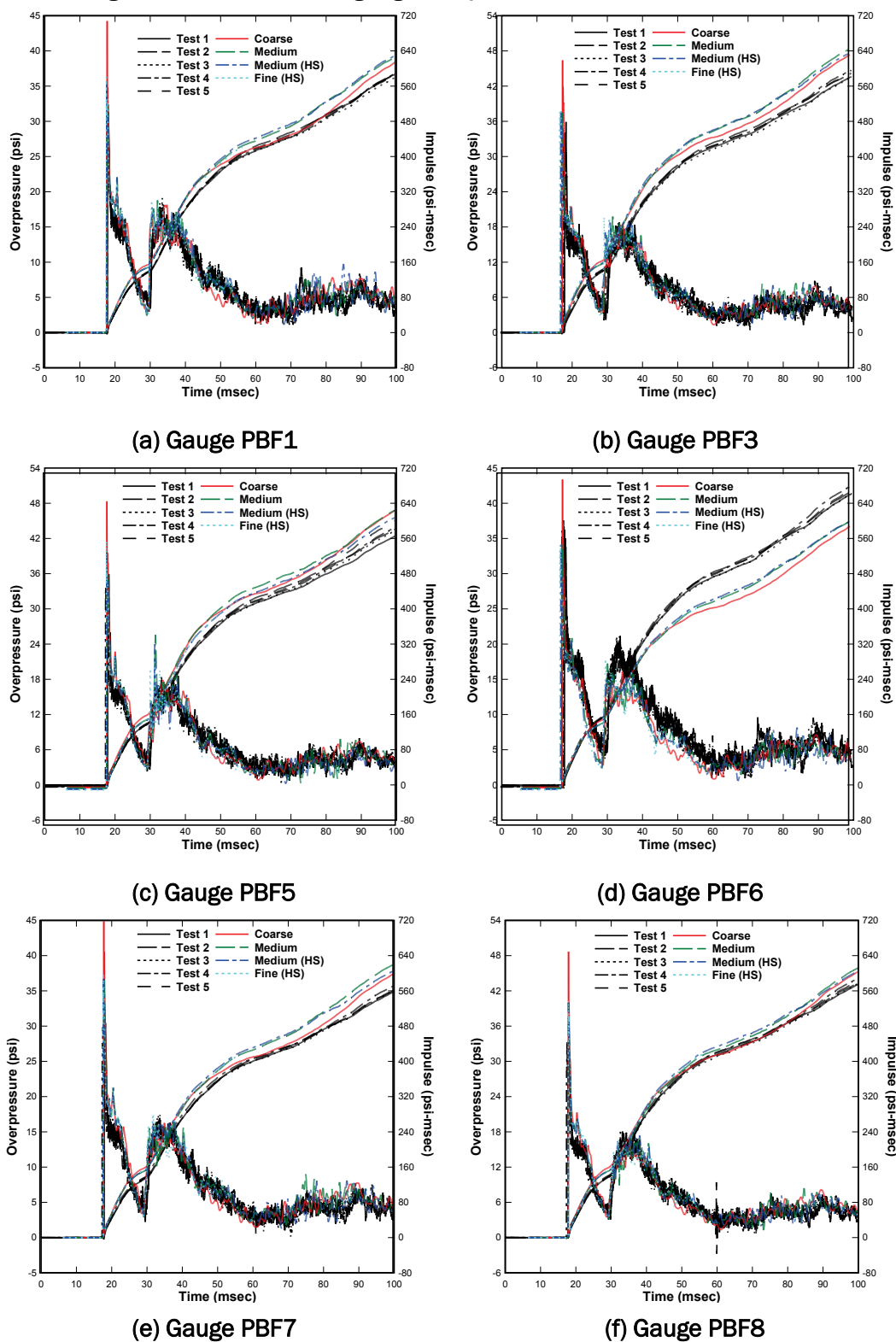
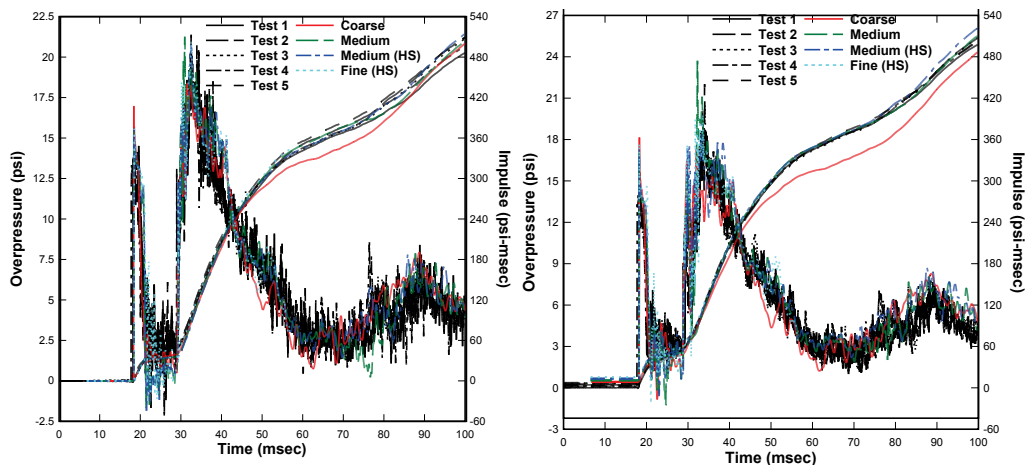


Figure E11. Time-shifted gauge comparisons for SHAMRC, front face.



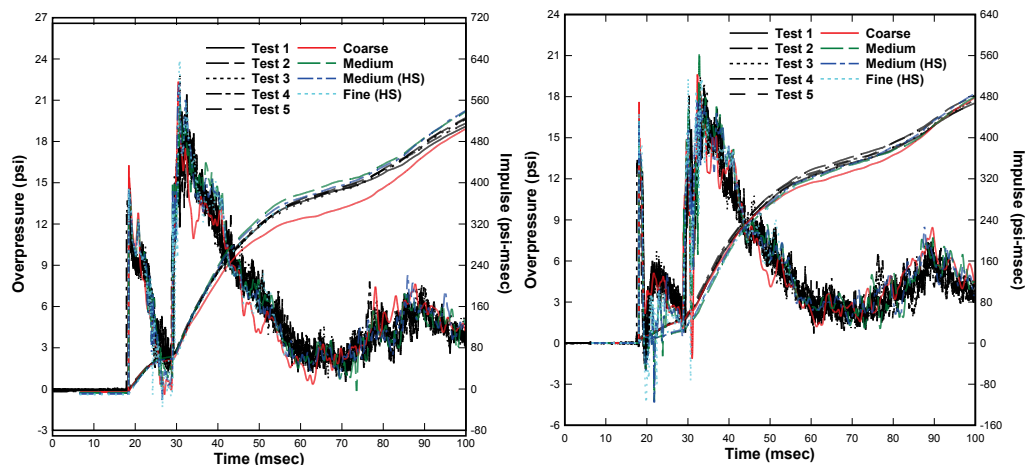
The comparisons for gauges on the left and right side of the box are shown in Figures E12 and E13, respectively. Both sets of results are not very different from each other. They all contain an initial pressure pulse of short duration followed by a second and larger pressure pulse that lasts longer. A third, less intense pressure pulse can be seen at about 80 msec.

Figure E12. Time-shifted gauge comparisons for SHAMRC, left face.



(a) Gauge PBL1

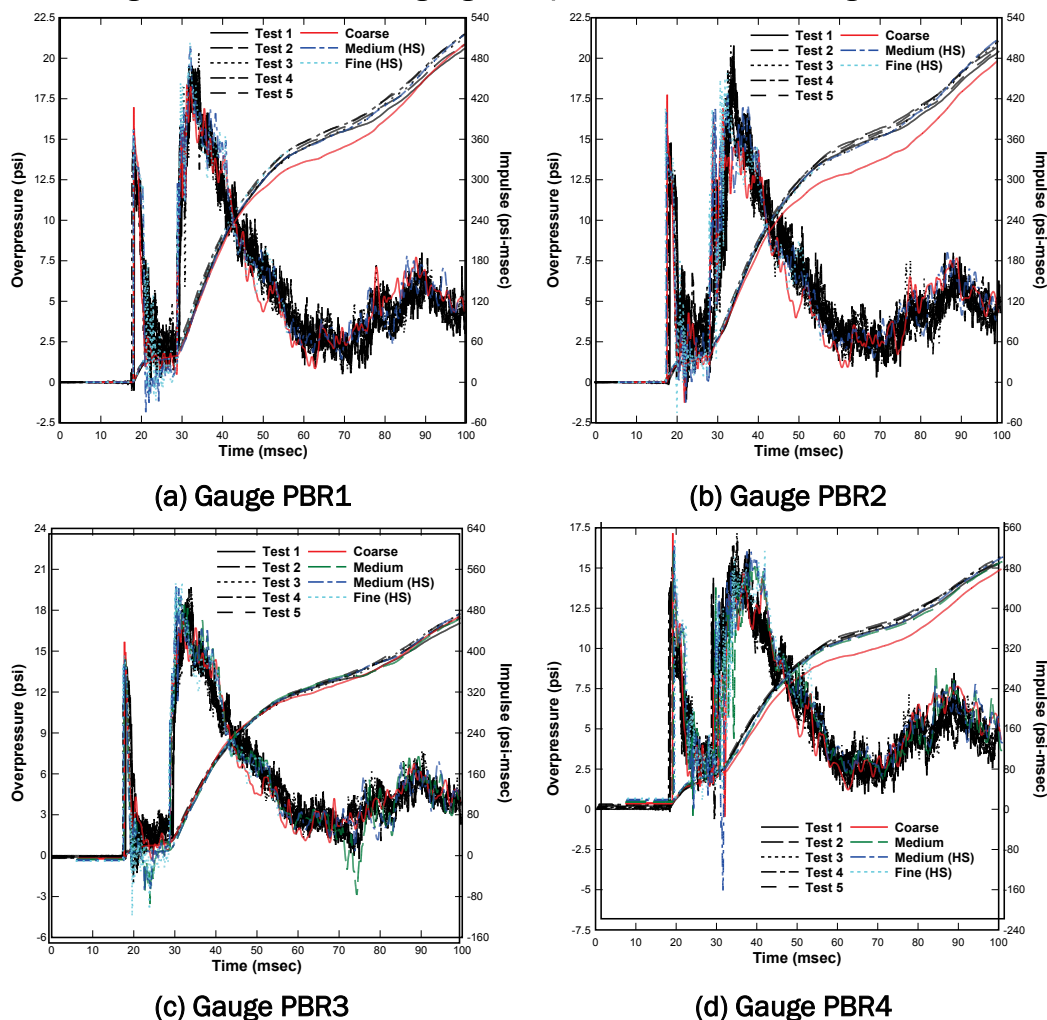
(b) Gauge PBL2



(c) Gauge PBL3

(d) Gauge PBL4

Figure E13. Time-shifted gauge comparisons for SHAMRC, right face.



Overall, the calculated results are in good agreement with the experimental data for gauges on the right and left side of the box, with the greatest disparities noted for the coarse-meshed model. On most pressure-time-histories shown in Figures E12 and E13, the final impulse for the coarse model is underpredicted by 5 to 10 percent. This is mostly the result of underpredicting the peak pressure during the second pressure pulse. Recall that gauges in the models are offset 1.5 cells away from the BLS component in which they are located to avoid issues with mixed cells, and that the model having the largest offset is the one with the largest cell size (i.e., the coarse model). It is likely that the gauges for the coarser model residing on both sides of the box experienced less reflected pressure than the gauges in finer models, resulting in the data for these gauges being less than that measured.

The comparisons for gauges located on the top face of the box are provided in Figure E14. These plots have a shape that is similar to the ones shown for gauges on the left and right side of the box. Moreover, the calculated results compare well with the measured data. The peak pressures are almost identical, and the duration of each pressure pulse is comparable. The measured impulse is bounded by the calculated ones on every plot. On three out of the five plots, the coarse model exhibits the lowest impulse. It is likely that this is related to the spatial offset of gauges in this model from the box, as it is larger for the coarse model than for any other one.

Figure E15 shows a top and side view of pressure contours displaying the compressed air wave interacting with the box. There are three relevant phenomena that can be observed in these images. First, one can see how the pressure front becomes almost planar as it nears the box. This planarity, however, does not translate into a constant magnitude of pressure as several shades of blue can be clearly seen inside of the compressed air, indicating different values of pressure. Secondly, a green intense color can be seen on the front of the structure in the 21.2- to 22.0-msec frames. This is caused by the wave reflecting from the box, resulting in an increase to the pressure magnitude. Finally, several low pressure regions can be observed on both sides of the box as well as above it as the pressure front engulfs the box. These dark blue spots are an indication of vortices occurring as the pressure wave impinges against the box and diffracts around it.

Figure E14. Time-shifted gauge comparisons for SHAMRC, top face.

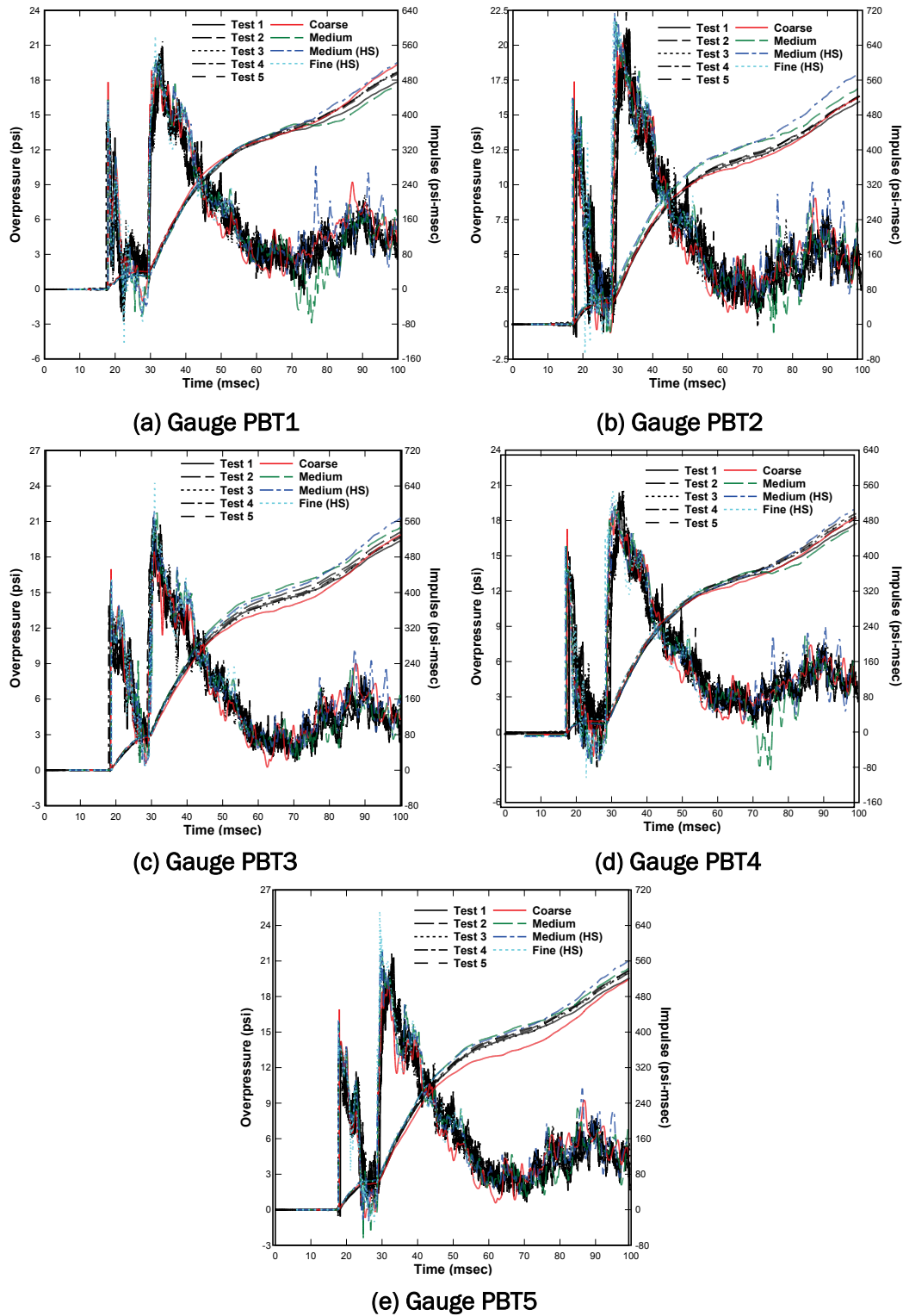
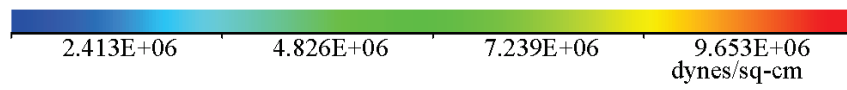
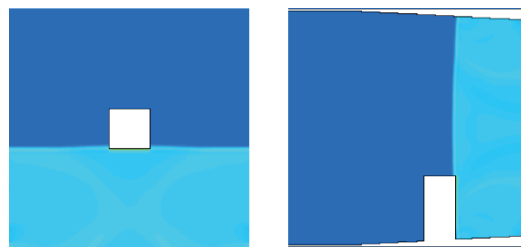


Figure E15. Pressure contours around box in SHARMC calculation.



(h) 20.8 msec



(b) 21.2 msec



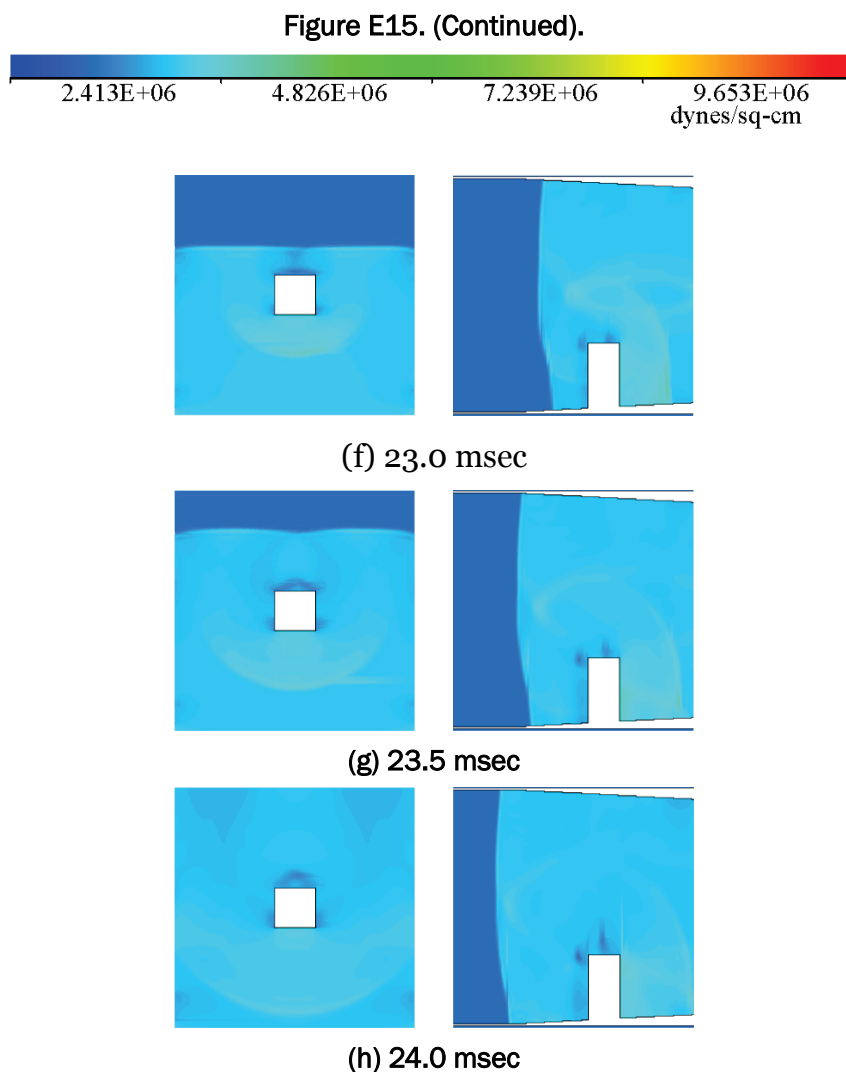
© 21.6 msec



(d) 22.0 msec



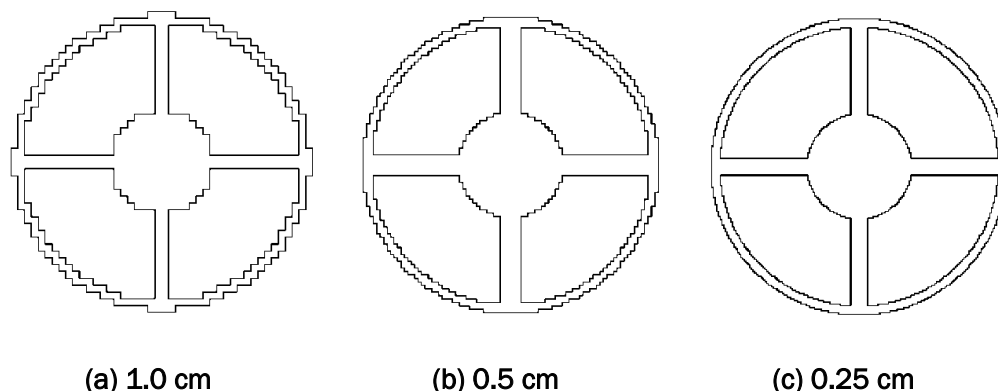
(e) 22.4 msec



Other spatial images

Various images are presented in this section showing how several BLS components were actually represented in models having different mesh resolution. The first image, shown in Figure E16, shows a cross-section view of the striker flange at the mid-section of the flange. The curvature of the flange structure is better represented as the mesh is refined. SHAMRC has an option termed “shores,” which can be used to alleviate these “stair-step” structures. Shores are essentially cells composed evenly of an island and a fluid. In this case, a shore boundary would pass through the diagonal of a cell for a more accurate representation of the structure. However, they are only available in 2-D calculations, and their use was not employed.

Figure E16. Striker flange cross-section.



As seen in the previous figure, the striker flange is composed of four bars that attach the outer ring to a smaller disk at the center of the flange. Attached to the front and back of this disk are the striker and spring mechanism, respectively. These were modeled as two cylinders of different diameters. Figure E17 shows a top view at half-width of the striker flange that was shown in the previous figure. The horizontal sections in these images are the two horizontal bars shown in the previous figure. The vertical section above the bars seen in the three images is the spring mechanism. The striker is below the bars and can only be seen in the last two images. As with the previous figure, Figure E17 shows how this component was actually represented in models having different resolutions. In the first image, one can see that the striker does not even show up in the model. Moreover, the thickness of the BLS wall around the striker flange appears to be greater than the one shown for the other two models. In the center image, the striker is visible and the thickness of the BLS wall appears to be less than in the first image. In the image on the right, one can actually notice a difference in the thickness and radius of the CVC-1 component inside the C1 section (above the horizontal bars of the striker flange) with respect to the striker flange and driver section (around and below the horizontal bars of the striker flange).

The grill, as it was represented in models having different resolution, is shown in Figure E18. The grill is better resolved as the mesh resolution increases. For the model having a cell size of 1.0 cm, the grill is poorly replicated. When the cell size is decreased by half, some of the features of the grill start showing up. However, at 0.5 cm, the grill is still missing six of the horizontal bars. It is not until the cells size is decreased to 0.25 cm that the grill is captured in its entirety.

Figure E17. Top view of striker and flange.

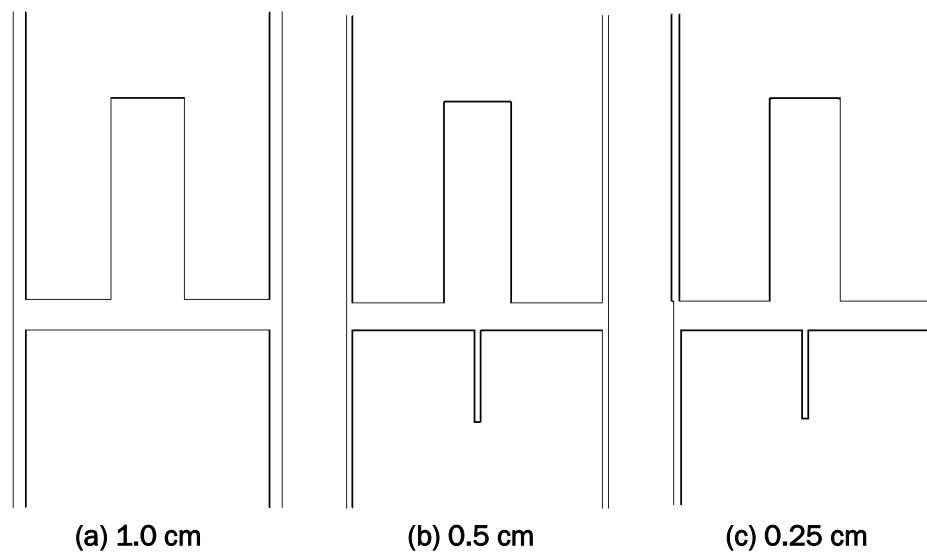


Figure E18. Grill cross-section.

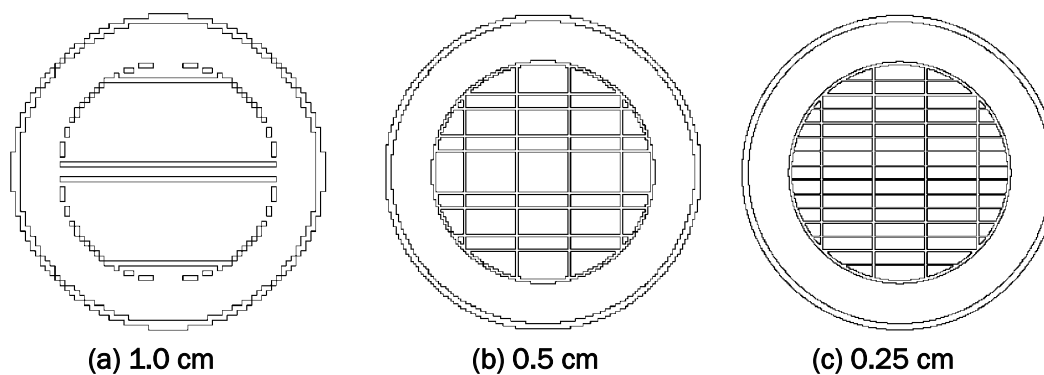
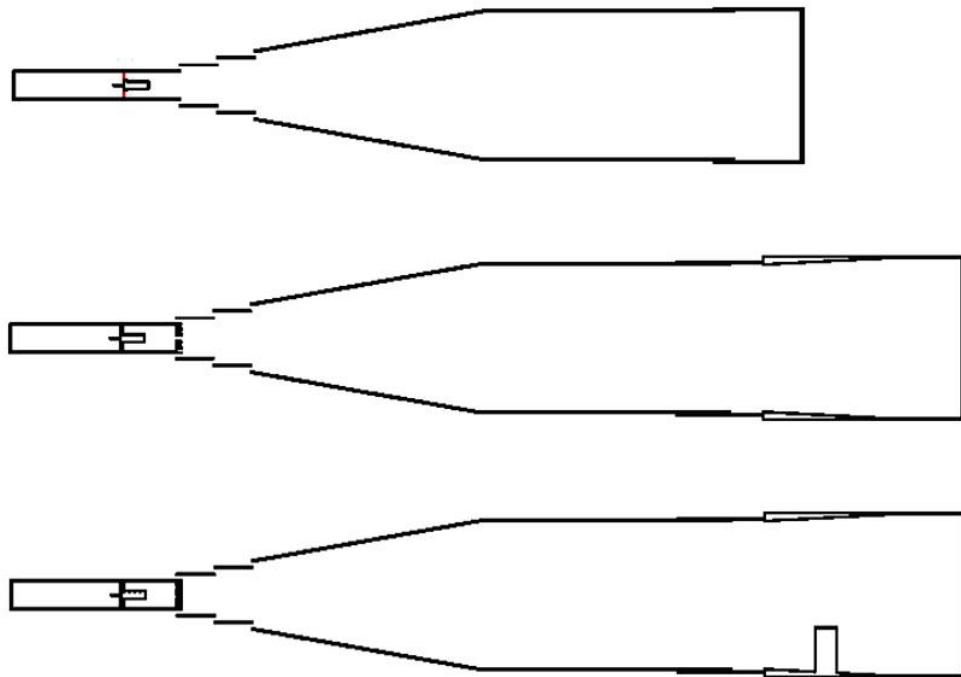


Figure E19 shows profiles at mid-width of the BLS for each of the cases considered. Several components can be seen in the images, including the striker, the striker flange, the spring mechanism, the grill and the instrumented box.

Issues

Several issues were noted while running SHAMRC. Two of these issues are related to generating plots using PULL, while the third one is about a warning message that kept showing up while the calculations were ongoing.

Figure E19. Cross-section of the BLS for the three cases considered.



The first issue worth mentioning is about generating spatial plots at specific times of the simulation using PULL. Like many other CFD codes, spatial plots can be created from times at which the code generated a “dump” file. A dump file contains all of the necessary information to restart the simulation. The file size for these dump files can be quite large, depending on the size of the computational grid. For the calculations shown in this appendix, these dump files were around a dozen gigabytes for the coarsest model to several hundred gigabytes for the finest one. So if one, as an example, wanted to create plots at 100 specific time-steps, one would first need to generate dump files at each of the time-steps. This will be a problem if one has limited disk space. Assuming that the size of a dump file is around 100 gigabytes, generating these 100 spatial plots would require 10,000 gigabytes of space.

The second issue worth mentioning is related to generating spatial plots for large problems (problems having more than 1 billion cells). In this case, the time needed to generate one spatial image is proportional to the number of cells in the problem. This is not an issue for problems having a relatively small amount of cells, but it is definitely perceptible for larger

problems. As an example, consider the half-symmetry fine-meshed model which consists of about 8.7 billion cells. It took the code about 79 min to generate the single spatial image depicted in Figure E19. So if one wanted to generate 20 spatial plots, it would take more than a full day to generate them. It is relevant to mention that the program PULL, used to generate spatial images, can only be run in serial.

The third and final issue worth mentioning is about a message that kept showing up in the output files of the models considered. The message warned about the energy being below 1.0E6 ergs in some areas of the mesh being used by a particular processor. Below is an example of such message:

```
On processor    19:
Energy below 1.e6 in MOVEY at i=  1 j= 162 k= 139
h:
  0.00000E+00 -8.61164E-02  7.23796E+04  2.23971E+09  1.53152E-04  1.01315E+06
Energy below location (2.500000E-01 -1.975000E+01  1.687500E+02).
```

The user's manual warns that this message is printed whenever the internal energy of a cell drops below 1.0E6 ergs in the advection phase. The code reacts by determining the energy deficit and reducing the kinetic energy of the cell by the deficit amount so that the total energy of the cell will be 1.0E6. According to the manual, this generally happens when the stability factor is too high for the calculation. Therefore, it was decided to choose stability factors that matched what was recommended by the user's manual. For the multiple 3-D simulations shown in this appendix, an initial value of 0.1 was chosen as the stability factor for the calculation of the Courant condition time-step. This factor was allowed to gradually increase by 0.02 up to a maximum of 0.5.

REPORT DOCUMENTATION PAGE

Form Approved
OMB No. 0704-0188

Public reporting burden for this collection of information is estimated to average 1 hour per response, including the time for reviewing instructions, searching existing data sources, gathering and maintaining the data needed, and completing and reviewing this collection of information. Send comments regarding this burden estimate or any other aspect of this collection of information, including suggestions for reducing this burden to Department of Defense, Washington Headquarters Services, Directorate for Information Operations and Reports (0704-0188), 1215 Jefferson Davis Highway, Suite 1204, Arlington, VA 22202-4302. Respondents should be aware that notwithstanding any other provision of law, no person shall be subject to any penalty for failing to comply with a collection of information if it does not display a currently valid OMB control number. **PLEASE DO NOT RETURN YOUR FORM TO THE ABOVE ADDRESS.**

1. REPORT DATE (DD-MM-YYYY) November 2016		2. REPORT TYPE Report 1		3. DATES COVERED (From - To)	
4. TITLE AND SUBTITLE Modeling the Blast Load Simulator Airblast Environment using First Principles Codes – Report 1, Blast Load Simulator Environment				5a. CONTRACT NUMBER	
				5b. GRANT NUMBER	
				5c. PROGRAM ELEMENT NUMBER U451186	
6. AUTHOR(S) Gregory C. Bessette, James L. O'Daniel, Stephen A. Akers, Alyson A. Armstrong, Gustavo Emmanuelli, Clayton Mord, and Richard A. Weed				5d. PROJECT NUMBER 444856	
				5e. TASK NUMBER 12	
				5f. WORK UNIT NUMBER 93D08B	
7. PERFORMING ORGANIZATION NAME(S) AND ADDRESS(ES) U.S. Army Engineer Research and Development Center Geotechnical and Structures Laboratory 3909 Halls Ferry Road Vicksburg, MS 39180-6199				8. PERFORMING ORGANIZATION REPORT NUMBER ERDC/GSL TR-16-31	
9. SPONSORING / MONITORING AGENCY NAME(S) AND ADDRESS(ES) Defense Threat Reduction Agency, Nuclear Technologies Directorate Ft. Belvoir, VA 22060-6201				10. SPONSOR/MONITOR'S ACRONYM(S)	
				11. SPONSOR/MONITOR'S REPORT NUMBER(S)	

Approved for public release; distribution is unlimited.

13. SUPPLEMENTARY NOTES

14. ABSTRACT

The Blast Load Simulator (BLS) at the U.S. Army Engineer Research and Development Center (ERDC) has been utilized for applying simulated blast loads on structures for more than a decade; however, the experimental efforts to date have not included a computational modeling component. The Defense Threat Reduction Agency tasked ERDC to conduct an integrated experimental/computational program to evaluate several first principles codes (FPCs) for modeling airblast environments typical of those encountered in the BLS. The FPCs considered were CTH, DYSMAS, Loci/BLAST, RAGE, and SHAMRC. These codes afforded a range of numerical solvers and equation of state options for the modeling effort. The FPCs were evaluated against data generated in the BLS. Three experimental configurations were considered for the validation. These included two empty configurations, with comparisons drawn against reflected pressures measured at the downstream end wall. The third included a box-like structure in the flow field. The structure was instrumented on the exposed surfaces to provide a more challenging scenario for the model comparisons. The purpose of the integrated program was to assess computational accuracy and cost of the aforementioned FPCs and identify any shortcomings in the physics modeling and areas for future improvement. Findings from the integrated program are discussed in this report.

15. SUBJECT TERMS			Shock (Mechanics)		Computer simulation	
Blast effect-Testing			Shock tubes		Numerical analysis	
Detonation waves			Scientific apparatus and instruments			
16. SECURITY CLASSIFICATION OF:			17. LIMITATION OF ABSTRACT	18. NUMBER OF PAGES	19a. NAME OF RESPONSIBLE PERSON	
a. REPORT	b. ABSTRACT	c. THIS PAGE			19b. TELEPHONE NUMBER (include area code)	
UNCLASSIFIED	UNCLASSIFIED	UNCLASSIFIED	SAR	206		